Development of a coherent ultrafast transmission electron microscope based on a laser-driven cold field emission source

Giuseppe Mario Caruso

THÈSE

En vue de l'obtention du

DOCTORAT DE L'UNIVERSITÉ DE TOULOUSE

Délivré par l'Université Toulouse 3 - Paul Sabatier

Présentée et soutenue par

Giuseppe Mario CARUSO

Le 20 mars 2019

Development of a coherent Ultrafast Transmission Electron Microscope based on a laser-driven Cold Field Emission source

---

Ecole doctorale : **SDM - SCIENCES DE LA MATIERE - Toulouse**

Spécialité : **Physique**

Unité de recherche :
CEMES - Centre d'Elaboration de Matériaux et d'Etudes Structurales

Thèse dirigée par
Arnaud ARBOUET et Florent HOUDELLIER

Jury

Mme Odile STéPHAN, Rapporteure
M. Angus KIRKLAND, Rapporteur
M. Xavier MARIE, Examinateur
M. Axel LUBK, Examinateur
M. Arnaud ARBOUET, Directeur de thèse
M. Florent HOUDELLIER, Co-directeur de thèse

Ad Alfio e Giuseppe

Contents

Outline **i**

1 Introduction **1**

1.1 Ultrafast dynamics in condensed matter 1

1.2 Transmission Electron Microscopy 4

1.2.1 Architecture of a TEM 5

1.2.2 Fundamental concepts in TEM 10

1.2.3 Electron Holography 16

1.2.4 Electron sources 19

1.2.5 Brightness 26

1.3 Time-resolved TEM 29

1.3.1 Dynamic TEM and Ultrafast TEM 30

1.3.2 Laser-driven electron emission 32

1.3.3 Influence of the electron dynamics on the electron energy distribution 34

1.3.4 Electron pulse broadening: influence on UTEM spectro-temporal properties 39

1.3.5 Conclusions 43

2 Instrumental development **45**

2.1 Presentation of the modified Hitachi HF2000 - FemtoTEM 45

2.1.1 Architecture of the laser-driven CFEG 47

2.1.2 Electron trajectories 51

2.1.3 Light injection and collection from inside the objective lens . . . 55

2.1.4 Ultrafast optics set-up 57

2.2 Properties of the CFEG UTEM 59

2.2.1 The ultrafast electron source 59

2.2.2 Probe current stability 62

2.2.3 FemtoTEM optimization 64

2.2.4 Measurement of brightness and angular current density 68

2.2.5 Demonstration of operation as a TEM 71

2.3 Conclusion 74

3 Electron pulse characterization **77**

3.1 Electron Energy Gain Spectroscopy 78

3.1.1 Electron-photon interaction 78

3.1.2 EEGS: theoretical formalism 81

3.1.3 Influence of experimental parameters on EEGS 85

3.2 Temporal characterization of ultrashort electron pulses 89

3.2.1 Characterization of chirped electron pulses 91

3.2.2 Gain spectra simulations and evaluation of the electron pulse duration 95

3.3 Conclusions 98

4 Ultrafast Electron Holography **99**

4.1 Holography: requirements and limits 99
4.1.1 Hologram figures of merit 101
4.1.2 Optimization 103
4.2 Electron holography using ultrashort electron pulses 105
4.2.1 Low-dose-like conditions 105
4.2.2 Electron holography with femtosecond electron pulses on MgO nanocubes 110
4.3 Towards ultrafast electron holography 113
4.4 Conclusion 117

Conclusions and perspectives **119**

Résumé **123**

Acknowledgement **167**

Bibliography **195**

Outline

The birth and development of Transmission Electron Microscopy (TEM) marked a real breakthrough in the investigation of the nanoscale world. Indeed, TEM provides material information in both direct and reciprocal space as well as Electron Energy Loss Spectra (EELS) with nanometer scale spatial resolution. The exploitation of extremely coherent electron sources [1, 2, 3] allowed to push the limits of the instrument further away. The minimization of the electron beam spot size and energy spread, as well as brightness improvement, allowed High Resolution Scanning TEM-EELS (STEM-EELS) and also the acquisition of electron holograms [4]. The analysis of the latter allows the electron beam phase reconstruction to map electric, magnetic and strain fields at the nanoscale [5].

Thanks to technological improvement over the years, TEM can now achieve a sub-ångström spatial resolution [6, 7] and an energy resolution close to 10 meV [8, 9]. Furthermore, new specimen holders [10] allowed the implementation of *in situ* experiments. These developments broadened the fields of application of TEM. Its versatility enables TEM to find applications in several fields of science such as physics, materials science [11, 12], biology [13, 14, 15], chemistry [16, 17, 18, 19], geology [20] and medicine [14]. However, until the late 1970s [21], TEM studies have been restricted to systems that do not evolve in time. *In situ* techniques [22] allow to monitor the evolution of a

sample under external stimuli such as mechanical traction [23], temperature variation [24] or applied bias [25]. These modifications can then be monitored by a CCD camera. Nevertheless, the temporal resolution is limited by the CCD frame rate, which reaches 1600 fps in the most recent and fastest cameras [26]. *In-situ* TEM allows to follow, for instance, nanoparticle assembling [27] or grain boundary motions [28]. But if one wants to look further into structural or electronic dynamics, the relevant timescale is in the pico- to femtosecond range and therefore *in situ* TEM can not provide the required temporal resolution. A new approach is therefore necessary to study ultrafast processes. Almost in parallel with the development of *in situ* electron microscopy, Oleg Bostanjoglo laid the foundations for the first time-resolved electron microscope [29, 30]. Its original concept of Dynamic Transmission Electron Microscope allowed to study non-reversible phenomena with a spatial resolution of hundreds of nanometer and a pulse duration around the nanosecond. Subsequently such an instrument has been improved in the Lawrence Livermore National Laboratory with a new illumination optics and acquisition system but the real breakthrough has been achieved in Caltech in the group of Ahmed Zewail that introduced the concepts of *single electron regime*. Achieving an unprecedented spatio-temporal resolution in the nanometer and femtosecond range, the Ultrafast Transmission Electron Microscopy (UTEM) was born.

The aim of this thesis is to reports on the development of the first Ultrafast Transmission Electron Microscope equipped with a Cold Field Emission Gun (CFEG), in order to improve the brightness of the electron source implemented in the UTEMs and push the instrument to applications in electron interferometry.

In the following, Chapter 1 introduces the fundamental concepts in conventional and time-resolved Transmission Electron Microscopy (TEM). Timescales in condensed matter are presented as well as the TEM architecture and main notions. Then, the dif-

ferences between Dynamic and Ultrafast TEM are addressed. Particular emphasis has been put on the laser-driven emission mechanism from a metallic nanotip.

Chapter 2 describes the instrumental development. The modified CFEG is detailed as well as the complete experimental set-up. The properties of the UTEM are described: probe current stability, brightness, angular current density and the achieved spatial and spectral resolutions.

Chapter 3 addresses the first time-resolved pump-probe experiment. The theory of Electron Energy Gain Spectroscopy (EEGS) and the influence of the experimental parameters on the gain spectrum are presented. The pulsed electron beam is then temporally characterized: the pulse duration and the electron chirp are evaluated and the experimental results are compared with simulations.

In Chapter 4, perspectives on off-axis electron holography using ultrashort electron pulse are given. First, requirements and limits in conventional electron holography are presented. Secondly, the drawbacks of working with a pulsed electron beam are identified and possible solutions to perform Ultrafast Electron Holography (UEH) are proposed.

Finally, the main results and some perspectives are summarized.

Chapter 1

Introduction to Ultrafast Transmission Electron Microscopy: important timescales and concepts

1.1 Ultrafast dynamics in condensed matter:main processes and timescales

As an introduction, we briefly describe the characteristic timescales of physical processes in atoms, molecules and condensed matter.

As we can appreciate from Figure 1.1, electronic motion in atomic systems occurs on the attosecond timescale. In particular, the revolution of an electron around the hydrogen atom nucleus in Bohr's model has a period of 152 as. Still considering particle motion, molecular vibration and rotation have, instead, characteristic timescales in the femto- to picosecond range. We want to shift now the focus on the dynamics of a solid

excited by a femtosecond light pulse, which is the first step in time-resolved TEM. On a timescale comparable to the laser pulse duration, the light pulse couples coherently to the nanostructure. In a metallic nanoparticle, for instance, such an interaction can excite a surface plasmon, namely a collective electronic excitation. This established coherent phase relation lasts $\sim 10\,\mathrm{fs}$, *i.e.* until the dephasing of the plasmon. After this initial step, electron-electron interactions take place and the electron gas goes back to a Fermi-Dirac distribution. In metals like gold and silver, this process takes around a few hundreds femtosecond. Also electron-lattice interactions occur in bringing the system back to equilibrium.

An ultrafast light pulse also places the lattice out of equilibrium, inducing mechanical vibrations. The vibration period of confined acoustic modes is L/v, linked to the nano-object size, L and the speed of sound, v. Typical values for nanosized systems $(10 - 100\,\mathrm{nm})$ lie in the $10 - 100\,\mathrm{ps}$ range. During its de-excitation, the nano-object also diffuses heat toward the environment.

Also magnetic systems are involved in ultrafast dynamics, as it is represented in Figure 1.1 where characteristic timescales are highlighted.

Figure 1.1 clearly shows that many important physical processes occur on a sub-nanosecond timescale, *i.e.* too fast to be detected using traditional cameras. Even if the first time-resolved electron microscopes had already been developed [31, 32, 33], it is only in 2005 that TEM became ultrafast [34, 35], achieving an unprecedented spatio-temporal resolution in the sub-nanometer and sub-picosecond range [36, 37, 38, 39, 40]. This breakthrough was based on the use of electron pulses containing only a few electrons, thereby minimizing the coulomb interparticle repulsion that deteriorated spatio-temporal resolution in the earlier time-resolved electron microscopes. In this so called *single electron regime*, images, Diffraction Patterns (DP) and spectra were

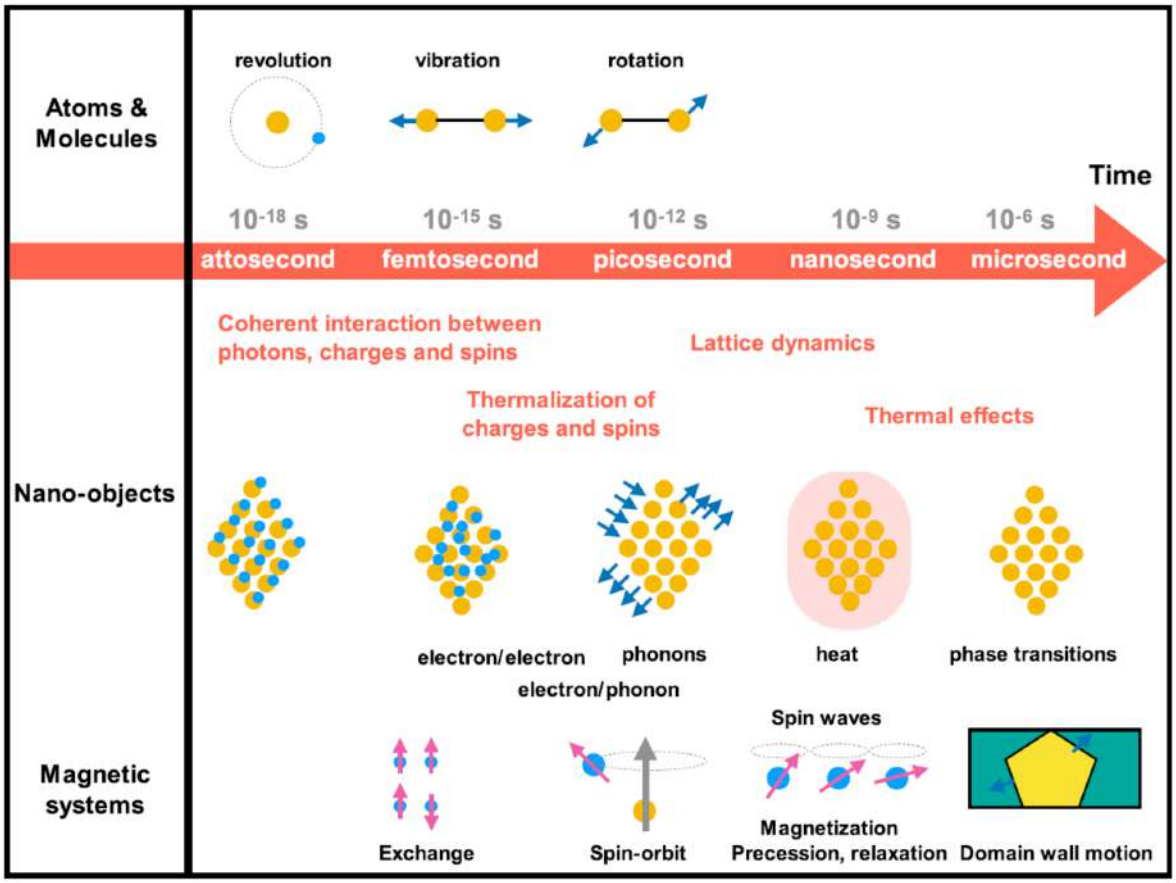

Figure 1.1: Characteristic timescales of ultrafast processes in particles, nano-objects and magnetic systems.

recorded from the accumulation of billions of excitation-detection cycles. Since 2005, the field of UTEM has kept on growing at a fast pace with an ever increasing number of groups, either from TEM or optical spectroscopy, developing or acquiring their own instrument.

In the next paragraphs a concise presentation of the fundamental concepts of electron microscopy will be given. The architecture of a transmission electron microscope will be discussed as well as the conventional techniques. Finally, the different type of continuous

electron sources are discussed, paying particular attention to the most important beam properties, such as the beam brightness.

1.2 Transmission Electron Microscopy

The high spatial resolution of TEM [7] is a consequence of the wave-particle dual nature of the electron. In 1923, De Broglie proposed in his Ph.D. the hypothesis [41] that a massive particle exhibits a wave-like behaviour. The associated *de Broglie wavelength* is given by

$$\lambda_B = \frac{h}{p} \tag{1.1}$$

where h is Planck's constant and p the particle momentum. For instance, a 150 keV electron has a wavelength $\lambda_B = 2.96\,\mathrm{pm}$[1]. It was soon realized that the small value of the de Broglie wavelength of the electron makes it ideal for microscopy. Indeed, the classical Rayleigh criterion [42] (originally applied to light microscopes) establishes that the minimum resolvable detail has a size given by:

$$R = 0.61\frac{\lambda}{\alpha} \tag{1.2}$$

where λ is the wavelength of the radiation used to illuminate the sample and α is the beam opening angle. Using deep UV laser light ($\lambda \sim 13\,\mathrm{nm}$) the resolution of an optical microscope can reach $\sim 38\,\mathrm{nm}$ [43, 44], but equation (1.2) shows that exploiting a $\lambda_B = 2.96\,\mathrm{pm}$, the minimum resolvable distance should be in theory smaller than 2 pm. The main reason why this resolution is far from being achieved in TEM lies in the electromagnetic lens aberrations that will be discussed in the following.

[1] for particles faster than $\sim 0.5c$, one has to consider the relativistic formula $\lambda_B = \frac{h}{\left[2m_0eV\left(1+\frac{eV}{2m_0c^2}\right)\right]^{1/2}}$

1.2.1 Architecture of a TEM

A transmission electron microscope can be divided in two main parts: *i.e.* the electron gun and the microscope column. The latter are traditionally evacuated between Ultra High Vacuum[2] (UHV) and High Vacuum[3], respectively. Vacuum is fundamental in TEM to allow electrons to travel freely from the electron source to the specimen and then the detector.

The electron gun

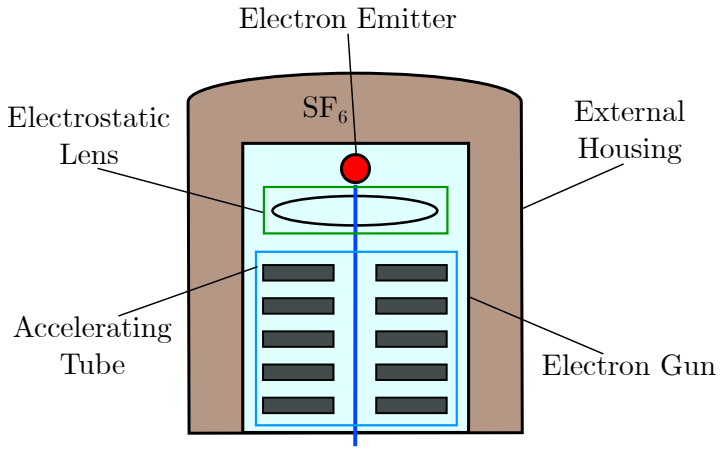

Figure 1.2: Schematic representation of an electron gun. The *external housing*, filled with pressurized SF_6 (in brown), ensures electrical insulation. The *electron gun* is composed of an *electron emitter*, an *electrostatic lens* and an *accelerating tube*. The electron gun is evacuated to UHV. In blue, an electron trajectory along the optical axis is sketched.

The purpose of the electron gun is to generate an accelerated electron beam. The general structure is given in Figure 1.2: the electron gun is enclosed inside an external housing filled with pressurized SF_6 (sulfur hexafluoride), used to provide electrical

[2] $< 10^{-5} Pa$ [45]
[3] $10^{-4} Pa - 10^{-5} Pa$ [45]

insulation.

The gun, located inside this insulating housing, can be decomposed in three parts: an electron source (further details on the different types of electron sources will be provided later in this chapter), a lens and an accelerating tube. The electron emitter (in red) can be described as a *point source*. The lens (highlighted in green) is located just below the electron source. Its role is to focus the emitted electrons into a *crossover*, *i.e.* an image of the source, which can either be real or virtual [46]. Electrons are finally accelerated in several steps, to reach a kinetic energy in the 100 - 300 keV range [47].

The microscope column

Once accelerated, the electron beam enters the column of the TEM. The one that we have modified in this thesis (an Hitachi HF2000) is sketched in Figure 1.3. The column is composed of a set of round electromagnetic lenses [48] and deflectors. An electromagnetic lens is used to focus the electron beam towards the optical axis and magnify or demagnify an object. Figure 1.4 shows a schematic representation of an electromagnetic lens, which is basically an electromagnet. A current circulates through a *coil* generating an electromagnetic field. The magnetic flux is then concentrated inside the gap of a *polepiece* made of pure iron, *permendur* (Fe-Co) or *permalloy* (Fe-Ni). The resulting magnetic induction, located in the polepiece gap, acts on the electron beam like a thin glass lens on light because of the Lorentz force. Exactly like in light optics, it is possible to define for these electromagnetic lenses specific *cardinal planes*, *i.e.* an *object plane*, a *focal plane* and an *image plane*. Electrostatic lenses [50] can be used in electron microscopy as well but their spherical and chromatic aberrations are worse than their electromagnetic counterpart at comparable focal distance [49]. In general, these lenses are used in guns where the integration of an electromagnetic lens is tech-

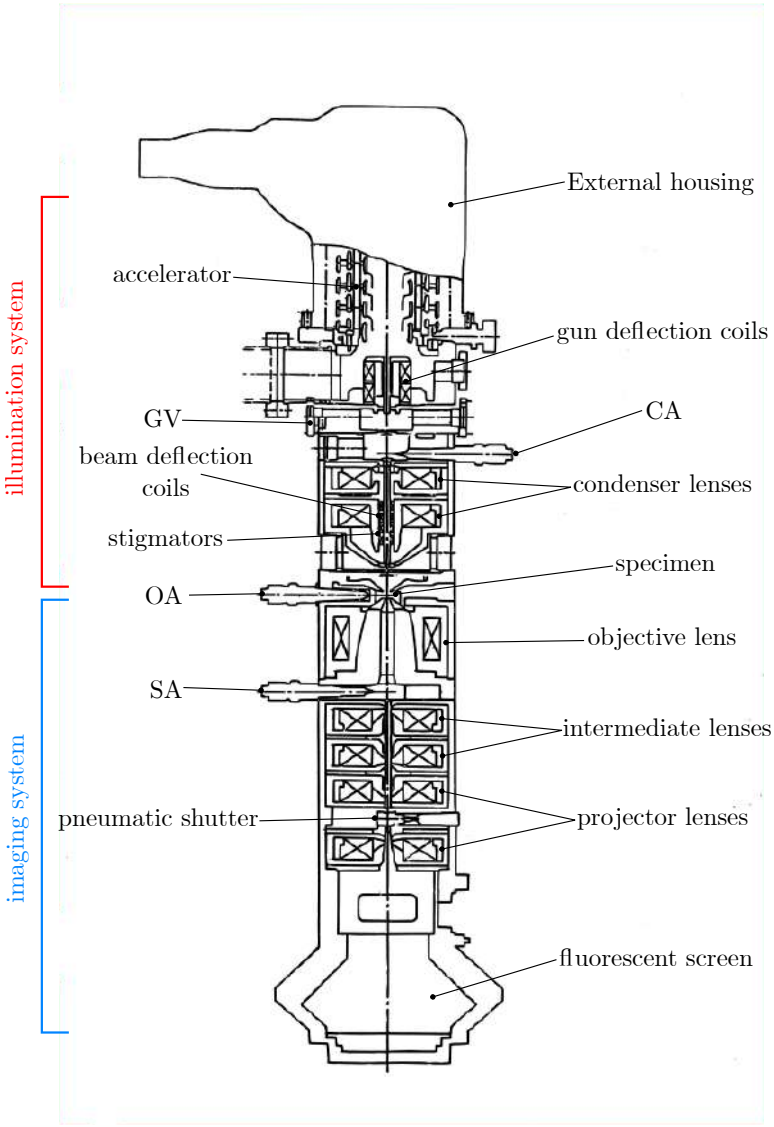

Figure 1.3: Scheme of a TEM HITACHI HF2000. GV: Gun Valve. CA: Condenser Aperture. OA: Objective Aperture. SA: Selected Area aperture.

.

nically complicated.

The first two lenses on the electron beam trajectory after the gun are called condenser

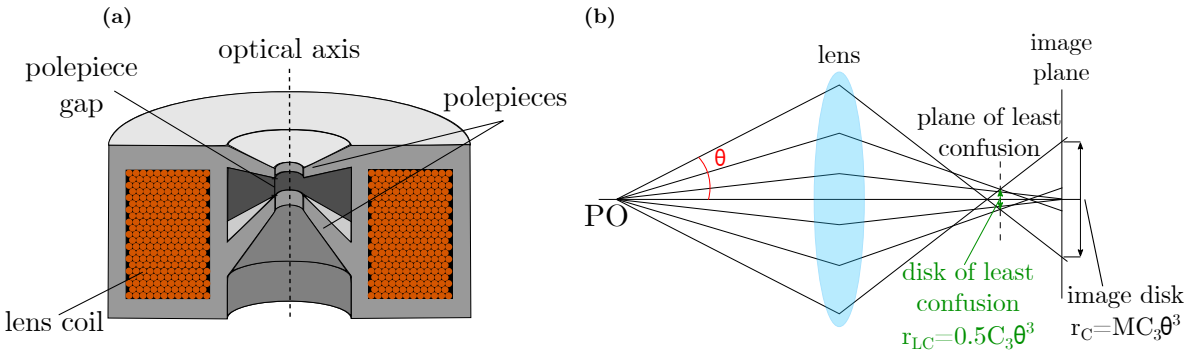

Figure 1.4: (a) Section of an electromagnetic lens. (b) Effect of the spherical aberration in a lens: the Point Object (PO) is imaged as a disk of radius r_C on the image plane. The *plane of least confusion* is where the smallest image of the PO is created: the radius of the *disk of least confusion* is $r_{LC} = 0.5\, C_3\theta^3$ [49].

.

lenses. These, together with the electron gun, change the illumination condition on the specimen: they form the *illumination system*. The electron beam then interacts with the specimen that has been previously installed on a suitable holder. The specimen holder is usually located *inside* the objective lens, which is therefore an immersion lens [51, 52].

Electromagnetic lenses suffer from aberrations. In general, the latter can be divided into *geometrical* [53] and *chromatic aberrations* [54]. The former are also called *Seidel aberrations* and among them the *spherical aberration* is the one which affects the spatial resolution of a TEM. Due to this aberration, paraxial electrons are less focused than the ones travelling far from the optical axis. This effect transforms a point object in a disk of radius $r_C = MC_3\theta^3$, M being the magnification, C_3 the object side spherical aberration coefficient [55, 56] and θ the collection angle. Spherical aberration has long been an insurmountable limitation: the development of spherical aberration correctors at the end of the 20$^{\text{th}}$ century [6, 57, 58, 59, 60, 61] was a real breakthrough in electron

microscopy. Finally, the image created by the objective lens is magnified by the intermediate and projector lenses and finally projected on a fluorescent screen or a CCD camera.

Other elements are present in a TEM column, such as *deflectors* [62], *stigmators* [62] and *apertures*. The first two are made of *multipolar* elements. In particular, deflectors are composed by a set of two dipoles, used to tilt or shift the electron beam, while a stigmator is a set of two quadrupole lenses [63] used to correct lens *astigmatism* [53].

Three sets of apertures are placed in the TEM column as reported in Figure 1.3. The *condenser aperture* is located in the illumination system and is used to limit the electron beam angular size [42]. The *Objective Aperture*, located in the objective lens (OL) focal plane, is used to create a contrast in the image by filtering the transmitted beam or one useful diffracted beam. The last set of apertures, called *Selected Area* (SA), is located in the objective lens image plane and allows to select a useful Region Of Interest (ROI) on the image.

Spectrometers

During the interaction with the specimen, electrons can lose part of their kinetic energy [64]. An Electron Energy Loss Spectrum (EELS) contains fundamental informations on the chemical composition and electronic structure of the sample. In order to discriminate the electrons as a function of the energy, a magnetic field is applied perpendicular to their trajectories. A magnetic sector [65] is installed after the column to disperse in energy and spatially focus the primary electron beam. The spectrum, located in the dispersion plane of the magnetic sector, is finally magnified and focused on a CCD using a set of multipolar lenses. Modern electron energy loss analysis systems are either Parallel EELS (PEELS) [66, 67], or imaging filters, such as a Gatan Imaging Filter

(GIF) [68]. The latter can record an EELS spectrum as well as an image of the sample filtered at a specific energy.

Detectors

A TEM is also equipped with appropriate detection systems. *Faraday cups* [69], for instance, are used to measure the electron beam current. They can be installed on specimen holders to evaluate the current on the sample (namely the *probe current*) or elsewhere in the column, for instance together with an aperture set, to measure the beam current in various optical planes of the microscope.
Image acquisition is achieved following two different approaches. In *indirect detection*, a scintillator converts electrons in photons that are then detected by a CCD or a CMOS sensor [70]. On the other hand, *direct electron detection* exploits a thin ($\sim 150\,\mu$m) silicon layer to create electron-hole pairs after the interaction with the electron beam. These charges are then accelerated toward electrodes where they are collected [71, 72, 73, 74].

1.2.2 Fundamental concepts in TEM

The interaction between the electron beam and the specimen is the foundation of imaging theory in TEM. In this work, the samples studied are solid and crystalline. This is why, in the following, the interaction between an incident electron wave and a crystalline lattice is discussed. The scattering of an electron beam from a family of parallel planes is due to the interaction of the beam with the crystalline lattice potential. An electron wave with a de Broglie wavelength λ_B, can be diffracted by a set of reticular planes defined by an intereticular distance d_{hkl} for a specific incoming angle θ_{Bragg}.

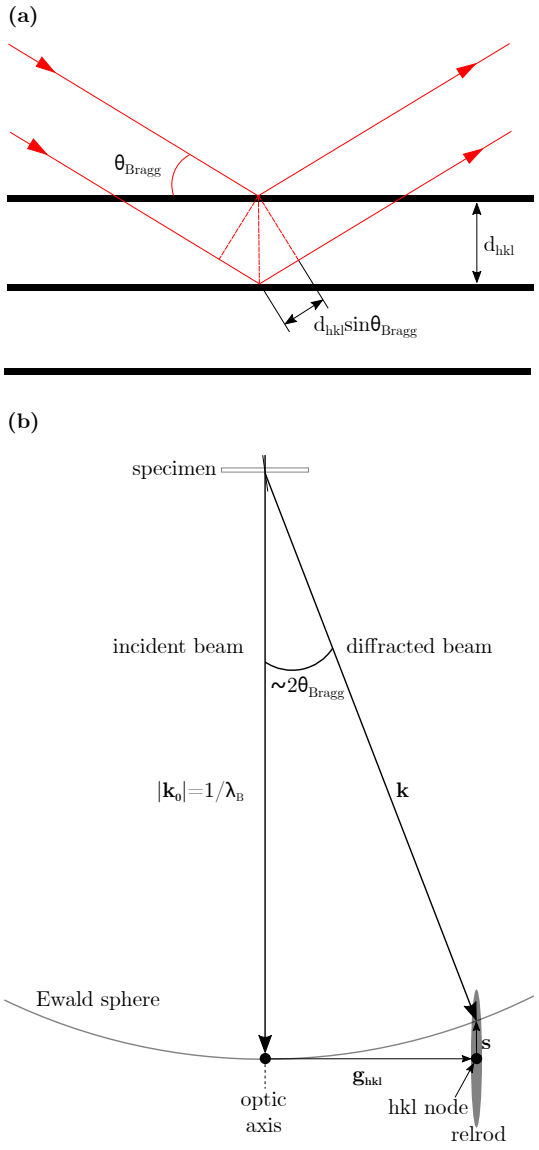

Figure 1.5: (a) Schematic representation of Bragg's law. For the sake of simplicity just two planes of the family (hkl) are sketched. $2d_{hkl}\sin\theta_{Bragg}$ represents the path difference between two waves. (b) Ewald sphere construction for electron diffraction: a set of (hkl) planes close to the Bragg orientation with respect to the incident beam is taken into account.

.

These three quantities, defined on Fig. 1.3 (a), are related by Bragg's law

$$2d_{hkl}\sin\theta_{Bragg} = \lambda_B \tag{1.3}$$

d_{hkl} and λ_B being respectively a property of the specimen and the electron beam. Equation (1.3) is only verified for certain angles called Bragg angles, θ_{Bragg}.

A way to easily visualize the Bragg conditions relies on the *Ewald sphere*, drawn in the reciprocal space and sketched in Figure 1.5 (b). The sphere is centred on the specimen and has a radius $|\mathbf{k_0}| = \frac{1}{\lambda_B}$. The lattice drawn in the bottom represents the *reciprocal lattice* [75, 76] of the crystal. The diffraction conditions can be retrieved from the intersection of the Ewald sphere with the reciprocal lattice *nodes* $|\mathbf{g_{hkl}}| = \frac{1}{d_{hkl}}$. This representation is valid in all diffraction experiments, such as X-Rays diffraction, for instance. However, in TEM due to the specimen thickness (between 20 and 100 nm), a relaxation of the Bragg condition occurs: electron diffraction can occur even if Bragg's law is not strictly verified. To take into account this relaxation, the reciprocal lattice nodes become *relrods* for thin planar sample (Figure 1.5 (b)). Their intersections with the Ewald sphere give the diffraction condition. The vector $\mathbf{s}$, represented in Figure 1.5 (b) is called *excitation* or *deviation vector*. It is directed perpendicularly to the sample surface, *i.e.* along the thinning direction. Diffraction condition is satisfied under a new condition: $\mathbf{k} - \mathbf{k_0} = \mathbf{g_{hkl}} + \mathbf{s}$ and the diffracted intensity depends on the intersection position between the Edwald sphere and the relrod. Intensities can be determined by either the *kinematical theory* [77, 78] that will consider only weak diffraction conditions, or *dynamical theory* [77, 79] in which multiple scatterings are taken into account (strong diffraction conditions).

Image formation

As already stated in the previous paragraph, in a (S)TEM the specimen is inserted inside the objective lens. Assuming, for the sake of simplicity, a parallel illumination on a crystalline specimen, Figure 1.6 shows the electrons ray path leading to the formation of a crystal Diffraction Pattern (DP) in the Back Focal Plane (BFP) of the objective lens and a specimen image on the image plane. The electron beam can be described by

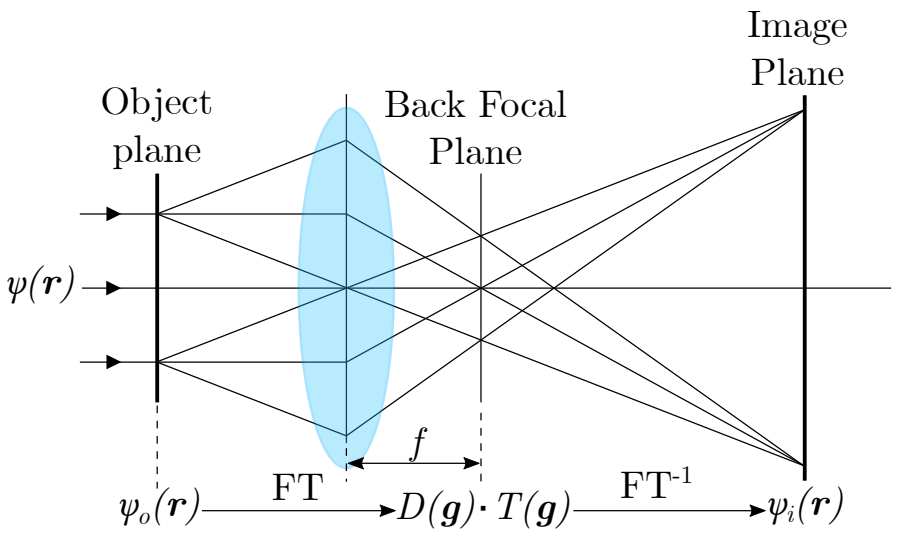

Figure 1.6: Abbe description of the image creation [80]. f represents the lens focal distance.

.

a complex wave

$$\psi(\mathbf{r}) = a(\mathbf{r})e^{i\phi(\mathbf{r})} \tag{1.4}$$

where $a(\mathbf{r})$ is the amplitude, $\phi(\mathbf{r})$ the phase and $\mathbf{r}$ a direct space vector. Calling $\psi_o(\mathbf{r})$ the electron wavefunction after the interaction with the specimen (namely the *object function*), the DP wavefunction is given by the product $D(\mathbf{g}) \cdot T(\mathbf{g})$, with $D(\mathbf{g}) = \mathbf{FT}(\psi_o(\mathbf{r}))$ the Fourier Transform (FT) of $\psi_o(\mathbf{r})$, $\mathbf{g}$ a vector belonging to Fourier space

and $T(\mathbf{g})$ the *objective lens transfer function*, defined as follows:

$$T(\mathbf{g}) = 2A(\mathbf{g}) \sin \chi(\mathbf{g}) \tag{1.5}$$

$A(\mathbf{g})$ being a function that takes into account the effect of the apertures on the electron beam [55]. $\chi(\mathbf{g})$ is called *Phase Contrast Transfer Function* (PCTF)

$$\chi(\mathbf{g}) = \pi C_1 \lambda g^2 + \frac{1}{2}\pi C_3 \lambda^3 g^4 \tag{1.6}$$

and depends on the defocus C_1 [4] and the spherical aberration coefficient, C_3 [5]. $\chi(\mathbf{g})$ (and therefore $T(\mathbf{g})$) relates the image contrast to the phase variation of the electron wave after the interaction with the specimen. Figure 1.6 also shows that applying an Inverse Fourier Transform (FT^{-1}) to $D(\mathbf{g}) \cdot T(\mathbf{g})$ an *image function* $\psi_i(\mathbf{r})$ can be defined.

Figure 1.7 shows the transfer function for the Hitachi HF2000 used in this thesis, with $C_3 = 1.2\,\mathrm{mm}$ and $\lambda_B = 2.96\,\mathrm{pm}$ ($K_e = 150\,\mathrm{keV}$[6]). Ideally, $T(\mathbf{g})$ should be a constant function so that the transfer of contrast is the same for all spatial frequencies (*i.e.* for all diffracted beams). In practice, for a microscope not corrected from the spherical aberration, the optimum condition is achieved by defocusing the OL by a certain amount called *Scherzer defocus* [81]

$$C_{1-sch} = -1.2(C_3\lambda)^{1/2}. \tag{1.7}$$

that is $C_{1-sch} = -71.5\,\mathrm{nm}$, in our case. High Resolution (HR) [55] imaging comes from the interference between overlapping transmitted and diffracted beams for a specimen oriented in *zone-axis*. This technique allows to observe the projection of the atomic

[4] in-focus images have $C_1 = 0\,\mathrm{mm}$

[5] The other aberrations are considered as negligible compared to C_3 and C_1.

[6] Is the energy used in the following of this work

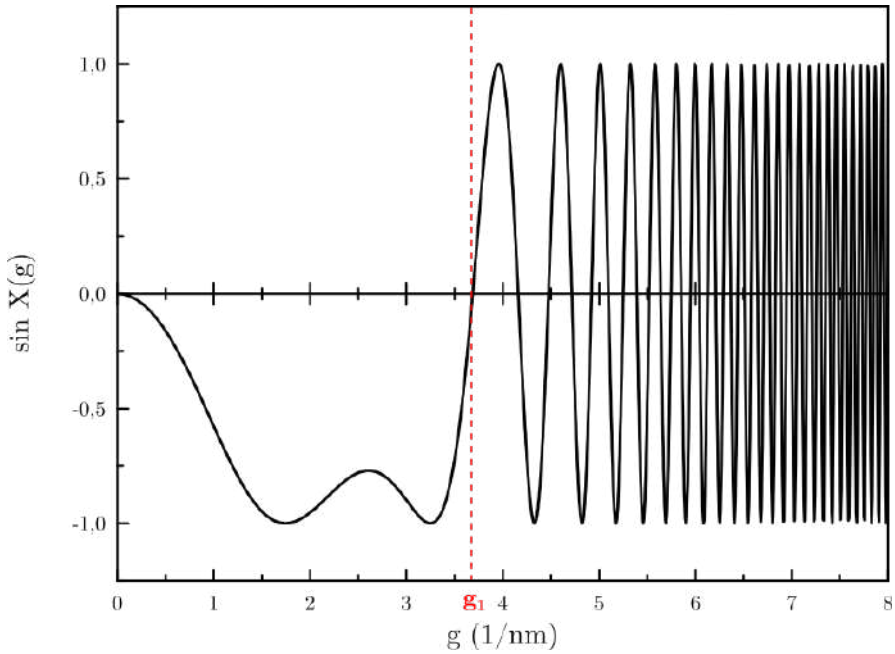

Figure 1.7: Transfer function for a Hitachi High Technologies HF2000 operating at 150 kV; $C_3 = 1.2\,\text{mm}$, $C_1 = -71.5\,\text{nm}$. A negative value of $T(\mathbf{g})$ indicates a *positive phase contrast* and the specimen image appears dark against a bright background. The inversion of $T(\mathbf{g})$ indicates a change of contrast. The vector $\mathbf{g} = \mathbf{g_1}$ is an important parameter defining the resolution limit of the instrument [55]. Transfer function also shows maxima that indicate a maximum transfer of contrast. Aberrations have not been taken into account.

structure of the sample thanks to multiple interferences due to the overlap of transmitted and diffracted beams in the image plane. Using the Scherzer defocus in a non corrected microscope, the contrast is called *phase contrast*. Other types of contrast can be found in TEM. The *mass-thickness contrast* [82], for instance, is used to study non crystalline materials or biological samples. *Diffraction contrast* [82] is obtained by selecting either the transmitted electron beam or one diffracted beam with the objective aperture. The resulting image is called Bright Field (BF) or Dark Field (DF), respectively. The techniques just listed above allow to create images that represent

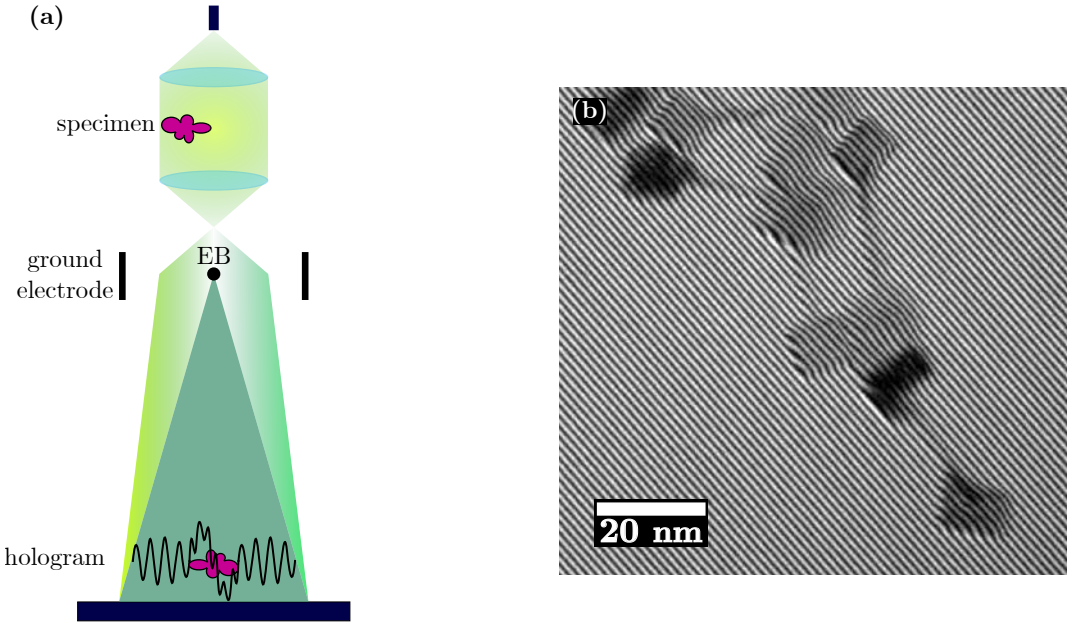

Figure 1.8: (a) Principle of off-axis electron holography. The phase variation in the hologram is due to the beam interaction with the specimen. (b) An electron hologram of iron cubes.

the distribution of the electron beam intensity, $I(\mathbf{r}) = |\psi_i(\mathbf{r})|^2 = |A_i(\mathbf{r})|^2$, after the interaction with the specimen. Therefore, the image does not give access to the phase of the electron wave.

1.2.3 Electron Holography

Proposed by Gabor as a new experimental method to improve the electron microscope resolution [4], electron holography offers the unique possibility to map electromagnetic [5, 83] or strain fields [84, 85] by measuring the variation of the phase of the electron wave induced by the Aharonov-Bohm (AB) effect [86, 87, 88, 89]. Experimentally evidenced by Tonomura *et al.* [90], the AB effect demonstrates the physical existence of the magnetic vector potential.

The idea behind electron holography is to create an interference pattern, called *hologram*, between the object phase wave and a reference wave. This hologram is then analysed providing the phase and the amplitude of the complex object phase wave. Several configurations have been proposed over the years [91], but we will describe only *off-axis electron holography*, *i.e.* the approach used in this thesis. As sketched in Figure 1.8 (a), a coherent parallel electron beam is used to illuminate the specimen. More precisely, half of the beam illuminates the ROI of the specimen under analysis while the other half travels in vacuum and will be used as reference wave. A Möllenstedt electron biprism (EB) [92, 93] is a charged wire surrounded by parallel-plate ground electrodes located above the objective lens image plane (Figure 1.8 (a) and Figure 2.1 (b)). A voltage between 0 V and 500 V can be applied on it. As a result, the EB splits the electron wave in two parts that overlap below the wire. The *reference beam*, *i.e.* the beam that propagates in vacuum, is overlapped with the beam that crossed the specimen. If the spatial coherence is sufficient, an interference pattern can be observed in the image plane. An example of such an electron hologram is shown in Figure 1.8 (b).

An electron hologram is determined by its width and the fringe spacing. Both can be modified by changing the biprism voltage and the electron optical conditions. More details will be provided in Chapter 4.

Hologram intensity

Considering the interference between two coherent electron waves $\psi_i(\mathbf{r})$ and $\psi_r(\mathbf{r})$, namely the image and the reference beam, expressed as in (1.4), the intensity of the hologram $I_{holo}(\mathbf{r}) = |\psi_i(\mathbf{r}) + \psi_r(\mathbf{r})|^2$ has the following expression [94, 95, 96]

$$I_{holo}(\mathbf{r}) = 1 + |A_i(\mathbf{r})|^2 + 2A_i(\mathbf{r})\ cos(2\pi \mathbf{g_c} \cdot \mathbf{r} + \Delta\phi). \tag{1.8}$$

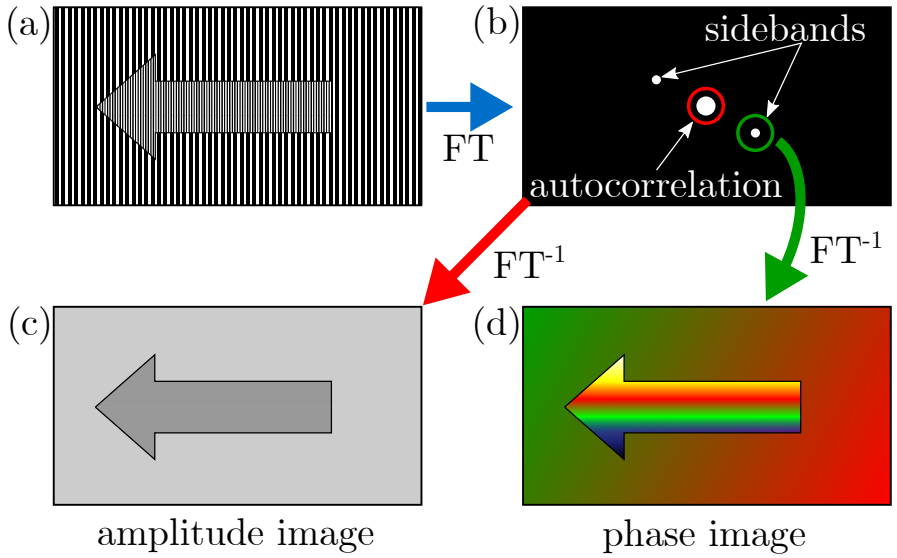

Figure 1.9: Procedure of the phase reconstruction from a hologram. Applying a Fourier Transform to a hologram (a), a diffraction pattern (b) containing the sidebands and the autocorrelation is obtained. By adding a mask to filter the former (the latter) and then applying an inverse Fourier transform, a phase (d) (an amplitude (c)) image can be reconstructed.

The first two terms represent the intensity of the two interfering waves (the reference wave amplitude is set to $A_R(\mathbf{r})$=1). The third term represents a system of fringes of amplitude $2A_i(\mathbf{r})$. From the latter, the information on the electronic phase can be extracted. The argument of the cosinus function contains the phase difference $\Delta\phi$ between the image and the reference wave. $\mathbf{g_c}$, known as the *hologram carrier frequency*, is related to the difference between the wavevectors of the image and the reference beams, *i.e.* the tilt angle between the two beams.

Phase reconstruction

Figure 1.9 shows schematically how to extract the phase and amplitude from the hologram. The Fourier Transform (FT) of equation (1.8) is:

$$\begin{aligned}\mathbf{FT}(I_{holo}(\mathbf{r})) =& \delta(\mathbf{g}) + \mathbf{FT}(|A_I(\mathbf{r})|^2) + \\ & \delta(\mathbf{g}+\mathbf{g_c}) \otimes \mathbf{FT}(2A_I(\mathbf{r})\ e^{i\Delta\phi}) + \\ & \delta(\mathbf{g}-\mathbf{g_c}) \otimes \mathbf{FT}(2A_I(\mathbf{r})\ e^{-i\Delta\phi})\end{aligned} \tag{1.9}$$

where the first two terms in equation (1.9) are a Dirac delta function and the FT of the image wave amplitude. Both of them correspond to the central area in Figure 1.9 (b) highlighted in red and called *central band* (or *autocorrelation*). The third and fourth terms are two peak functions centred on the carrier frequencies $\mathbf{g} = -\mathbf{g_c}$ and $\mathbf{g} = \mathbf{g_c}$ representing the FT of the image wave and its complex conjugate. The latter are called *sidebands*. They contain the phase information and since one is the complex conjugate of the other, the extracted information will be the same.

To extract the phase, one has to use a *mask* to select one of the two sidebands, as shown in Figure 1.9 (b) (green circle). Applying then an inverse Fourier transform, the complex wavefunction and therefore the phase of the electron wavefunction can be extracted. To avoid artefacts, the sidebands and the autocorrelation should be well separated. The spatial resolution of the reconstructed amplitude or phase is given by the mask size. Placing instead a mask on the autocorrelation, the reconstructed image contains just the amplitude, as in conventional TEM imaging (Figure 1.9 (c)). Decreasing the mask dimension in Fourier space increases the signal-to-noise ratio and deteriorates the resolution in direct space.

1.2.4 Electron sources

Several sources of electrons are available: *thermionic*, *cold field emission* and *Schottky* electron sources. We here describe the physical mechanisms involved in electron emission.

The highest occupied electronic energy level inside a material at $T = 0\,\mathrm{K}$ is called the

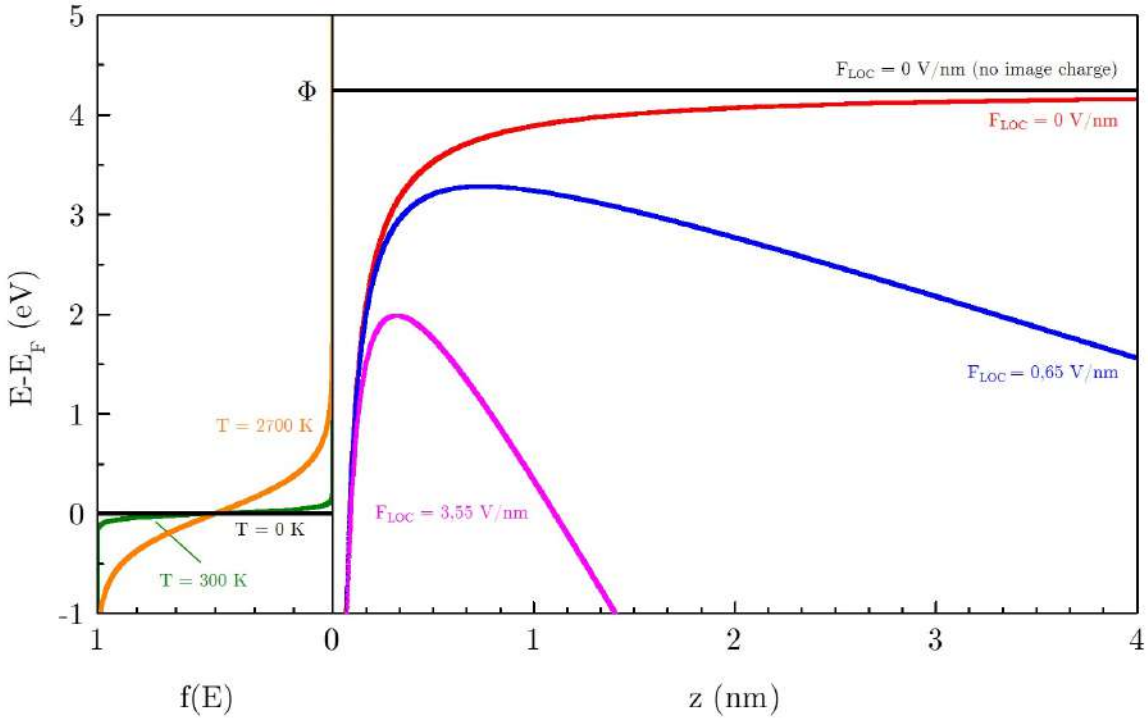

Figure 1.10: *Left side.* Fermi-Dirac (F-D) distribution at three different temperatures: $T = 0\,\mathrm{K}$ (black curve), $T = 300\,\mathrm{K}$ (green curve), $T = 2700\,\mathrm{K}$ (orange curve) that is the typical temperature used for thermionic emission from tungsten. *Right side.* Potential barrier at a metal-vacuum interface for $< 310 >$-oriented tungsten ($\phi = 4.25\,\mathrm{eV}$) for different values of the applied electric field. The black curve represents the potential barrier without any applied electric field and neglecting the image charge contribution. The coloured curves take into account the image charge in three cases: no applied field (red), Schottky electron gun $F_{LOC} = 0.65\,\mathrm{V/nm}$ (blue) and Cold Field Emission Guns $F_{LOC} = 3.55\,\mathrm{V/nm}$ (magenta). **z** is perpendicular to the metal surface.

Fermi level, E_F. When the temperature of the system is increased, some electrons can gain energy and be promoted to higher energy levels [76]. The occupation number $f(E,T)$ describes the probability of having an electron on a state of energy E. It is

given by the *Fermi-Dirac* (FD) distribution

$$f(E,T) = \frac{1}{\exp\left(\frac{E-E_F}{k_B T}\right)+1} \tag{1.10}$$

where k_B is Boltzmann's constant.

As shown in Figure 1.10, at $T = 0\,\mathrm{K}$ the FD distribution is a step function (black curve) that changes with the temperature of the system.

To be emitted in vacuum, an electron inside a material at the Fermi level requires an extra energy at least equal to the *material work function*, Φ. At high temperature, the F-D distribution includes an appreciable fraction of occupied electronic states with energies above the work function and therefore these electrons are emitted in vacuum. This is the basis of *thermionic emission*, in which electrons are extracted by heating a metallic filament. The case depicted in Figure 1.10 corresponds to a $< 310 >$-oriented monocrystalline W ($\Phi = 4.25\,\mathrm{eV}$ [1]). The unit vector $\hat{\mathbf{z}}$ is taken perpendicular to the emitting surface of the source. In absence of applied field the potential is a step function (black curve) that is modified due to the image charge (red curve). An applied electric field F_{loc} modifies the potential step (blue and magenta curves) as follows:

$$V(z) = \Phi - eF_{loc}z - \frac{e^2}{16\pi\epsilon_0 z}. \tag{1.11}$$

These combined effects can cause electrons to be emitted directly from the Fermi level, by quantum mechanical tunnelling through the barrier [97, 98]. This is called *field emission*. F_{loc} also decreases the exit work function barrier by a quantity

$$\Delta\Phi = \sqrt{\frac{e^3 F_{loc}}{4\pi\epsilon_0}}. \tag{1.12}$$

This is called the *Schottky effect* [99].

Thermionic electron source

The current density, J, emitted by a material heated at a temperature T is described by Richardson's law [100]:

$$J = A_R T^2 \exp\left(-\frac{\phi}{k_B T}\right) \tag{1.13}$$

where A_R is a specific constant defined as

$$A_R = \frac{e m_e {k_B}^2}{2\pi^2 \hbar^3} \tag{1.14}$$

e is the elementary charge, m_e the electron mass and $\hbar$ the reduced Planck constant. Figure 1.11 (a) shows the architecture of a thermionic electron source. It consists of

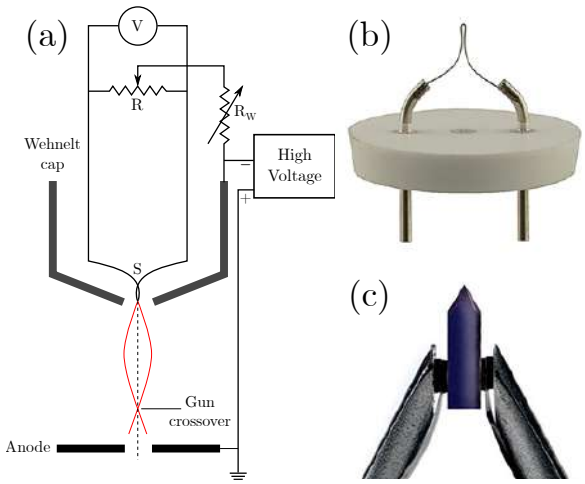

Figure 1.11: (a) Schematic representation of a thermionic electron gun. The electron emitter, S, is a filament of resistance R on which a voltage V is applied. The bias between the cathode and the Wehnelt can be modified by varying R_W. An optimal bias confines the electron emission and focuses the beam into a crossover. In red, two electron trajectories are sketched. (b) A tungsten hairpin filament, $\Phi = 4.5\,\text{eV}$. Image from [101]. (c) A LaB_6 crystal, $\Phi \sim 2.5\,\text{eV}$. Image from [102].

three components: the *electron emitter*, S, the *Wehnelt cap* and the *acceleration anode*.

Between the source and this anode a difference of potential, known as *accelerating voltage*, is applied. The emitter is kept at a negative potential, while the anode is grounded. Thermal emission occurs from the entire emitter and the Wehnelt cap is used to confine the emitted electrons, as depicted in Figure 1.11 (a). By choosing an appropriate voltage difference (the *gun bias*) between source and Wehnelt cap, a *real* crossover is created. The electron emitters normally used in this type of gun are polycristalline tungsten (W) hairpin filament ($\Phi_W = 4.5\,\text{eV}$) or LaB_6 (Lanthanum Hexaboride) monocrystal ($\Phi_{LaB_6} = 2.5\,\text{eV}$). Both of them are displayed in Figure 1.11 (b) and (c), respectively. Routine operation temperature is $\sim 2700\,\text{K}$ for tungsten, while LaB_6-based emitters operate at lower temperature ($\sim 1800\,\text{K}$) due to the reduced exit work function.

Cold Field Emission Gun

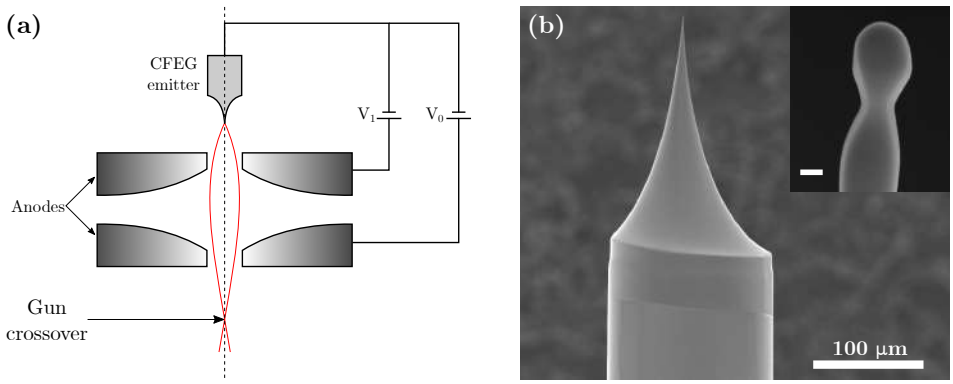

Figure 1.12: (a) Butler type CFE architecture. The first anode is used to extract the electrons from the emitter while the second accelerates the beam to the desired energy. Two electron trajectories are sketched in red. (b) SEM micrograph of the CFE emitter shape. The nanometric apex size allows the generation of an intense electric field due to the lighting rod effect. Inset: zoom of the tip apex. Scale: 100 nm.

The Cold Field Emission (CFE) source is not heated and operates at room temperature ($T \sim 300\,\mathrm{K}$). The current density emitted from a metal surface under an applied electric field [1, 103, 104] is described by the Fowler-Nordheim (F-N) equation [105]:

$$J = \frac{1.54 \cdot 10^{-6}}{\Phi} F_{loc}^2 \, exp\left(\frac{10.4}{\sqrt{\Phi}}\right) exp\left(- \frac{6.44 \cdot 10^9 \Phi^{3/2}}{F_{loc}}\right). \tag{1.15}$$

Figure 1.12(a) shows the architecture of a standard CFE source, known as Butler type CFE. A voltage, V_1, is applied between the emitter and the first anode (called *extraction anode*), while the voltage applied to the second anode is V_0. V_1 and V_0 are called *extraction* and *acceleration voltage*, respectively. Figure 1.12(b) shows the peculiar shape of the CFE cathode. The latter can be fabricated via an electrochemical attack in a $2\,\mathrm{mol/L}$ $NaOH$ solution [106]. A $< 310 >$-oriented monocrystalline W filament ($D = 0.125\,\mathrm{mm}$) is shaped into a tip with an apex size of $\sim 200 - 300\,\mathrm{nm}$ [104, 106].

Schottky Field Emission Gun

The emission process involved in Schottky sources is a combination of the two mechanism already described. It can be called *field-assisted thermionic emission*. The emission current depends both on the cathode temperature and the applied electric field. It is given by:

$$J = A_R T^2 \exp\left(- \frac{\Phi - \Delta\Phi}{k_B T}\right) \frac{\pi q}{\sin \pi q} \tag{1.16}$$

where $\Delta\Phi$ has been defined in equation (1.12) and q is the following dimensionless parameter

$$q = 1.656 \cdot 10^{-4} \frac{F_{loc}^{3/4}}{T}. \tag{1.17}$$

The equation (1.16) is known as the *extended Schottky law* [109]. A schematized Schottky source is represented in Figure 1.13. The architecture is very similar to the one already seen for the CFE source, except for the additional presence of a *suppressor cap*

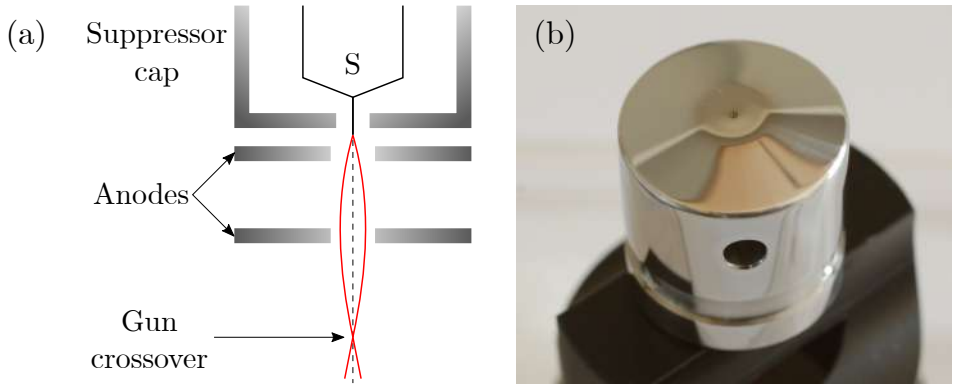

Figure 1.13: (a) Architecture of a SFE Gun. By correctly selecting the different potentials between emitter (S), suppressor cap and extraction anode (the one closer to the cathode), the size of the emission region can be changed [107]. Two electron trajectories are sketched in red. (b) Image of a Schottky electron source. The tungsten tip comes out by $\sim 250\,\mu$m from the top hole of the suppressor cap. Image from [108]

and the anode geometry. A Schottky emitter is a $< 100 >$-oriented monocrystalline tungsten tip with an apex dimension of $\sim 1\,\mu$m [110]. Furthermore, contrary to the CFE case, the Schottky Field Emission (SFE) emitter includes a reservoir of zirconia (ZrO) on the tip shank. Increasing the cathode temperature will create a zirconia wetting layer on the $< 100 >$ tungsten surface. This wetting layer reduces the work function of the ZrO/W emitter to $\sim 2.95\,$eV [110]. The suppressor electrode is used to confine the electron emission to the tip apex. A typical value for the applied electric field is $F_{loc} = 0.65\,$V/nm.

The most relevant characteristics of electron sources are listed in Table 1.1.

	Thermionic		Schottky FE	CFE
Cathode Material	W	LaB_6	ZrO/W[100]	W[310]
Work Function Φ $[eV]$	4.5	~ 2.5	2.95	4.25
Operating temperature $[K]$	2700	1700	1800	300
Angular current density $[\mu A/sr]$			100-200	10
Surface current density $[A/cm^2]$	~ 3	~ 30	$\sim 10^4 - 10^5$	$10^4 - 10^6$
Total emission current	$\sim$ mA	$\sim$ mA	$\sim 100\,\mu$A	$\sim 10\,\mu$A
Probe current noise [%]	< 1	< 1	< 1	< 2
Emission decay	No decay	No decay	No decay	$< 20\%$ of probe current in ~ 2 hours
Brightness (@ 100 kV) $[A/m^2 sr]$	10^{10}	$5 \cdot 10^{11}$	$5 \cdot 10^{12}$	10^{13}
Energy spread (@ 100 kV) $[eV]$	3	1.5	0.7	0.3
Vacuum $[Pa]$	$\sim 10^{-2}$	$\sim 10^{-4}$	$\sim 10^{-6}$	$\sim 10^{-9}$

Table 1.1: Characteristics of the principal electron sources used in conventional TEM

1.2.5 Brightness

Brightness is a fundamental source property defined as the current emitted per unit area and unit solid angle:

$$B = \frac{I_E}{(\pi r_0 \frac{\alpha_1}{2})^2} \tag{1.18}$$

I_E being the emitted current, $2r_0 = d_0$ the (virtual or real) source size and $\frac{\alpha_1}{2}$ the divergence semi-angle. It is expressed in $\mathrm{A/cm^2 \cdot sr}$. This quantity is conserved throughout an optical instrument with no lens aberrations [42, 111].

We will see now how the source brightness is related to the electron source spatial coherence.

To understand this relation one can consider, as in paragraph 1.2.3, the interference between two coherent waves. Equation (1.8) expresses the interference pattern intensity

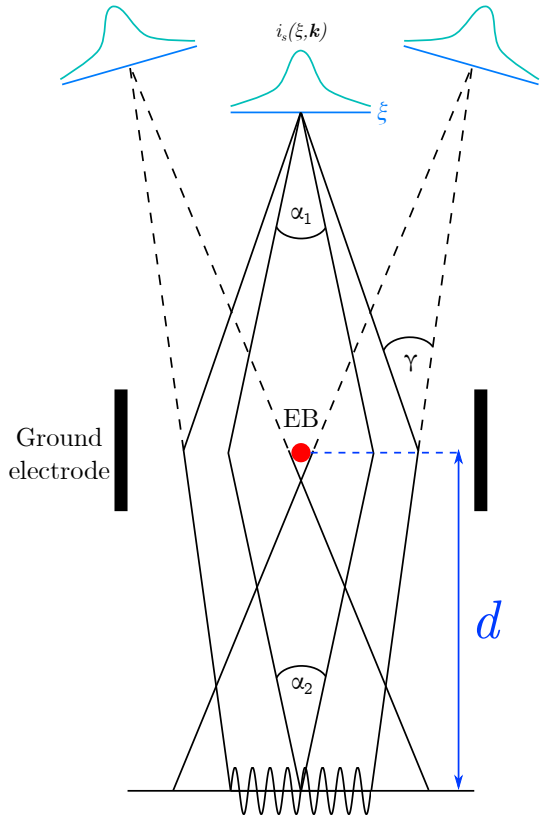

Figure 1.14: Geometry to acquire electron holograms in *off-axis* configuration. The Electron Biprism (EB) is located inside the TEM. Intensity distribution of the source in space and wavenumber is defined by ξ, the source spatial extension in three dimensions and $\mathbf{k}$, *i.e.* the source emitted wavenumbers. d is the distance between the biprism and the image plane.

of an ideal hologram, *i.e.* it assumes an ideal point source. However, as illustrated in Figure 1.14, a real electron source is never perfectly a point source and can therefore be defined by an intensity distribution $i_S(\xi, \mathbf{k})$, ξ and $\mathbf{k}$ being direct and reciprocal space vectors, respectively. For simplification, we will consider in the following a 1-D source. We can consider the source distribution as a sum of incoherent point sources without phase relation. Furthermore, assuming that each of these sources emits the same spectrum $s(\xi, \mathbf{k})$, defined by $\int i(\xi)d\xi = 1$ and $\int s(\mathbf{k}))d\mathbf{k} = 1$, equation (1.8) can

be rewritten as:

$$I_{holo}(x) = 2(1 + |\gamma| cos(2\pi \mathbf{g_c} \cdot x + \Delta\phi)) \tag{1.19}$$

$\gamma = |\gamma| e^{i\Delta\phi}$ being the *complex degree of coherence*. The latter can be expressed as the product of the *spatial* and the *temporal degree of coherence*, $\gamma = \gamma_{spa}\gamma_{temp}$ with

$$\gamma_{spa}(\alpha_1) = |\gamma_{spa}(\alpha_1)| e^{i\Delta\phi_{spa}\alpha_1} = \int i(\xi) e^{-2\pi i k_0 \alpha_1 \xi} d\xi \tag{1.20}$$

$$\gamma_{temp}(x) = |\gamma_{temp}(x)| e^{i\Delta\phi_{temp}x} = \int s(\kappa) e^{-2\pi i k_0 \alpha_2 x} dx. \tag{1.21}$$

The angles α_1 and α_2 are sketched in Figure 1.14 and $\kappa = k - k_0$, with k_0 the wavevector of the source [112].

Equations (1.20) and (1.21) are known as the *van Cittert-Zernike* and the *Wiener-Khintchine* theorems, respectively. The latter state that the spatial (temporal) degree of coherence is the Fourier transform of the spatial (spectral) distribution of the source. For high voltage electron sources ($> 100\,\mathrm{keV}$) with a typical energy spread $\sim 1\,\mathrm{eV}$ the temporal coherence does not affect the interference pattern [113]. However, this is different for the spatial contribution. Assuming a Gaussian intensity distribution of the electron source

$$i(\xi) = \frac{1}{\pi r_0^2} e^{-\left(\frac{\xi}{r_0}\right)^2} \tag{1.22}$$

and considering the definition of brightness given in equation (1.18) it is possible to relate the brightness to the source spatial coherence. As demonstrated in Arbouet *et al.* [112], substituting equations (1.18) and (1.22) in (1.20), we can obtain the coherent current, I_C, available to capture an hologram of contrast $C = |\gamma_{spa}|$ as

$$I_C(C) = -B\frac{ln(C)}{k_0^2} \tag{1.23}$$

Equation (1.23) shows that the coherent current is strictly related to the source brightness.

As stated in the van Cittert-Zernike theorem (equation (1.20)), smaller sources provide beams with the highest spatial coherence. Table 1.1 reports the typical brightness of various electron sources. Due to their small source size, high brightness FE emitters (*i.e.* SFE and CFE) are the only sources suitable for electron interferometry.
So far, the effect of aberrations has not been taken into account. Aberrations deteriorate the beam brightness both in the electron gun optics and microscope column. This degrades both the temporal and spatial coherences [114]. Usually, the detrimental effect of lens aberrations on the phase contrast transfer function of the microscope is taken into account through so-called *spatial* and *temporal envelope functions*, respectively given by :

$$\begin{aligned} E_S(\mathbf{g}) &= exp\{-\pi^2 q_0^2 (C_1 \lambda_B \mathbf{g} + C_3 \lambda_B^3 \mathbf{g}^3)^2\} \\ E_F(\mathbf{g}) &= exp\{-0.5\pi^2 \Delta^2 (\lambda_B \mathbf{g}^2)^2\}. \end{aligned} \tag{1.24}$$

In equations (1.24) $\Delta \propto C_c$, the chromatic aberration coefficient and q_0 is the illumination probe size on the specimen [114]. Multiplying $E_S(\mathbf{g})$ and $E_F(\mathbf{g})$ by $T(\mathbf{g})$ (eq. (1.5)) we obtain the *effective phase contrast transfer function*.

1.3 Time-resolved TEM

The birth of time-resolved TEM can be dated back to the end of the 1970s, when Bostanjoglo's group at the Technical University of Berlin developed the first time resolved electron microscope [29]. The so-called *High-speed electron microscope* was subsequently improved at the Lawrence Livermore National Laboratory, in particular the illumination optics and the acquisition system [33, 115, 116]. A significant breakthrough was achieved in 2005 at the California Institute of Technology [34], thanks to the introduction of the *single electron regime* by Nobel laureate Ahmed Zewail and his group.

1.3.1 Dynamic TEM and Ultrafast TEM

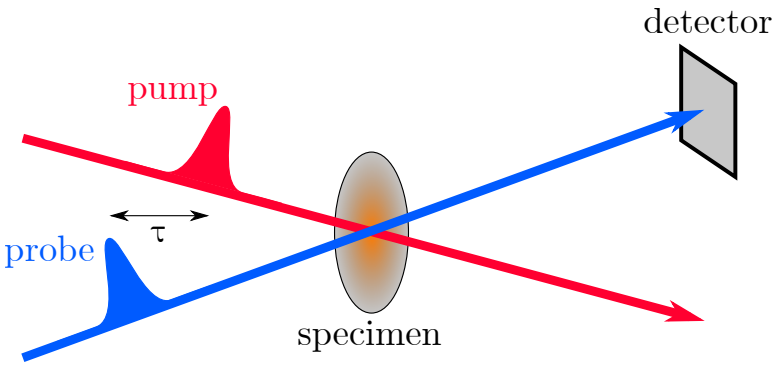

Figure 1.15: Principle of *pump-probe* experiments. An ultrafast laser beam (the pump) is focused onto the specimen, bringing it out of equilibrium. A delayed second pulse, the probe, is used to detect the specimen evolution. In time-resolved electron microscopy the probe pulse is a packet of electrons.

Time-resolved electron microscopy allows to study the dynamics of fast processes, typically in the nano- to femtosecond range. The followed approach is called *pump-probe* and is schematized in Figure 1.15: it involves a *pump pulse* to bring the specimen out of equilibrium and a *probe pulse* to investigate the system at a certain delay, τ, during its relaxation.

In the field of time-resolved TEM, the pump pulse is usually an external optical stimulus that excites the specimen but also different excitations (acoustic, thermal, mechanical, etc) can be used for this purpose. The probe is an electron packet triggered by a pulsed laser. Two operation modes exist in time-resolved TEM. The use of a single electron pulse containing $> 10^6$ electrons [33] to probe the system dynamics is called *single-shot* mode (Figure 1.16 (a)).

Using a high speed beam deflector synchronized with the laser source, it is possible to record several frames on a CCD detector at different delays with respect to the pump pulse. This is called *movie-mode* and it is sketched in Figure 1.16 (b). A TEM operating

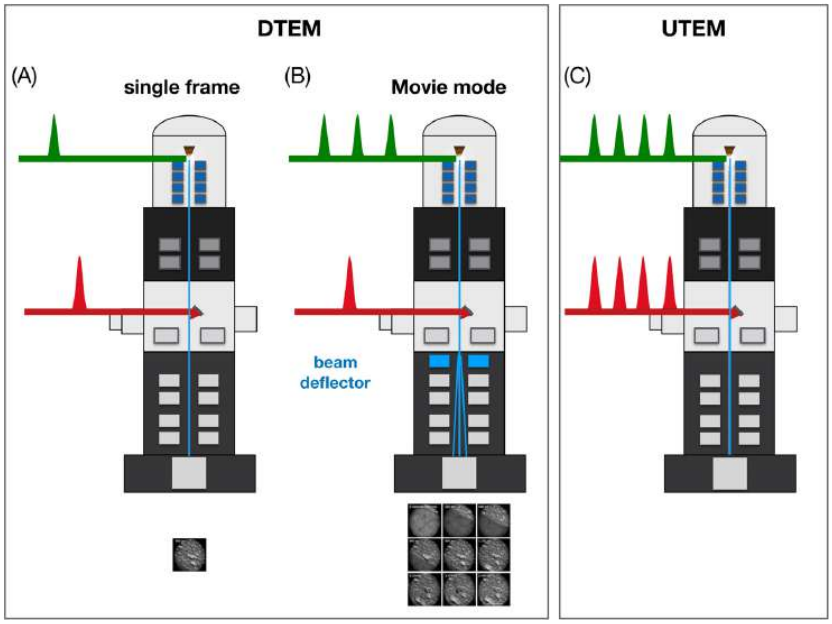

Figure 1.16: Different operation modes in time-resolved TEM. (a) Single shot mode: a single pulse containing $\sim 10^8$ electrons is used to probe the specimen after the laser excitation. (b) Movie mode: a sequence of electron pulses probe the specimen evolution at different temporal delays after a single laser excitation. (c) Ultrafast TEM in stroboscopic pump-probe mode: $\sim 10^8$ excitation/detection cycles are used to probe the specimen dynamics at a certain temporal delay. With only few electrons in each pulse, the Coulomb repulsion is less important and the temporal resolution can be pushed to the sub-picosecond regime.

in single-shot mode is called a *Dynamic TEM* (DTEM) or high-speed TEM.

The second operation mode, the *stroboscopic* mode, relies on a high number ($\sim 10^7 - 10^9$) of excitation-observation cycles [34] to accumulate enough electrons to form an image, diffraction pattern, spectrum or hologram. It is depicted in Figure 1.16 (c). The delay between the pump and the probe can be adjusted with a translation stage in order to explore the dynamics of the desired process. A translation $D = 1.5\,\mu$m of the delay line, for instance, produces a $\tau = 2D/c = 10\,$fs delay [7]. The main difference between

[7] c is the speed of light in vacuum

the two modes is the number of electrons in each pulse. In stroboscopic mode the electron beam only contains a few electrons per pulse. The minimization of the Coulomb repulsion among electrons allows to push the time resolution up to the femtosecond timescale [34, 40]. This is known as the *single electron regime*. Time-resolved TEMs operating in this mode are called ultrafast TEMs (UTEMs).

In the following, we will explain how the pulsed electron beam is created, adressing the various laser-driven emission mechanisms. Subsequently, the modification of the electron pulse properties along the UTEM column will be presented, paying attention to the influence of the number of electrons per pulse.

1.3.2 Laser-driven electron emission

The combination of an ultrafast laser and an electron source allows the generation of ultrashort electron pulses [117, 118]. As reported in [119], electron emission from a material with a work function Φ is possible thanks to the absorption of photons of energy $E_{ph} = \hbar\omega > \Phi$. This phenomenon is known as *one-photon photoemission* (Figure 1.17(a), case A) and the emitted current is linearly dependent on the incident light intensity. This process can not occur if the photon energy is smaller than the material work function. Nevertheless, *multiphoton photoemission* (MPP), sketched in Figure 1.17 (a), case B is possible. The cross-section for such a non-linear process decreases with the required number of photons and the emitted current density is proportional to the n^{th} power of the laser intensity I [120, 121, 122]:

$$J \propto I^n \tag{1.25}$$

with n the number of photons. Multiphoton photoemission is the dominant emission mechanism for laser intensities smaller than typically $10^{11}\,\frac{W}{cm^2}$. At higher laser intensities ($I > 10^{12}\,\frac{W}{cm^2}$), the associated electric field can be strong enough to modulate

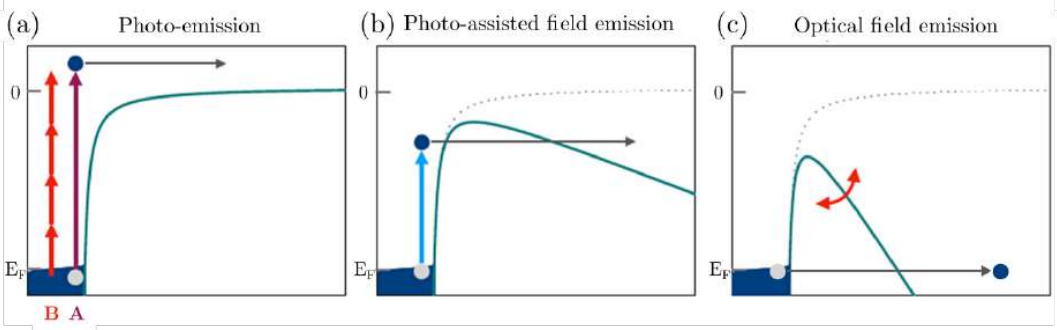

Figure 1.17: Emission processes in laser-driven electron emission. (a) One photon photoemission (A) and multiphoton photoemission (B): one or more photons are absorbed, allowing electron emission over the barrier. (b) Photo-assisted field emission: the combination of two mechanisms enable electron emission. (c) Optical field emission: a strong laser electric field modulates the potential barrier allowing electron tunnelling from the Fermi level.

the potential barrier and allow electron tunnelling. This process is called *optical field emission* and depicted in Figure 1.17 (c).

In order to discriminate the two emission processes, we can evaluate the *Keldysh parameter* [123, 124], figure of merit of the Keldysh theory on the ionization of atoms and solid bodies:

$$\gamma = \frac{\omega\sqrt{2m\Phi}}{eF_L} \tag{1.26}$$

where ω is the laser angular frequency, F_L the laser peak electric field, m and e the electron mass and charge. The Keldysh parameter is the ratio between the tunnelling time and the optical cycle duration: $\gamma << 1$ is characteristic of the optical field emission, while $\gamma >> 1$ indicates that the dominant mechanism is MPP.

Other emission mechanisms depend on the combination of laser intensity and extraction voltage, such as *Photo-assisted field emission*, schematized in Figure 1.17(b). In this case the absorption of one photon allows electrons to tunnel through the barrier thanks to the help of a continuous applied electric field.

1.3.3 Influence of the electron dynamics on the electron energy distribution

The interaction of an ultrashort laser pulse with a tungsten nanoemitter modifies the electron distribution inside the metal at a given temperature. In order to evaluate the influence of the electron dynamics on the temporal and spectral properties of a time resolved TEM, a computational model based on previous works [125, 126, 127, 128] has been developed. The model describes a gas of free electrons interacting with a femtosecond laser pulse. The vacuum-metal interface is considered flat and a DC electric field lying in the $0.5 - 3\,\mathrm{V/nm}$ range is applied on the metallic nanotip.

The time-dependent electron distribution, $f(\mathbf{k}, t)$, can be computed from Boltzmann's equation:

$$\frac{df(\mathbf{k},t)}{dt} = \left.\frac{df(\mathbf{k},t)}{dt}\right|_{e-e} + \left.\frac{df(\mathbf{k},t)}{dt}\right|_{e-ph} + F(\mathbf{k},t) \tag{1.27}$$

where the three terms account for the electron-electron interaction, the electron-phonon interaction and the laser excitation on the nanotip, respectively. The electron dispersion relation in the conduction band has been considered parabolic ($E(\mathbf{k}) = \hbar^2\, k^2/2m$) and the Fermi energy for tungsten is $E_F = 9.2\,\mathrm{eV}$. Before excitation by the femtosecond laser pulse, electrons and phonons follows the Fermi-Dirac (F-D) and the Bose-Einstein distribution, respectively. Excitation of the electron gas as well as electron-electron and electron-phonon interactions are taken into account at each step of the simulation. Figure 1.18 shows the evolution of the electron distribution. As soon as the laser pulse starts interacting with the nanoemitter (sketched with a parabolic shape), the occupation of electronic states is modified due to the excitation of the electron gas: the electron population is distributed over several electronic states due to multiple excitations and decays. The spectro-temporal properties of the electron pulse have been deduced from the optically excited electron distribution. The number of electrons

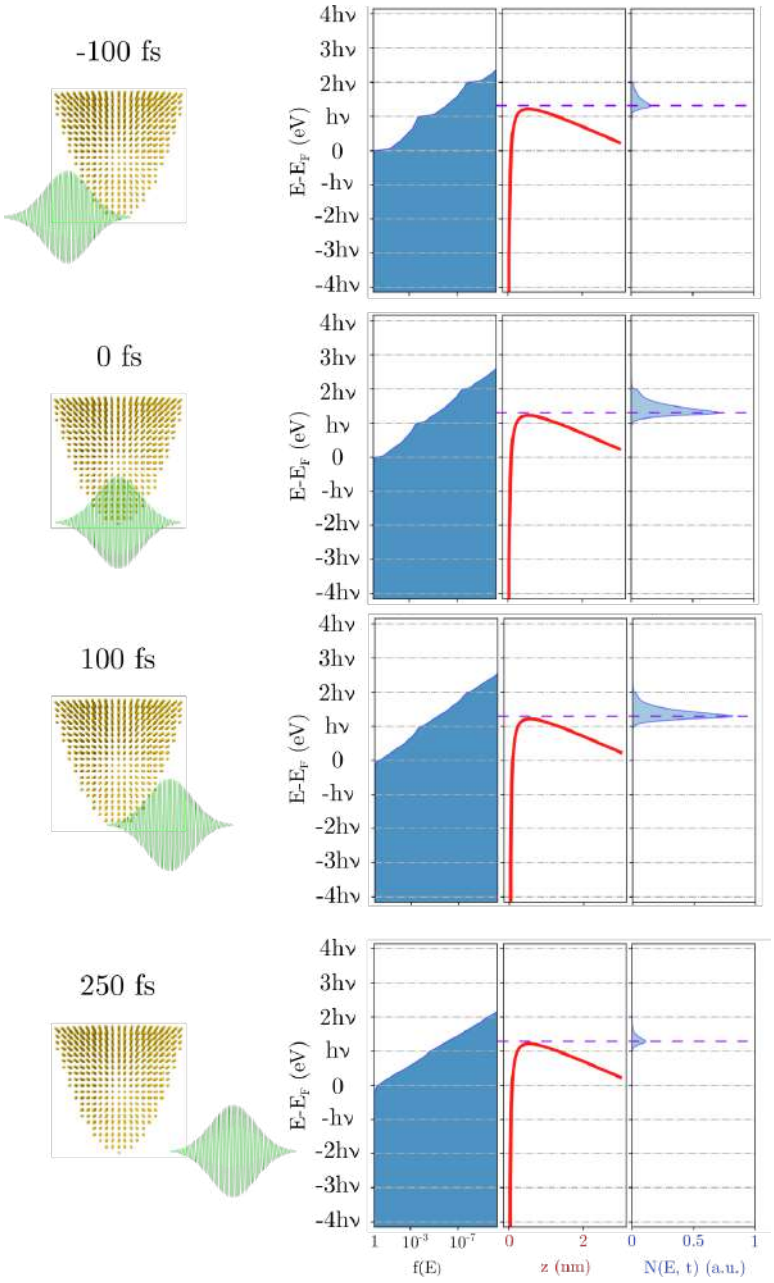

Figure 1.18: Ultrafast optical excitation of an electron gas. The tungsten nanoemitter is sketched with a parabolic shape. The three graphs represent (from left to right): the electron occupation number $f(E,t)$ (dark blue curve), the potential barrier (red curve) and the number of emitted electrons $N(E,t)$ (light blue curve). We considered a laser pulse of $\lambda = 515\,\mathrm{nm}$ and a FWHM pulse duration of 250 fs. The electron-phonon thermalization time is 400 fs. The applied DC electric field is $F_{loc} = 1.19\,\mathrm{V/nm}$.

emitted at a certain time t per unit area and unit time with a total energy between E and $E + dE$ is given by:

$$N(E,t) = \int_0^E N(E,W,t)D(W)\,\mathrm{d}W \tag{1.28}$$

$N(E,W,t)$ represents the number of electrons with a total energy between E and $E+dE$ and an energy normal to the emitting surface between W and $W + dW$. $D(W)$ is the electron transmission probability through the potential barrier $V(z)$ in Wentzel-Kramers-Brillouin (WKB) approximation. The expression of $V(z)$ is given in equation (1.11). $N(E,W,t)$ can be expressed in the framework of the free-electron theory of metals as:

$$N(E,W,t) = \frac{m_e}{2\pi^2\hbar^3} f(E,t). \tag{1.29}$$

The total current emitted at time t is finally calculated from:

$$J(t) = -e\int_0^{+\infty} N(E,t)\,\mathrm{d}E. \tag{1.30}$$

In our experimental conditions we can notice that the electron emission is triggered by two processes. Indeed, electrons occupying states over the potential barrier are emitted by MPP while the others can tunnel through the upper part of the potential barrier by photo-assisted field emission.

Looking carefully at the electron spectral distribution, we can notice that the symmetry of the Zero Loss Peak (ZLP) in laser-driven mode appears different compared to the one of a conventional CFEG. This difference is visible in Figure 1.19, in which two simulated electron energy spectra are sketched. Figure 1.19 (a) shows the ZLP of a CFEG TEM operating in DC mode. The typical asymmetry of the curve is due to both the electron occupation distribution (F-D statistics at $T = 300\,\mathrm{K}$ - sketched in Figure 1.10) and the tunnelling probability given by the F-N theory [105]. Therefore, on the loss side of the electron energy spectrum, the distribution decreases due to the low

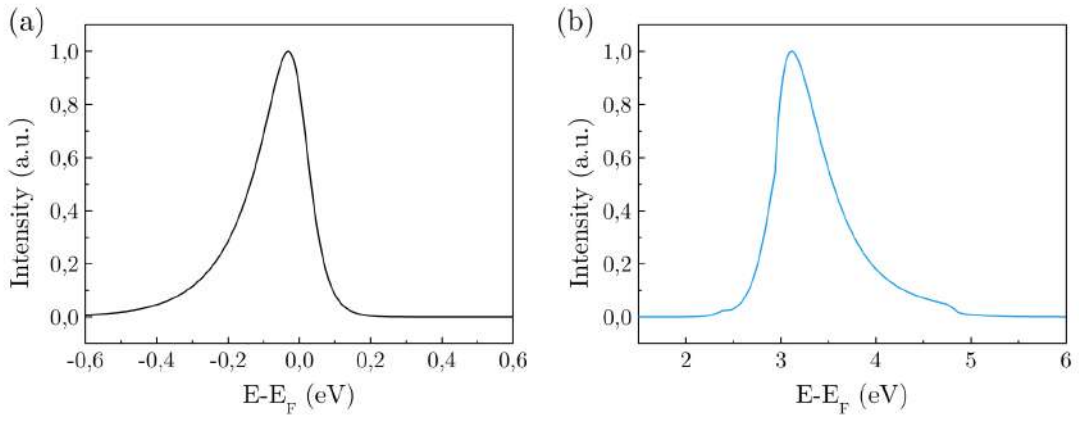

Figure 1.19: (a) Simulated ZLP of a CFEG TEM working in DC mode. (b) Simulated ZLP of our CFEG based TEM operated in pulsed mode (E_{ph} = 2.4 eV, F_{loc} = 1.19 V/nm). The spectrum has been obtained by integrating the electron energy distribution over the laser pulse duration.

occupation number, while on the gain side the decrease is related to the low transmission probability of the potential barrier. Figure 1.19 (b) shows the ZLP simulated using the model described in this paragraph. In this case, the ZLP asymmetry appears inverted. As represented in Figure 1.18, an abrupt drop in the energy spectrum appears on the loss side due to the effect of the potential barrier on electrons emitted by photo-assisted field emission. On the other hand, the few electrons with energy greater than the barrier are emitted by MPP. Figure 1.20 shows simulated curves of the number of emitted electrons per pulse per unit surface, the electron pulse duration and the energy spread as a function of the energy absorbed by the emitter. The latter has been estimated from electrodynamical simulations to be in the range 0.1 - 1 eV/nm^3. In Figure (a) we can see that the electron emission (black curve) start departing from the 2-photon photoemission process for 0.2 eV/nm^3 of absorbed energy. By taking into account an experimental value of 0.4 eV/nm^3, we expect a pulse duration of 400 fs and 0.65 eV of energy spread. Two conclusions can be drawn from Figure 1.20. First, for

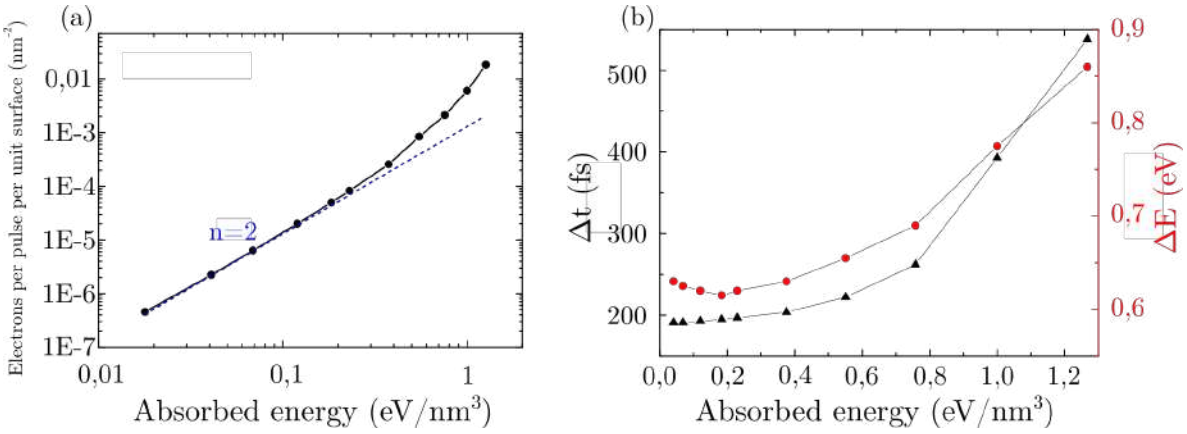

Figure 1.20: (a) Simulated number of electrons per pulse per unit surface emitted from a tungsten nanotip as a function of the absorbed energy. The black line shows how the electron emission varies under our experimental conditions. The blue dashed line indicates a 2-photon photoemission process. (b) Variation of the electron pulse duration and energy spread as a function of the absorbed energy.

low values of the deposited energy the emission process is a second-order nonlinear process yielding temporal and energy widths essentially governed by the laser pulse duration and the nonlinearity order. For strong perturbations of the electron gas of the metallic emitter, the strongly out-of-equilibrium electronic distribution impacts the spectro-temporal properties of the emitted electron pulse. In this case, the effective non-linearity departs from 2 and depends on the excitation level. Furthermore, the temporal and spectral distributions of the emitted electrons broaden and depend on the laser intensity incident on the tungsten nanotip. After the emission, the electron pulse broadens during its propagation along the microscope column. This effect and its causes will be addressed in the next paragraph.

1.3.4 Electron pulse broadening: influence on UTEM spectro-temporal properties

Electron-electron interactions during the propagation of the electron pulse deteriorate the spectro-temporal properties of the UTEM. Therefore, the temporal resolution of such an instrument does not depend only on the electron emission mechanism but also on the propagation inside the TEM column. Gahlman *et al.* [38] theoretically described these two effects and studied separately their influence on the electron beam properties.

Influence of the initial energy spread on the electron pulse duration

Emitted electrons have a certain initial energy distribution, ΔE_i, that determines a temporal broadening

$$\Delta t_{KE} \approx \frac{d}{eV}\Delta p_i = \frac{d}{eV}\sqrt{\frac{m_0}{2}}\frac{\Delta E_i}{\sqrt{E_i}} \tag{1.31}$$

d being the anode-cathode distance, V the extraction voltage, E_i the electron initial energy, e and m_0 the electron charge and mass, respectively. Assuming an isotropic conduction band and a two photon-photoemission process, an electron on the Fermi level ($E_F = 9.2\,\mathrm{eV}$) gains $4.8\,\mathrm{eV}$ ($E_{ph} = 2.4\,\mathrm{eV}$). We can then consider an initial energy $E_i = 14\,\mathrm{eV}$. ΔE_i has been evaluated using the model described in paragraph 1.3.3. The time-dependent electron distribution has been evaluated, then the emitted current has been calculated taking into account the electron distribution and their probability to tunnel through the potential barrier. The nanotip in our experiment is placed in a DC electric field of magnitude $F = 1.19\,\mathrm{V/nm}$ (calculated taking into account a tip-anode distance $d = 5\,\mathrm{mm}$, an extraction voltage $V_1 = 4\,\mathrm{kV}$ and the influence of an optical component - the *mirror holder* - surrounding the nanoemitter (more details on the electron gun will be given in the next chapter). With the computed value $\Delta E_i = 0.6\,\mathrm{eV}$, an anode-cathode distance $d = 5\,\mathrm{mm}$ and an extraction voltage

$V = 4\,\mathrm{kV}$, we can estimate $\Delta t_{KE} \approx 338\,\mathrm{fs}$.

The laser pulse duration, $\Delta t_{h\nu}$, also contributes to the temporal broadening. Neglecting electron repulsion, we can write:

$$\Delta t = \sqrt{\Delta t_{h\nu}^2 + \Delta t_{KE}^2}. \tag{1.32}$$

Influence of space-charge effects on the pulse duration and energy spread

We discuss now the effect of the Coulomb repulsion inside the electron pulse. Several studies have addressed space-charge effects in electron pulses [38, 129, 130]. Following a mean-field approach, the electron pulse can be modelled as a homogeneously charged cylindrical slab of radius R and length L. The repulsion among electrons induces an increase both of L and R and a degradation of the UTEM temporal, spatial and spectral resolution. Evaluating the Coulomb force inside the electron packet, it can be shown that the electron pulse dimensions obey the following system of coupled differential equations [38]:

$$\frac{1}{2}\frac{d^2L}{dt^2} = \frac{Ne^2}{2m_0\epsilon_0\pi R^2}\frac{2}{1+\left(\frac{L}{R}\right)+\sqrt{1+\left(\frac{L}{R}\right)^2}} \tag{1.33}$$

$$\frac{d^2R}{dt^2} = \frac{Ne^2}{m_0\epsilon_0\pi R^2} \tag{1.34}$$

where ϵ_0 is the vacuum permittivity, N is the number of electrons per pulse. The resolution of equation (1.33) allows to evaluate the temporal and energy broadening of the electron pulse:

$$\Delta t_{SC} = \frac{L}{v_0} \tag{1.35}$$

$$\Delta E_{SC} = m\, v_0\, \frac{dL}{dt} \tag{1.36}$$

v_0 is the electron velocity after the acceleration. The resolution of equation (1.34) gives, on the other hand, the possibility to evaluate the effect of the coulombic repulsion on

the electron spot size. In Figure 1.21 the pulse broadening is evaluated as a function of propagation time for different numbers of electrons per pulse. The computation has been performed for 150 keV-electrons and the contribution from equation (1.31) is not taken into account. The initial conditions for L have been chosen to match the

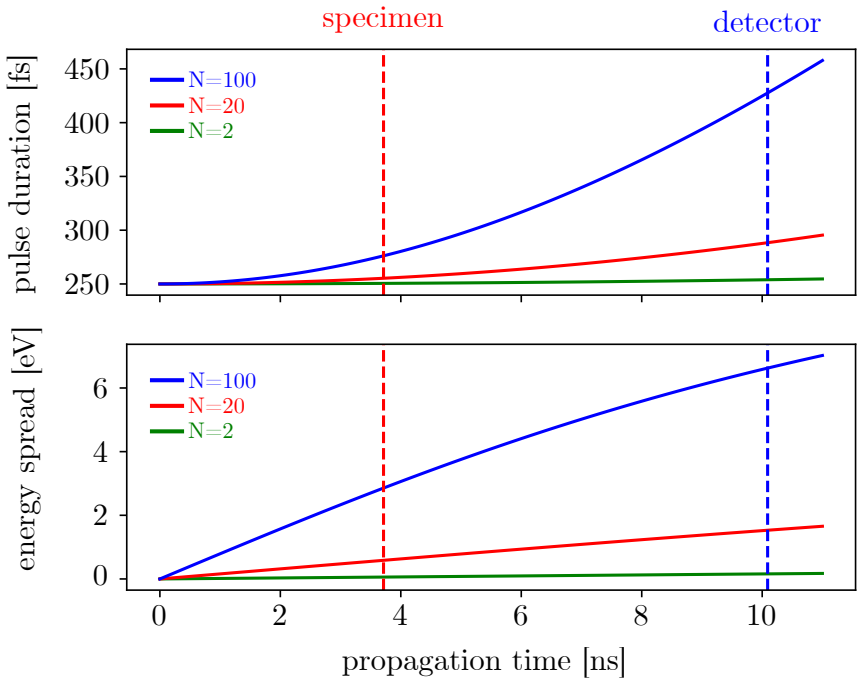

Figure 1.21: Effect of the number of electrons per pulse, N, on temporal and energy broadening. Dashed lines show when the electron pulse arrives on the specimen (red line) and detector (blue line) in the HF2000.

laser pulse duration, $L = v_0 \cdot \Delta t_{h\nu}$. $R = 125\,\mu$m has been calculated through SIMION simulation [131]. An initial energy spread $\Delta E_i = 0\,$eV has been considered. Dashed lines indicate the time when electrons arrive onto the specimen (red) and the CCD camera (blue). The $N = 2$ case shows that the electron pulse duration at the detector is increased by 1.3 % and its energy spread is $\sim 0.14\,$eV. For $N = 20$, the temporal

broadening at the detector is 281 fs and the energy spread increases to ~ 1.38 eV. An electron pulse containing $N = 100$ electrons, instead, arrives at the CCD with a temporal duration increased by 58 % ($\Delta t = 395$ fs) and an energy resolution of 6.12 eV. However, this situation is never achieved practically with FE based ultrafast sources, as the one used in this thesis. Pulses containing $N = 2$ and $N = 20$ electrons are typically used in stroboscopic pump-probe experiments in UTEM. However, in single shot mode each pulse contains up to 10^8 electrons and the electron beam spatio-temporal properties are deeply affected. Figure 1.22 shows the pulse broadening in single shot

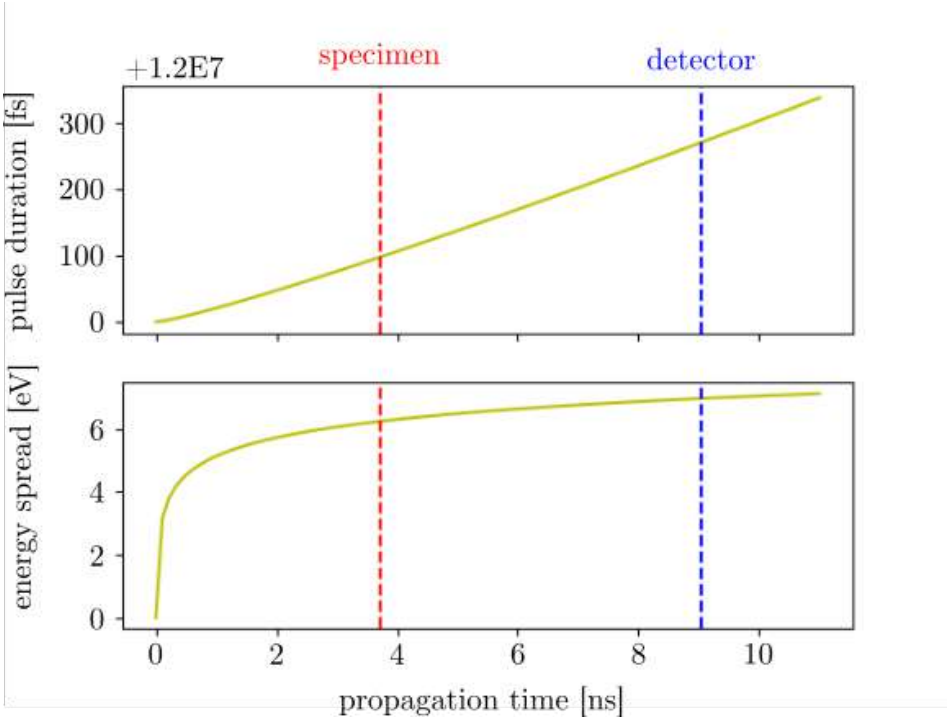

Figure 1.22: Temporal and energy broadening of an electron pulse in the single shot mode. The pulse contains $N = 10^8$ electrons. The laser pulse duration is $\Delta t_{h\nu} = 12$ ns.

mode taking into account a laser pulse duration of $\Delta t_{h\nu} = 12$ ns. The pulse duration at the detector is nearly constant and the pulse energy spread reaches ~ 6.7 eV. The

simulation shows that electrons strongly repel each other. The energy spread reaches 5 eV approximately 1 ns after the emission. The energy spread then increases more slowly as the electrons get further apart and interact less.

Whereas the operation of UTEMs in the single electron regime has enable a dramatic improvement of their spatio-temporal properties, the poor brightness of photocathode-based electron guns still limit their application field, making them inadequate for demanding applications such as ultrafast electron holography. The solution appeared with laser driven emission from metallic nanotips [132, 133, 134], that laid the foundations for Field Emission Gun (FEG) UTEMs.

1.3.5 Conclusions

In this first chapter we first addressed the limits of TEM in investigating the dynamics of physical processes. *In-situ* TEM techniques allow to explore phenomena occurring in the millisecond time scale but experiments with temporal resolution in the nanosecond range or faster rely on the *pump-probe* approach. Originally developed in the field of ultrafast optical spectroscopy, pump-probe experiments have then been implemented in TEM. Thanks to the interaction between a ultrafast laser source and a metallic emitter, a pulsed electron beam can be used to probe the modifications induced on a specimen by external stimuli. Time-resolved TEM provides two approaches: the *single-shot* and the *stroboscopic* mode. The first is performed in *Dynamic TEMs* and is used to investigate irreversible phenomena: a single electron pulse contains a sufficient number of electrons to get an exploitable signal. The second is followed to study reversible phenomena by using a high number of excitation-observation cycles and is performed in *Ultrafast TEMs*. In order to minimized the effect of the Coulomb force among particles, the beam contains only few electrons. This is called *single-electron regime*.

In fact, strong repulsions deeply affect the spatio-temporal properties of the instrument.

Further limitations concerns the electron emitter: the first ultrafast instruments were brightness-limited by the use of photocathodes-based electron guns. The first implementation of a laser-driven field emission source has been achieved at Caltech, in a Scanning Electron Microscope (SEM), equipped with a Schottky FEG [135, 136]. Some years later, at Göttingen University, a JEOL 2100-FEG TEM equipped with a 200 kV SFEG has been converted into a UTEM [137]. In order to further push the UTEM and to widen its application field to electron holography [138] and interferometry applications [139], the *FemtoTEM* project started in 2010 at CEMES-CNRS in Toulouse. This project, within which this thesis work has been conducted, aims at developing an UTEM based on a CFEG architecture [140, **?**]. Details on the development of such an instrument will be addressed in the next chapter.

Chapter 2

Instrumental development: design and characterization

In this chapter a detailed description of the CEMES-CNRS UTEM will be given. The design and the fabrication of the Ultrafast CFEG as well as the light injection system will be described. The CFEG UTEM characterization will also be presented: the emission current, the beam spot size and the current stability will be analysed. The microscope brightness will be evaluated. Finally, a demonstration of the microscope performance in several TEM techniques will be given.

2.1 Presentation of the modified Hitachi HF2000 - FemtoTEM

The microscope that has been modified to develop the CFEG UTEM (referred as FemtoTEM in the following) at CEMES-CNRS is a Hitachi HF2000, a CFEG 200 kV-TEM manufactured by Hitachi High Technologies (HHT) in 1989 [3]. The development of a

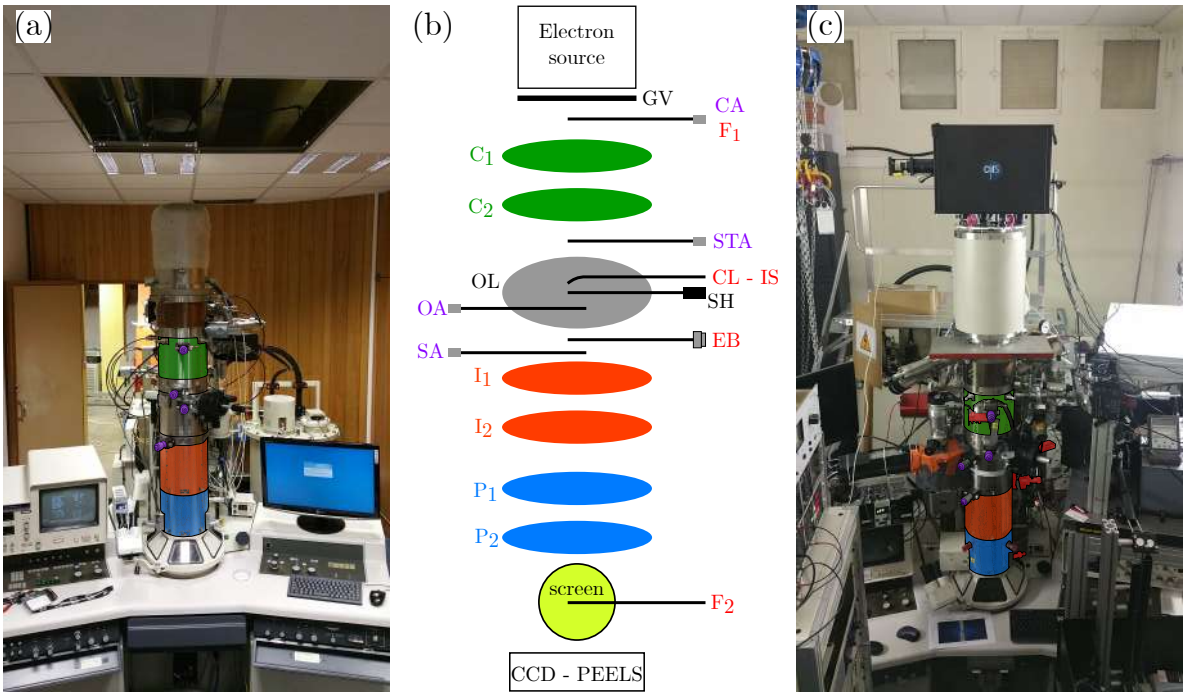

Figure 2.1: (a) Picture of the original HHT HF2000 at CEMES-CNRS. (b) Schematic of the TEM column. Red labels indicate the modified parts. Purple labels indicates the TEM apertures. (c) Picture of the FemtoTEM. The optical head is visible on the gun housing. Lens systems highlighted as in (b). Apertures are highlighted in purple in both (a) and (c). Modified parts highlighted in red in (c).

UTEM by modifying such a conventional TEM presents some challenges. Figure 2.1(a) shows a picture of the original HHT HF2000. There is no optical access to inject the laser beams neither inside the gun nor in the objective lens. To provide a path for the light inside the electron source, the original external housing (called *gun housing*) has been replaced with a modified one, as shown in Figure 2.1(c). The objective lens has also been modified. It is now equipped with an optomechanical system to inject and focus the laser on the specimen through a parabolic mirror. The same system can be used to collect the cathodoluminescence emitted by the sample. We will refer to the

latter as the Cathodoluminescence-Injection system (CL-I). Despite the modifications, the microscope column, sketched in Figure 2.1(b), keeps the same electron optics properties.

The original vacuum system has been improved. Two Faraday cups, F_1 and F_2, have been mounted, one on the Condenser Aperture (CA) and one on the beam block above the fluorescent screen. They are connected to a Keithley 6514 picoammeter to measure the current emitted in ultrafast mode. In the course of this thesis, we refer to the emission current as the one measured by F_1. The current measured by F_1 is half of the total emission current measured in the gun. An electron biprism (EB) has been inserted in the Selected Area aperture (SA) plane to perform Ultrafast Electron Holography. The UTEM has also been equipped with a Gatan 4k x 4k Ultrascan camera and a modified parallel detection spectrometer Gatan PEELS 666 [66, 141]. Indeed, the original Gatan CCD camera has been replaced by a PIXIS 256. The latter is coupled with a telescopic doublet lens located between the scintillator and the camera CCD sensor.

2.1.1 Architecture of the laser-driven CFEG

A detailed scheme of the modified CFEG is given in Figure 2.2 (a). The gun can be divided in two parts. The top part (*i.e.* the black box in Figure 2.1 (b)) is called the *optical head*. It contains optomechanical components that allow to align the laser beam on the tip apex and control the laser power and polarization. These components are attached on an optical breadboard fixed on the gun housing. The laser beam is sent in the optical head thanks to a periscope. The former goes first through an attenuator composed of a half-wave plate and a polarizing cube, then onto two piezoelectric mirrors used to remotely scan and align the laser beam on the tip apex. The laser beam polarization is controlled by a second half-wave plate. The CCD camera allows to

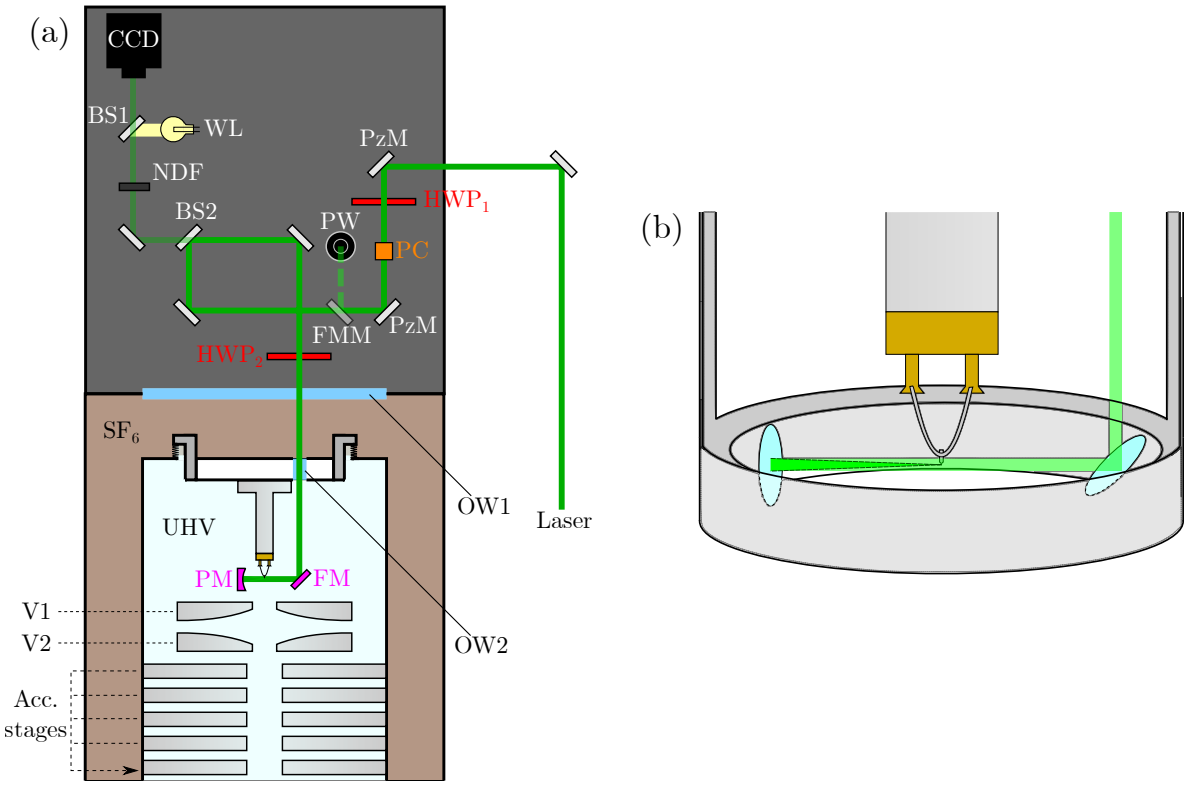

Figure 2.2: (a)Ultrafast CFEG and optical head. HWP: Half-Wave Plate. FMM: Flip Mount Mirror. PW: Power meter. PzM: Piezoelectric Mirror. BS: Beam Splitter. WL: White Light source. OW: Optical Window. FM: Flat Mirror. PM: Parabolic Mirror. PC: Polarizing Cube. (b) Sketch of the CFEG tip mounted on a HHT support and the mirror holder.

visualize the nanoemitter as well as the alignment procedure using a white light source. It can also be used to inspect the flash cleaning operation.

To allow the laser to enter inside the SF_6 region, a first optical window has been created and mounted on the top of the gun housing. The gun itself has been modified [142]. The CFEG emitter is mounted on a customized metal/ceramic CF40 flange that includes a second optical window (6 mm of diameter) to inject the laser from the SF_6 to the UHV region. The laser is then reflected at 90° by a flat mirror and focused by a

parabolic mirror ($f = 8\,\text{mm}$) into a $\sim 3\,\mu\text{m}$ spot radius ($1/e^2$) at the tip apex, as shown in Figure 2.2 (b). These two mirrors are nested inside a system, called *mirror holder* (MH). To minimize the influence of the latter on the distribution of the electric field in the vicinity of the tip, its geometry is cylindrically symmetric. The diameters of the flat and the parabolic mirror are, respectively, 8 and 6 mm. An optical pre-alignment of the mirror holder with respect to the tip apex is realized on a dedicated optical bench. The modified CF40 is placed on a support, then the laser beam is sent on the tip apex. To maintain the mirror holder in a stable position, a set of mirror polished screws is used. Particular attention has been paid to the materials. Both the mirror holder and the tip support have been produced using non magnetic steel 304L to avoid any difference in thermal expansion coefficients. Furthermore, all surfaces have been mirror polished to reach a surface roughness $R_a = 0.1\,\mu\text{m}$. After the pre-alignment, the tip-MH-CF40 system is mounted inside the extractor assembly. The gun is then evacuated to $\sim 10^{-7} - 10^{-8}\,\text{Pa}$. To ensure UHV operation conditions, the electron gun is finally baked at 350 °C for nine hours. Eventually, the alignment and focusing are refined with the two piezoelectric mirrors of the optical head and an external telescope. Figure 2.3 (a) shows the high voltage configuration of the HF2000. The tip and the mirror holder are maintained at the same voltage $V_0 = -150\,\text{kV}$. The extraction anode is set at a voltage V_1 relatively to the tip. V_1 can be varied between 2 and 7 kV. The distance between the tip and the anode is $d = 5\,\text{mm}$, while the MH is at less than 1 mm from the extractor surface. The first anode of the accelerating tube is called *focusing anode* or *gun lens*. It is set at a potential V_2 relatively to the tip. The voltage between V_2 and the ground electrode is equally distributed between the different acceleration stages. The *interstage voltage* is therefore defined as:

$$V_{IS} = \frac{V_0 + V_2}{N} \tag{2.1}$$

where N represents the number of acceleration stages. ($V_{IS} = 26\,\text{kV}$ for $V_0 = -150\,\text{kV}$, $V_2 = 20\,\text{kV}$ and $N = 5$). The ratio $R = \frac{V_2}{V_1}$ can be varied between 2 and 13 to change the position of the full gun crossover.

In the original HF2000, continuous electron emission is obtained for an extraction

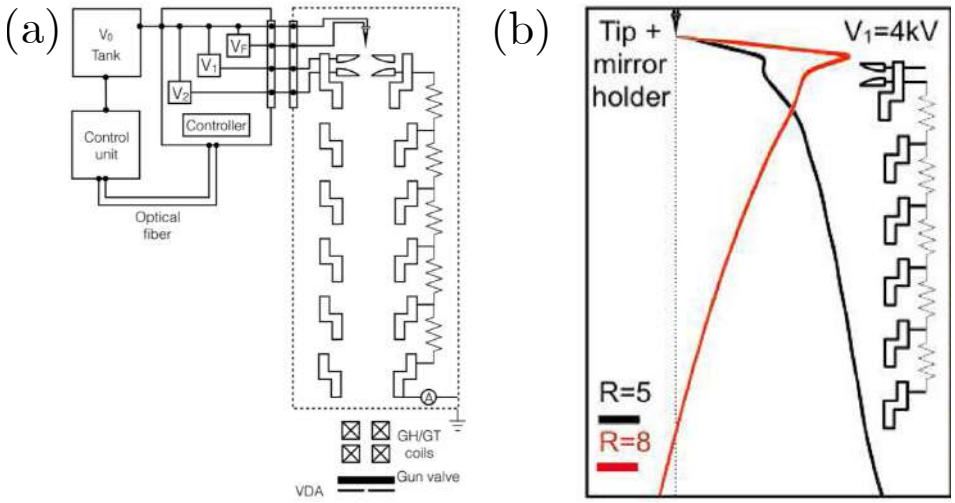

Figure 2.3: (a) High Voltage configuration of the HHT HF2000. V_0 represents the acceleration voltage, V_1 the extraction voltage, V_2 the gun lens voltage and V_F the voltage applied to the tip during the flash. GH: Gun Horizontal. GT: Gun Tilt. VDA: Vacuum Differential Aperture. (b) Electron trajectories inside the modified CFEG computed using SIMION 8.1 for different ratios $R = \frac{V_2}{V_1}$.

voltage $V_1 \sim 2\,\text{kV}$ while, in our modified FemtoTEM, the onset for DC emission is at $V_1 \sim 5.2\,\text{kV}$ for the same tip, due to the presence of the mirror holder. However, in ultrafast operation mode, the electron emission is triggered by the pulsed laser and the extraction voltage is kept smaller than $5.2\,\text{kV}$ to avoid DC emission. In this case V_1 can be used as a free parameter to adjust the crossover position and the strength of the gun lens.

Figure 2.3 (b) shows two different electron trajectories computed using SIMION 8.1, an electron trajectory simulator [143, 144]. These have been obtained for two different

ratios $R = 5$ and $R = 8$ to create a *virtual* and a *real crossover*, respectively.

2.1.2 Electron trajectories

All the modifications on the original CFEG have been performed above the extraction anode, in order to preserve the original electron optics properties. To confirm this hypothesis, a model of the entire gun has been created using SIMION 8.1 [143, 144], a Finite Difference Method (FDM) software. The electric field distribution and the electron trajectories inside the original HF2000 and in the FemtoTEM electron gun have been computed and compared. Each electrode of the electron gun, except the electron emitter and the MH, have been obtained from a three dimensional CAD model, then imported into SIMION and finally converted into a potential array (PA), *i.e.* a rectangular grid of points in space, each having a specific voltage. Each element of the grid is called a *grid unit* (gu). All the elements are finally combined in the so-called *workbench*, defined in (x, y, z) components.

The gun model

The potentials have been calculated using cylindrical coordinates (r,z) where r is the radial coordinate and z the coordinate along the optical axis. The origin is set at the tip axis. The entire gun is sketched in Figure 2.4 (a). It is composed of three parts (called PA instances), defined by different mesh sizes (expressed in mm/gu). They are finally combined in a unique *workbench*. Peculiar attention has been paid to the vicinity of the nanotip apex where the finest mesh of 10^{-5} mm/gu has been used (Figure 2.4 (c)). The choice of a proper mesh size is crucial in this region in order to calculate the electric field and the electron trajectories. In the next instance a mesh size of 0.0005 mm/gu and a specific extension have been chosen to minimize the calculation time (Figure

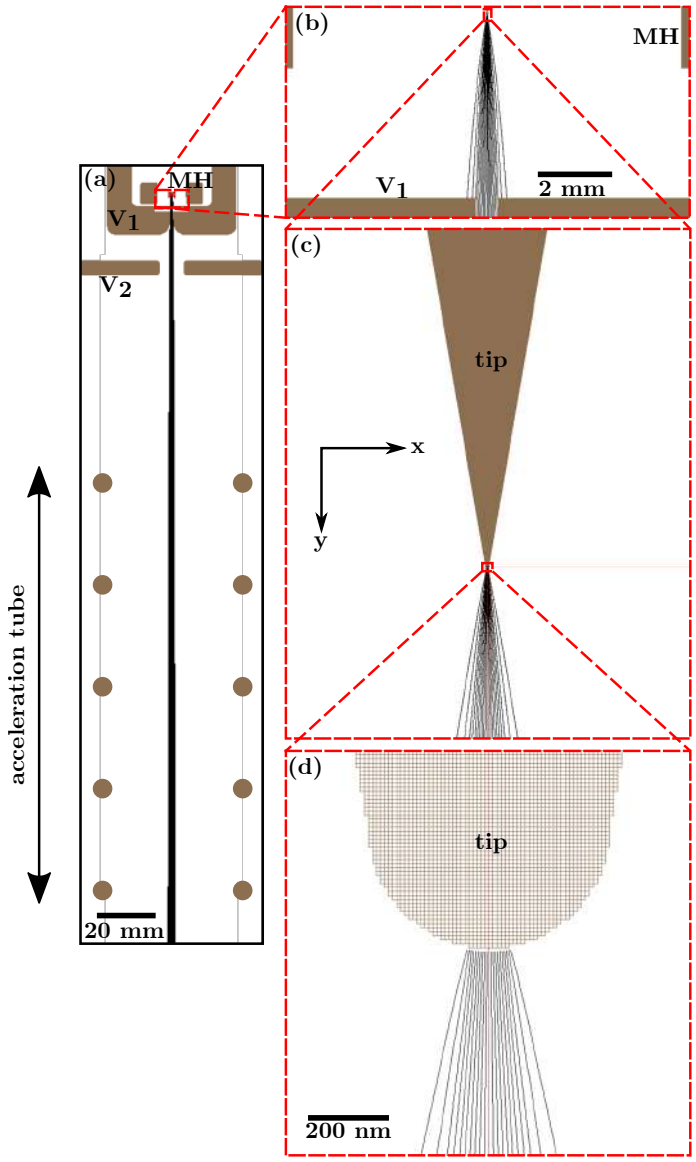

Figure 2.4: FemtoTEM gun model: 21 electron trajectories are shown. (a) Coarsest mesh (0.045 mm/gu). The circles represent the acceleration anode positions. (b) 0.0005 mm/gu PA istance. Part of the mirror holder and the extraction anode have been used as boundary conditions. (c) Finest mesh (10^{-5} mm/gu). (d) Zoom on the tip apex.

2.4 (b)). Finally, the lowest priority instance has been created with a mesh size of 0.045 mm/gu (Figure 2.4 (a)). It is extended until the end of the CFEG through the acceleration tube. In order to compare with the original gun, another model has been created without the MH.

Electron trajectories computation

Electrostatic fields and potentials between electrodes are calculated with SIMION by resolving the Laplace equation knowing the boundary conditions given by the applied voltages. In this model the cathode is maintained at $V_0 = -150\,\mathrm{kV}$, as well as the MH.

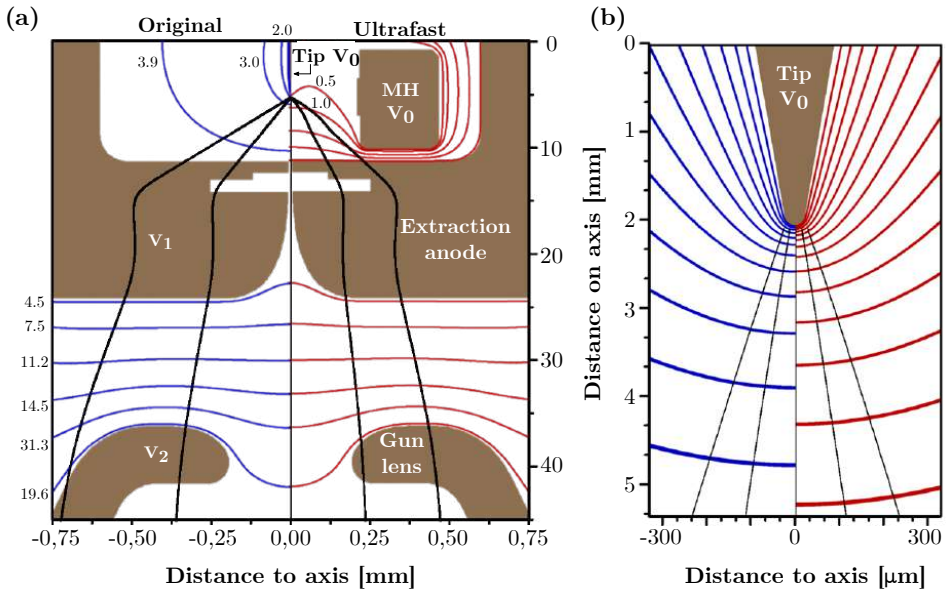

Figure 2.5: (a) Electron trajectories inside the entire gun. The figure is divided in two parts to compare the original and the modified CFEG. Equipotential lines are displayed in blue (original CFEG) and red (modified CFEG): all of them have the same value. 5 computed trajectories are shown. (b) Effect of the MH on the electric potential around the tip apex.

The extraction voltage applied to the anode is $V_1 = 4\,\mathrm{kV}$ relatively to the tip while a

potential difference $V_2 = 20\,\mathrm{kV}$ is applied between the electron source and the gun lens. The electrodes below the latter are kept at a potential such that $V_{\mathrm{IS}} = 26\,\mathrm{kV}$, following eq. (2.1). The electron initial positions have been set 10 nm away from the tip surface (as displayed in Figure 2.4(d)). The particles are distributed on a circle [131]. Figure 2.5 (a) shows the results of the electron trajectory simulation. It is divided in two parts: the left side represents a section of the original HF2000 gun while the right part represents the modified CFEG, in which the mirror holder has been added to the model. Five electron trajectories have been computed in this case. By comparing the trajectories in the original and modified electron gun, it can be clearly seen that the mirror holder slightly confines the emitted electrons. Comparing the outermost trajectories, it can be noticed that the position at the entrance of the condenser aperture ($\phi \sim 250\,\mu\mathrm{m}$) is different in the two cases by about 37 %. Such a difference is clearly visible in Figure 2.5 (a), looking at the enlarged electron trajectories. To better understand the influence of the MH on the gun optical properties, Electron Optic Design (EOD) simulations have been performed on a model of the modified gun, with special attention paid to the spherical and chromatic aberration coefficients [140, 145, 146]. A C_3 value of 35 mm has been calculated for the original gun and 33 mm for the modified source. The small discrepancy is probably due to the MH confinement before the gun lens. Electrons are slightly focused with a smaller incidence angle inside the gun lens, decreasing its contribution to the spherical aberration. Under the same electron optical conditions, the chromatic aberration coefficient has been evaluated as well. The calculated value is $C_C \approx 10\,\mathrm{mm}$, which lies in the same range as the unmodified CFEG. Another MH side effect has been evaluated by numerical simulations using SIMION and the Finite Element Method (FEM) software COMSOL Multiphysics [147]: the magnitude of the electrostatic field around the tip is reduced by a factor between 2.5 and 3, depending

on the tip-anode distance [140]. This effect is clearly visible in Figure 2.5 (a): on both sides the same equipotential lines are displayed and the potential gradient, *i.e.* the electric field, can be evaluated. Figure 2.5 (b) gives a detailed view of the zone around the tip apex.

2.1.3 Light injection and collection from inside the objective lens

The CL-I system has been designed to inject, align and focus the laser on the specimen or to collect light emitted from the sample. This system, originally developed in LPS-Orsay, has been adapted for FemtoTEM in close collaboration with the colleagues from LPS. It is composed of a parabolic mirror placed above the specimen holder inside the 4.5 mm polepiece gap of the HF2000, as shown in Figure 2.6 (b). The mirror has a focal distance $f = 1\,\text{mm}$ and a $300\,\mu\text{m}$ hole allowing the electron beam to pass through. It can be moved from outside by a XYZ translation stage equipped with three micrometric screws. Figure 2.6 (a) shows the external part of the system. A 10 mm-thick optical window has been sealed on a tube enabling the laser to be injected inside the column. The parabolic mirror is mounted at its extremity and the tube can be inserted or removed. Due to the limited size of the polepiece gap, a suitable specimen holder has been designed and fabricated. Its shape, visible in Figure 2.6 (a) and (b), allows to set the sample in the eucentric position and insert the parabolic mirror at the same time. A CCD camera has been mounted on the standard cold trap port, replacing the original cold finger, to monitor the insertion-removal procedures to avoid mechanical interferences. As shown in Figure 2.1 (b), an optical breadboard has been installed in proximity of the OL for the injection optical set-up. The latter is sketched in Figure 2.7 (a). A piezoelectric mirror is used to precisely align the injection beam on the

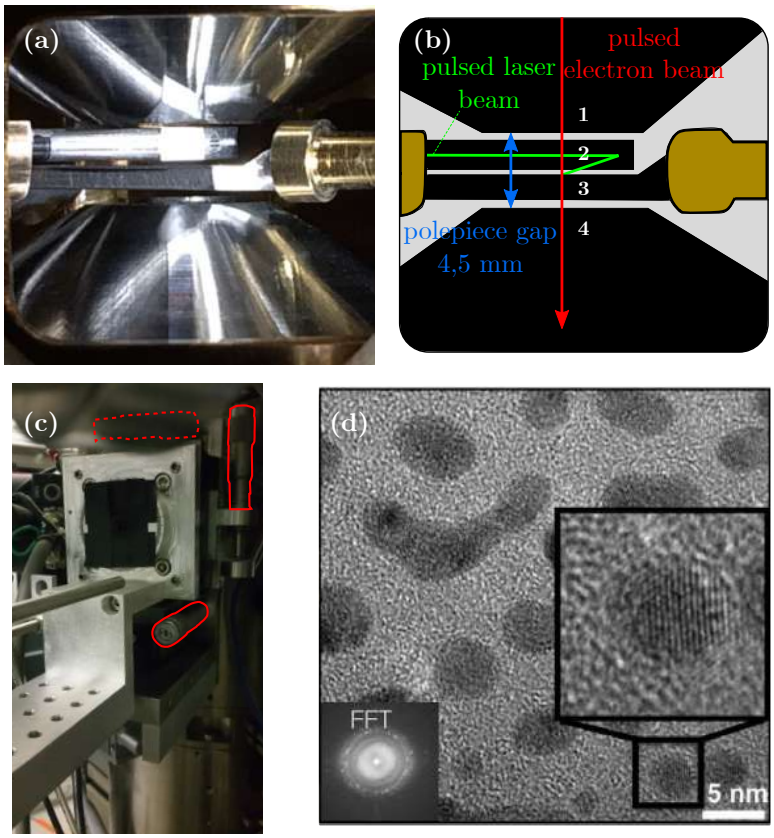

Figure 2.6: (a) Picture of the OL polepiece gap of the FemtoTEM. (b) Description of (a). 1: objective lens upper polepiece. 2: injection tube. The parabolic mirror is installed at its extremity. 3: specimen holder. 4: objective lens lower polepiece. (c) External view of the injection system. The positions of the three micrometric screws are highlighted in red. (d) High Resolution TEM image obtained with the modified TEM operated in DC emission mode on gold nanoparticles. This confirms that no significant deterioration of the spatial resolution is introduced by the modification performed on the original HF2000.

specimen with the help of a CCD, used to monitor the procedure. A half-wave plate has been installed before the optical window to control the laser beam polarization. For cathodoluminescence experiments, a spectrometer Andor SR303i coupled with a photodetector (Andor Newton EMCCD) are available on the set up (Figure 2.7 (b)).

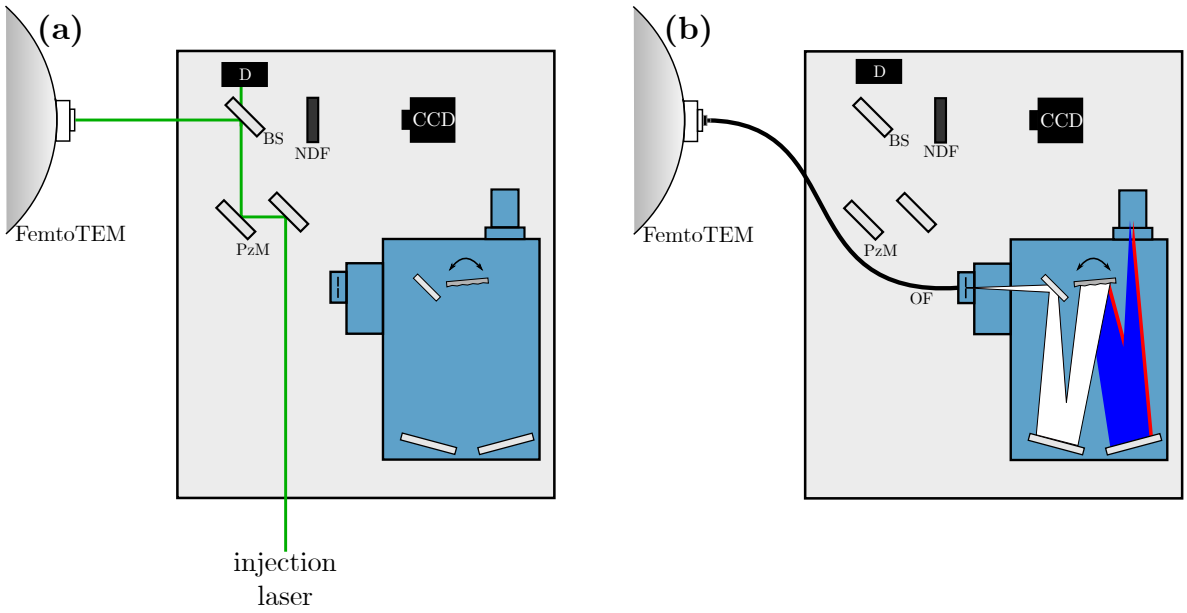

Figure 2.7: (a) and (b): scheme of the CL-I optical breadboard. (a) Injection configuration. (b) CL configuration. NDF: Neutral Density Filter. OF: Optical Fiber.

An optical fiber can be inserted inside the injection tube to maximize the collected light.

Despite the modifications, the objective lens aberrations remain unchanged and are, respectively $C_S = 1.2\,\text{mm}$ and $C_C = 1.4\,\text{mm}$. Figure 2.6 (d) reports an HR image of gold nanoparticles showing that the injection system does not affect the microscope performances. The image has been acquired with FemtoTEM operating at 200 kV in DC mode and a resolution of 0.2 nm has been achieved.

2.1.4 Ultrafast optics set-up

Our laser system is a compact ultrafast fiber laser (Satsuma, Amplitude Systèmes), delivering ultrashort (350 fs), high energy (up to $20\,\mu\text{J}$) pulses at 1030 nm with a tunable repetition rate from single shot to 2 MHz. Figure 2.8 shows a sketch of the optical

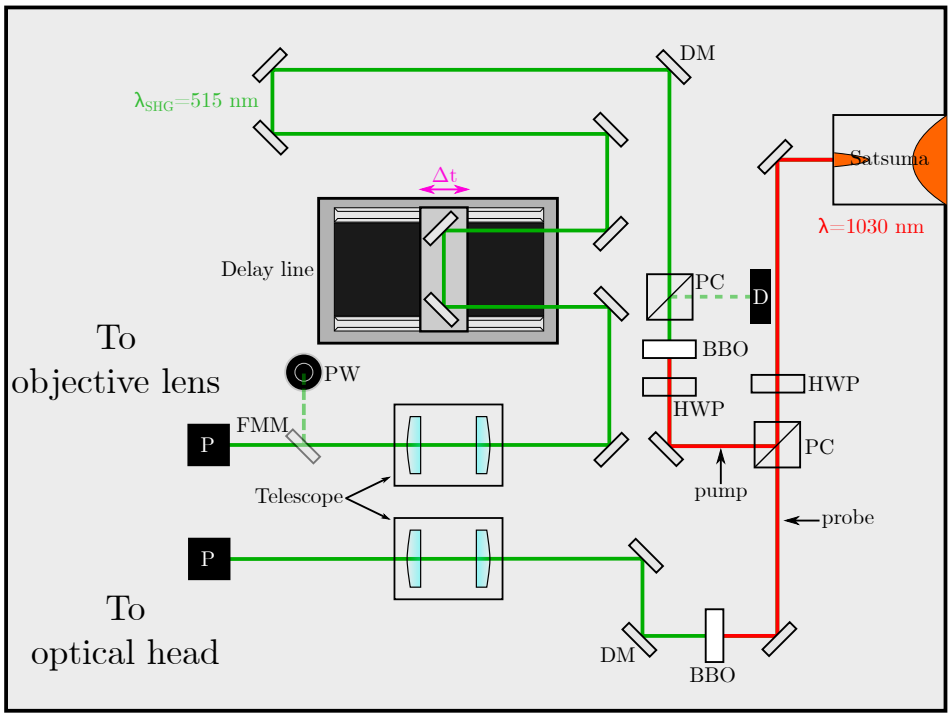

Figure 2.8: Scheme of the optical set-up. PC: polarizing cube. BBO: beta barium borate. DM: dichroic mirror. HWP: half-wave plate. PW: power meter. FMM: flip mount mirror. P: periscope. D: dump.

set-up. The primary beam is separated by a polarizing beam splitter cube into one pump and one probe beam. The maximum power available in the two lines is set by a half-wave plate placed before the polarizing cube. The laser beam in the *probe line* is sent on a 3 mm-thick beta barium borate (BBO) crystal to generate femtosecond pulses at 515 nm by Second Harmonic Generation (SHG). A computer controlled mechanical *delay line* is installed in the *pump line* to vary the delay between the laser pump and electron probe pulses. A second half-wave plate is used to adjust the injected pump power. Both the *pump* and *probe* beams are sent toward the CL-I breadboard by two periscopes (Figure 2.7 (a) and (b)) . Dichroic mirrors are installed after the BBOs to

filter out the residual fundamental infrared beam. Two telescopes are used to precisely adjust the laser focusing on the CFEG emitter and the specimen.
In the next section we first characterize the modified electron gun as well as the microscope properties. Finally, a demonstration of several TEM operation modes are given.

2.2 Properties of the CFEG UTEM

The characterization of the pulsed electron source is the first step. Thanks to the results presented in the following, it is possible to understand the emission mechanism, evaluate the emission region of the nanotip and measure the electron pulse duration.

2.2.1 The ultrafast electron source

Figure 2.9 (a) is a map of the probe current detected by F_1. It has been obtained by scanning the laser on the tip apex using one of the piezoelectric mirrors of the optical head. The emission region, evaluated by fitting the current map, has a FWHM of $2.95 \pm 0.07\,\mu\mathrm{m}^2$. With an incident laser power of 4.5 mW at a repetition rate $f = 1\,\mathrm{MHz}$, the maximum value of probe current is $\sim 2.7\,\mathrm{pA}$. The average number of emitted electrons per pulse is 18. Such a scan is routinely recorded when starting the experiment just after the initial flash-cleaning and the high voltage build-up. The laser position on the tip apex as well as the focus are finely adjusted to maximize the emitted current. The latter lies in the $2-3\,\mathrm{pA}$ for a laser power $W_{LAS} = 5\,\mathrm{mW}$ at $f = 1\,\mathrm{MHz}$. When the laser is properly focused on the tip apex, the emitted current is maximum when the laser electric field is oriented parallel to the tip axis [132]. On the contrary, when the electrons are emitted from the tip shank, the maximum current is obtained

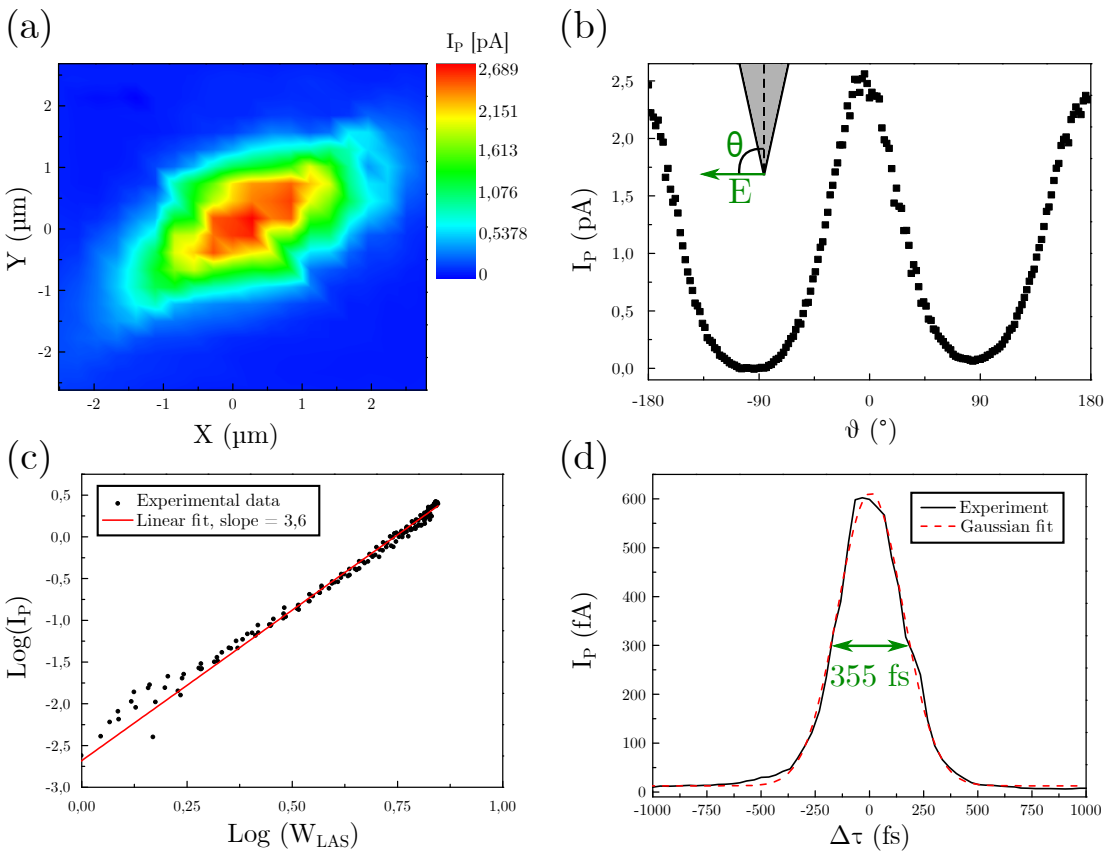

Figure 2.9: (a) Map of the probe current measured by F_1. (b) Dependence of the probe current on the polarization angle. (c) Logarithmic plot of the probe current as a function of the average laser power. (d) Autocorrelation measurement of the probe current.

for an incident polarization perpendicular to the tip axis. Figure 2.9 (b) shows the probe current polarization dependence and demonstrates that the electrons are emitted at the tip apex.

Figure 2.9 (c) presents an example of measurement of the dependence of the probe current on the incident laser power. The values of the nonlinearity order that we have deduced from our experiments span a broad range between 2.5 and 3.5. This is probably related to their sensitivity to several experimental parameters such as the focusing of the laser beam on the nanotip apex. As shown in the theoretical results of Figure 1.20, the fact that the effective nonlinearity is larger than 2 suggests that the electron gas is strongly perturbed in our experimental conditions. In this case, the temporal and spectral widths depend on the laser intensity incident on the nanotip. This motivates the investigations described in the next chapter aiming at characterizing in-situ the spectro-temporal properties of the electron pulse. Finally, two-pulse autocorrelation measurements of the probe current are reported in Figure 2.9 (d). The laser beam has been split into two paths, then recombined and sent onto the CFEG emitter. One of the two paths involves a delay line used to change the delay between two laser pulses. The probe current is recorded as a function of the delay. The FWHM of the autocorrelation signal is 360 fs. The 515 nm laser pulses used in our experiments have a time FWHM of 250 fs. The intensity autocorrelation measurement of these laser pulses has a FWHM of 400 fs. The fact that the FWHM of our correlation measurements on the probe current is smaller than 400 fs is due to the increased nonlinearity order of the emission in our experimental conditions. These results also suggest that cumulative heating effect can be neglected. This conclusion is also supported by an estimation of the temperature increase inside the nanotip apex which is of the order of 10 K.

2.2.2 Probe current stability

Figure 2.10 (a) shows the long-term stability of the probe current. The red curve displays the probe current evolution during 9 hours. The nanotip has been flash-cleaned before the experiment. An initial current $I_P \sim 2.7\,\mathrm{pA}$ has been obtained with an average laser power $W_{LAS} = 7.15\,\mathrm{mW}$, a repetition rate $f = 1\,\mathrm{MHz}$, an extraction voltage $V_1 = 4\,\mathrm{kV}$ and a ratio $R = 5$. Usually, the decrease in current in a DC CFEG is due to the tip surface contamination, but in laser-driven emission optical misalignments can also contribute. In order to discriminate the two effects, we repeated the same experiment, re-optimizing the laser position on the nanoemitter every hour. The inset of Figure 2.10 (a) shows the laser position on the tip apex each hour after the optimization, confirming the stability of the optical set-up. As the black curve in Figure 2.10 (a) shows, the current decreases similarly even with a periodic reoptimization of the optical alignment. This confirms that the main reason of the long term drift of the probe current is the contamination, as for a normal DC CFEG. Current fluctuations have been studied by Todokoro *et al.* [148]. This study highlighted the influence of the ion bombardment on the tip surface and the importance of the vacuum quality inside the electron gun. Improvements in UHV conditions as well as new flash-cleaning technology will allow to improve the long-term current stability. Short-term stability, also known as *flicker noise* [149], has been studied by recording the emitted current during 5 minutes several times. Our ultrafast CFEG has a flicker noise of approximately 8%. This value is larger than DC CFEGs, which have a flicker noise of approximately 1%. The main causes of flicker noise in DC cold field emission are: absorption/desorption of atoms and molecules as well as their migration on the tip surface and thermally induced transition of bonding states of adsorbed molecules [1]. In ultrafast electron emission, another cause of flicker noise could be the variation in the SHG intensity. To discriminate this

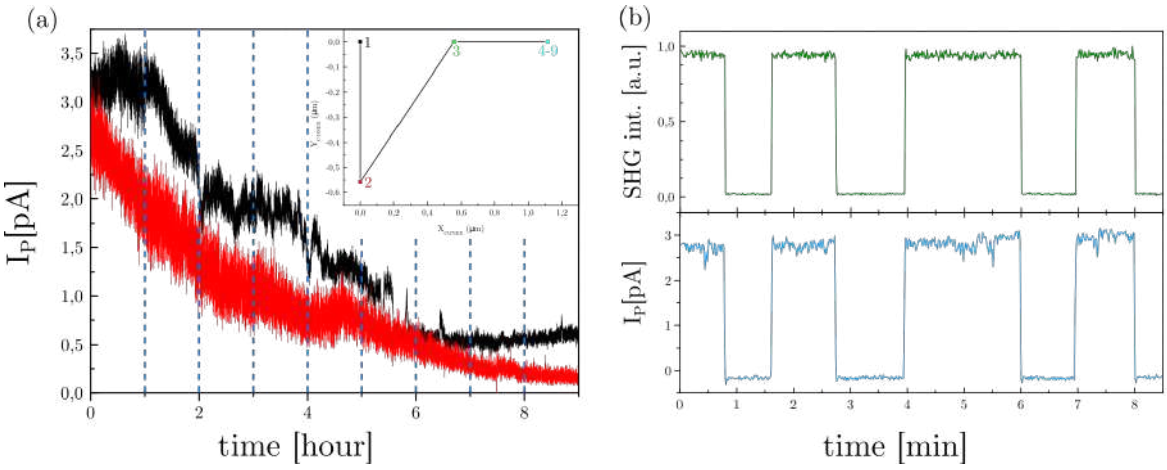

Figure 2.10: (a) Long term current stability measurements. The tip has been flash-cleaned before the experiment. The red curve is the probe current evolution measured during 9 hours. The black curve has been obtained by optimizing the laser position every hour. Inset: position of the laser on the nanotip each hour. (b) Short term stability of the probe current (bottom) and simultaneous measurement of the SHG intensity (top).

effect, both the probe current and the laser intensity have been acquired, as shown in Figure 2.10 (b). The probe current noise is detected even blanking the laser beam directed to the electron emitter, *i.e.* when the current is zero. In order to evaluate the influence of the SHG intensity fluctuations on the overall probe current noise, we can consider from equation (1.25) that the number of electrons, N_e, emitted through a n-photon photoemission process is proportional to the n^{th} power of the number of incident photons, N_{ph}:

$$N_e = \alpha_n N_{ph}^n \tag{2.2}$$

where α_n takes into account several factors, such as the absorbing material and the emission probability [150]. We can evaluate the fluctuation in the number of photoelectrons as follows:

$$\frac{\Delta N_e}{N_e} = n\frac{\Delta N_{ph}}{N_{ph}}. \tag{2.3}$$

If we consider the $\frac{\Delta N_{ph}}{N_{ph}} = 2\%$ variation in the SHG intensity of our set-up and a two-photon photoemission process ($n = 2$), the consequent oscillation of the electron number is 4%. This shows that SHG intensity fluctuations are not the only cause of current instabilities, but play a major role together with contamination, particles diffusion and detection noise.

2.2.3 FemtoTEM optimization

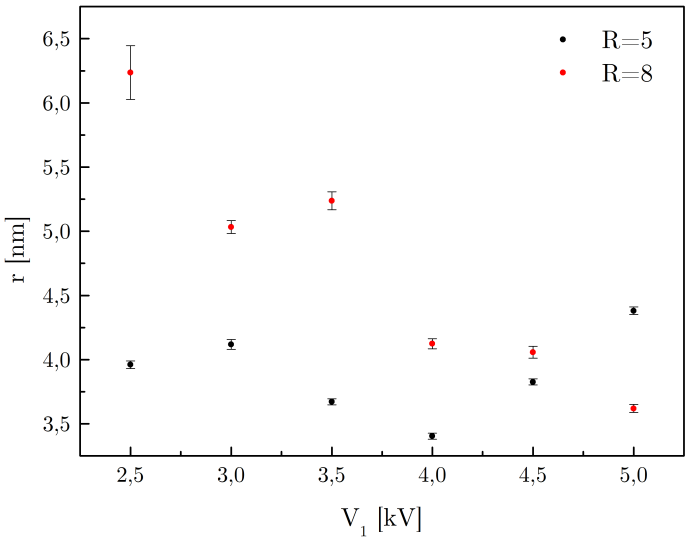

Figure 2.11: Electron spot radius as a function of the extraction voltage in virtual ($R = 5$) and real ($R = 8$) crossover modes.

The optimization of the electron optics properties allowed to push FemtoTEM to optimal performances depending on the chosen technique. The electron spot size, current and brightness have been studied as a function of the extraction voltage, the ratio $R = \frac{V_2}{V_1}$ and the number of electrons per pulse. Figure 2.11 reports the variation of the

spot radius in both real and virtual crossover configuration as a function of the extraction voltage. The electron beam has been triggered by a laser power $W_{LAS} = 6\,\mathrm{mW}$ ($\lambda_{SHG} = 515\,\mathrm{nm}$) at a repetition rate $f = 1\,\mathrm{MHz}$. The line profile of electron spots has been extracted from a UTEM image, then the spot radius has been evaluated from the FWHM of a gaussian fit. In virtual crossover condition ($R = 5$), the electron spot radius slightly varies from 3.4 to $\sim 4.4\,\mathrm{nm}$ and the smallest size has been obtained for $V_1 = 4\,\mathrm{kV}$. On the contrary, in real crossover mode, the spot size decreases from ~ 6.3 to $\sim 3.6\,\mathrm{nm}$. The large confidence interval for $V_1 = 2.5\,\mathrm{kV}$ is related to the low signal to noise ratio due to the reduced probe current. These systematic experiments allowed to select the optimum V_1 and V_2 values that give the smallest spot size. A further optimisation of the gun alignment by gun deflection coils adjustment has yielded a smaller spot size ($d = 4.42\,\mathrm{nm}$ for $R = 5$ and $d = 3.2\,\mathrm{nm}$ for $R = 8$). Figure 2.12 shows the

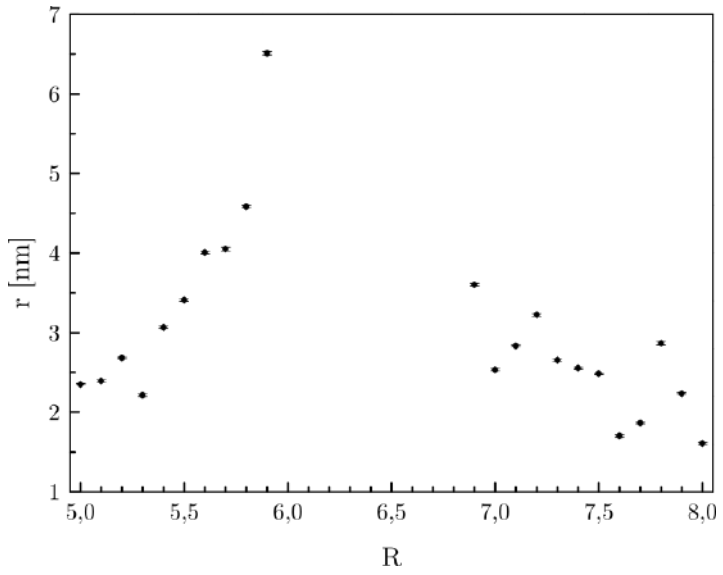

Figure 2.12: Electron spot radius as a function of R. A parallel beam, obtained for ratios between 6 and 6.8, do not present crossovers.

spot size evolution as a function of the ratio R. The extraction voltage has been set to

$V_1 = 4\,\mathrm{kV}$. For $R = 5$, a virtual crossover is formed in the tip apex. Increasing the ratio, the effect of the gun lens (V_2) becomes more important and the gun crossover position changes. The illumination system after the gun demagnifies the source image

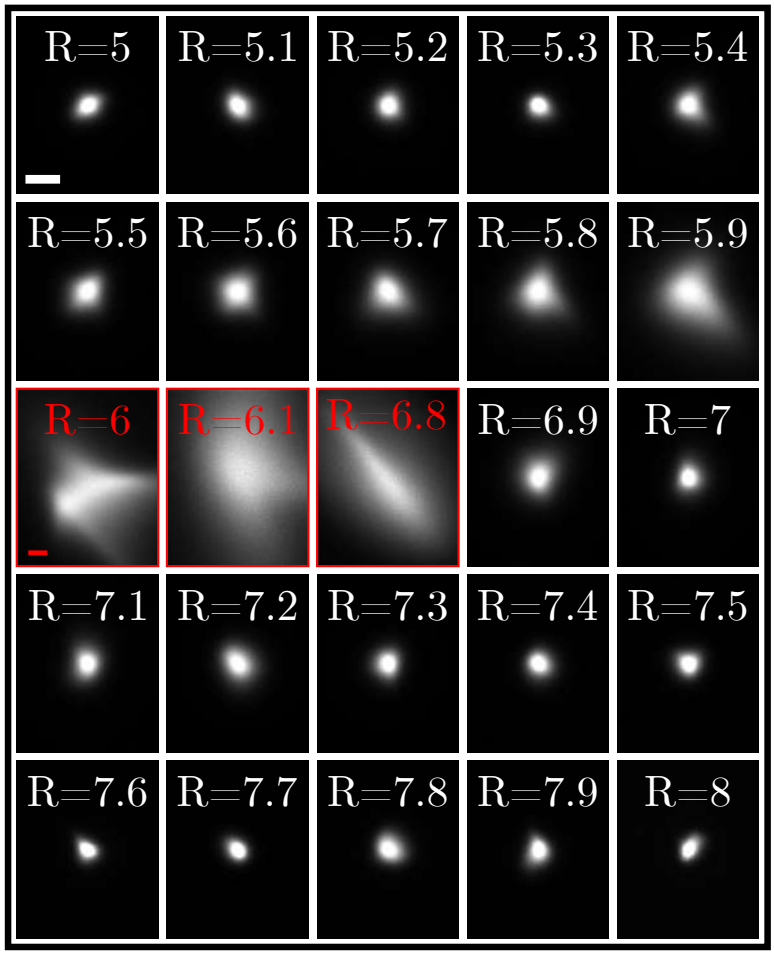

Figure 2.13: Electron spots for different ratios. Data framed in red show the spot size and shape for a parallel beam. Scales: 10 nm

and its effect is stronger when the crossover position is farther from the first condenser lens. This is visible in both Figure 2.12 and Figure 2.13, which report that the spot radius increases up to 6.5 nm for $R = 5.9$. Ratios between 6 and 6.8, cannot be used

practically due to the strong influence of the gun aberrations: when the source switches between virtual and real crossover, the electron beam appears as shown in Figure 2.13, inside the red rectangles. For $R \geq 6.9$ the microscope is in real crossover condition. In this case, a stronger V_2 brings the gun crossover away from the first condenser lens, reducing the spot size to $\varnothing \sim 1.6\,\text{nm}$ for R=8.

Figure 2.14 shows how the spot radius changes as a function of the energy per pulse (E_{PP}). These experiments have been performed with the extraction voltage $V_1 = 4\,\text{kV}$, the ratio $R = 5$ and the laser repetition rate $f = 2\,\text{MHz}$. The measured radius varies from $1.4\,\text{nm}$ ($E_{PP} \sim 2.2\,\text{nJ}$), to $\sim 2\,\text{nm}$ ($E_{PP} \sim 3.75\,\text{nJ}$). Our hypothesis is that both the coulombic repulsion inside the pulse and the effect of higher laser powers triggering electron emission from a larger zone, increase the virtual source size and hence the spot dimension.

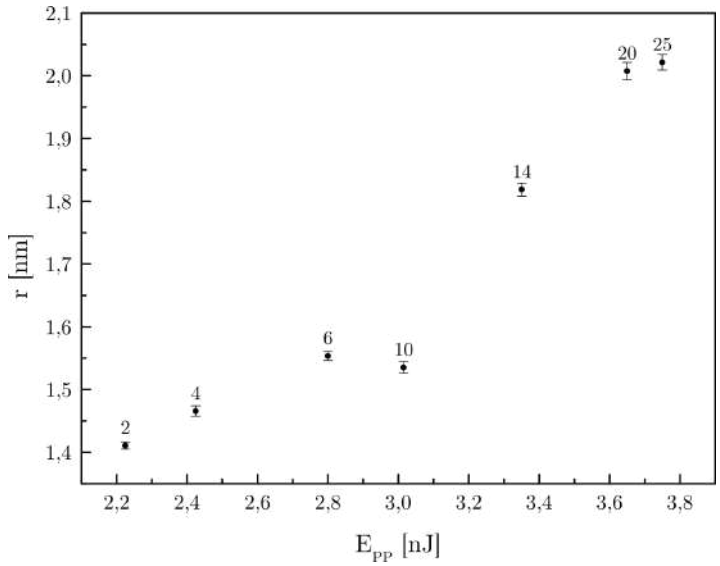

Figure 2.14: Electron spot radius a function of the energy per pulse. Label: number of electrons per pulse.

2.2.4 Measurement of brightness and angular current density

To conclude the characterization of the UTEM electron source, the brightness has been experimentally evaluated. However, in the case of a UTEM, the electron beam is pulsed at the same frequency as the laser. Therefore, instead of using equation (1.18), we have to introduce the time-averaged brightness, B_{AVG}:

$$B_{AVG} = \frac{fNe}{(\pi r \alpha_1)^2} = \frac{fI_E}{(\pi r_0 \frac{\alpha_1}{2})^2} = fB. \tag{2.4}$$

f being the laser repetition rate, N the number of electrons per pulse and e the elementary charge. $2r_0 = d_0$ and $\frac{\alpha_1}{2}$ are the source size and the divergence semi-angle, respectively. We have determined the time-averaged brightness in both virtual and real cross-over conditions (trajectories in Figure 2.3 (b)). The microscope has been set in ANALYSIS mode (equivalent to NANOPROBE or CBD mode in FEI and Jeol microscopes, respectively) to maximize the demagnification of the illumination system and a 30 μm STEM aperture has been used to limit the effect of the condenser lenses spherical aberration. For this experiment we set $V_1 = 4\,\mathrm{kV}$. Figure 2.15 shows the required information to calculate the microscope brightness, obtained in virtual crossover mode ($R = 5$). Figure 2.15 (a) allows to measure a spot radius $r_0 = 2\,\mathrm{nm}$ (evaluated from the FWHM of the intensity profile shown in Figure 2.15 (b)), while Figure 2.15 (c) allows to evaluate the beam convergence semi-angle ($\alpha_1/2 \sim 6\,\mathrm{mrad}$, in this configuration) from the size of the associated Convergent Beam Electron Diffraction (CBED) disk [151]. A probe current of $\sim 80\,\mathrm{fA}$ at 1 MHz has been measured with the Faraday cup F_2. By neglecting the aberration contribution to the spot size, the brightness is $B = 5.8 \cdot 10^7\,\mathrm{A \cdot m^{-2} \cdot Sr^{-1}}$. Under the same experimental conditions, the probe current measured by F_1 is $\sim 2.5\,\mathrm{pA}$. The difference between the two currents is due to aberrations. The HF2000 is an almost 30-years-old microscope and thus the

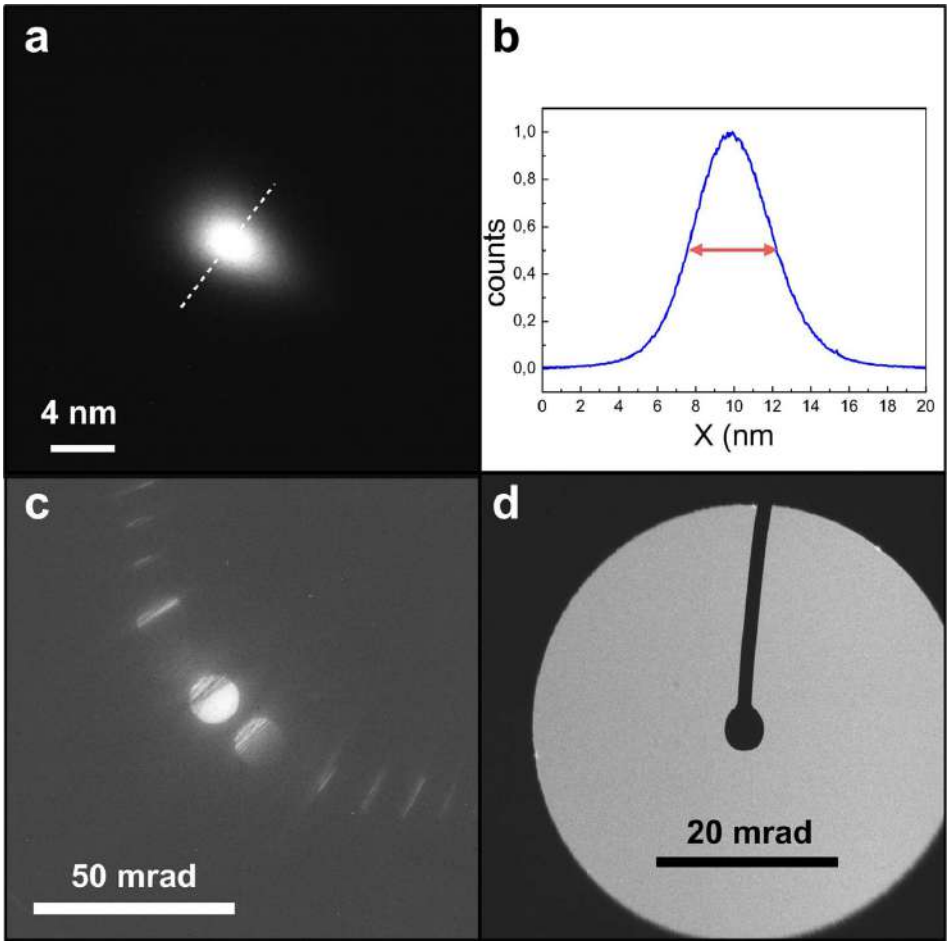

Figure 2.15: Experimental measurement of the brightness in virtual crossover mode.(a) Electron spot of 4 nm diameter acquired with a 30 μm STEM aperture. (b) Line profile of the spot shown in (a). (c) CBED pattern of a Si specimen oriented in the (220) direction. (d) CBED transmitted disk obtained with a 100 μm STEM aperture. The shadow image of the beam block/F_2 is visible inside the disk.

performances of the new ultrafast CFEG should be improved with a recent state-of-the-art TEM. Nevertheless, even if the experiment has been performed at $f = 1\,\mathrm{MHz}$ instead of $f = 250\,\mathrm{kHz}$ (as reported in [137]), the measured brightness is the highest ever measured in an ultrafast TEM.

The brightness has also been evaluated in real crossover condition ($V_1 = 4\,\mathrm{kV}, R = 8$). With a spot size radius $r_0 = 4\,\mathrm{nm}$, $\alpha_1/2 \sim 6\,\mathrm{mrad}$ and a current measured by F_2 of $\sim 122\,\mathrm{fA}$ the brightness is $B = 2.2 \cdot 10^7\,\mathrm{A \cdot m^{-2} \cdot Sr^{-1}}$. By considering that each $\sim 350\,\mathrm{fs}$-electron pulse is emitted every $1\,\mu\mathrm{s}$, the brightness obtained for a hypothetical continuous emission with the same instantaneous number of electrons is of the order of $10^{13}\mathrm{A \cdot m^{-2} \cdot Sr^{-1}}$, comparable to conventional DC CFEG TEMs. This confirms that despite the modifications of the electron gun the electron optics properties of the microscope are maintained. However, the main drawback of the ultrafast operation mode is the considerable decrease of the total beam current, as we will see in the next studies.

We will now evaluate the angular density, which is an important figure of merit. Figure 2.15 (d) shows the CBED transmitted disk obtained with a $100\,\mu\mathrm{m}$ STEM aperture. The current measured by F_2 allows to evaluate an angular current density of $2\,\mathrm{nA \cdot Sr^{-1}}$. Once the brightness and the angular current density are known, it is possible to calculate the virtual source size dimension. The latter lies in the $5 - 10\,\mathrm{nm}$ range and is comparable to the one measured in a standard CFEG [1]. This result is in line with the results of Ehberger *et al.* [138] who demonstrated that the virtual source size of a nanoemitter in DC and laser driven emission are similar. The discrepancy between the source size reported in their study and the one we calculated [**?**] is probably due to a difference in the apex dimension of the W nanotip used in the two experiments ($r \sim 10\,\mathrm{nm}$).

In the following the potential of FemtoTEM for conventional TEM experiments will be

presented. Imaging, diffraction in parallel (Selected Area Electron Diffraction, SAED) and convergent beam (CBED) as well as Electron Energy Loss Spectroscopy (EELS) have been performed using the femtosecond electron beam at 150 keV.

2.2.5 Demonstration of operation as a TEM

Figure 2.16 (a) shows a TEM image of a silicon lamella while Figure 2.16 (b) and (c) reports High Resolution (HR) images of a Catalase crystal. In Figure 2.16 (d) and (e) electron diffraction patterns in SAED and CBED are shown, respectively. Figure 2.16 (d) shows a SAED pattern of a Titanium aluminide (TiAl) γ-phase crystal and Figure 2.16 (e) a CBED pattern close to the [110] zone axis of a silicon crystal. The resolution in both diffraction and HR are comparable to the ones obtained with the original HF2000. A lattice spacing of 0.9 nm in a Crocidolite crystal has been resolved in ultrafast operation mode. The achieved resolution in ultrafast mode is slightly worse than the 0.2 nm obtained with DC emission on gold nanoparticles (Figure 2.7 (d)). This difference is mainly due to mechanical instabilities during the long exposure time (150 s) required by the low-dose conditions of the ultrafast operation. In DC CFEG TEMs, the emission current is typically set to 10 μA and the corresponding probe current, with a 30 μm STEM aperture in ANALYSIS mode, is usually around 100 pA. Under the same electron optical conditions ($V_1 = 4$ kV, $R = 5$), with an average laser power $W_{LAS} = 6$ mW at $f = 1$ MHz, the emission current is ~ 2.5 pA (corresponding to 15 epp) and the probe current is ~ 80 fA. Current values are limited by the tip withstand. The tungsten tip endurance has been studied on a nanoemitter (apex size ~ 100 nm) irradiated with 800 nm femtosecond laser pulses at 1 kHz repetition rate [152]. They reported that the laser power to yield 10 epp is close to the damage threshold. However, several experiments have been performed in FemtoTEM using up to ~ 40 epp

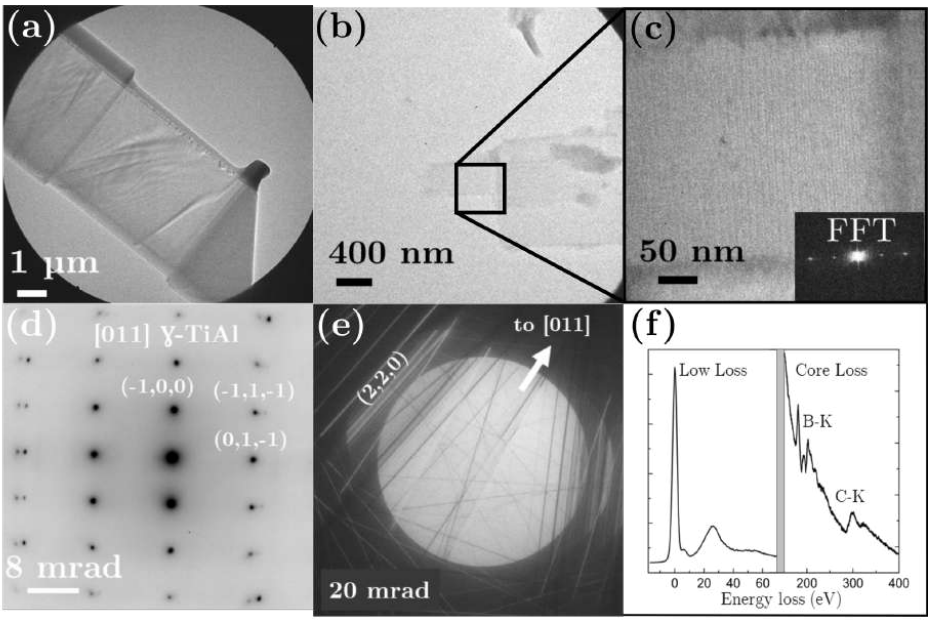

Figure 2.16: (a) Ultrafast TEM image of a Si lamella (repetition rate $f = 1\,\mathrm{MHz}$, number of electrons per pulse $N_{epp} = 12.5$, exposure time $t_{exp} = 100\,\mathrm{s}$, binning 1). (b) and (c) Ultrafast HR images of biological Catalase crystal ($f = 2\,\mathrm{MHz}$, $N_{epp} = 11$, $t_{exp} = 150\,\mathrm{s}$, binning 4). (d) Ultrafast SAED pattern of TiAl γ-phase crystal oriented in [110] direction ($f = 1\,\mathrm{MHz}$, $N_{epp} = 12.5$, $t_{exp} = 150\,\mathrm{s}$, binning 2). (e) Ultrafast CBED pattern oriented close to the [110] direction of a Si crystal ($f = 1\,\mathrm{MHz}$, $N_{epp} = 12.5$, $t_{exp} = 100\,\mathrm{s}$, binning 1). (f) Ultrafast EELS of a boron nitride crystal ($f = 2\,\mathrm{MHz}$, $N_{epp} = 6.25$, $t_{exp} = 1\,\mathrm{s}$ for the low loss region, 60 s for core loss).

(*i.e.* $I_E = 6.4\,\mathrm{pA}$ at $1\,\mathrm{MHz}$) and no modifications in the source performance have been noticed. This discrepancy could be attributed to the difference in the dimension of the apexes and in the optical parameters (laser wavelength, repetition rate, pulse duration). The shorter optical wavelenght used in our experiments indeed yields a higher emission efficiency. Further experiments are necessary to better clarify this aspect.

Figure 2.16 (f) reports a Boron Nitride (BN) ultrafast EELS obtained in virtual crossover condition. The microscope has been set in ANALYSIS and diffraction mode with 0.15 m camera length. The bulk plasmon signal is visible in the low-loss region, while the

boron and carbon K edge are observed in the core-loss region (188 eV and 284 eV, respectively). The Zero Loss Peak (ZLP) has been studied to determine the influence

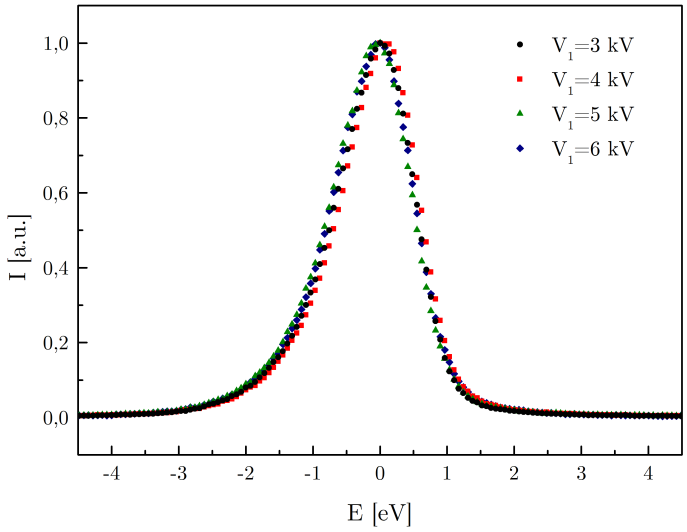

Figure 2.17: Zero Loss Peak acquired for different extraction voltages: $V_1 = 3$, 4, 5 and 6 kV. FWHM are $\Delta E = 1.32$, 1.33, 1.38 and 1.41 eV, respectively.

of the extraction voltage and the number of electrons per pulse on the energy resolution. Figure 2.17 shows the ZLP intensity as a function of the extraction voltage V_1. The laser average power is set to 8 mW at 2 MHz. The ratio $R = \frac{V_2}{V_1} = 5$. Each pulse contains 6 electrons. For $V_1 = 4$ kV the ZLP has a FWHM of 1.32 eV while for $V_1 = 6$ kV the FWHM is 1.41 eV. Therefore, the extraction voltage has only a weak or no influence on the electron energy spread in our CFEG-UTEM. The energy spread of our femtosecond electron pulses is significantly larger than the one of conventional DC CFEG TEMs. It is related both to the ultrafast dynamics of the electron gas and to Coulomb interactions among the emitted electrons during their propagation along the UTEM column [125].

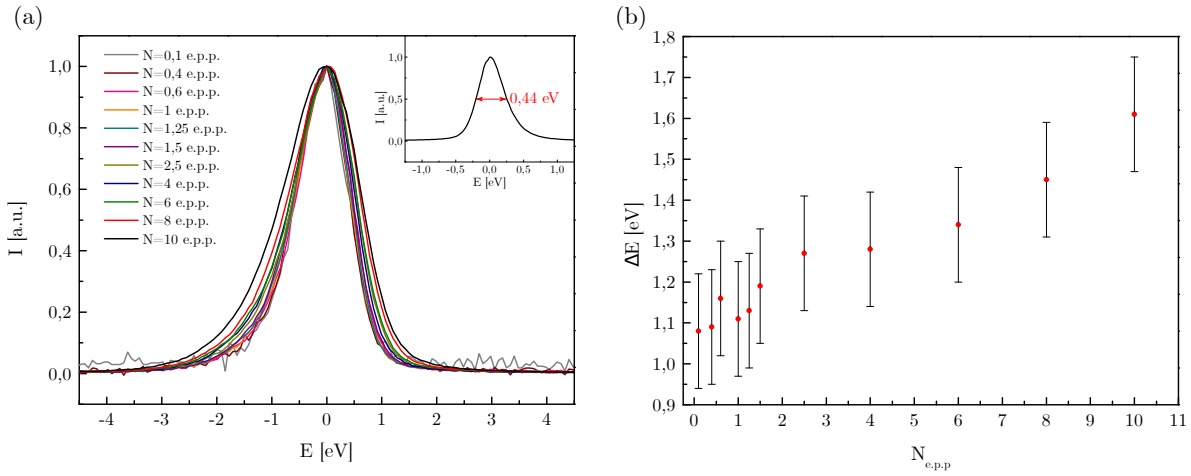

Figure 2.18: (a) ZLPs acquired for different numbers of electrons per pulse. Inset: A ZLP acquired in an unmodified HHT HF2000 CFEG-TEM. (b) FemtoTEM energy resolution as a function of N_{epp}.

Figure 2.18 reports on the energy resolution variation as a function of the number of electrons per pulse. $V_1 = 4\,\mathrm{kV}$, $R = 5$ and the repetition rate is set to 2 MHz. From the ZLP analyses in Figure 2.18 (b) we notice that the FWHM decreases from 1.61 eV at 10 epp to 1.08 eV for 0.1 epp. This ultimate energy resolution has been obtained for less than one electron per pulse. In this case, the coulombic repulsion does not play any role. As discussed in paragraph 1.3.3, it is the ultrafast electron dynamics that determines this minimum value of the energy spread. The experimental ZLPs show the same asymmetry as the simulated spectrum in Figure 1.19 (b), confirming the reliability of the model.

2.3 Conclusion

In this chapter FemtoTEM has been presented. First, we showed the modifications on the original Hitachi HF2000 CFEG and objective lens, then we described the ultrafast

optical set-up. Secondly, characteristics and performances of the machine have been given.

By employing the ultrafast laser source and electron beam we will show in the next chapter how to exploit them to perform the first pump-probe experiment by using a UTEM technique: Electron Energy Gain Spectroscopy.

Chapter 3

In-situ characterization of the spectro-temporal properties of the ultrashort electron pulses

This chapter reports on the first ultrafast pump-probe experiment performed in FemtoTEM. The spectro-temporal resolution of the instrument is characterized in-situ in an electron-photon cross-correlation experiment based on the detection of electron energy gains. We first summarize the theoretical description of the interaction between an ultrashort electron pulse and a femtosecond laser pulse as proposed by Park *et al.* [153]. Afterwards, the theoretical model is used to study the influence of different experimental parameters on the gain spectra. We then extract the electron pulse chirp under different conditions from the experimental Electron Energy Gain maps. Finally, numerical simulations are performed to determine and compare to experiments the electron pulse duration.

3.1 Electron Energy Gain Spectroscopy

Electron Energy Gain Spectroscopy (EEGS) is a UTEM technique that characterizes the optical or vibrational excitations of nanostructured systems from the detection of electrons which have gained energy during their interaction with the sample. Howie first proposed the possibility to observe the electron energy gains induced on a specimen simultaneously illuminated by an electron and a laser beam, both in a STEM image or in electron loss spectra. In the latter, a very weak gain peak was expected [154]. The optical characterization of nanosystems in electron microscopes has been intially performed using Electron Energy Loss Spectroscopy [155]. However, the exploration of the low-energy region of the spectrum to extract signatures of the optical excitations is made difficult by the tail of the ZLP. Garcia de Abajo and Kociak [156] proposed Electron Energy Gain Spectroscopy (EEGS) as an alternative to overcome this limitation by exploiting the interaction of fast electrons with the evanescent electric field in the vicinity of a nanostructure. The first experimental observation of an EEG spectrum has been achieved by Barwick *et al.* [157]. By filtering the electrons that have gained energy, they succeeded in imaging the optical near-field around a multiwalled carbon nanotube and silver nanowires with a spatial resolution around 5 nm and a temporal resolution of 100 fs.

3.1.1 Electron-photon interaction

The coupling between electrons and photons in free space is forbidden due to the energy-momentum mismatch. As sketched in Figure 3.1, an electron passing from a state k_I to a state k_F experiences a variation of energy and momentum ΔE and Δp. The ratio $\frac{\Delta E}{c\Delta p}$ is the local slope of the dispersion relation highlighted by the purple line in Figure 3.1. A photon can provide the required energy but not the related momentum at the

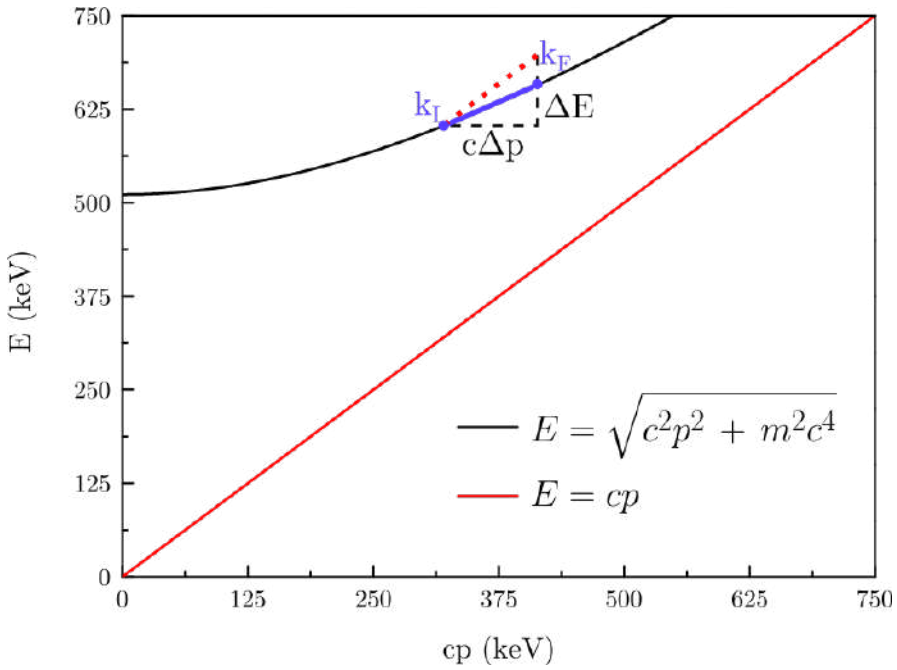

Figure 3.1: Relativistic dispersion relation of electrons (black) and photons (red).

same time (or vice-versa) as can be noticed from the red dotted line. In order to couple electrons and photons, both the energy and momentum must be conserved and hence the two slopes must be the same. In free space, this is the case for instance when electrons are travelling faster than light in the medium. This is the case of the *(inverse) Cherenkov effect* [158].

Electrons and photons can couple in free space by mean of a third system or a particle as in the *Kapitza-Dirac effect* [159]. An electron is sent onto a stationary light wave, which acts as an *optical grating*. The latter transfers a momentum to the electron that is elastically scattered at an angle equal to the angle of incidence, like in Bragg's law [159]. Although theoretically predicted in 1933, the lack of powerful enough light source precluded the experimental demonstration of this effect until the end of the last century [160, 161]. The *inverse Smith-Purcell effect* is another example of electron-photon

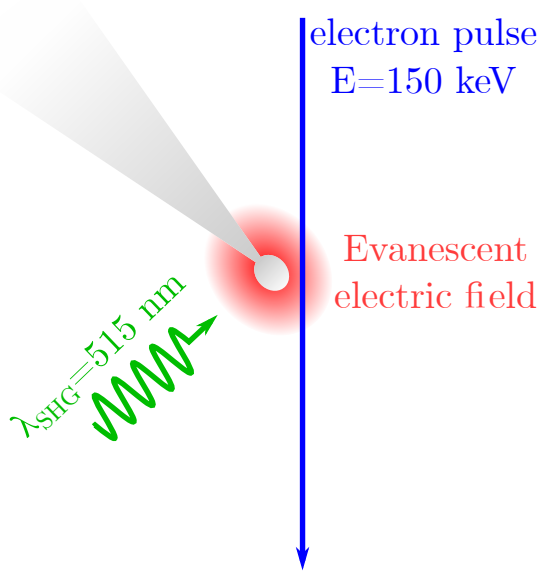

Figure 3.2: Schematic representation of the electron-photon interaction obtained in FemtoTEM. The nanosized extremity of the tungsten emitter has been used to create the evanescent electric field.

coupling via a third body. In this case, a metallic grating is used to meet the energy and momentum conservation requirements [162].

Electron-photon coupling can also result from the confinement of either the electron or the electromagnetic field. For instance, an electromagnetic wave incident on a nanostructure creates an evanescent electric field that can provide the necessary extra momentum to couple electrons and photons (Figure 3.2). In particular, the field component parallel to the electron motion yields efficient interactions between electrons and light. In the next paragraph, more details on the coupling via a scattered electric field will be given as well as the theoretical formalism of the process.

3.1.2 EEGS: theoretical formalism

The theoretical formalism described in the following has been proposed by Park *et al.*. Its main conclusions are in agreement with the prior work by Garcia de Abajo and Kociak [156]. All numerical simulations presented in the following are based on this approach. In particular, we use it to evaluate the effect of the experimental parameters (*i.e.* incident laser electric field, electron probe size, electron and laser pulse duration) on the EEG spectrum [153]. The description of the interaction between an ultrashort electron pulse and a femtosecond laser pulse is based on the resolution of the time-dependent Schrödinger equation.

We assume that an electromagnetic field polarized in the $\hat{x}$-direction with angular frequency ω is incident on a nanostructure. This incident electric field polarizes the nanostructure. This polarization is the source of a secondary electric field that acts back on the electrons. The electron wavefunction at a certain time t is defined as follows:

$$\psi(z,t) = g(z - v_e t, t) exp[i(k_e z - \omega_e t)] \tag{3.1}$$

where ω_e is the electron wave angular frequency and k_e the wavenumber. $g(z - v_e t, t)$ is called the *moving envelope function*. It describes the electron pulse profile at time t. The electron interaction with the evanescent electric field created around the nanostructure is described by the following Hamiltonian [163]:

$$H = \frac{1}{2m_e}(\boldsymbol{p_e} - q_e \boldsymbol{A})^2 + q_e V \tag{3.2}$$

in which m_e, $q_e = -e$ and p_e are the electron mass, charge and momentum. $\mathbf{A}$ and V are the vector and scalar potential, respectively. Choosing the Coulomb gauge ($\nabla \cdot \mathbf{A} = 0$) and in absence of charge density ($V = 0$), the Hamiltonian in equation (3.2) becomes:

$$H = \frac{\boldsymbol{p_e}^2}{2m_e} + \left(\frac{e}{m_e}\right)\boldsymbol{A} \cdot \boldsymbol{p_e} + \frac{e^2 A^2}{2m_e} \approx -\frac{\hbar^2 \nabla^2}{2m_e} - i\frac{e\hbar}{2m_e}\left(\frac{\tilde{E}}{i\omega_p} + \frac{\tilde{E}^*}{-i\omega_p}\right) \cdot \nabla \tag{3.3}$$

ω_p being the photon angular frequency. Because p_e is large, the term $\mathbf{A}\cdot\hat{p_e}$ is dominant and the A^2-term is negligible. $\tilde{E} = \mathbf{E}(\mathbf{r}; k_p, E_0)\, exp[-i\omega_p t]$ is the complex representation of the scattered electric field. The term in equation (3.3) containing $\tilde{E}$ and $\tilde{E}^*$ determines the processes of absorption and emission of photons. Solving the time-dependent Schrödinger equation $i\hbar(\partial/\partial t)\Psi(\mathbf{r},t) = H\Psi(\mathbf{r},t)$ yields the envelope function after the interaction, *i.e.* at time $t \to \infty$:

$$g(z',+\infty) = g(z',-\infty)\exp\left[-i\frac{e}{\hbar\omega_p}\left\{\exp\left[-\frac{(z'+v_e\tau)^2}{4v_e^2\sigma_p^2}\right]\right\}\left\{\mathrm{Im}\left(\exp\left[i\frac{\omega_p}{v_e}z'\right]\tilde{F}_z\left(\frac{\omega_p}{v_e}\right)\right)\right\}\right] \tag{3.4}$$

where $z' = z - v_e t$ and σ_p is the standard deviation of the gaussian representing the temporal profile of the laser pulse. $g(z',-\infty)$ is the envelope function before the interaction. The term $\tilde{F}_z(\frac{\omega_p}{v_e})$ that appears in equation (3.4) is the Fourier transform of the z-component of the scattered electric field:

$$F_z(\frac{\omega_p}{v_e}) \equiv \int_{-\infty}^{+\infty} E_z(z'',0)\exp\left[-i\left(\frac{\omega_p}{v_e}\right)z''\right]\mathrm{d}z'' \tag{3.5}$$

where we set $z'' = z' + v_e t$. The component of the electric field along the electron trajectory governs the electron-photon coupling. F_z depends on different parameters reported in Figure 3.3, such as the impact parameter b and the angle ϕ with respect to the light polarization. Replacing equation (3.4) in (3.1), we obtain the electron wavefunction after the interaction:

$$\Psi(z, t\to\infty) = g(z',-\infty)\sum_{n=-\infty}^{+\infty}\xi_n(z')\exp[i(k_e + n\frac{\omega_p}{v_e})z - i(\omega_e + n\omega_p)t]. \tag{3.6}$$

The latter is a superposition of wavelets with energy and momentum respectively given by $E = \hbar(\omega_e + n\omega_p)$ and $p = \hbar(k_e + n\frac{\omega_p}{v_e})$. Their amplitude coefficients are given by

$$\xi_n(z') \equiv \left(\frac{\tilde{F}_z}{|\tilde{F}_z|}\right)^n J_n\left(-\frac{e}{\hbar\omega_p}|\tilde{F}_z|\exp\left[-\frac{(z'+v_e\tau)^2}{4v_e^2\sigma_p^2}\right]\right). \tag{3.7}$$

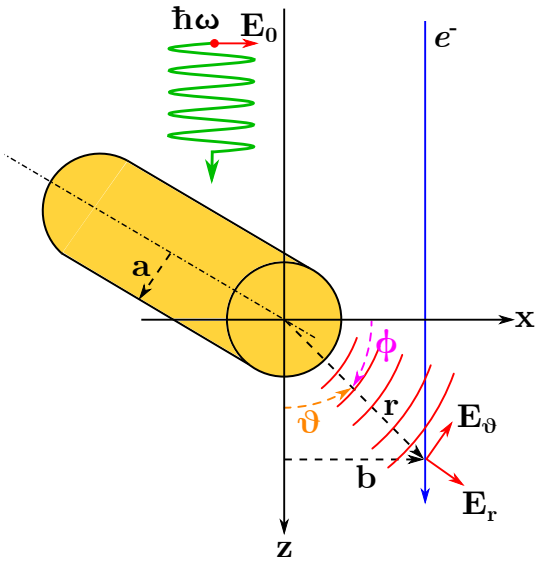

Figure 3.3: Electron-photon coupling in the vicinity of a nanocylinder. A propagating electron, the incident radiation, the scattered field and the nanocylinder section (radius a) are represented. b is the impact parameter of the electron. The electron and incident laser beam propagate both along the $\hat{z}$ direction. The incident light field is polarized along the $\hat{x}$ direction. The $\hat{y}$ direction is the cylinder symmetry axis.

J_n are Bessel functions of the first kind of order n. Each wavelet in equation 3.6 represents a quantum state in which electrons have absorbed or emitted n photons. Finally, the occupation probability of this n^{th} state can be obtained by integrating over the entire electron pulse envelope:

$$\begin{aligned} P(n) = |<n|\Psi>|^2 = \int_{-\infty}^{+\infty} dz' |\Psi_n(z', +\infty)|^2 = \\ = \int_{-\infty}^{+\infty} dz' \left| g(z', -\infty) J_n\left(-\frac{e}{\hbar\omega_p} |\tilde{F}_z| \exp\left[-\frac{(z' + v_e\tau)^2}{4v_e^2\sigma_p^2} \right] \right) \right|^2 . \end{aligned} \tag{3.8}$$

As $|J_n(x)|^2 = |J_{-n}(x)|^2$, the probabilities of emission and absorption of n photons are the same.

For low intensity of the incident radiation, *i.e.* $\frac{e\tilde{F}_z}{\hbar\omega} \ll 1$, Bessel functions can be

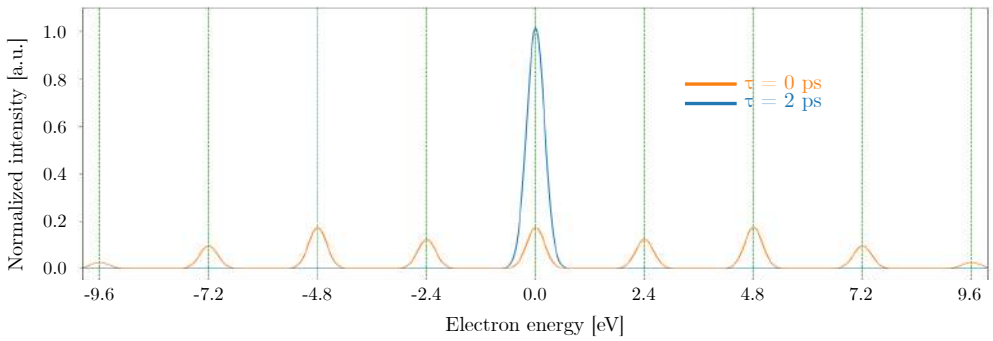

Figure 3.4: Electron energy spectra at different time delays. (a) At time $\tau = 2\,\text{ps}$, electrons do not interact with photons and the energy spectrum, in absence of any other interaction, is a ZLP. (b) When pump and probe are temporally overlapped, electrons interact with the evanescent field around the nanostructure and the entire population is distributed in sidebands that are all spectrally separated by the energy of incident photons (2.4 eV in this case). Sideband positions are marked with blue dashed vertical lines. The spectra have been simulated for a tungsten nanocylinder ($a = 50\,\text{nm}$) using equation (3.11). The electron beam passes 10 nm away from the cylinder surface and has an energy spread $\Delta E = 0.4\,\text{eV}$. The laser intensity has been set to $7.5 \cdot 10^8\,\text{W/cm}^2$. Electron and laser pulse durations are 350 fs and 280 fs, respectively.

approximated as $(J_n \approx (1/n!)(eF_z/2\hbar\omega)^2)$. The probability is then directly related to the intensity of the incident radiation:

$$P(n) \propto I^n \propto \exp\left[-\frac{n(z' + v_e\tau)^2}{2v_e^2\sigma_p^2}\right]. \tag{3.9}$$

In the particular case $n = 1$, equation (3.9) is reduced to [164]:

$$P(n=1) = \left[J_1\left(-\frac{e}{\hbar\omega_p}|\tilde{F}_z|\right)\right]^2 \approx \left(\frac{1}{2}\frac{e}{\hbar\omega_p}|\tilde{F}_z|\right)^2. \tag{3.10}$$

In the case of high power optical excitation ($e\tilde{F}_z/\hbar\omega \gg n^2$), higher order interactions develop between the optical field and free electrons yielding a more complex dynamics characterized by multiple photon sidebands. By manipulating equation (3.4) it is

possible to obtain an analytical expression of the probability $P(n)$:

$$P(n) = \sum_{j=0}^{\infty}\sum_{k=0}^{\infty} C_j^n C_k^{n^*} (1 + S_{njk} R_\sigma^2)^{-1/2} \exp\left[- \frac{S_{njk} R_\tau^2}{2(1 + S_{njk} R_\sigma^2)} \right] \tag{3.11}$$

where

$$C_j^n = \frac{1}{(|n| + j)!(j)!} \left(\frac{e\tilde{F}_z}{2\hbar\omega_p} \right)^{n+j} \left(- \frac{e\tilde{F}_z^*}{2\hbar\omega_p} \right)^{j} \tag{3.12}$$

$$S_{njk} = n + j + k \tag{3.13}$$

$$R_\sigma = \frac{\sigma_e}{\sigma_p} \tag{3.14}$$

$$R_\tau = \frac{\tau}{\sigma_p} \tag{3.15}$$

Figure 3.4 shows a typical EEGS spectrum (orange curve) and a Zero Loss Peak (ZLP) (blue curve) computed in the vicinity of an infinite tungsten cylinder. The electric field has been computed with the Mie theory. From the comparison between the two, we can notice that in EEGS the ZLP is depleted and *sidebands* appear. The latter are populated by electrons that absorbed or emitted photons during the interaction with the evanescent electric field. The energy spacing between the peaks is equal to the incident photon energy $\hbar\omega$ (2.4 eV in our case).

EEGS is a powerful technique allowing to obtain informations on the local electric field in proximity of a nano-sized system illuminated by a laser pulse. However, other parameters such as the electron pulse duration and the electron spot size modify the spectrum.

3.1.3 Influence of experimental parameters on EEGS

The following simulations have been performed by exploiting equations (3.11) to (3.15). A tungsten nanocylinder ($a = 200$ nm) has been considered. The electron energy spread

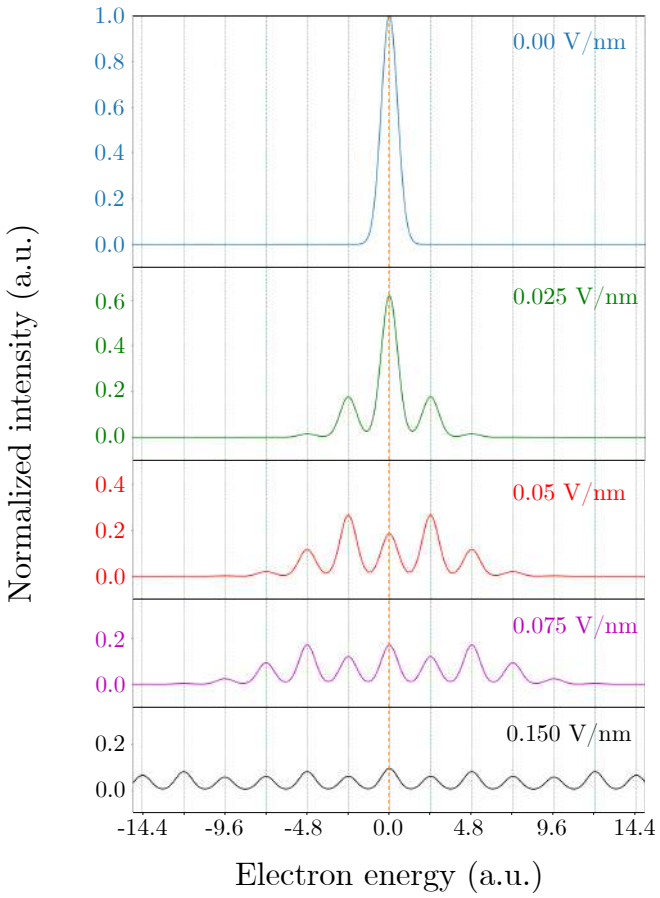

Figure 3.5: EEGS for different incident laser electric field strength. The electron pulse duration has been set to 350 fs and the spot size is 1 nm.

has been set to 1.1 eV. The laser pulse duration is 280 fs. We investigated the influence of the laser electric field strength, the electron pulse duration and the electron spot size. The incident laser intensity determines the magnitude of the evanescent field created around the nanostructure that couples with free propagating electrons. Figure 3.5 shows how EEGS is modified depending on the incident laser electric field strength. If the nanostructure is not illuminated, electron-photon interaction does not occur. Electrons neither lose nor gain energy and their energy distribution, in absence of any sample,

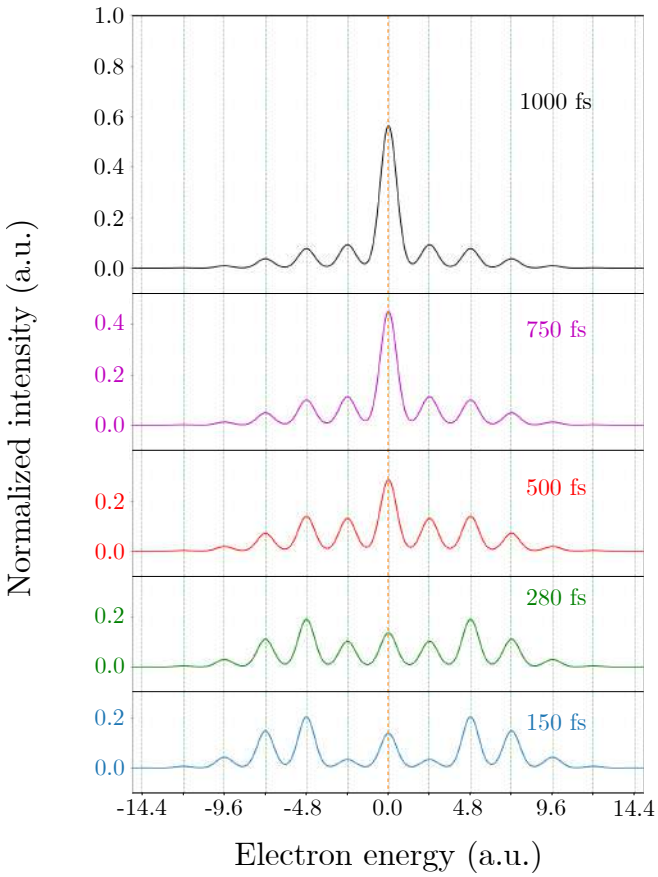

Figure 3.6: EEGS for different electron pulse durations. The incident electric field has been set to 0.075 V/nm and the spot size is 1 nm.

is a ZLP (blue curve). With moderate laser intensity ($I_L = 8.3 \cdot 10^6\,\mathrm{W/cm^2}$, $E_0 = 0.025\,\mathrm{V/nm}$), the scattered electric field has a non-zero component along the electron motion direction and the coupling becomes possible. By increasing the incident laser intensity, the scattered photon population increases and multiple photon absorption (or emission) is more probable as confirmed by equations (3.11). In this case, higher energy sidebands are occupied.

Figure 3.6 shows how the electron pulse duration σ_e affects electron energy gains. The

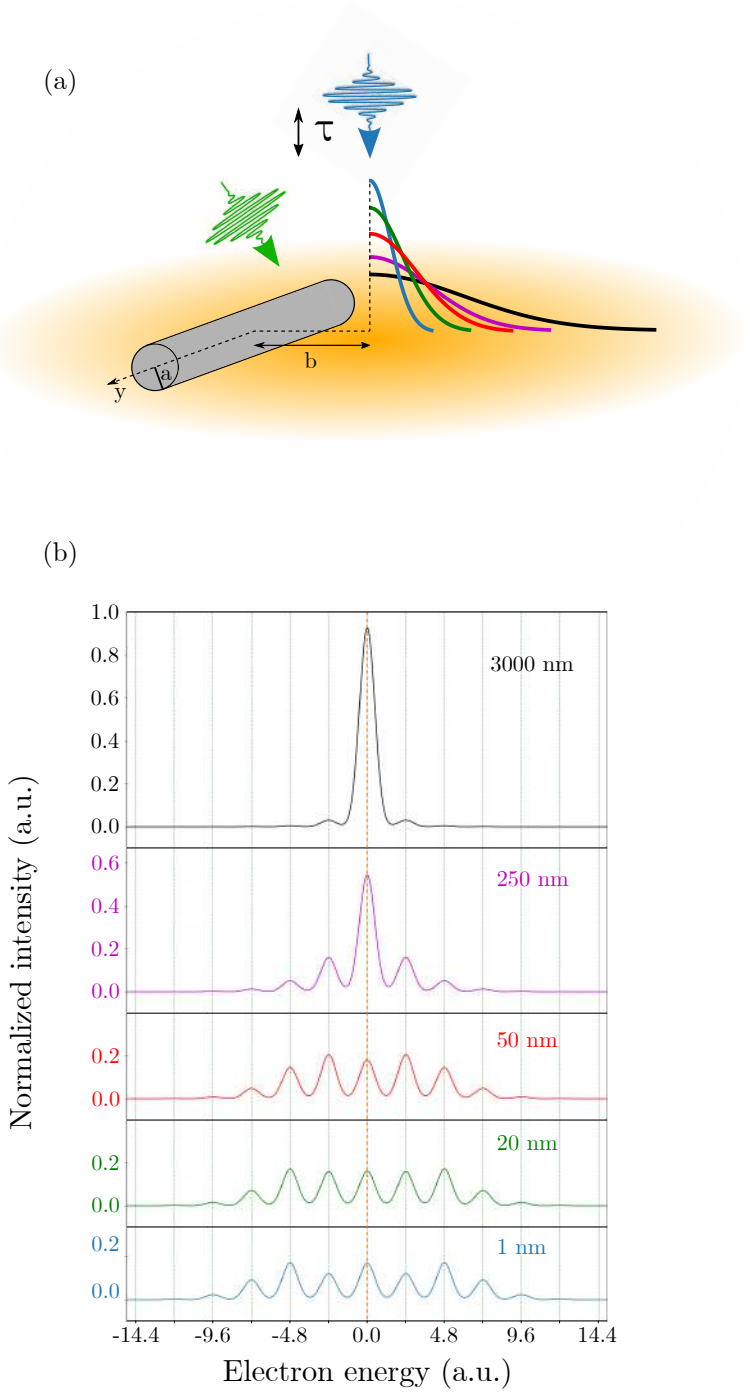

Figure 3.7: (a) Schematic representation of the simulation. The laser and electron pulses are drawn in green and blue, respectively. The evanescent electric field is sketched in orange. The half-normal distributions represent the electrons that interact with the scattered photons. (b) EEGS for different electron spot sizes. The incident electric field has been set to 0.075 V/nm and the electron pulse duration to 280 fs. In label the FWHM of the gaussian spatial distribution of the electron pulse.

modifications of the spectra are related to the fraction of electrons that interacts with the 280 fs laser pulse. This fraction becomes smaller and smaller as σ_e increases.
Figure 3.7 (b) shows how critical is the spot size. 5 different spot sizes (1 nm, 20 nm, 50 nm, 250 nm, 3000 nm) have been taken into account. These dimensions refer to the FWHM of a gaussian spatial intensity profile. In order to investigate the influence of the spot size keeping the same laser electric field intensity, we supposed that the electron gaussian spatial profile has its average value at 5 nm from the cylinder surface, as sketched in Figure 3.7 (a). Using a small electron probe size (1 nm), it is possible to obtain a fingerprint of the electric field at a certain position. This allows to map the evanescent field around the nanostructure. The increase of the electron spot size causes a loss of information. Since the electric field spatial extension is limited by the nanostructure geometry, a large electron spot collects several contributions from regions where the electric field is zero. This explains the very low EEGS signal for a 3 μm electron spot.

3.2 Temporal characterization of ultrashort electron pulses

In addition to the detection of the electric field and the investigation of the optical excitations in nanostructures, EEGS allows the temporal characterization of an electron packet [157, 164, 137]. After emission, an electron pulse develops a *chirp*, *i.e.* an energy-time correlation, because electrons with higher energies lead, while those with lower energies lag. This effect is enhanced in pulses containing a high number of electrons due to the coulombic repulsion among particles.
To control the electron chirp allows to change and improve the spatio-temporal and

spectral resolution of the instrument [164]. During the propagation, an electron pulse expands both in longitudinal and transverse directions. While the latter can be partially compensated by the focusing effect of electromagnetic lenses, longitudinal broadening is harder to control and several solutions have been proposed. For instance, the use of a so called *reflectron*, *i.e.* an electrostatic mirror, or radiofrequency (RF) electric fields [165] can be used to reverse the chirp and hence reduce the electron pulse duration [166]. The latter, in fact, alternatively produces a deceleration of leading electrons inside the pulse and an acceleration of the trailing ones but the design and realization of such cavities, as well as the synchronization between the electron pulses and the RF electric field are quite challenging.

EEGS allows to determine the electron pulse chirp as the stroboscopic pump-probe approach allows to temporally select electrons and obtain informations on their energy distribution. Reconstructing a map of electron spectra at different time delays, it is possible to visualize the chirp as the slope of the time-energy maps. The theoretical description of EEGS previously presented does not take into account the chirp of the electron pulse. To this purpose, we have to consider the temporal overlap between the pump optical pulse and the electron probe, as described in ref. [164]. We define $\bar{t}_\epsilon$ and $\bar{t}_p$ as the time when the electron and the laser pulse arrive on the sample, respectively. At positive time delay, $\tau \equiv \bar{t}_\epsilon - \bar{t}_p > 0$, the laser pulse arrives first. Faster electrons with average energy E' interact with the optical pulse and part of this population will occupy sidebands with a certain probability (described by equations (3.8) and (3.11)). Reducing the delay, the temporal overlap between the laser and electron pulses increases and the average energy of interacting electrons is $E < E'$. For negative time delays the electron pulse arrives on the specimen plane before the laser pulse and only slower electrons ($E'' < E$) interact with the scattered photons. This is schematically described

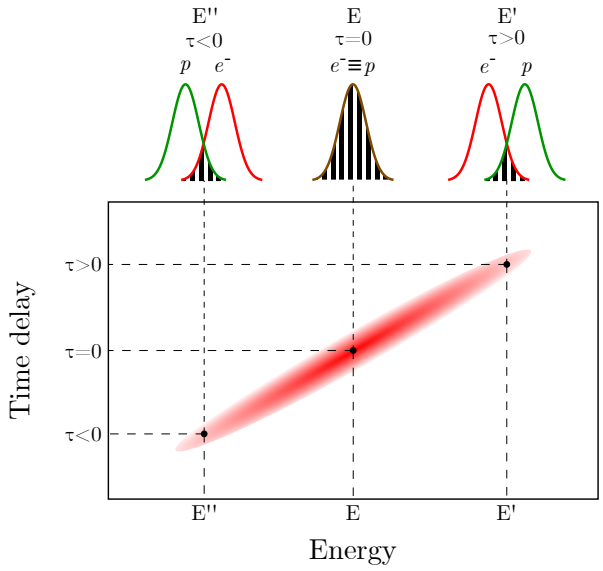

Figure 3.8: Schematic representation of the electron chirp. Green, red and brown curves represent the time distribution of photons (p), electrons (e^-) and the perfect overlap between the two. For the sake of simplicity, pulses have been considered having the same duration. Black and white vertical stripes represent the photon and electron population interacting during the temporal overlap. E, E' and E'' are the average energy of the fraction of interacting electrons. Electrons with different energies contribute to the chirped electron signal.

in Figure 3.8.

3.2.1 Characterization of chirped electron pulses

In order to temporally characterize the electron pulse and evaluate its chirp, a TEM sample has been prepared by Focused Ion Beam (FIB) by cutting the extremity of a traditional TEM tungsten $< 310 >$-oriented nanotip and positioning it on a FIB lift-out grid, as shown in Figure 3.9. Once the specimen position has been optimized in FemtoTEM to properly visualize the nanotip, the laser beam has been aligned and focused on the tip apex with the help of the CCD installed on the CL-I optical bread-

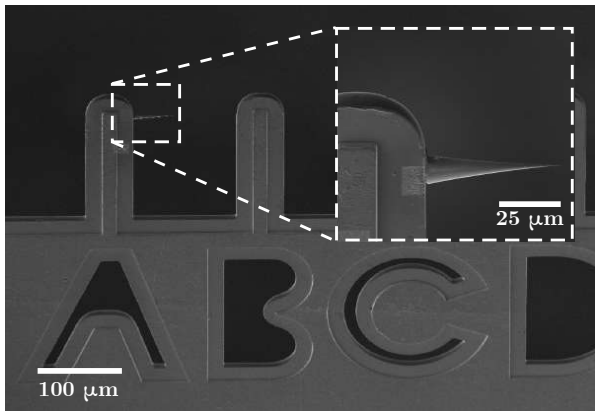

Figure 3.9: $< 310 >$-oriented tungsten nanotip mounted on a FIB lift-out grid.

board (Figure 2.7 (a) and (b)) that records the image of the specimen collected by the parabolic mirror inserted inside the polepiece gap. The pump wavelength is 515 nm and the pulse average power measured on the optical bench (Figure 2.8) was 595 mW. The repetition rate has been set to 2 MHz. FemtoTEM has been set in diffraction mode. The position of the electron beam with respect to the nanotip has been optimized by looking at the *shadow image* inside the transmitted spot.

A sequential acquisition of 52 EEG spectra with a step of 50 fs has been interspersed with the same number of ZLP acquisitions to correct *a posteriori* a drift in the spectrometer. Each spectrum has been acquired for $t = 10$ s. The prism entrance aperture was 1 mm and the energy dispersion 0.05 eV/channel. Figure 3.10 reports on electron absolute (left column) and difference (central column) spectra as a function of the time delay for different numbers of electrons per pulse. Difference spectra have been obtained by subtracting from the EEGS signal a spectrum acquired at a large time delay (*i.e.* a ZLP). The wavy profile is due to instabilities of the spectrometer that have been only partially corrected. In the absolute spectra is clearly visible the variation of the electron population as a function of the time delay: when the electron and laser pulses

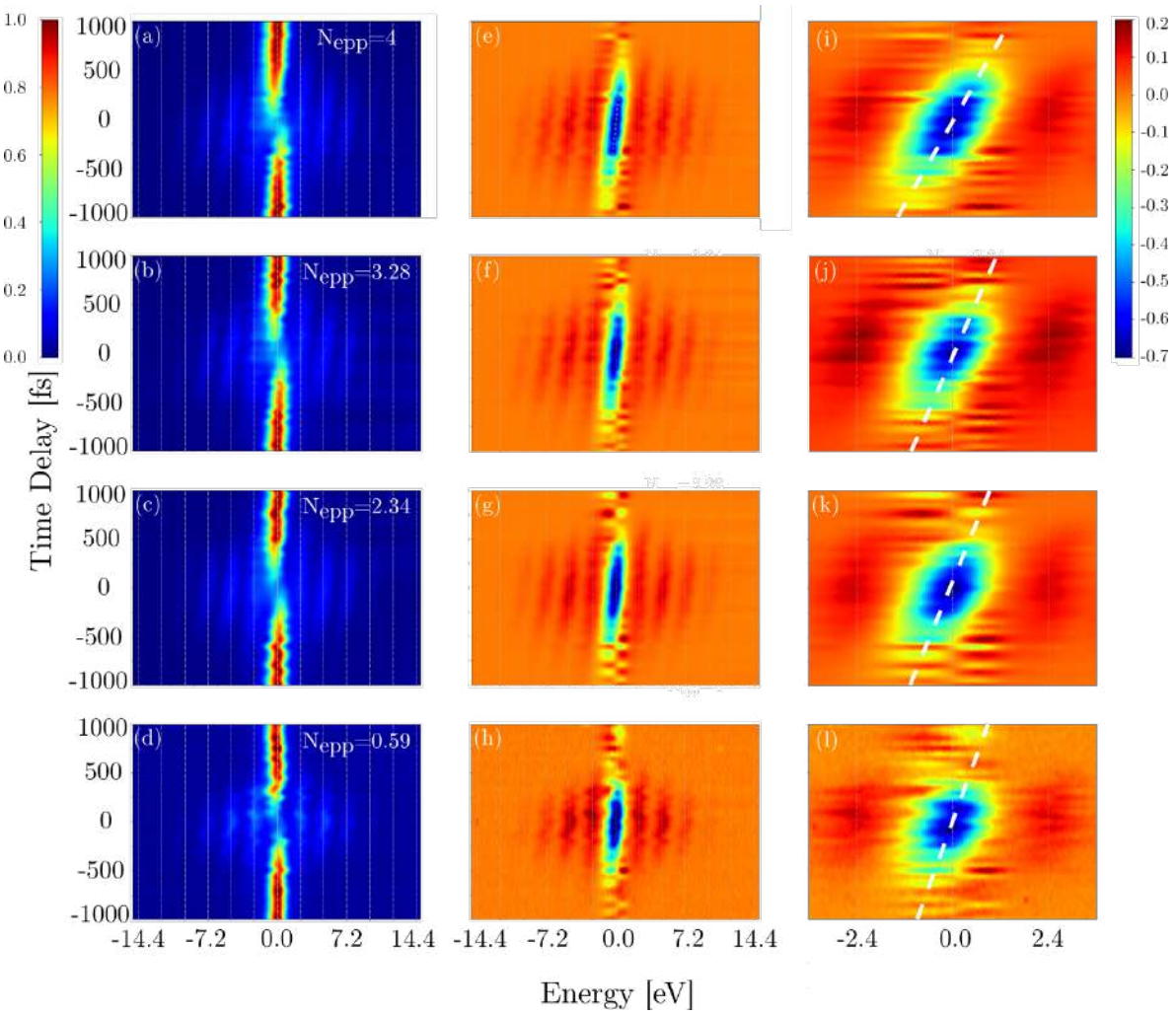

Figure 3.10: Energy gain absolute (left) and difference (center) spectra maps acquired for different numbers of electrons per pulse. (a) and (e): 4 epp. (b) and (f): 3.28 epp. (c) and (g): 2.34 epp. (d) and (h): 0.59 epp. Each map is composed of 52 EEGS spectra acquired every 50 fs. Spectra drift has been corrected during the map reconstruction. Right column: evaluation of the electron chirp in four different gain difference maps. Dashed lines represent linear fit on experimental results.

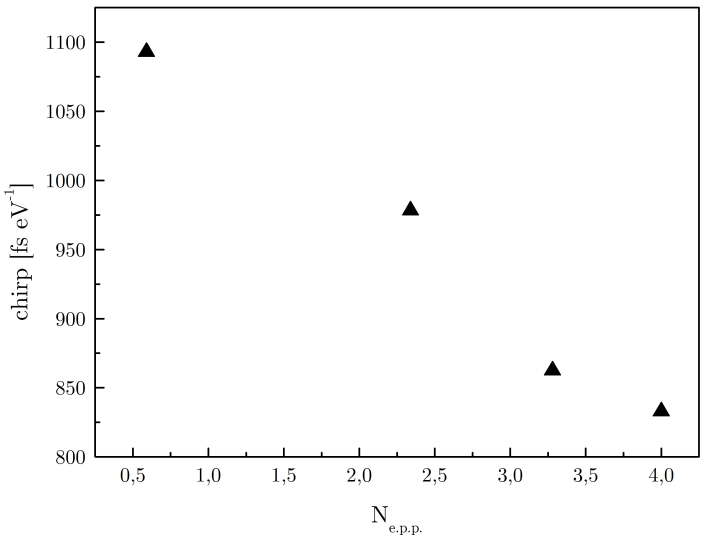

Figure 3.11: Electron chirp plotted as a function of the number of electrons per pulse.

are synchronized, the Zero Loss Peak (ZLP) depletes and the electrons populate the sidebands. This explains the large negative intensity in the difference spectra.

The electron chirp coefficient, $\partial \bar{t}_E / \partial E$, is visible in both cases and highlighted in Figure 3.10 (right column) by white dashed lines. It has been evaluated by a home-made software, taking into account the coordinates $(E', \bar{\tau}_\epsilon)$ of the signal minima in the difference spectra for each acquired spectrum. As Figure 3.11 reports, the chirp decreases by increasing the number of electrons per pulse due to the coulombic repulsion. Once the electron chirp has been evaluated, it is possible to use the theoretical formalism of *Park et al.* [153] to simulate the experimental maps shown in Figure 3.10 and to characterize the electron pulse. In the next paragraph, the results of these simulations are presented.

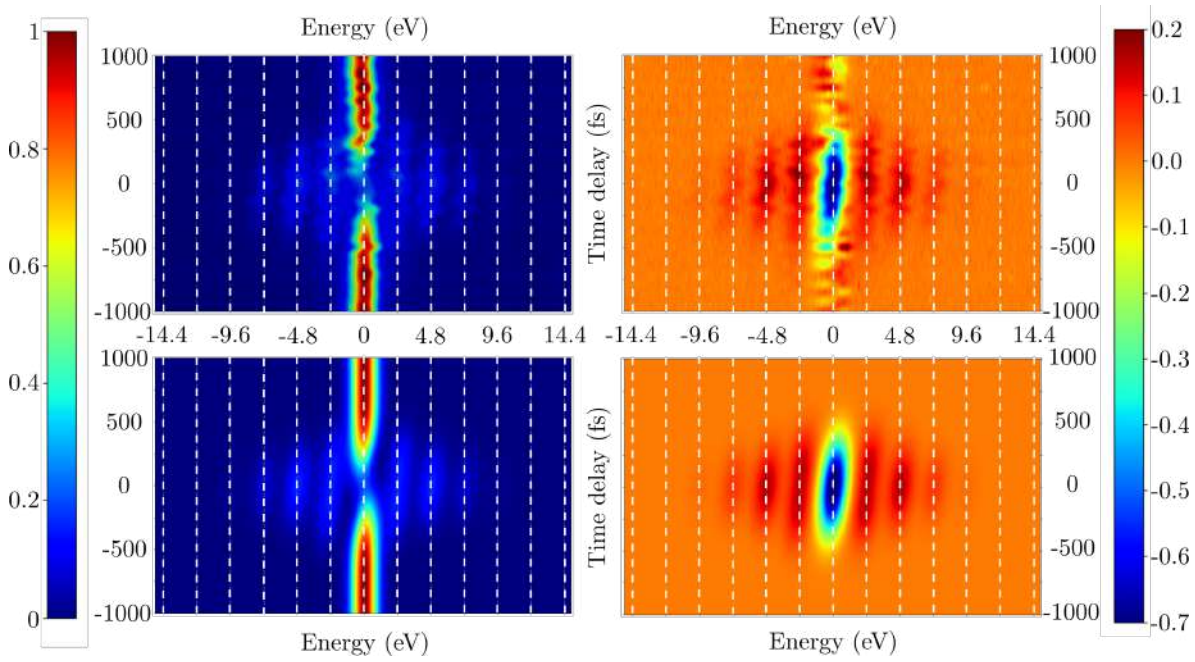

Figure 3.12: Comparison between experimental (top row) and simulated (bottom row) EEGS maps. The intensity scale on the left (right) sides refer to the EEGS absolute (difference) maps. The case with $N_{epp} = 0.59$ has been reported.

3.2.2 Gain spectra simulations and evaluation of the electron pulse duration

EEG spectra have been simulated for $N_{epp} = 0.59$, 2.34, 3.28 and 4 taking also into account the electron chirp values. The tungsten nanotip used in the experiment has been approximated by a nanocylinder with a radius $a = 200\,\text{nm}$. We assumed that a laser pulse of 280 fs in FWHM passes 15 nm away from the cylinder surface. The incident laser electric field is $E_0 = 0.075\,\text{V/nm}$, corresponding to an intensity of approximately $7.5 \cdot 10^8\,\text{W/cm}^2$. The electric field in the vicinity of the cylinder is computed from Mie theory. Figure 4.28 reports on the comparison between the experimental and simulated EEGS maps in the case $N_{epp} = 0.59$. In order to evaluate on the simulation accuracy,

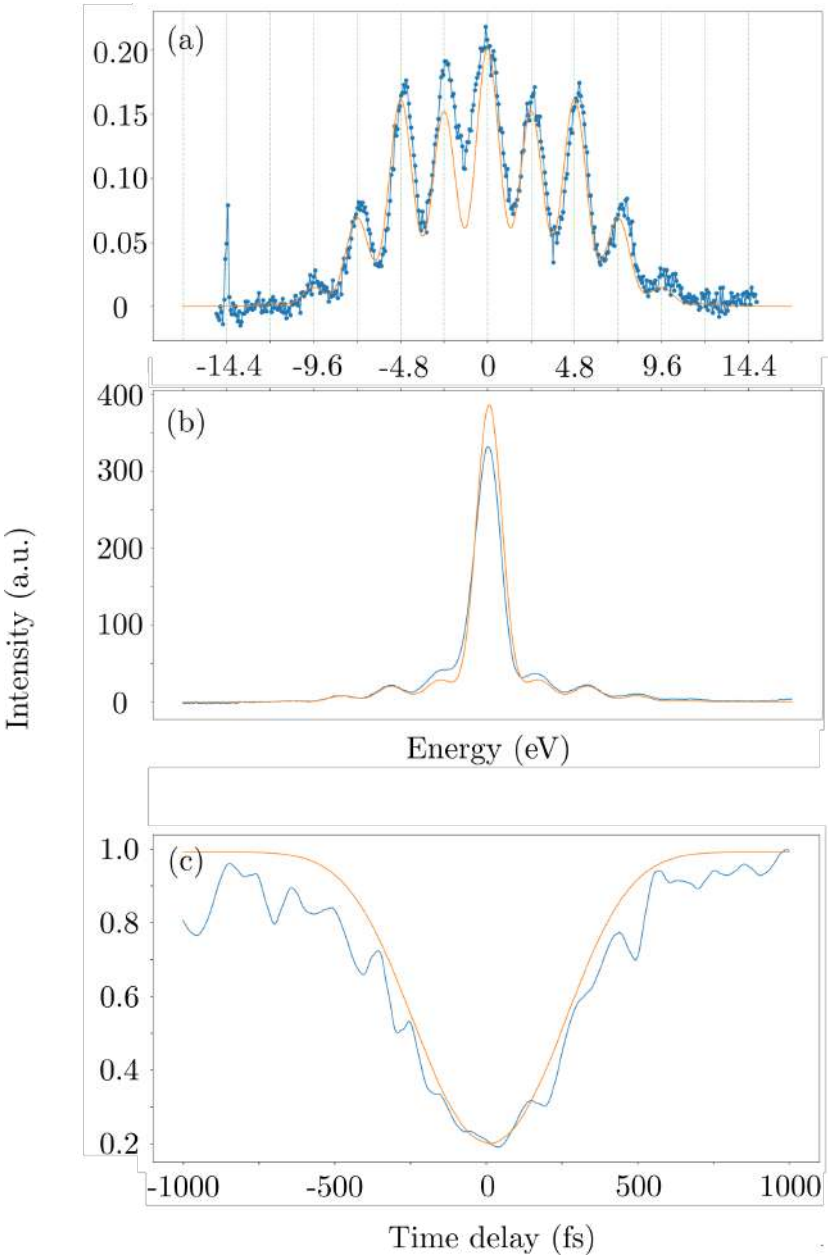

Figure 3.13: Comparison between experimental (blue) and simulated (orange) data. (a) EEG spectrum at $\tau = 0\,\text{fs}$. (b) EEGS map integrated on the time axis. The vertical scale indicates the integral values for the different energies in arbitrary units. (c) Map profile at $E = 0\,\text{eV}$. In both (a) and (c) the vertical scales represent the normalized EEGS signal in arbitrary units.

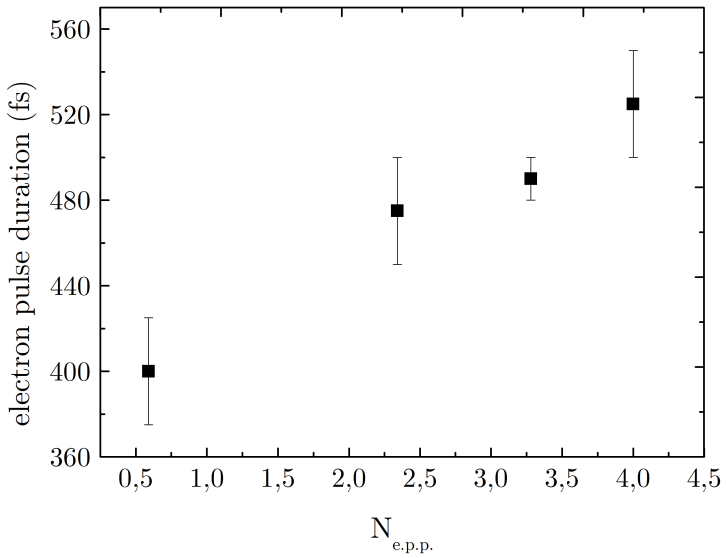

Figure 3.14: Electron pulse duration as a function of the number of electrons per pulse.

different sections of the map as well as the integrated signal have been extracted and the results are shown in Figure 3.13. Blue curves represent the experimental results and orange curves the simulated ones. In particular, in Figure 3.13 (a) we have the *time-slice* of the map at a delay $\tau = 0\,\text{fs}$. The experimental signal is noisy due to the low probe current and the short acquisition times (10 s). We can notice that despite the difference in shape between the sample and the simulated nanocylinder, the two curves are in good agreement. To further confirm the precision of the model, two *energy-slices* at $E = 0\,\text{eV}$ have been extracted from the experimental and simulated absolute maps and then superposed (Figure 3.13 (c)). Figure 3.13 (b) represents the overall signal integrated on the time axis. The difference in the ZLP intensity can be explained by the variation of intensity in the measured signal, as can be noticed from the experimental EEGS map.

By recurring to the simulations and using the elements in Figure 3.13 as a feedback, we evaluate the electron pulse duration (Figure 3.14). We can see that for the case $N_{epp} = 0.59$ the duration in FWHM is 400 fs with a precision of 6%. Slightly increasing the number of electrons per pulse, we determined an increase of approximately 31% of the duration in the case of 4 electrons per pulse.

3.3 Conclusions

In this chapter the first pump-probe experiment performed in FemtoTEM has been reported. At the beginning, the theoretical approach of Park *et al.* [153] has been presented. Following the theory, EEG spectra have been simulated to show the effect of the experimental parameters (electric field, electron pulse duration, electron spot size). Finally the experimental results have been presented. EEGS maps recorded with different numbers of electrons per pulse have been shown and the electron chirp evaluated. Through the simulated maps it has been possible to calculate the electron pulse duration. The importance of EEGS lies beyond the mere characterization of the electron pulse duration. Thanks to the possibility to its direct link with the electric field, the detection of energy gains allow to map the optical near field of nano-objects [157]. Besides, thanks to the possibility to temporally select the electrons it is possible to obtain short and high coherent electron pulses [164]. This is the principle of the so-called *photon gating* technique [167, 168].

Chapter 4

Towards Ultrafast Electron Holography using FemtoTEM

In this last chapter, perspectives towards Ultrafast Electron Holography (UEH) using off-axis configuration will be discussed. In the beginning, practical aspects of experimental off-axis electron holography (*i.e.* electron sources coherence, noise, instabilities, illumination) performed with a continuous electron beam will be given. Subsequently, obstacles in performing electron holography using ultrashort electron pulses will be presented and possible solutions will be discussed. Finally, we will show the results of the first experiments performed using the FemtoTEM microscope.

4.1 Practical requirements and detection limits in conventional off-axis electron holography

In paragraph 1.2.3 the principles of electron holography and the theoretical description of electron beam phase extraction have been presented. Here, we want to describe the

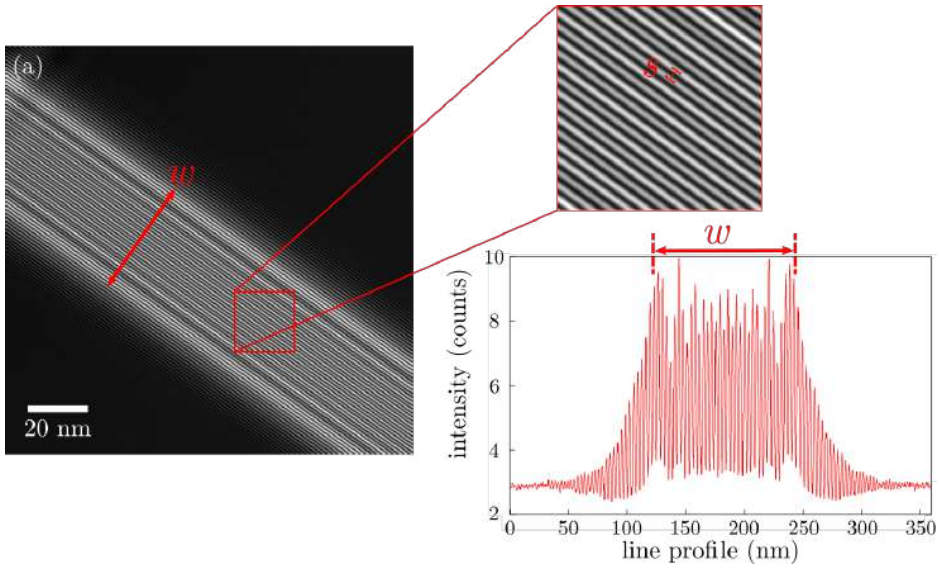

Figure 4.1: (a) A reference hologram acquired in the vacuum. The hologram width and the interfringes distance are highlighted. (b) Line profile evidencing the extension of the electron hologram. The number of counts is reduced of a factor 10^3.

key technical requirements to acquire electron holograms with optimum contrast.

In order to produce an interference pattern, a high coherence electron source is necessary. As already discussed in Chapter 1, FEGs, with their high brightness, are the optimum sources. Indeed, thanks to their small source size, they can emit a high spatial coherence electron beam, as described by the *van Cittert-Zernike* theorem (equation (1.20)). This allows to generate a coherent electron beam over a large area, extended over hundreds of ångström [169]. This high quality beam can then be used to illuminate both the specimen and a vacuum area, known as the image and the reference beam respectively. The hologram, generated by the coherent superposition of the two beams, is then obtained thanks to an electron biprism (EB).

Figure 4.1 shows an hologram acquired without specimen on which useful parameters are reported. The hologram width w is the size of the interference zone and s the

interference fringe spacing. Both can be set by adjusting the biprism voltage and the distance between the image and the biprism planes, called d in Figure 1.14. For a fixed distance d by increasing the biprism voltage, the hologram width increases while the interfringe distance decreases [94]. However, they can be also varied independently by using a double-biprism configuration [170]. As reported in Chapter 1, the figure of merit of a hologram is the *fringe contrast*:

$$C = \frac{I_{max} - I_{min}}{I_{max} + I_{min}} \tag{4.1}$$

where I_{max} and I_{min} correspond to maximum and the minimum of fringe intensities, respectively. Useful values of contrast, *i.e.* allowing to extract a phase with enough signal over noise ratio and good spatial resolution, are commonly accepted to be higher than 15% [171]. Electron holograms are recorded using pixelated cameras and their Modulation Transfer Function (MTF), as well as their Detective Quantum Efficiency (DQE) will also need to be taken into account in the contrast measurement. In addition, the number of electrons per pixel N_{epx} and the exposure time are fundamental to optimize the hologram contrast. The evaluation of N_{epx} is possible by considering the number of counts per pixel from a hologram micrograph. This number is then converted in current after a proper calibration of the detector performed by measuring the current using a Faraday's cup.

4.1.1 Hologram figures of merit

Electron holography is used to quantitatively map the image beam phase modified by the interaction with the specimen. In order to optimise the phase resolution, we first need to describe the dependence of the reconstructed phase standard deviation upon the key parameters reported in the previous paragraph. The electron beam noise can be

described by a Poisson distribution, known as *shot noise* [172]. Using such a description, *de Ruijter and Weiss* reported that the standard deviation of a reconstructed phase can be written [173]:

$$\sigma_\phi = \sqrt{\frac{2c}{C^2\, N_{epx}}} \tag{4.2}$$

in which the constant $c = 1$ when part of the incoming electron beam propagates in vacuum. This assumption reflects our experimental conditions. C is the contrast of the hologram and N_{epx} the number of electrons per pixel. Furthermore, the latter is strongly influenced by the quantum efficiency, defined by $DQE = SNR_{out}(\mathbf{g})/SNR_{in}(\mathbf{g})$, where $SNR_{out}(\mathbf{g})$ and $SNR_{in}(\mathbf{g})$ are signal-to-noise ratios at input and output of the detection system at a spatial frequency $\mathbf{g}$. Hence, for a given $\mathbf{g}$, equation (4.2) can be rewritten as [173, 172]:

$$\sigma_\phi = \sqrt{\frac{2}{DQE \cdot C^2 \cdot N_{epx}}}. \tag{4.3}$$

Using equation (4.3), it appears that the reconstructed phase standard deviation can be optimised by increasing the number of electrons per pixel if the hologram contrast remains unaffected. This will correspond to an improvement of the coherent current as defined in (1.23). An easy way to increase the number of electrons per pixel will be to increase the exposure time but, in this way, the hologram contrast will be more affected by all the experimental set-up instabilities. Another useful figure of merit of the hologram quality encountered in literature is the *phase detection limit*, *i.e.* the smallest detectable phase difference, which for a given spatial frequency $\mathbf{g}$ is defined as [174]:

$$\delta\phi = SNR\sqrt{\frac{2}{DQE \cdot C^2 \cdot N_{epx}}} \tag{4.4}$$

where the desired signal-to-noise ratio SNR is a given parameter. To properly determine the result of an experiment without ambiguity, it is generally admitted that a

SNR between 3 and 10 is necessary [112]. Since the fringe contrast contributes to $\delta\phi$ with an exponent 2 inside the square root, it has a key role in the phase detection limit compared to the other parameters.

Lehmann *et al.* proposed to introduce the effect of external perturbations through their influence on the hologram contrast. Indeed, in addition to the experimental set-up instabilities already introduced, the hologram contrast will be also affected by the partial coherence of the electron source, by inelastic interactions of the electron beam inside the specimen and by the Modulation Transfer Function (MTF) of the detector for a given interfringe distance s. A useful expression of the contrast used to take into account all these contributions is:

$$C = C_{coh}C_{inel}C_{inst}MTF \tag{4.5}$$

where C_{inst}, C_{inel} and C_{coh} correspond the influence of instabilities, inelastic scattering and partial coherence, respectively.

4.1.2 Optimization

Among the factors on which the contrast (and hence the phase detection limit) depends, the partial coherence is one that needs to be treated with special care during an electron holography experiment. The coherence length of an electron beam on a given optical plane depends on the original degree of spatial coherence of the source, *i.e.* the brightness and also on the illumination conditions. Indeed, using a small condenser aperture it is possible to increase the spatial coherence length due to the decrease of the source size at the cost of a loss of the total current (equation (1.23)). Then, longer acquisitions will be necessary and the influence of instabilities will become severe.

Considering the electron biprism symmetry, the coherence length needs to be optimised only in the beam overlap direction, *i.e.* perpendicularly to the biprism axis. As a con-

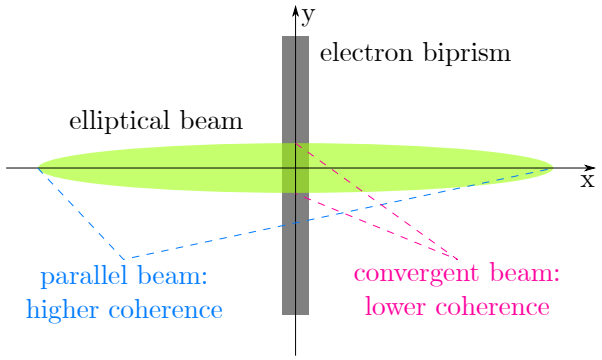

Figure 4.2: Representation of the elliptical illumination in reference to the electrostatic biprism.

sequence, it is well known that an elliptical beam can be used to optimise the coherence length in the desired direction, minimising the exposure time. Practically, using the condenser lens stigmators, it is possible to produce two different focii for the $\hat{x}$ and $\hat{y}$ direction of the beam. Spreading the electron beam as in Figure 4.2, an almost parallel beam along the ellipse major axis and a convergent beam on $\hat{y}$ are achieved. Then, the coherence length will be maximised along the $\hat{x}$ direction. An optimum ratio between the minor and the major axis is around 0.1 [96].

The illumination condition is not the only parameter we can adjust to optimise the hologram contrast. In fact, the influence of the detector MTF depends on the detector type and its usual settings, such as binning and also on the number of pixels per hologram fringes, related to the magnification of the hologram plane onto the camera. Regarding instrumental instabilities, various approaches have been proposed to overcome their tremendous effects. Chang *et al.*, for instance, proposed a model that can be used to determine the optimum exposure time for given hologram characteristics (fringe spacing, interference width and pixel size) to minimize the instability contribution on the hologram contrast [175]. Other approaches are based on the acquisition of image stacks, in which each hologram is acquired with a short exposure time. Then,

a post-processing numerical realignment of the fringes allows to reconstruct a high signal-to-noise ratio interference pattern [176]. However, image stacks can be highly demanding in terms of memory space and, for this reason, an innovative solution has been proposed. It is based on an advanced real-time drift measurement and correction of the hologram fringes movement using beam (or gun) tilt deflectors [177]. The use of such an advanced feedback loop between the acquisition and the microscope electronics allows to suppress the instability contributions and acquire electron holograms with an almost unlimited exposure time.

4.2 Electron holography using ultrashort electron pulses

4.2.1 Low-dose-like conditions

As already stated in paragraph 2.2.5, there is a difference of approximately six orders of magnitude in the emission current between DC and laser-driven mode, under the same electron optical conditions. Typical values lie in the microampere and picoampere range, respectively. In the latter the current is reduced due to the effect of the laser repetition rate, f (Figure 4.3). The small probe current in laser-driven mode influences the phase detection limit. The number of electrons per pixel in equation (4.4) can be determined by the relation:

$$N_{epx} = N_{ppx} \cdot f \cdot t_{exp} \tag{4.6}$$

where f is the laser repetition rate, t_{exp} the exposure time and $N_{ppx} = \frac{N_{epp}}{N_{px}}$ the number of electrons per pulse per pixel. N_{epp} indicates the number of electrons per pulse and N_{px} the total number of pixel in the measurement area. Substituting equation (4.6) in

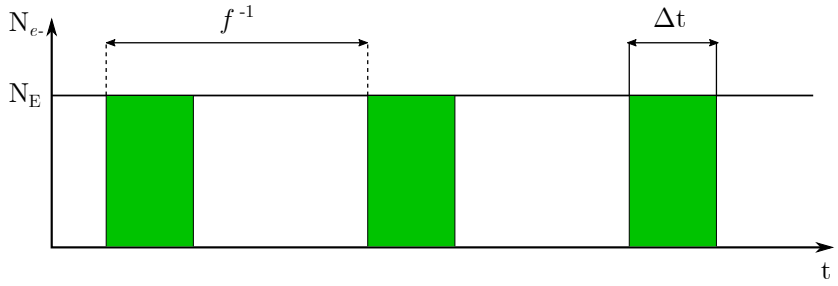

Figure 4.3: Qualitative explanation of current reduction. In DC emission, an average number of electrons, N_E is stochastically emitted by the cathode. In laser-driven mode, the electron emission happens only during the pulse duration, Δt. f^{-1} is the pulse period, f the laser repetition rate.

equation (4.4), we obtain the *phase detection limit* for a given spatial frequency **g**:

$$\delta\phi = \frac{SNR}{C_{coh}\, C_{inst}\, MTF} \sqrt{\frac{2 \cdot N_{px}}{DQE\, N_{epp}\, f\, t_{exp}}} \tag{4.7}$$

where the contrast C has been expressed as in equation (4.5), assuming the contribution of inelastic scatterings to be negligible. The number of electrons emitted per laser pulse is:

$$N_{epp} = \frac{I_P}{ef} \tag{4.8}$$

I_P being the probe current and e the elementary charge. By replacing equations (4.8) and (1.25) in (4.7), we explicit the relation between $\delta\phi$ and the average laser power, W_{LAS}:

$$\delta\phi \propto \frac{SNR}{C_{coh}\, C_{inst}\, MTF} \sqrt{\frac{2e \cdot N_{px}}{DQE\, W_{LAS}^{n}\, t_{exp}}} \tag{4.9}$$

where n is the number of photons involved in the emission process. In this case, we are assuming a simple n-photon photoemission process as described in paragraph 1.3.2.
As in DC mode, the spatial coherence, C_{coh}, is maximised with the highest brightness source and using an appropriate elliptical illumination while the MTF depends on the detector and the parameters set during the experiment (*i.e.* camera binning, hologram

magnification, spatial frequency, biprism voltage). In equations (4.7) and (4.9) there are new parameters related to the optical excitation. By changing the laser power, it is possible to adjust the number of electrons per pulse, N_{epp}. However, the latter is limited for two reasons: the cathode damage threshold and the probe current properties. The first reason is due to the FEG cathode material and its small apex, the second is shared between all the UTEMs. Indeed, we want to avoid a too large number of electrons per pulse in order not to deteriorate the microscope resolution (spatial, temporal, spectral). The laser repetition rate f in equation (4.7) cannot be freely changed to improve the phase detection limit because it is limited by the dynamics of the specimen to be investigated. Indeed, in stroboscopic mode, the system has to relax before another pulse arrives to trigger again the dynamics of the specimen [112]. The exposure time is another free parameter that can be easily adjusted. As in the case of holography performed with a continuous beam, an increase of t_{exp} can improve the phase detection limit by increasing the number of electrons per pixel but it will also increase the effect of instabilities. In this case, the phase detection limit will be reduced through the term C_{inst} in equations 4.7 and 4.9.

Optimisation of the experimental parameters

The choice of the optimum exposure time is important in electron holography and especially using low-dose-like conditions. Acquisition times in DC emission are typically of the order of the second or tens of seconds for experiment requiring a high S/N ratio. However, as can be seen from Figure 4.4 (a), this is not the case with an ultrafast electron probe. Using 10 s of exposure time, the contrast of the hologram performed with 18 V of biprism voltage is too weak to reconstruct a phase with enough signal over noise ratio (Figure 4.4 (b) and (c)). Larger exposure times increase the number of

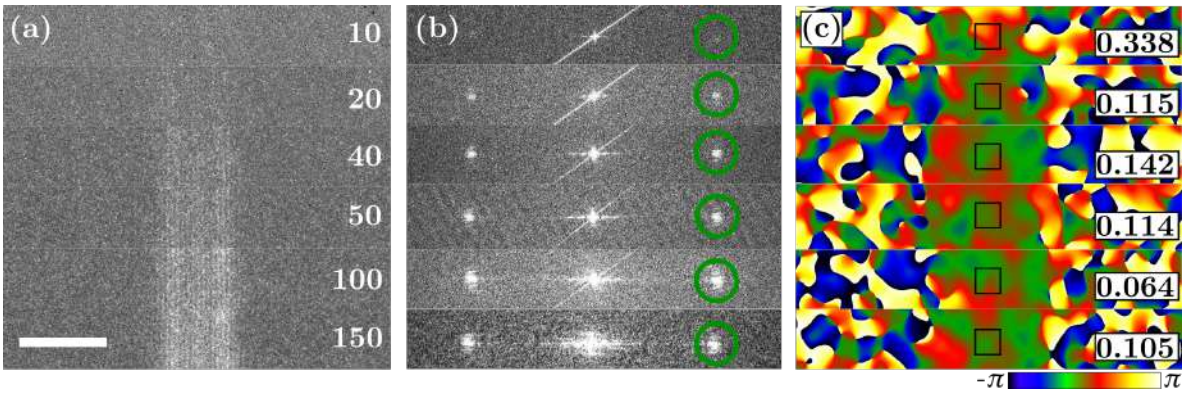

Figure 4.4: Influence of the exposure time on the hologram. (a) Electron holograms acquired in vacuum. Exposure times in seconds are displayed in white. Scale: 5 nm. (b) Power spectrum of the holograms. Green circles indicate the mask position in the Fourier space. The achieved spatial resolution is 2 nm. (c) Reconstructed phases. Standard deviations calculated inside the black square are displayed. Experimental conditions: biprism voltage 18.8 V, $W_{LAS} = 8$ mW, $f = 2$ MHz, $N_{epp} \sim 9$, binning 1, magnification 200 kX.

electrons per pixels and, as a consequence, the interference fringes contrast

as long as the instabilities do not affect

. As already stated, the standard deviation of the reconstructed phase will be improved while the instabilities will not affected the contrast during the exposure time. From the comparison of the reconstructed phases in Figure 4.4 (c) , we can notice that the case $t_{exp} = 100$ s reports the lowest standard deviation. For longer exposure times we expect smaller standard deviations due to the influence of instabilities. In a first approximation we can state that in our conditions, exposure times between 100 and 150 s are optimum.

The next step is the choice of the optimal biprism voltage. Usually it depends on the desired hologram overlap and spatial resolution of the reconstructed phase, related to the interfringes distance. However, in pulsed beam conditions, by increasing the

biprism voltage (and hence the spatial frequencies) the instabilities strongly degrade the contrast. As a consequence, using 150 s of exposure time, the range of voltages is limited. In Figure 4.5 several cases are reported. As we can see in Figure 4.5 (c), it is possible to extract the hologram phase with a good standard deviation for low biprism voltages (15 V - 20 V). However, in these cases the hologram field of view is too small to be useful in practice. On the other hand, for biprism voltages higher than 35 V the influence of instabilities on the fringe contrast is too severe using 150 s of acquisition time and the standard deviation of the reconstructed phase becomes too high. Experimentally, with 150 s of exposure time and 200 kX of total magnification, the possible useful biprism voltages for a future experiment have been found in the 20 V - 35 V range. Figure 4.6 shows an electron hologram acquired under optimum conditions *i.e.* 35 V, 150 s of exposure time and 200 kX of total magnification. The microscope has been set in ZOOM mode (equivalent to the microprobe or TEM mode in FEI and Jeol microscopes, respectively). A condenser aperture of 100 μm and an elliptic illumination with an optimum ratio have been used [96]. The probe current is 100 fA, acquired in virtual crossover mode ($V_1 = 4$ kV and $R = 5$). The electron dose at the specimen plane is $\sim 7e^-/\text{Å}^2$. The hologram exhibits 20% of fringe contrast measured by equation (4.5) and averaging the fringe intensity. The reported contrast has a low SNR: 30 counts of mean intensity over 14 counts of noise due to the low probe current. Assuming an ideal situation with a $SNR = 3$ and C_{inst}=1, the phase detection limits for two point separated by 1 nm is $\delta\phi = 3$ rad.

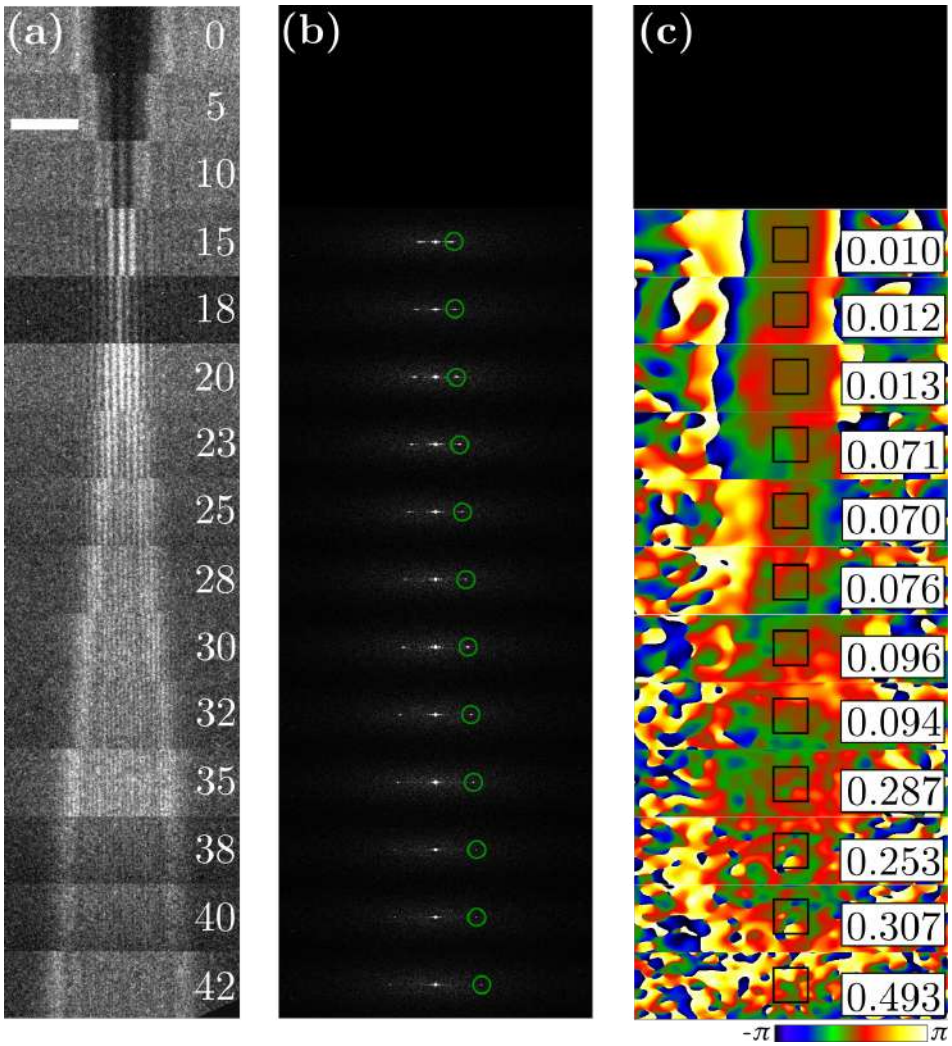

Figure 4.5: Influence of the biprism voltage on the hologram. (a) Electron holograms acquired in vacuum. Biprism voltages in volts are displayed for each case. Scale: 15 nm. (b) Power spectrum of the holograms. The green circles represent the 2 nm resolution mask in the Fourier space. (c) Reconstructed phases. Standard deviations calculated inside the black square are displayed. Experimental conditions: exposure time 150 s, $W_{LAS} = 7.5\,\mathrm{mW}$, $f = 2\,\mathrm{MHz}$, $N_{epp} \sim 12.5$, binning 1. Magnification: 200 kX

4.2.2 Electron holography with femtosecond electron pulses on MgO nanocubes

Once determined the optimum values of the exposure time and biprism voltage, we tested electron holography in laser-driven mode on a manganese oxide (MgO) cube,

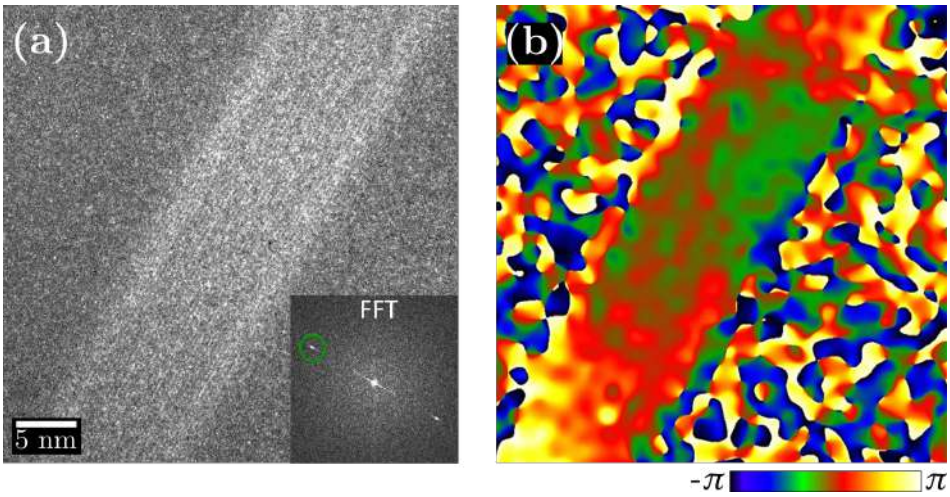

Figure 4.6: (a) Ultrafast off-axis electron hologram acquired in vacuum. Inset: FFT of the hologram. The green circles represents the 1 nm resolution mask in the Fourier space. (b) Reconstructed phase map. Experimental conditions: exposure time 150 s, $W_{LAS} = 9.5\,\mathrm{mW}$, $f = 2\,\mathrm{MHz}$, $N_{epp} \sim 11$, binning 4.

displayed in Figure 4.7 (a). Figure 4.7 (b) shows the classical steps used in the phase reconstruction. H_1 corresponds to the specimen hologram and H_0 is the reference hologram acquired without specimen. The purple square indicates the cube position relatively to the hologram region. The reconstructed phase of the specimen reported inside the green square has been obtained after substraction of the reference hologram. It clearly shows the influence of the MgO mean inner potential. Figure 4.7 (c) shows the effect of the mask size (*i.e.* the phase spatial resolution) on the reconstructed phase. Increasing the mask size in Fourier space improves the spatial resolution of the phase image R. However, the consequence is an increase of the phase standard deviation, as reported in Figure 4.7 (c).

Due to the low probe current of our coherent UTEM and despite the high brightness, off-axis electron holography remains very challenging. The main reason is the high

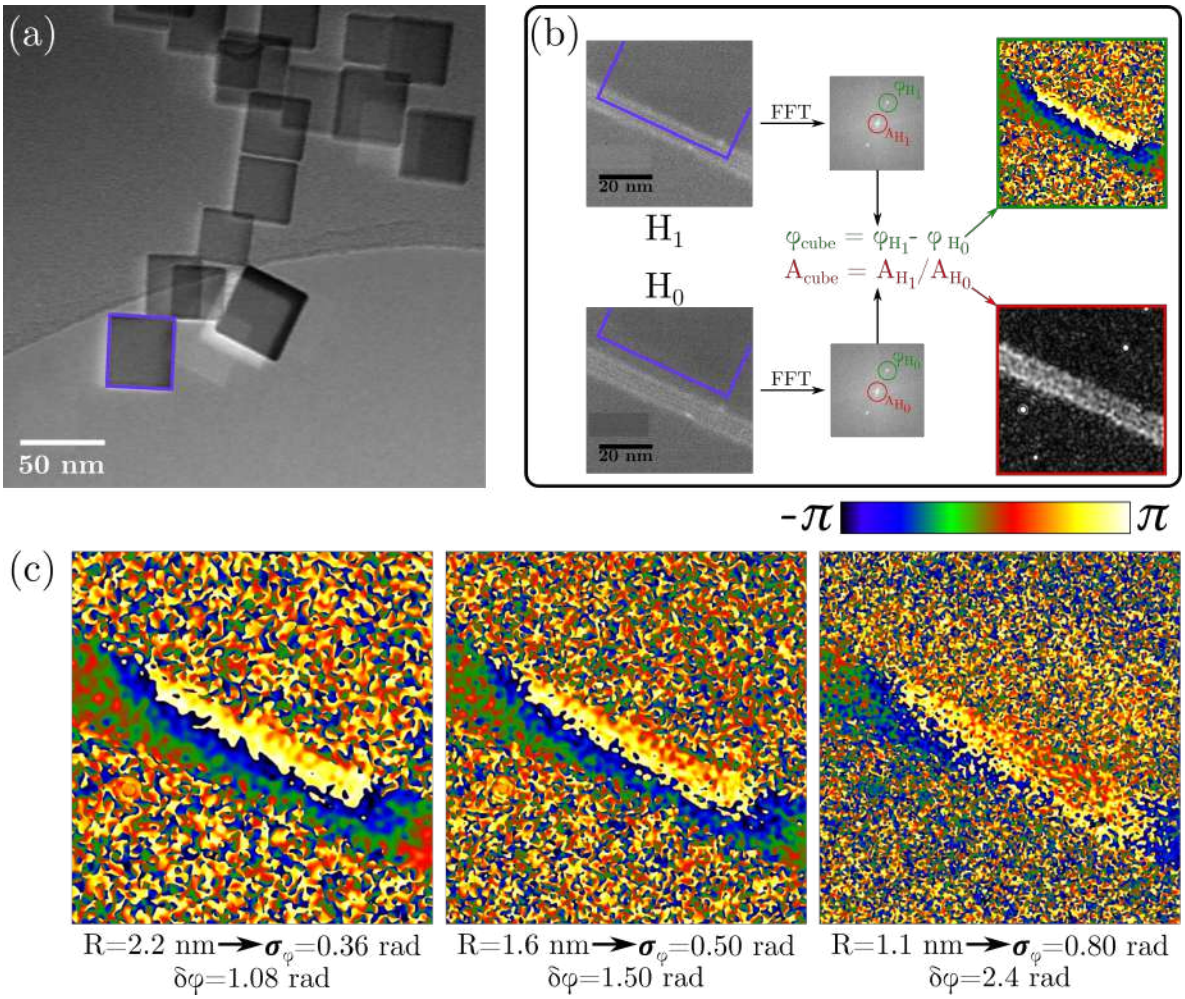

Figure 4.7: MgO cube phase reconstruction using ultrafast electron holography. (a) TEM micrograph of MgO cubes deposited on a carbon foil. (b) Phase and amplitude reconstruction using the specimen and reference hologram. (c) Effect of the mask size in Fourier space on the phase standard deviation. Phase detection limits are calculated under ideal conditions ($SNR = 3$, $C_{inst} = 1$). Experimental conditions: biprism tension 28 V, exposure time 150 s, $W_{LAS} = 8$ mW, $f = 2$ MHz, $N_{epp} \sim 8$, binning 1. Magnification: 200 kX

influence of instabilities over long exposure times. In the next paragraph we will show how the use of image stacks can contribute to reduce the effect of instabilities.

4.3 Towards ultrafast electron holography

Image stacks consist in a sequential acquisition of several holograms. Using a stack of a high number of holograms with short exposure times allows to correct the effect of instabilities. However, due to the latter, simply summing all the hologram fringes would not improve the contrast. The resulting hologram would corresponds to a standard one acquired with a total exposure time equal to $t_{exp} \cdot N_{holo}$, where t_{exp} is the acquisition time of each individual hologram and N_{holo} the number of holograms in the stack. In order to properly exploit hologram stacks, a realignment process is required. Data processing has been performed using home-made scripts developed in CEMES by Christophe Gatel. First of all, dead pixels are filtered out: these are detected in each individual hologram of the stack and then replaced with the average intensity of the adjacent pixels in order to avoid any artefact in the phase reconstruction.

As already described, due to the edge of the biprism wire, Fresnel fringes are superimposed on the hologram fringes. Hologram instabilities can be induced by mechanical instabilities of the biprism and also those of the microscope electronics, which can induce random tilt or shift of the incoming electron beam. In order to take care of the biprism mechanical instabilities between each hologram, a first image alignment is performed using the Fresnel fringe position. Then, to correct beam instabilities, hologram fringes are aligned by comparing their positions. In each individual hologram in the stack, the phase is determined and compared with one selected as a reference. The phase difference is then converted into a number of pixels used to realign each individual hologram relatively to the reference one. Once completed these alignment processes, all the individual holograms are finally summed. Figure 4.8 shows the effect of the correction for two different biprism voltages. In the *Not corrected* row, individual holograms in the stack have only been summed without corrections. At low biprism

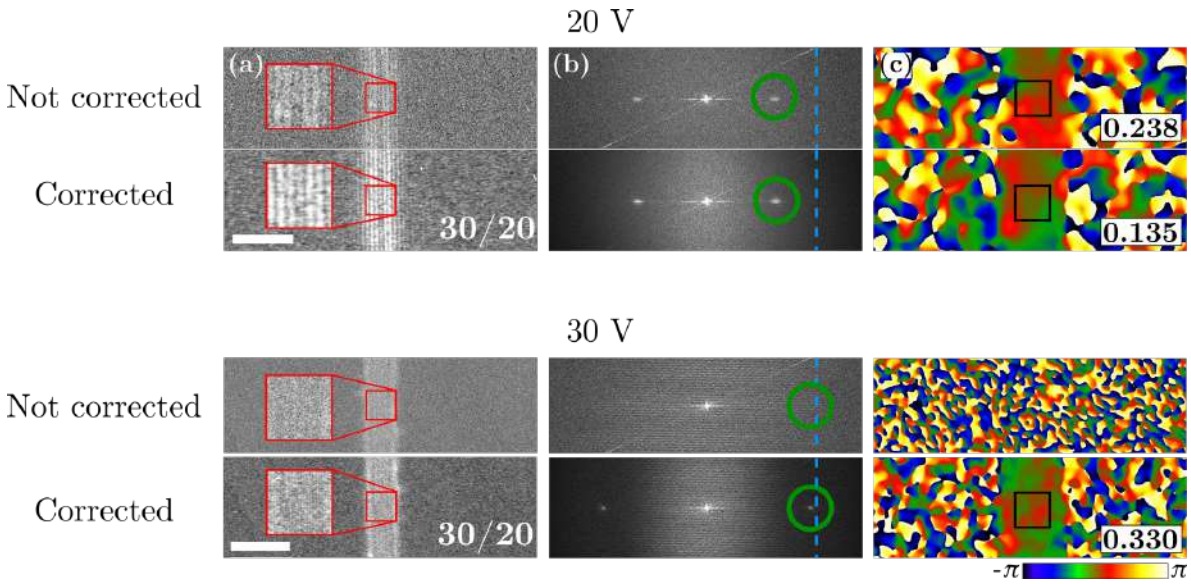

Figure 4.8: Effect of individual hologram instabilities correction for two different biprism voltages. (a) The numbers indicate the number of images in the stack and the acquisition time of each of them (in second). In the 20 V and 30 V cases the scales are 10 and 20 nm, respectively. (b) Power spectrum of the holograms. The green circles represent the 2.5 nm resolution mask in the Fourier space. The blue dashed line shows the position of the spatial frequency $(4 \cdot \text{pixel})^{-1}$. (c) Reconstructed phases. Standard deviations calculated inside the black square are displayed. Experimental conditions:$W_{LAS} = 8\,\text{mW}$, $f = 2\,\text{MHz}$, $N_{epp} \sim 6$, binning 2. Magnification: 200 kX.

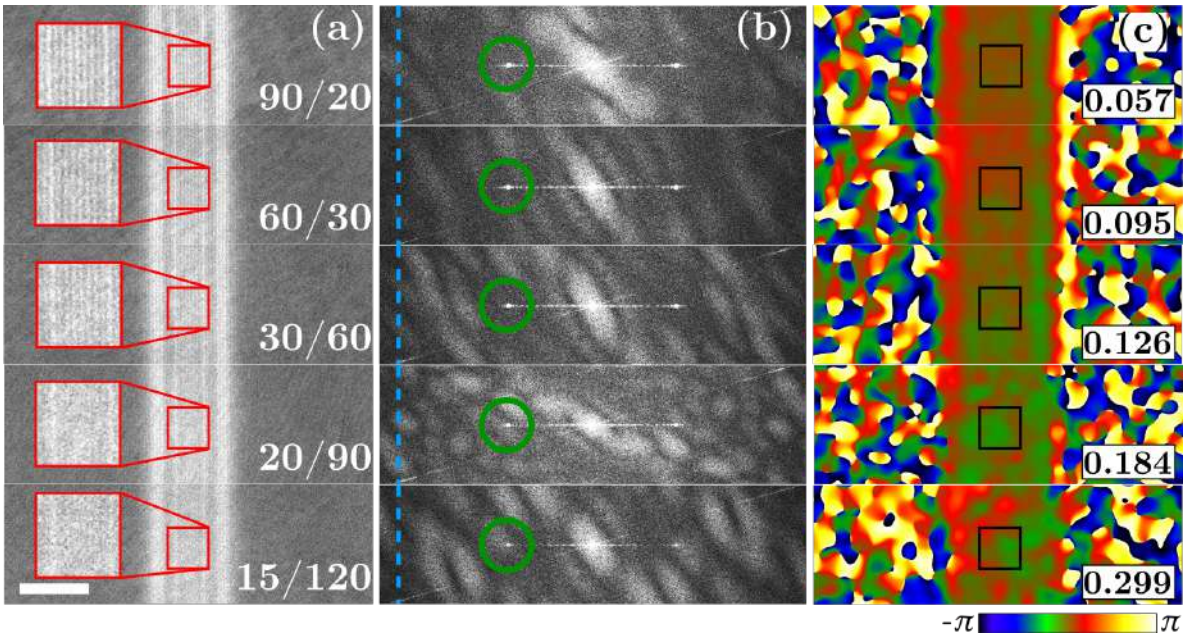

Figure 4.9: The effect of the individual hologram exposure time in summed corrected hologram stacks. (a) The numbers indicate the number of images in the stack and the individual acquisition time. The total exposure time remains constant. Scale: 10 nm. (b) Power spectrum of the holograms. The green circles represent the 2.5 nm resolution mask in Fourier space. The blue dashed line shows the position of the spatial frequency $(4 \cdot \text{pixel})^{-1}$. (c) Reconstructed phases. Standard deviations calculated inside the black square are displayed. Experimental conditions: $W_{LAS} = 8\,\text{mW}$, $f = 2\,\text{MHz}$, $N_{epp} \sim 6$, binning 2. Magnification: 400 kX. Biprism tension: 30 V.

voltages, the effect of instabilities is less problematic than using higher voltages. Phase reconstruction can be even possible in these cases. However, applying the correction, the hologram fringes contrast is improved and the noise in the reconstructed phase is strongly reduced. The standard deviation is improved by approximately a factor 2. The need to apply instability corrections becomes obvious at higher biprism voltages. For instance, in the 30 V case without correction the sidebands in the power spectrum are not detected and it is then impossible to retrieve the hologram phase. Figure 4.9

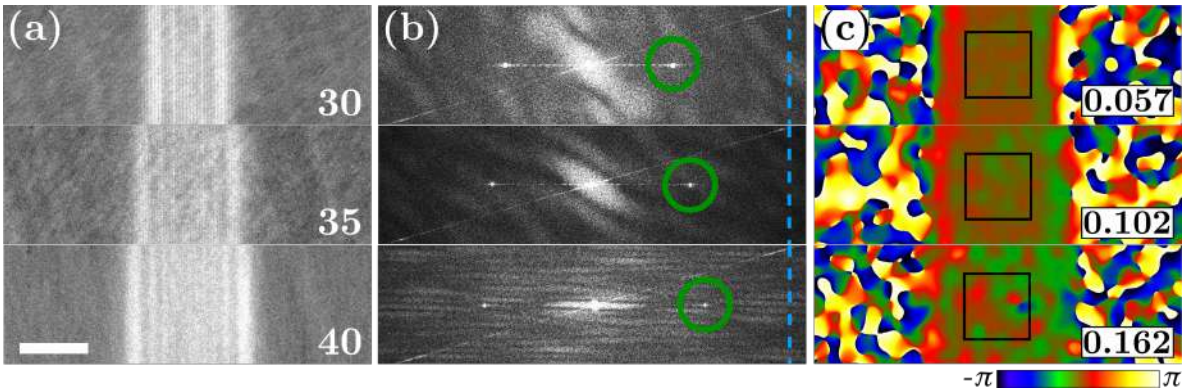

Figure 4.10: The effect of the biprism voltage in the summed corrected hologram. (a) The numbers indicate the biprism voltage (in volt). Scale: 10 nm. (b) Power spectrum of the holograms. The green circles represent the 2.5 nm resolution mask in the Fourier space. The blue dashed line shows the position of the spatial frequency $(4 \cdot \text{pixel})^{-1}$. (c) Reconstructed phases. Standard deviations calculated inside the black square are displayed. Stack of 90 and 20 s of exposure time have been acquired. Experimental conditions: $W_{LAS} = 8\,\text{mW}$, $f = 2\,\text{MHz}$, $N_{epp} \sim 6$, binning 2. Magnification: 400 kX.

shows the effect of the individual hologram exposure time and the threshold of instability contribution in the hologram contrast. The total exposure time remains constant at 1800 s. We can clearly see that by increasing the individual acquisition time the effect of instabilities becomes more important. The summed hologram fringe contrast decreases and hence the standard deviation of the reconstructed phases increase (Figure 4.9 (a) and (c)). As a consequence, stacks composed of a high number of individual holograms acquired with shorter exposure times should improve even more the contrast. Nevertheless, there is one major drawback that prevents to use this approach. Indeed, with exposure times shorter than a limit value, the hologram contrast might not be sufficient (as already reported in Figure 4.4) for the correction algorithm to be used properly. Individual acquisition times between 20 and 30 s seem to be optimal. In Figure 4.10 three summed corrected holograms are displayed for different biprism volt-

ages. By comparing the holograms acquired under the same electron optical conditions but with a different total exposure time (150 s for the single not-corrected hologram and 20 s for each of the 90 holograms composing the stack), there is an improvement of 40% and 64% of their phase standard deviations for the 30 and 35 V case, respectively. Moreover, we can notice that using 40 V of biprism voltage the standard deviation is even smaller than the value obtained for the 35 V case with $t_{exp} = 150$ s for the same spatial resolution in the reconstructed phase.

4.4 Conclusion

We have introduced in this chapter the requirements to perform off-axis electron holography with an ultrafast electron beam. The low probe current in the CFEG-UTEM represents the main difficulty. In order to acquire an exploitable hologram from which a useful phase can be extracted, acquisition times between 100 and 150 s are needed. However, under this condition, the influence of instabilities becomes preponderant and also the choice of useful biprism voltages (and as a consequence useful fields of view) remains limited. To overcome these issues, we use image stacks in order to sequentially acquire a high number of individual holograms with an optimum low exposure time lying in the 20 - 30 s range. In this way, instabilities can be compensated using dedicated alignment algorithms. The next step in improving off-axis electron holography in UTEM consists in the automation of the hologram correction. This is possible both in implementing the correction algorithm during the acquisition and controlling in real time the gun tilt coils to compensate drifts of the hologram fringes [177]. The future transfer of technology on a recent state-of-the-art TEM, will give us the possibility to move towards this direction and the use of direct electron camera providing a higher DQE should also strongly improve the live-correction process.

Conclusions and perspectives

In this thesis, the development of the first coherent UTEM based on a modified CFEG has been reported. In Chapter 1 the motivation and the scope of this work have been presented as well as the emission mechanism during the interaction between a tungsten metallic nanotip and an ultrafast laser source. Particular attention has been paid to understand the influence of the electron dynamics on the electron energy distribution. This allowed us to clarify the non-linear emission process and the electron energy distribution. Finally, the influence of the space-charge effect on the pulsed electron beam properties has been addressed.

Chapter 2 reports on the modifications on the original 200 kV FE-TEM HF 2000. The integration of the optics inside the modified gun has been explained in details. The electron trajectories simulations inside the modified CFEG have been presented to demonstrate that the electron optics properties remain unchanged. We have also shown the modification of the objective lens with the implementation of a systems designed to inject the laser on the specimen or collect the light emitted by cathodoluminescence. Despite this modification we did not report any significant alteration on the instrument spatial resolution. The properties of the CFEG-UTEM have also been discussed. We experimentally confirmed the emission process already theoretically discussed in Chapter 1 and that electron emission is limited to the apex. Furthermore,

thanks to autocorrelation experiments we exclude any heating of the emitter due to cumulative effect of the ultrafast laser pulses. The probe current stability has been studied. We found that the perturbations come from contamination, particle diffusion and detection noise as in DC CFEGs together with the oscillation in the SHG intensity. The electron optics has been optimised and the brightness has been evaluated. The value of $5.8 \cdot 10^7\,\mathrm{A \cdot m^{-2} \cdot Sr^{-1}}$ is the highest reported among all the UTEMs. Finally, FemtoTEM has been tested using conventional TEM techniques, reporting a spatial resolution close to 0.2 nm and an energy resolution around 1.3 eV due to the electron dynamics in the nanoemitter during the laser-metal interaction.

Chapter 3 reports on the EEGS theory and presents the first pump-probe experiment. EEG spectra have been simulated as a function of three experimental parameters: incident laser electric field, electron pulse duration and electron spot size. Finally, ultrashort electron pulses have been characterized. Energy gain maps have been acquired under different condition and the electron chirp value has been extracted. We found that varying the number of electrons per pulse from 0.59 to 4, the chirp increased by 30%. It has been possible to faithfully simulate the EEGS maps and determine the electron pulse duration using the experimental parameters. We determined an increase of the electron pulse duration from 400 to 525 fs in FWHM for the $N_{epp} = 0.59$ and $N_{epp} = 4$ cases, respectively.

In Chapter 4, off-axis electron holography performed with a high brightness pulsed electron beam has been discussed. We showed that due to the low probe current in CFEG-UTEM, exposure times between 100 and 150 fs are necessary to acquire an electron hologram with a fringe contrast that allows to retrieve the hologram phase. During such long acquisition times the effect of instabilities becomes very important and limits the range of useful biprism voltages between 20 and 35 V. Through the acquisition of

stacks containing tens of short exposure time holograms and thanks to post-process correction of fringes drift, it is possible to correct the effect of instabilities and strongly improve the standard deviation of the reconstructed phase. Thanks to this implementation it has also been possible to increase the size of the overlap region of the hologram. Since its birth, time-resolved Transmission Electron Microscopy allowed to explore the nanoscale world in various fields of science such as nanomechanics, nanomagnetism, chemistry, biology and nano-optics [112]. The development of FemtoTEM led to the creation of a joint laboratory between the CEMES-CNRS and Hitachi High Technologies Corporation that started very recently in July 2018. Thanks to this partnership, a transfer of the ultrafast technology from the old HF2000 to a recent state-of-the-art microscope, the 300 kV FE-TEM HHT HF3300 is planned for 2019. This will boost further the applications of coherent UTEM towards new techniques as the time-resolved off-axis electron holography, which will be strongly improved thanks to the implementation of automated feedback control, as already done in CEMES using the same generation of HF microscopes [177].

Résumé

La naissance et le développement de la microscopie électronique en transmission (MET) ont marqué une réelle percée dans l'investigation du monde nanométrique. En effet, la MET fournit des informations du échantillon sous analyse dans les espaces directs et réciproques, ainsi que des spectres de perte d'énergie électronique (EELS) avec une résolution spatiale inférieure à l'ångström et une résolution d'énergie proche de 10 meV. L'exploitation de sources d'électrons extrêmement cohérentes ont permis de repousser les limites de l'instrument plus loin. La minimisation de la taille du spot du faisceau d'électrons et de la résolution en énergie, ainsi que l'amélioration de la brillance, ont permis la MET-EELS à balayage (STEM-EELS)en haute résolution et aussi l'acquisition d'hologrammes électroniques. L'analyse de ceux derniers permet la reconstruction de la phase du faisceau électronique pour cartographier les champs électriques, magnétiques et de contrainte à l'échelle nanométrique. De plus, de nouveaux porte-échantillons ont permis la réalisation d'expériences in-situ. Ces développements ont élargi les champs d'application de la MET en physique, matériaux et science des matériaux, biologie, chimie, géologie et médecine. Les techniques in-situ permettent de suivre l'évolution d'un échantillon sous stimuli externes par une caméra CCD mais la résolution temporelle est limitée par la cadence de la CCD, qui atteint 1600 fps dans les caméras les plus récentes et les plus rapides. Mais si on veut étudier la dynamique structurelle ou

électronique, l'échelle de temps pertinente est dans la gamme de la pico-femtoseconde et, par conséquent, une nouvelle approche est donc nécessaire pour étudier les processus ultra-rapides. Après le travail innovants de Bostanjoglo à la TU Berlin, la microscopie électronique en transmission ultra-rapide (UTEM) a connu un élan spectaculaire au début du siècle quand A. Zewail au California Institute of Technology démontré la MET ultra-rapide avec une résolution temporelle de la picoseconde et une résolution spatiale nanométrique. Le but de cette thèse est de rendre compte du développement du premier MET ultra-rapide équipé d'un canon électronique à émission de champ froid (CFEG), pour améliorer la brillance de la source d'électrons mis en œuvre dans les UTEM et pousser l'instrument aux applications en interférométrie électronique.

Chapitre 1 - Introduction

La figure I montre clairement que de nombreux processus physiques importants se déroulent sur une échelle de temps inférieure à la nanoseconde, c'est-à-dire trop rapidement pour être détectés à l'aide de caméras traditionnelles. Même si les premiers microscopes électroniques résolus dans le temps avaient déjà été développés, ce n'est qu'en 2005 que la MET est devenu ultra-rapide, atteignant un niveau de résolution spatiotemporelle sans précédent, inférieure au nanomètre et à la picoseconde. Cette avancée repose sur l'utilisation d'impulsions électroniques contenant très peu d'électrons, minimisant ainsi la répulsion interparticulaire de Coulomb qui détériorait la résolution spatio-temporelle dans les premiers METs résolus temporellement. Dans un régime dit single électron, des images, des clichés de diffraction (DP) et des spectres ont été enregistrés à partir de l'accumulation de milliards de cycles de détection-excitation. Depuis 2005, le domaine de UTEM a continué à croître à un rythme rapide avec un nombre toujours croissant de groupes, de la spectroscopie TEM ou optique, développant ou

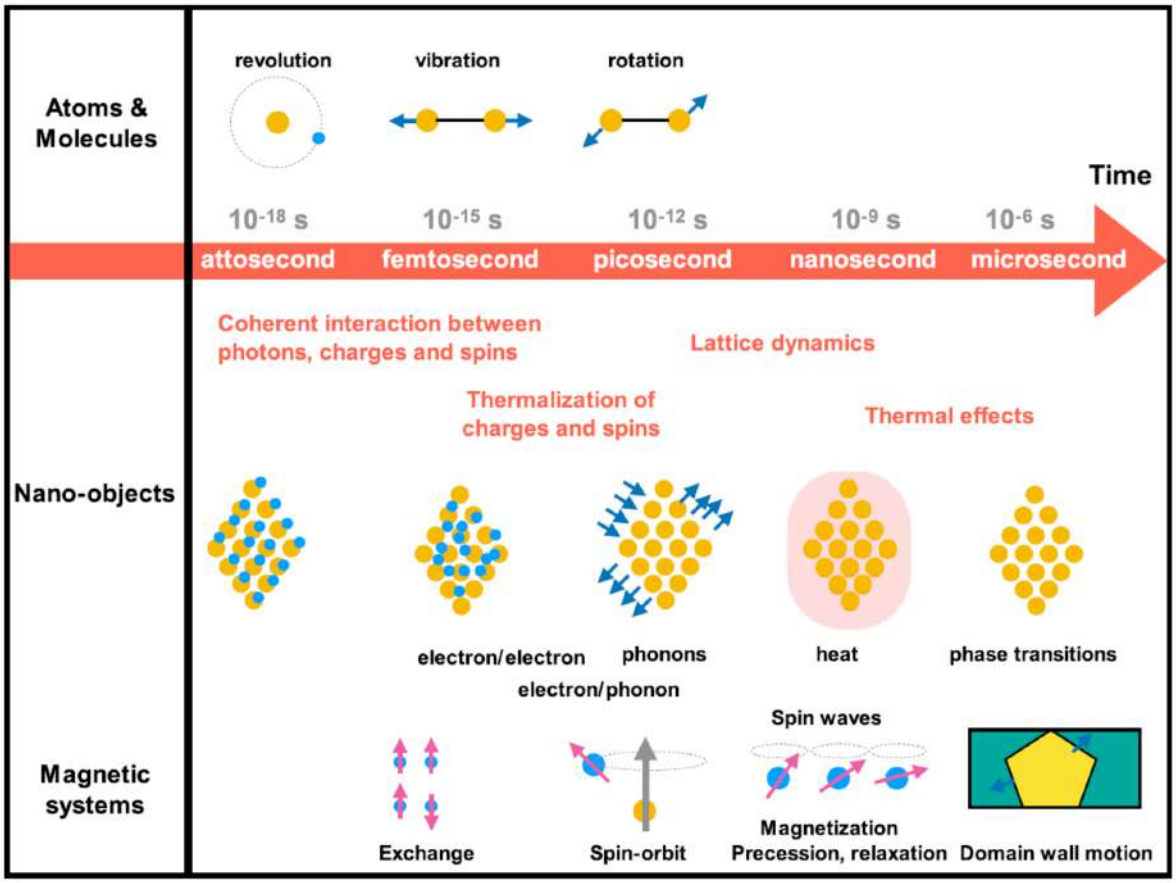

Figure I: Échelles de temps caractéristiques des processus ultra-rapides dans les systèmes de particules, de nano-objets et magnétiques.

acquérant leurs propres instrument.

1.1 MET dynamique et MET ultra-rapide

La microscopie électronique résolue en temps permet d'étudier la dynamique de processus rapides, typiquement dans la gamme nano – femtoseconde. L'approche suivie s'appelle pompe-sonde et est schématisée à la figure II: une impulsion de pompe amené le

spécimen hors d'équilibre et une impulsion de sonde est utilisée pour étudier le système à un certain délai, τ, pendant sa relaxation. Dans le domaine de la MET résolue en

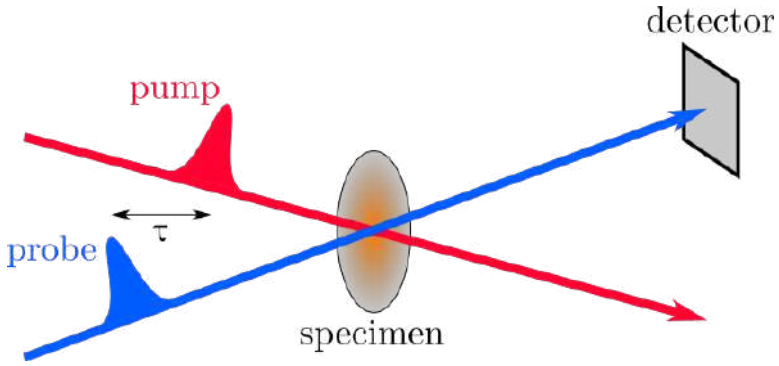

Figure II: Principe des expériences pompe-sonde. Un faisceau laser ultra-rapide (la pompe) est focalisé sur le spécimen, le faisant sortir de l'équilibre. Une seconde impulsion retardée, la sonde, est utilisée pour détecter l'évolution du spécimen. En microscopie électronique à résolution temporelle, l'impulsion de sonde est un paquet d'électrons.

temps, l'impulsion de pompe est généralement un stimulus optique externe qui excite l'échantillon mais aussi différentes excitations (acoustiques, thermiques, mécaniques, Etc.) peuvent être utilisé à cet effet. La sonde est un paquet d'électrons déclenché par une impulsion laser. Il existe deux modes de fonctionnement dans la MET résolue en temps. L'utilisation d'une seule impulsion électronique contenant plus de 106 électrons pour sonder la dynamique du système est appelée single shot mode (Figure III (a)). En utilisant un déflecteur de faisceau à grande vitesse synchronisé avec la source laser, il est possible d'enregistrer plusieurs images (ou cliché de diffraction, spectres) sur un détecteur CCD avec des retards différents par rapport à l'impulsion de pompe. Cela s'appelle *movie mode* (Figure III (b)). Un TEM fonctionnant en single shot mode est appelé TEM dynamique (DTEM) ou High Speed TEM. Le second mode opératoire, le mode stroboscopique, repose sur un nombre élevé (107 - 109) de cycles d'observation par excitation pour accumuler suffisamment d'électrons pour former une image, cliché

de diffraction, spectre ou hologramme. Il est représenté par la figure III (c). Le retard entre la pompe et la sonde peut être réglé avec une ligne de translation afin d'explorer la dynamique du processus souhaitée. Une translation $D = 1,5\,\mu$m de la ligne de retard, par exemple, produit un retard $\tau = 2D = c = 10$fs. La principale différence entre les deux modes est le nombre d'électrons dans chaque impulsion. En mode stroboscopique, le faisceau d'électrons ne contient que quelques électrons par impulsion. La minimisation de la répulsion de Coulomb parmi les électrons permet de pousser la résolution temporelle jusqu'à l'échelle temporelle de la femtoseconde. C'est ce qu'on appelle le *single electron regime*. Les MET résolus dans le temps qui fonctionnent dans ce mode sont appelés des METs ultra-rapides (UTEM).

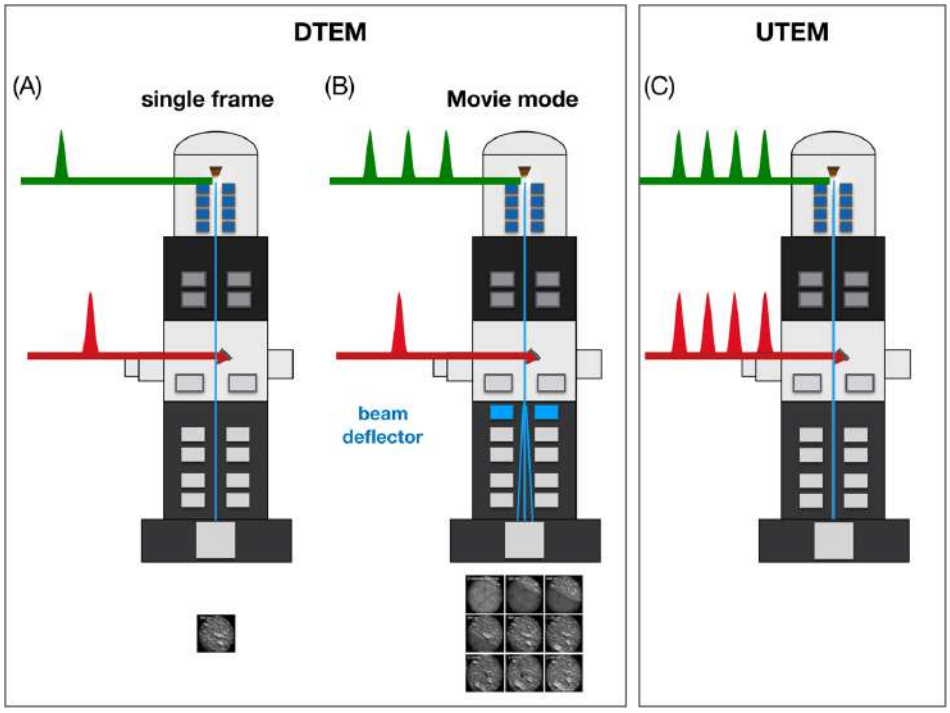

Figure III: Différents modes de fonctionnement dans le TEM à résolution temporelle. (a) Mode single-shot. (b) Mode *movie*. (c) MET ultra-rapide.

1.2 Mécanismes d'émission électronique déclenchées par laser

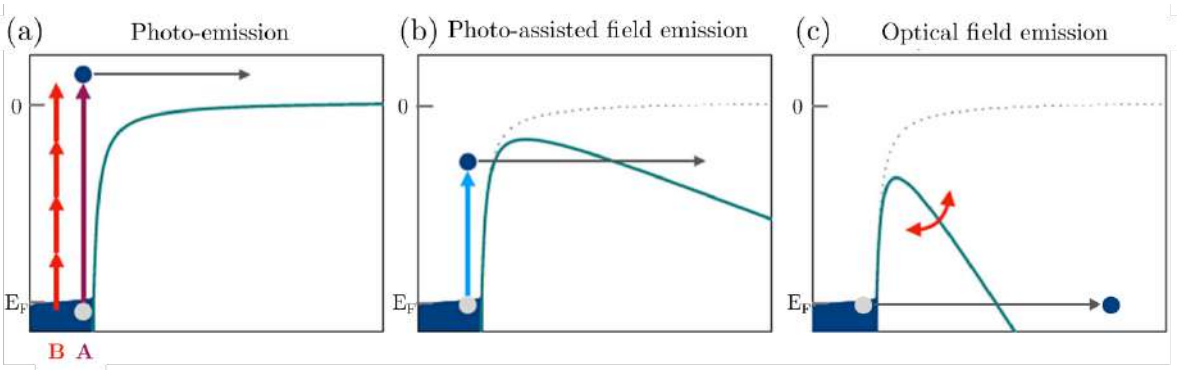

Figure IV: Processus d'émission d'électrons déclenchés par laser.

La combinaison d'un laser ultra-rapide et d'une source d'électrons permet de générer des impulsions électroniques ultra-courtes. Comme indiqué dans, l'émission d'électrons d'un matériau avec une fonction de travail Φ est possible grâce à l'absorption de photons d'énergie $E_{ph} = h\nu > \Phi$. Ce phénomène est appelé *photoémission à un photon* (Figure IV (a), cas A) et le courant émis dépend linéairement de l'intensité de la lumière incidente. Ce processus ne peut pas se produire si l'énergie des photons est inférieure à celle de la fonction de travail du matériau. Néanmoins, la photoémission à multiphotons (MPP), illustrée à la figure IV (a), cas B, est possible. La section transversale pour un tel processus non linéaire diminue avec le nombre de photons requis et la densité de courant émis est proportionnelle à la puissance n-ième de l'intensité laser I:

$$J \propto I^n$$

avec n le nombre de photons. La photoémission à multiphotons est le mécanisme d'émission dominante pour des intensités laser inférieures à $10^{11}\,\mathrm{W/cm^2}$. À des intensités laser plus élevées ($I > 10^{12}\,\mathrm{W/cm^2}$), le champ électrique associé peut être

suffisamment puissant pour moduler la barrière de potentiel et permettre le *tunneling* des électrons. Ce processus est appelé *émission de champ optique* et est représenté à la figure IV (c). Afin de discriminer les deux processus d'émission, nous pouvons évaluer le *paramètre de Keldysh*, figure de mérite de la théorie de Keldysh sur l'ionisation des atomes et des corps solides. Le paramètre de Keldysh est le rapport entre le temps de *tunneling* et la durée du cycle optique: un valeur $\ll 1$ est caractéristique de l'émission du champ optique, alors que $\gg 1$ indique que le mécanisme dominant est le MPP. D'autres mécanismes d'émission dépendent de la combinaison de l'intensité du laser et de la tension d'extraction, telle que l'*émission de champ photo-assistée*, schématisée à la figure IV (b). Dans ce cas, l'absorption d'un photon permet aux électrons de traverser la barrière grâce à l'ajout d'un champ électrique continu.

1.3 Influence de la dynamique électronique sur la distribution en énergie des électrons

L'interaction d'une impulsion laser ultracourte avec un nanoémetteur de tungstène modifie la répartition des électrons à l'intérieur du métal à une température donnée. Afin d'évaluer l'influence de la dynamique électronique sur les propriétés temporelles et spectrales d'une MET résolue dans le temps, un modèle de calcul basé sur des travaux antérieurs a été développé. Le modèle décrit un gaz d'électrons libres interagissant avec une impulsion laser femtoseconde. L'interface vide-métal est considérée plate à et un champ électrique continu (compris entre 0,5 et 3 V / nm) est appliqué sur la nanopointe métallique.

La distribution électronique en fonction du temps, f(k; t), peut être calculée à partir de

l'équation de Boltzmann:

$$\frac{df(\mathbf{k},t)}{dt} = \frac{df(\mathbf{k},t)}{dt}\bigg|_{e-e} + \frac{df(\mathbf{k},t)}{dt}\bigg|_{e-ph} + F(\mathbf{k},t)$$

où les trois termes représentent l'interaction électron-électron, électron-phonon et l'excitation laser sur la nanopointe, respectivement. La relation de dispersion des électrons dans la bande de conduction a été considérée comme parabolique et l'énergie de Fermi pour le tungstène est $E_F = 9.2\,\mathrm{eV}$. Avant l'excitation par l'impulsion laser femtoseconde, les électrons et les phonons suivent respectivement les distributions de Fermi-Dirac (F-D) et de Bose-Einstein. La figure V montre l'évolution de la distribution électronique. Dès que l'impulsion laser commence à interagir avec le nanoémetteur (tracé de forme parabolique), l'occupation d'états électroniques est modifiée en raison de l'excitation du gaz d'électrons : la population d'électrons est répartie sur plusieurs états électroniques en raison d'excitations et de désexcitations multiples. Les propriétés spectro-temporelles de l'impulsion électronique ont été déduites de la distribution électronique excitée optiquement. En regardant attentivement la distribution spectrale des électrons, on peut remarquer que la symétrie du ZLP (Zero Loss Peak) en mode laser-driven semble différente de celle d'un CFEG classique. Cette différence est visible à la figure 1.19 (Chapitre 1 du manuscrit), dans laquelle deux spectres d'énergie d'électrons simulés sont esquissés.

1.4 Élargissement du pulse électronique: influences sur les propriétés spectro-temporelles du UTEM

Les interactions électron-électron au cours de la propagation de l'impulsion électronique détériorent les propriétés spectro-temporelles de l'UTEM. Par conséquent, la résolution temporelle d'un tel instrument ne dépend pas seulement du mécanisme d'émission

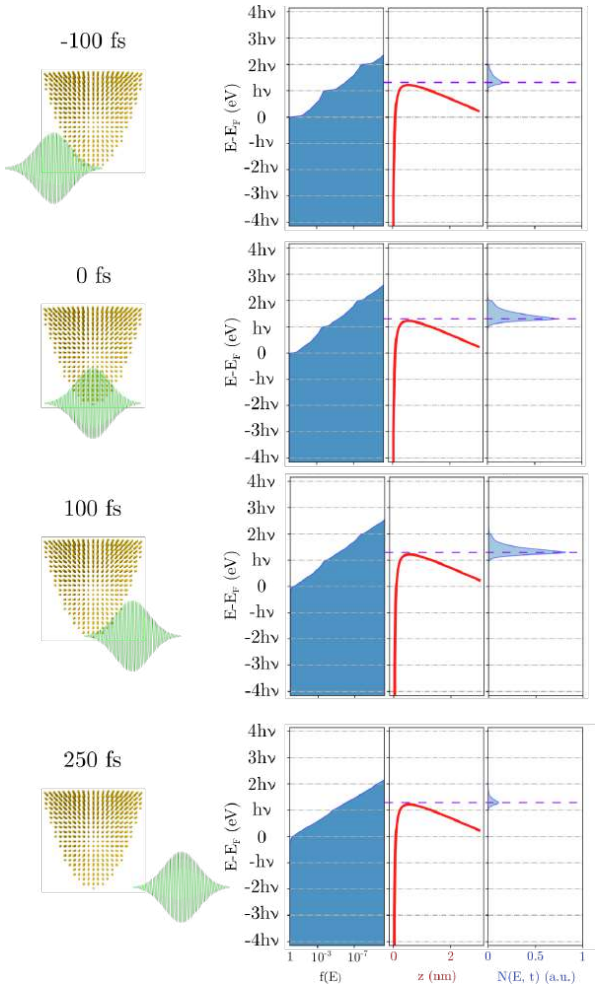

Figure V: Excitation optique ultra-rapide d'un gaz d'électrons. Le nanoémetteur de tungstène est esquissé avec une forme parabolique. Les trois graphiques représentent (de gauche à droite) : le numéro d'occupation des électrons *f(E;t)* (courbe bleu foncé), la barrière de potentiel (courbe rouge) et le nombre d'électrons émis *N (E ; t)* (courbe bleu clair). Nous avons considéré une impulsion laser de $\lambda = 515\,\text{nm}$ et une durée d'impulsion FWHM de 250 fs. Le temps de thermalisation électron-phonon est de 400 fs. Le champ électrique CC appliqué est $F_{loc} = 1,19\,\text{V/nm}$.

d'électrons, mais également de la propagation à l'intérieur de la colonne TEM. Gahlman *et al.* ont décrit théoriquement ces deux effets et étudié séparément leur influence sur

les propriétés du faisceau d'électrons :

- **Influence de la distribution d'énergie initiale sur la durée de l'impulsion électronique.** Les électrons émis ont une certaine distribution d'énergie initiale, ΔE_i qui détermine un élargissement temporel, Δt_{KE}. Ce dernier, ainsi que la durée de l'impulsion laser, contribuent à l'élargissement temporel global:

$$\Delta t = \sqrt{\Delta t_{h\nu}^2 + \Delta t_{KE}^2}$$

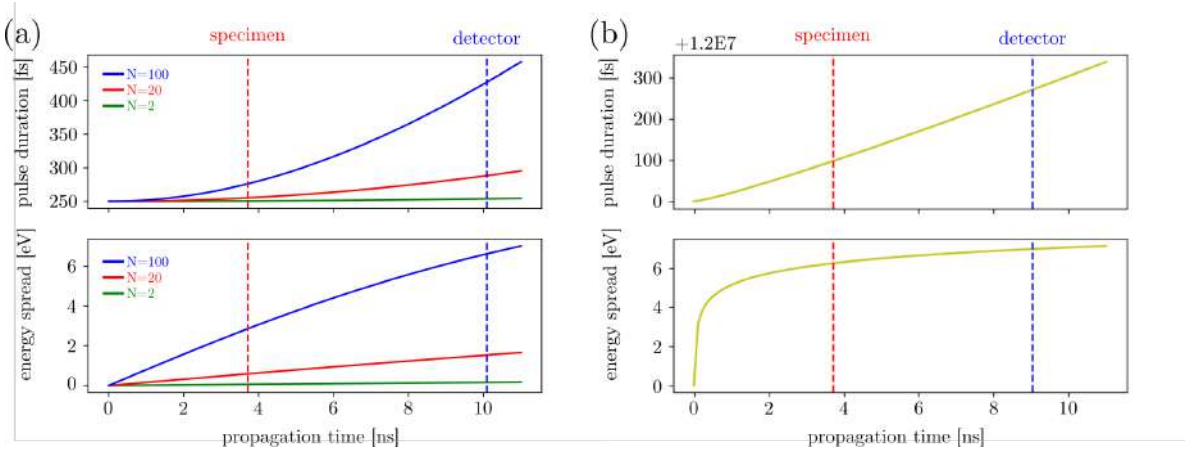

Figure VI: Effet du nombre d'électrons par pulse, N, sur l'élargissement temporel et énergétique. Le cas (b) prend en compte le mode single-shot ($N \sim 10^8$).

- **Influence de l'effet de la charge d'espace sur la durée du pulse et la résolutions en énergie.** La répulsion des électrons à l'intérieur d'une impulsion induit une augmentation de sa dimension et, par conséquent, une dégradation de la résolution temporelle, spatiale et spectrale de l'UTEM. Sur la figure VI

(a), l'élargissement des impulsions est évalué en fonction du temps de propagation pour différents nombres d'électrons par impulsion (2, 20, 100). Les lignes pointillées indiquent l'heure à laquelle les électrons arrivent sur l'échantillon (rouge) et la caméra CCD (bleue).

Les impulsions contenant $N = 2$ et $N = 20$ électrons sont généralement utilisées dans les expériences stroboscopiques à pompe-sonde dans UTEM. Cependant, en mode single shot, chaque impulsion contient jusqu'à 10^8 électrons et les propriétés spatio-temporelles du faisceau d'électrons sont profondément affectées. La figure VI (b) montre l'élargissement des impulsions en mode single shot en tenant compte d'une durée d'impulsion laser de $\Delta t_{h\nu} = 12\,\mathrm{ns}$. Alors que le fonctionnement des UTEM en régime à un électron a permis une amélioration spectaculaire de leurs propriétés spatio-temporelles, la faible luminosité des canons à électrons basés sur des photocathodes limite encore leur champ d'application, les rendant inadéquats pour des applications exigeantes telles que l'holographie électronique ultra-rapide. La solution est apparue avec une émission laser de nanopointes métalliques, qui a jeté les bases pour les UTEM basés sur des sources électroniques à émission de champ (FEG).

Chapitre 2 - Développement Instrumental

Le microscope qui a été modifié pour développer le CFEG-UTEM (désigné ci-après par FemtoTEM) au CEMES-CNRS est un Hitachi HF2000, un CFEG 200 kV-TEM fabriqué par Hitachi High Technologies (HHT) en 1989. Le développement d'un UTEM en modifiant un TEM conventionnel présente certains défis. Figure VII (a) montre une image du HHT HF2000 d'origine. Il n'y a pas d'accès optique pour injecter les faisceaux laser, ni à l'intérieur du canon ni dans la lentille objective. Afin de fournir

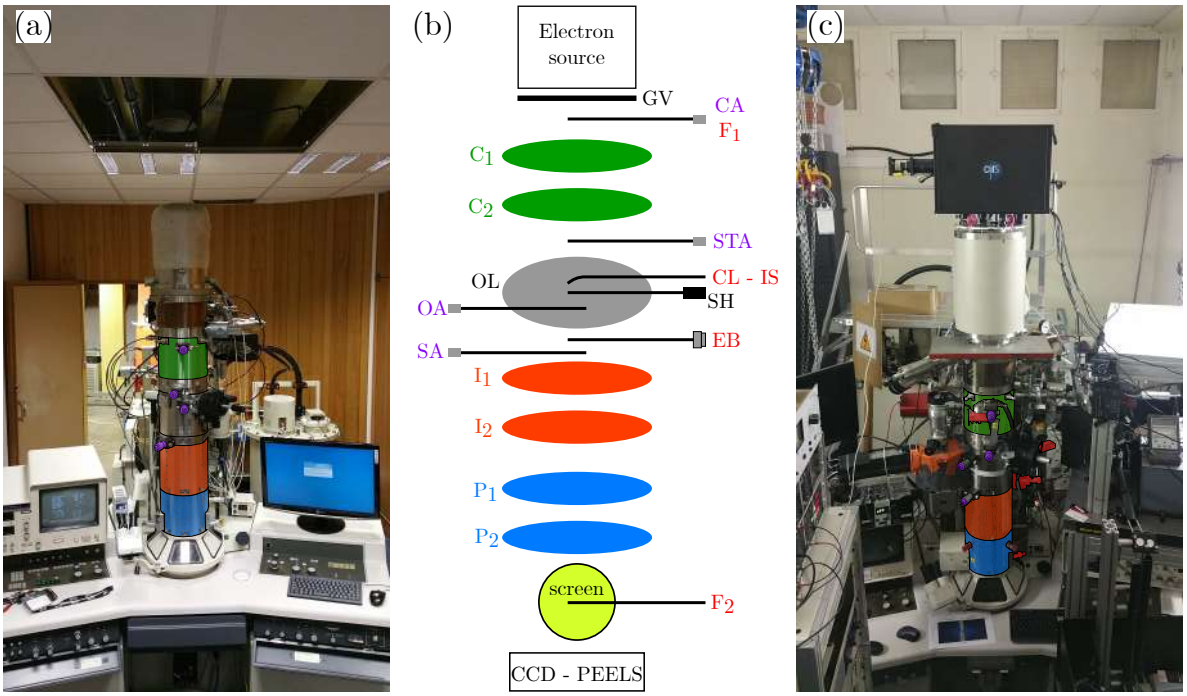

Figure VII: (a) Photo du HHT HF2000 d'origine au CEMES-CNRS. (b) Schéma de la colonne du MET. Les étiquettes rouges indiquent les pièces modifiées. Les étiquettes violettes indiquent les ouvertures TEM. (c) Image du FemtoTEM. La tête optique est visible sur le boîtier du canon. Systèmes de lentilles mis en évidence comme dans (b). Les ouvertures sont surlignées en violet dans (a) et (c). Pièces modifiées surlignées en rouge dans (c).

un chemin pour injecter le laser à l'intérieur de la source d'électrons, le boîtier externe d'origine (appelé *gun housing*) a été remplacée par une version modifiée, comme illustré à la figure VII (c). La lentille objective a également été modifiée. Elle est maintenant équipée d'un système optomécanique pour l'injection et la focalisation du laser sur l'échantillon par un miroir parabolique. Le même système peut être utilisé pour collecter la cathodoluminescence émise par l'échantillon. Nous nous référerons à ce dernier comme le *système d'injection de cathodoluminescence* (CL-I). Malgré les modifications,

la colonne de microscope, esquissée à la figure VII (b), conserve les mêmes propriétés d'optique électronique. Le système de vide d'origine a été amélioré. Deux cavités de Faraday, F_1 et F_2, ont été monté, l'une sur l'ouverture du condenseur (CA) et l'autre sur le *beam block* au-dessus de l'écran fluorescent. Ils sont connectés à un picoammeter Keithley 6514 pour mesurer le courant émis en mode ultra-rapide. Au cours de cette thèse, nous nous référons au courant d'émission comme celui mesuré par F_1. Le courant mesuré par F_1 est la moitié du courant d'émission total mesuré dans le canon électronique. Un biprisme électronique (EB) a été inséré dans le plan du diaphragme de sélection d'aire (SA) pour effectuer des études de holographie électronique ultrarapide. L'UTEM a également été équipé d'une caméra Ultrascan Gatan $4K \times 4K$ et d'un spectromètre à détection parallèle Gatan PEELS 666. En effet, la camera CCD Gatan d'origine a été remplacée par une PIXIS 256. Cette dernière est couplée à une double lentille télescopique située entre le scintillateur et le capteur CCD de la caméra. Un schéma détaillé du CFEG modifié est présenté à la figure VIII (a). Le canon peut être divisé en deux parties. La partie supérieure (c'est-à-dire la boîte noire de la figure VIII (b)) est appelée la tête optique. Elle contient des composants optomécaniques permettant d'aligner le faisceau laser sur l'apex de la pointe et contrôler la puissance du laser et la polarisation. Ces composants sont fixés sur une breadboard optique fixée sur le boîtier du canon. La caméra CCD permet de visualiser le nanoémetteur ainsi que la procédure d'alignement à l'aide d'une source de lumière blanche. Pour permettre l'injection du laser à l'intérieur du canon à électrons, deux fenêtres optiques ont été créées sur le dessus du boîtier du canon et sur une bride métal / céramique CF40 personnalisée. Le laser est ensuite réfléchi à 90 deg par un miroir plat et finalement focalisé via un miroir parabolique ($f = 8\,\mathrm{mm}$) dans un rayon de $3\,\mu$m situé au apex de la pointe. Les deux miroirs sont imbriqués dans un système à symétrique cylindrique appelé *port-miroir*

(*mirror holder*, MH, en anglais). La pointe et le port-miroir sont maintenus à la même tension $V_0 = -150\,\mathrm{kV}$. En s'agissant d'une émission d'électrons déclenchée par un laser pulsé, la tension d'extraction, V_1, peut être utilisée comme paramètre libre pour régler la position du crossover et la force de la gun lens, appelée V_2. La tension de chaque étage d'accélération est définie comme suit : $V_{IS} = (V_0 + V_2)/N$, où N est le nombre d'étages ($N = 5$, en notre cas particulier). Toutes les modifications sur le CFEG original

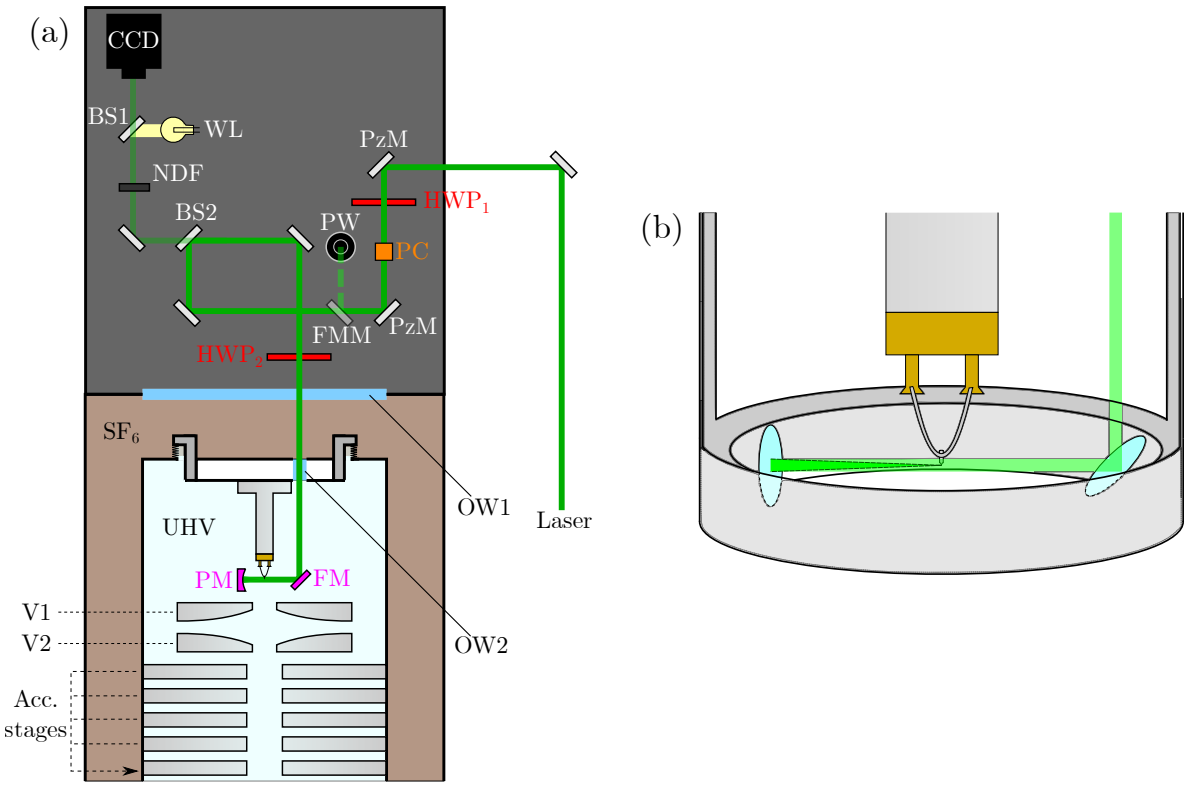

Figure VIII: (a) CFEG ultra-rapide et tête optique. HWP: Lame demi-onde. FMM: Flip Mount Mirror. PW: capteur de puissance. PzM: miroir piézoélectrique. BS: Miroir semi-réfléchissant. WL: source de lumière blanche. OW: Fenêtre optique. FM: miroir plat. PM: Miroir Parabolique. PC: cube polariseur. (b) Pointe CFEG montée sur support HHT et porte-miroir.

ont été effectuées au-dessus de l'anode extractrice, afin de préserver les propriétés optiques d'origine du faisceau d'électrons. Pour confirmer cette hypothèse, un modèle de l'ensemble du canon a été créé avec SIMION 8.1, un logiciel de méthode de différence finie (FDM). La distribution du champ électrique et les trajectoires électroniques à

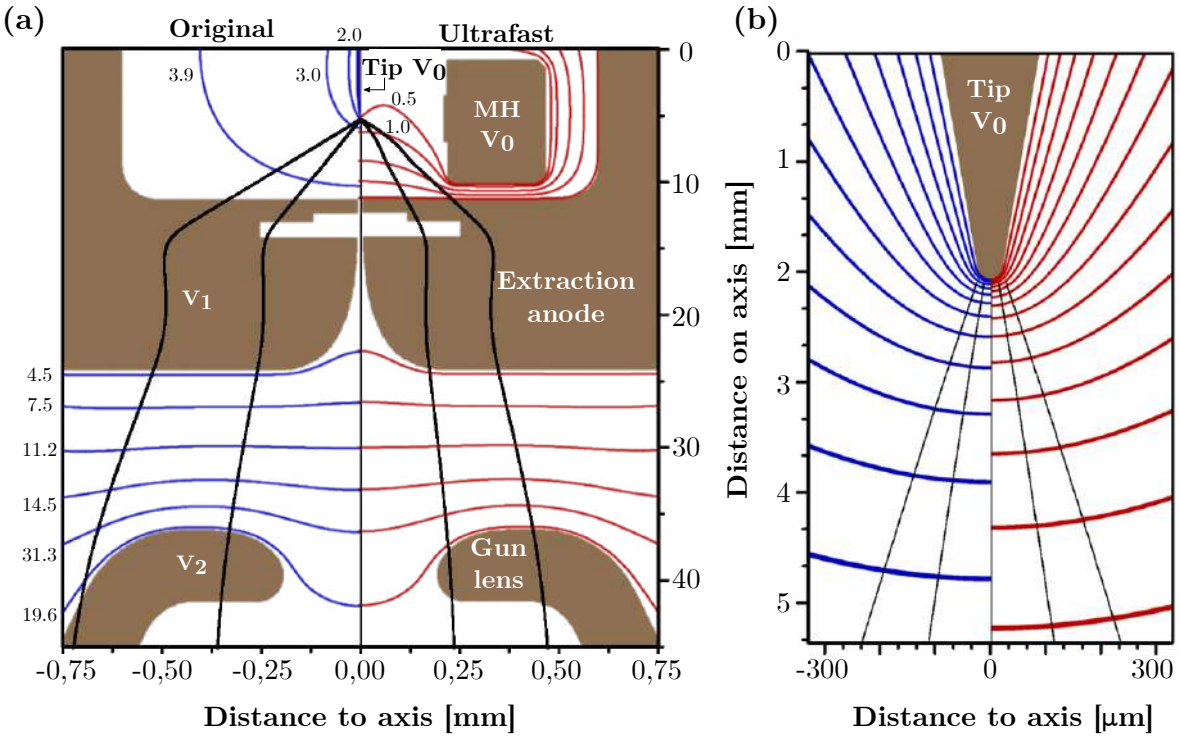

Figure IX: (a) Trajectoires des électrons à l'intérieur du canon. (b) Effet du porte-miroir sur le potentiel électrique autour de l'apex.

l'intérieur du HF2000 d'origine et dans le canon modifié ont été calculés et comparés (Fig.IX). Figure IX (a) montre les résultats de la simulation de trajectoire électronique. Il est divisé en deux parties : le côté gauche représente une section du canon du HF2000 d'origine, tandis que la partie droite représente le CFEG modifié, dans lequel le MH a été ajouté au modèle. En comparant les trajectoires dans les deux canons à électrons,

on voit clairement que le *port miroir* confine légèrement les électrons émis. Pour mieux comprendre l'influence des propriétés optiques du canon, des simulations par Electron Optic Design (EOD) ont été effectuées sur un modèle de canon modifié, avec une attention particulière portée aux coefficients d'aberration sphérique et chromatique. Une valeur C_3 de 35 mm a été calculée pour le canon d'origine et de 33 mm pour la source modifiée. La figure IX (b) donne une vue détaillée de la zone autour du apex de la pointe. Le système CL-I a été conçu pour injecter, aligner et focaliser le laser sur l'échantillon ou pour collecter la lumière émise par lui-même. Ce système est composé d'un miroir parabolique placé au-dessus du porte-échantillon à l'intérieur de l'espace entre les *pièces polaires* (4, 5 mm) du HF2000, comme illustré dans la Figure X (a) et (b). L'ensemble du système peut être déplacé de l'extérieur par un étage de translation

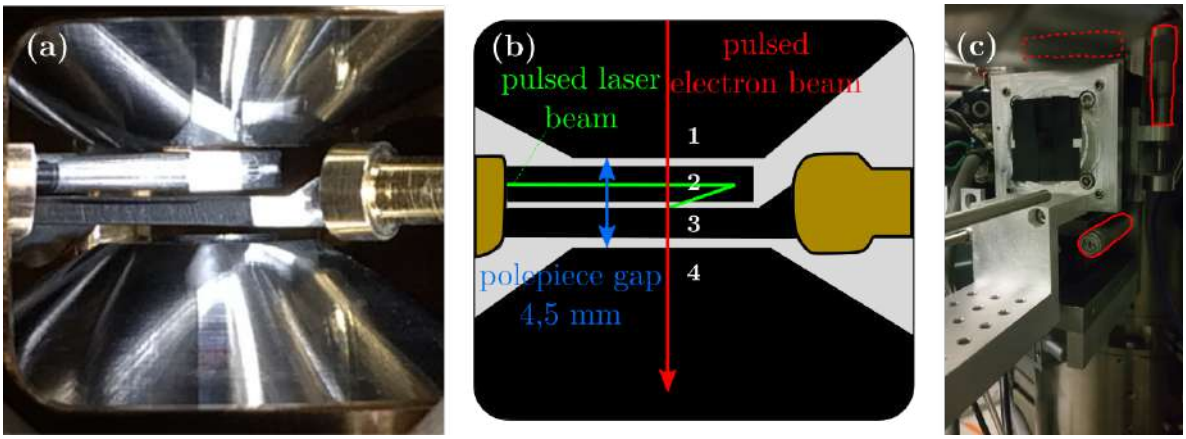

Figure X: (a) Image de l'espace entre les pièces polaires de la lentille objectif du FemtoTEM. (b) Description de (a). 1: piece polaire supérieure de la OL. 2: tube d'injection. Le miroir parabolique est installé à son extrémité. 3: porte-object. 4: pièce polaire inférieur de la OL. (c) Vue externe du système d'injection. Les positions des trois vis micrométriques sont surlignées en rouge.

XYZ équipé de trois vis micrométriques (Figure X (c)). Une *breadboard* optique a été in-

stallée à proximité de la lentille objectif (OL) pour installer les optiques d'injection. Elle comprend un spectromètre pour le CL, un ensemble de miroirs piézoélectriques et une caméra CCD pour suivre l'alignement et la procédure d'insertion-retrait du système CL-I. Malgré les modifications, les coefficients d'aberration de l'objectif restent inchangées et sont respectivement $C_S = 1,2\,\text{mm}$ et $C_C = 1,4\,\text{mm}$. Le système laser présent dans la configuration optique ultra-rapide est un laser fibrée ultra-rapide et compact (Satsuma, Amplitude Systèmes) délivrant des impulsions ultra-courtes (350 fs) de haute énergie (jusqu'à $20\,\mu\text{J}$) à 1030 nm avec un taux de répétition réglable, du single shot à 2 MHz. Le faisceau primaire est séparé par un cube polariseur en un faisceau de pompe et un faisceau de sonde. Les faisceaux pompe et sonde sont tous deux envoyés vers des cristaux de bêta-borate de baryum (BBO) afin de générer des impulsions femtosecondes à 515 nm par la génération de deuxième harmonique (SHG). Ensuite, ils sont envoyés à l'intérieur de l'OL et du canon à électrons, respectivement. La source d'électrons ultra-rapide a été caractérisée pour comprendre le mécanisme d'émission, évaluer la région d'émission de la nanopointe et mesurer la durée de l'impulsion électronique. La figure XI (a) montre une carte du courant de sonde détecté par F_1. La région d'émission a une FWHM de $2.95 \pm 0,07\,\mu\text{m}^2$. Le courant émis est maximum lorsque le champ électrique du laser est orienté parallèlement à l'axe de la pointe. La Figure XI (b) montre la dépendance de la polarisation du courant de sonde et montre que les électrons sont émis à l'apex de la pointe. La Figure XI (c) présente un exemple de mesure de la dépendance du courant de sonde sur la puissance laser incidente. Les valeurs de l'ordre de non-linéarité comprises entre 2.5 et 3.5 suggèrent que le gaz d'électrons est fortement perturbé dans nos conditions expérimentales. Enfin, des mesures d'autocorrélation à deux impulsions du courant de sonde sont rapportées à la figure XI (d). La largeur totale à mi-hauteur du signal de corrélation est de 360 fs, comme attendu de la durée

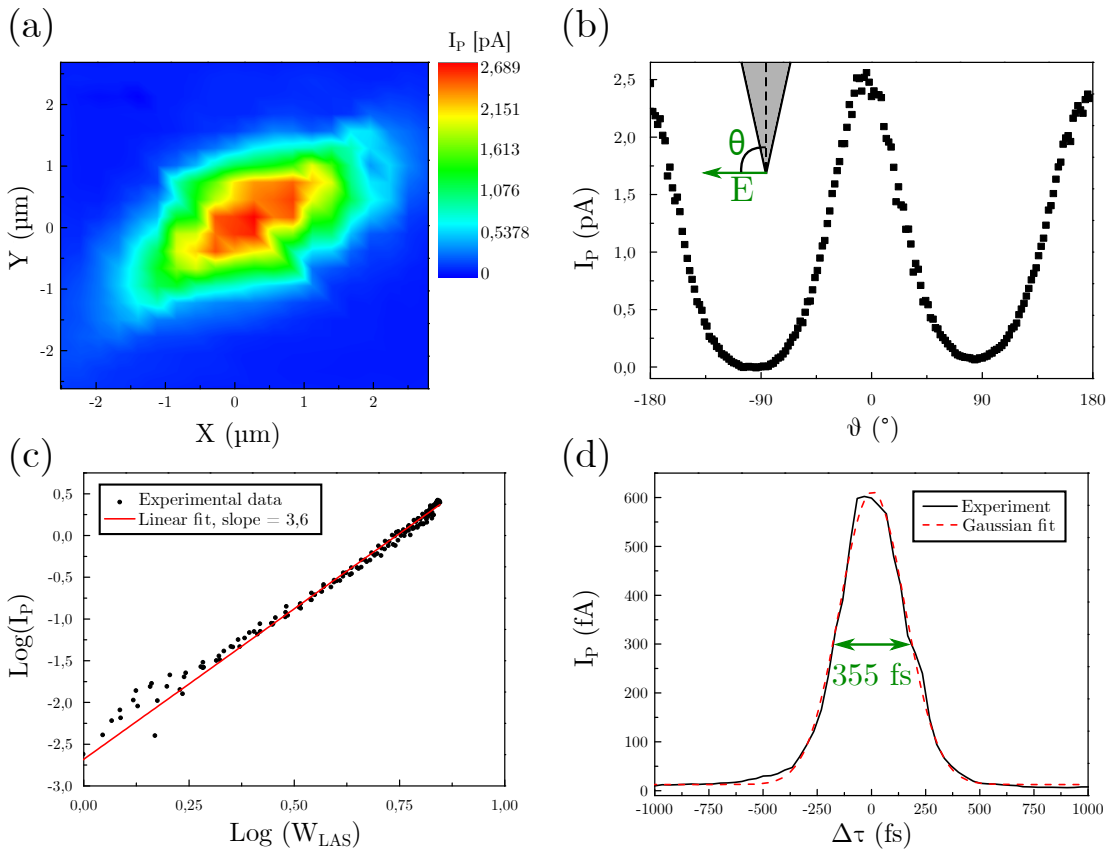

Figure XI: (a) Carte du courant de sonde mesurée par F1. (b) Dépendance du courant de sonde sur l'angle de polarisation. (c) Courant de sonde en fonction de la puissance moyenne du laser. (d) Mesure d'autocorrélation du courant de sonde.

de l'impulsion laser et de la non-linéarité du processus d'émission. Cela montre que la durée de l'impulsion électronique au niveau de la nanopointe est limitée par la durée de l'impulsion laser et que les effets de chauffage cumulatifs peuvent être ignorés.

La stabilité du courant de la sonde a été contrôlée après le *flash cleaning*. La courbe rouge de la figure XII représente l'évolution du courant de sonde mesurée pendant

9 heures. La courbe noire a été obtenue en optimisant la position du laser toutes les heures. L'encart montre l'évolution de la position du laser. Le fait que les deux courants décroissent de façon similaire est une confirmation que la principale raison de la dérive à long terme du courant de sonde est la contamination, comme pour un CFEG normal. Cependant, la stabilité du courant de sonde à court terme est plus élevée dans notre CFEG modifié. Outre le bombardement ionique, la migration des particules en surface

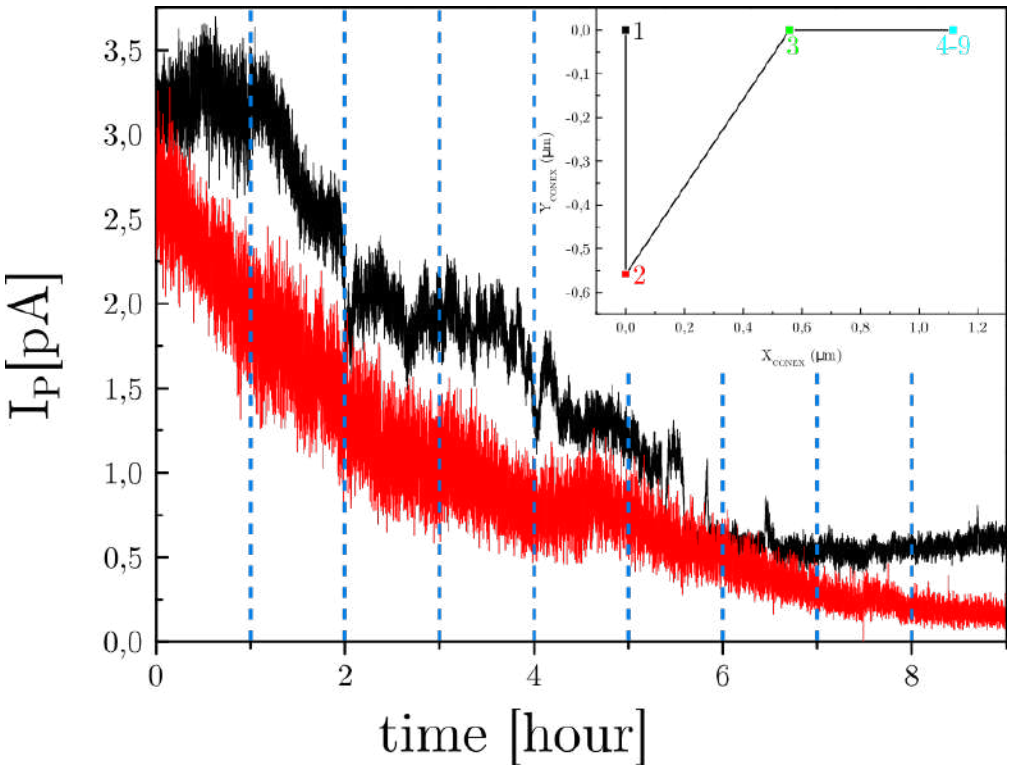

Figure XII: Mesures de stabilité du courant à long terme. La pointe a été nettoyé par *flash-cleaning* avant l'expérience. Encart: position du laser sur la nanopointe chaque heure.

et la transition des états de liaison des molécules adsorbées, typiques d'un CFEG conventionnel, l'instabilité de l'intensité du SHG représente également une cause de *flicker noise*. Avant de tester FemtoTEM sur des techniques TEM classiques, les propriétés

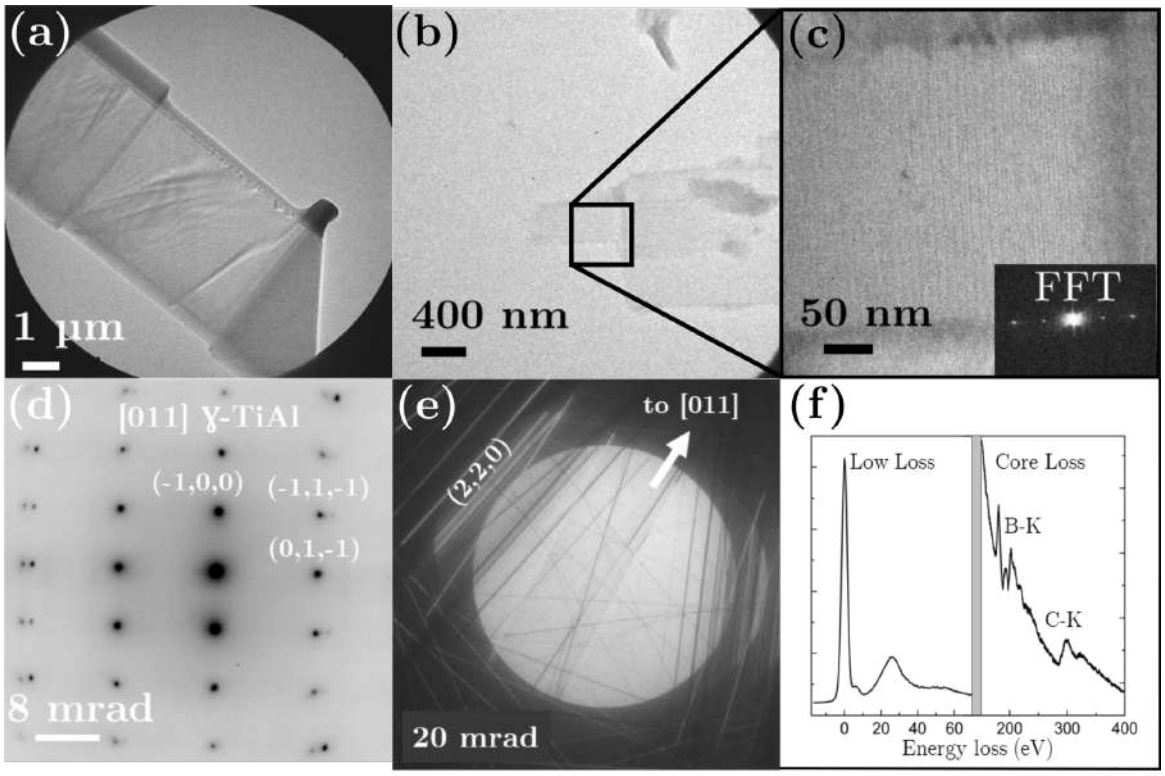

Figure XIII: (a) Image TEM ultra-rapide d'une lamelle de Si (taux de répétition $f = 1\,\mathrm{MHz}$, nombre d'électrons par pulse $N_{epp} = 12.5$, temps d'exposition $t_{exp} = 100\,\mathrm{s}$, binning 1). (b) et (c) montrent des images en haute résolution en mode ultra-rapides d'un cristal biologique de Catalase ($f = 2\,\mathrm{MHz}$, $N_{epp} = 11$, $t_{exp} = 150\,\mathrm{s}$, binning 4). (d) SAED en mode ultra-rapide d'un cristal de TiAl en phase γ orientée dans la direction [110] ($f = 1\,\mathrm{MHz}$, $N_{epp} = 12.5$, $t_{exp} = 150\,\mathrm{s}$, binning 2). (e) cliché CBED en mode ultra-rapide d'un cristal de Si orienté à proximité de la direction [110] ($f = 1\,\mathrm{MHz}$, $N_{epp} = 12.5$, $t_{exp} = 100\,\mathrm{s}$, binning 1). (f) EELS en mode ultra-rapides d'un cristal de nitrure de bore ($f = 2\,\mathrm{MHz}$, $N_{epp} = 6.25$, $t_{exp} = 1\,\mathrm{s}$ pour la région *low loss*, 60 s pour la région *core loss*).

d'optique électronique ont été optimisées. Avec une tension d'extraction $V_1 = 4\,\mathrm{kV}$, un rapport $R = V_2/V_1 = 5$ et à $f = 2\,\mathrm{MHz}$, le rayon du spot électronique varie de $1.4\,\mathrm{nm}$ (obtenu par une énergie par pulse laser $E_{PP} = 1.4\,\mathrm{nJ}$) à $2\,\mathrm{nm}$ ($E_{PP} = 3.75\,\mathrm{nJ}$). Pour

évaluer le potentiel du nouveau microscope électronique à transmission ultra-rapide (UTEM), nous avons calculé la brillance de la sonde électronique ultra-rapide. Dans le cas d'un UTEM, le faisceau d'électrons est pulsé à la même fréquence que le laser. Par conséquent, nous pouvons introduire la brillance moyennée dans le temps, définie comme suit :

$$B_{AVG} = \frac{f I_E}{(\pi r_0 \frac{\alpha}{2})^2} \tag{4.10}$$

ou f est le taux de répétition du laser, I_E le courant d'émission, r_0 la taille de la source électronique et α l'angle de divergence.

En prenant en compte un faisceau convergent et en négligeant les aberrations du condenseur, nous avons calculé une brillance de $2,2 \times 10^7\,\mathrm{Am^{-2}Sr^{-1}}$ à 1 MHz de taux de répétition. C'est la plus haute valeur jamais enregistrée dans les UTEM, jusqu'à présent. Nous avons également calculé la densité angulaire de courant dans notre CFEG-UTEM sous les mêmes conditions électro-optiques. Nous pourrons évaluer la taille de la source virtuelle, comprise entre 5 et 10 nm, comme dans un CFEG conventionnel.

La figure XIII présente les performances du CFEG-UTEM. Malgré la modification, la résolution en diffraction et en haute résolution est compatible avec le HF2000 d'origine. La résolution obtenue en mode ultra-rapide (0,9 nm) est légèrement inférieure à celle obtenue avec une émission en continu (0,2 nm). Cette différence est principalement due aux conditions de faible courant du mode d'opération ultra-rapide. En fait, en ce cas, le courant de sonde est réduit d'un facteur 10^6. Une étude sur le pic du Zero Loss (ZLP) du CFEG-UTEM a montré que la résolution d'énergie de FemtoTEM est fortement liée à la dynamique du gaz électronique et à la répulsion coulombienne au cours de la propagation des impulsions électroniques le long de la colonne. Une résolution d'énergie de 1 eV a été obtenue avec moins de 1 électron par pulse.

Chapitre 3 - Characterisation *in-situ* des propriétés spectro-temporelles des impulsions électronique ultra-courtes

Ce chapitre présente la première expérience de pompe-sonde ultra-rapide réalisée dans FemtoTEM. La résolution spectro-temporelle de l'instrument est caractérisée *in-situ* en une expérience de cross-corrélation électron-photon basée sur la détection du gain d'énergie des électrons. Nous résumons d'abord la description théorique de l'interaction entre une impulsion électronique ultra-courte et une impulsion laser femtoseconde, comme proposé par Park *et al.*. Ensuite, le modèle théorique est utilisé pour étudier l'influence de différents paramètres expérimentaux sur les spectres de gain. Nous extrayons ensuite le *chirp* des impulsions électroniques sous des conditions différentes par des cartes expérimentales de gain d'énergie. Finalement, des simulations numériques sont effectuées et comparées aux expériences pour déterminer la durée d'impulsion électronique.

3.1 Spectroscopie Electronique de gain d'énergie

La spectroscopie électronique de gain d'énergie (EEGS) est une technique UTEM qui caractérise les excitations optiques ou vibratoires de systèmes nanostructurés via la détection des électrons qui ont gagné de l'énergie lors de leur interaction avec l'échantillon. La première observation expérimentale d'un spectre EEG a été réalisée par Barwick *et al.*. En filtrant les électrons qui ont gagné l'énergie, ils ont réussi à imager le champ proche optique autour d'un nanotube de carbone multi-parois et des nanofils d'argent avec une résolution spatiale d'environ 5 nm et une résolution temporelle de

100 fs.

3.1.1 Interaction électron-photon

Le couplage entre électrons et photons dans l'espace libre est interdit en raison du décalage énergie-quantité de mouvement. Comme le montre la Figure XIV, un électron passant d'un état k_I à un état k_F subit une variation d'énergie et de quantité de mouvement ΔE et Δp. Le rapport $\Delta E/c\Delta p$ est la pente locale de la relation de dispersion mise en évidence par la ligne mauve de la Figure XIV. Un photon peut fournir l'énergie nécessaire, mais pas la quantité de mouvement associée en même temps (ou vice versa), comme le montre la ligne pointillée rouge. Afin de coupler électrons et photons, il est nécessaire de conserver l'énergie et la quantité de mouvement, et donc les deux pentes doivent être identiques. C'est le cas par exemple dans l'espace libre lorsque les électrons se déplacent plus rapidement que la lumière dans un milieu. C'est le cas du effet Tcherenkov (inverse). Les électrons et les photons peuvent se coupler dans l'espace libre au moyen d'un troisième système ou d'une particule comme dans l'effet Kapitza-Dirac. L'effet Smith-Purcell inverse est un autre exemple de couplage électron-photon via un troisième corps. Ce couplage peut également résulter du confinement de l'électron ou du champ électromagnétique. Par exemple, une onde électromagnétique incidente sur une nanostructure crée un champ électrique évanescent qui peut fournir l'impulsion supplémentaire nécessaire pour coupler électrons et photons. En particulier, la composante de champ parallèle au mouvement des électrons permet des interactions efficaces entre les électrons et la lumière.

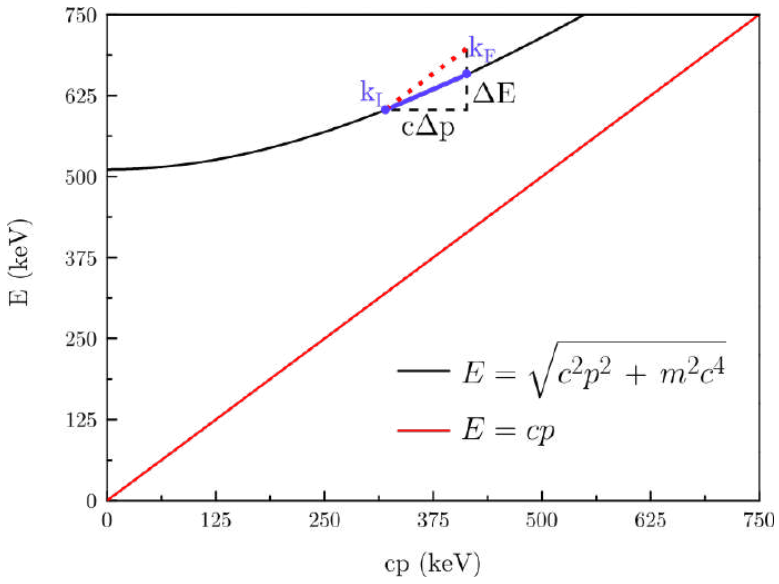

Figure XIV: relation de dispersion des électrons (noir) et photons (rouge).

3.1.2 EEGS : formalisme théorique

Le formalisme théorique décrit ci-après a été proposé par Park *et al.*. Ses principales conclusions sont en accord avec les travaux antérieurs de Garcia de Abajo et Kociak. Toutes les simulations numériques présentées ci après sont basées sur cette approche. Nous l'utilisons notamment pour évaluer l'effet des paramètres expérimentaux (c.-à-d. champ électrique incident du laser, taille de la sonde électronique, durée de l'impulsion électronique et laser) sur le spectre de gain. La description de l'interaction entre une impulsion électronique ultra courte et une impulsion laser femtoseconde est basée sur la résolution de l'équation de Schroedinger en fonction du temps. Les électrons interagissent avec le champ évanescent autour de la nanostructure et la population entière est répartie dans des bandes latérales séparées par l'énergie des photons incidents ($\hbar_{\omega p} = 2.4\,\mathrm{eV}$ dans ce cas). La probabilité d'occupation du n-ième état peut être

obtenue en intégrant sur toute l'enveloppe des impulsions électroniques :

$$P(n) = |<n|\Psi>|^2 = \int_{-\infty}^{+\infty} dz' |\Psi_n(z', +\infty)|^2 =$$
$$= \int_{-\infty}^{+\infty} dz' \left| g(z', -\infty) J_n\left(-\frac{e}{\hbar\omega_p} |\tilde{F}_z| \exp\left[-\frac{(z' + v_e\tau)^2}{4v_e^2\sigma_p^2} \right] \right) \right|^2 .$$

où J_n sont des fonctions de Bessel du premier type d'ordre n. v_e c'est la vitesse des électrons, $z' = z - v_e t$ et σ_p est l'écart type de la gaussien qui représente le profil temporel de l'impulsion laser. $g(z', -\infty)$ est la fonction d'enveloppe du pulse électronique avant l'interaction, $\tilde{F}_z$ est la transformé de Fourier de la composante z du champ électrique diffusé. τ est le retard établi entre pompe et sonde. Comme $|J_n(x)|^2 = |J_{-n}(x)|^2$, les probabilités d'émission et d'absorption de n photons sont les mêmes. Une expression analytique de la probabilité $P(n)$:

$$P(n) = \sum_{j=0}^{\infty} \sum_{k=0}^{\infty} C_j^n C_k^{n^*} (1 + S_{njk} R_\sigma^2)^{-1/2} \exp\left[-\frac{S_{njk} R_\tau^2}{2(1 + S_{njk} R_\sigma^2)} \right]$$

où

$$C_j^n = \frac{1}{(|n| + j)!(j)!} \left(\frac{e\tilde{F}_z}{2\hbar\omega_p} \right)^{n+j} \left(-\frac{e\tilde{F}_z^*}{2\hbar\omega_p} \right)^j$$
$$S_{njk} = n + j + k$$
$$R_\sigma = \frac{\sigma_e}{\sigma_p}$$
$$R_\tau = \frac{\tau}{\sigma_p}$$

σ_e est l'écart type de la gaussien qui représente le profil temporel du pulse électronique. EEGS est une technique très puissante permettant d'obtenir des informations sur le champ électrique local à proximité d'un système nanométrique éclairé par une impulsion laser. Cependant, d'autres des paramètres tels que la durée de l'impulsion électronique et la taille du point de l'électron modifient le spectre.

3.1.3 Influence des paramétrés expérimentaux sur le spectres de gain

Des simulations ont été effectuées en exploitant l'expression analytique de la probabilitè definie dans le dernier paragraph. Un nanocylindre de tungstène (rayon = 200 nm) a été envisagé. La spread en énergie du faisceau électronique a été fixée à 1.1 eV. La durée de l'impulsion laser est de 280 fs. Nous avons étudié l'influence de la force du champ électrique du laser, de la durée de l'impulsion électronique et de la taille du spot électronique. L'intensité du laser incident détermine la magnitude du champ évanescent créé autour de la nanostructure qui se couple avec les électrons libres. La figure XV (a) montre comment le spectre de gain est modifié en fonction de la force du champ électrique incident du laser. Si la nanostructure n'est pas éclairée, aucune interaction électron-photon ne se produit. Les électrons ni perdent ni gagnent énergie et leur distribution d'énergie, en absence du échantillon, est une ZLP (courbe bleue). Intensité laser modérée ($I_L = 8.3 \cdot 10^6\,\mathrm{W/cm^2}$, $E_0 = 0.025\,\mathrm{V/nm}$), le champ électrique diffusé a une composante non nulle le long de la direction de propagation de l'électron et le couplage devient possible. En augmentant l'intensité du laser, la population de photons dispersés augmente et l'absorption (ou l'émission) multiple de photons est plus probable, comme le confirme l'expression analytique de $P(n)$. Dans ce cas, les bandes latérales avec une énergie sont occupées. La figure XV(b) montre comment la durée d'impulsion électronique σ_e affecte les gains d'énergie des électrons. Les modifications des spectres sont liées à la fraction d'électrons qui interagit avec l'impulsion laser 280 fs. Cette fraction devient de plus en plus petite à mesure que σ_e augmente. La figure XV (c) montre l'importance de la taille du spot. 5 tailles de spots différents ont été prises en compte. Ces dimensions se réfèrent à la FWHM d'un profil d'intensité spatiale gaussien. Afin d'étudier l'influence de la taille du spot en gardant la même intensité de champ électrique laser, nous avons supposé que le profil spatial gaussien de l'électron

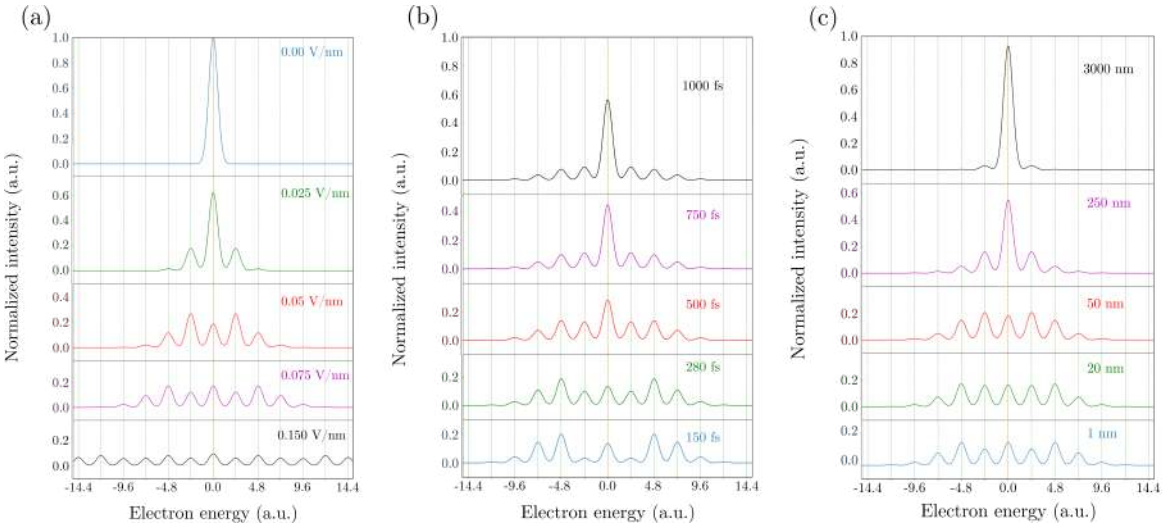

Figure XV: Effet de la variation des paramètres expérimentaux sur EEGS : (a) champ électrique incident , (b) durée de l'impulsion électronique, (c) taille du spot électronique.

a sa valeur moyenne à 5 nm de la surface du cylindre. En utilisant une petite taille de sonde électronique (1 nm), il est possible d'obtenir une empreinte du champ électrique à une certaine position. Cela permet de cartographier le champ évanescent autour de la nanostructure. L'augmentation de la taille des spots d'électrons provoque une perte d'informations. L'extension spatiale du champ électrique étant limitée par la géométrie de la nanostructure, un grand spot électronique recueille plusieurs contributions de régions où le champ électrique est nul. Ceci explique le très faible signal EEGS pour un spot électronique de $3\,\mu$m.

3.2 Caractérisation temporelle des impulsions électronique

Outre la détection du champ électrique et l'étude des excitations optiques dans les nanostructures, la spectroscopie EEG permet la caractérisation temporelle d'un pa-

quet d'électron. Après l'émission, dans une impulsion électronique se produit un *chirp*, c'est-à-dire une corrélation énergie-temps, car les électrons à haute énergie se propagent en avance, alors que ceux à basse énergie sont en retard. Cet effet est renforcé dans les impulsions contenant un nombre élevé d'électrons en raison de la répulsion coulombienne parmi les particules. Contrôler le *chirp* d'électrons permet de modifier et d'améliorer la résolution spatio-temporelle et spectrale de l'instrument. EEGS permet de déterminer le *chirp* des impulsions d'électrons, étant donné que l'approche pompe-sonde stroboscopique permet de sélectionner temporellement des électrons et d'obtenir des informations sur leur distribution d'énergie. En reconstruisant une carte des spectres des électrons à différents retards temporels, il est possible de visualiser le chirp comme la pente des cartes temps-énergie.

3.2.1 Caractérisation des impulsions électronique *chirpées*

Afin de caractériser temporellement l'impulsion électronique et d'évaluer son chirp, une lame MET a été préparé par Focused Ion Beam (FIB) en coupant l'extrémité d'un nanopointe MET traditionnel en tungstène orienté ¡310¿ et en la positionnant sur un grille FIB, comme illustré à la Figure XVI. Une fois optimisée la position de l'échantillon dans FemtoTEM pour visualiser correctement la nanopointe, le faisceau laser a été aligné et focalisé sur l'apex de la pointe à l'aide d'une CCD installée sur la breadboard optique contenant le système CL-I qui enregistre l'image du échantillon créée par le miroir parabolique inséré entre les pièces polaires. La longueur d'onde de la pompe est de 515 nm et la puissance moyenne des impulsions mesurée sur le banc optique était de 595 mW. Le taux de répétition a été fixé à 2 MHz. FemtoTEM a été réglé en mode diffraction. La position du faisceau d'électrons par rapport à la nanopointe a été optimisée en regardant l'image phantom à l'intérieur du spot transmis. Une acquisition

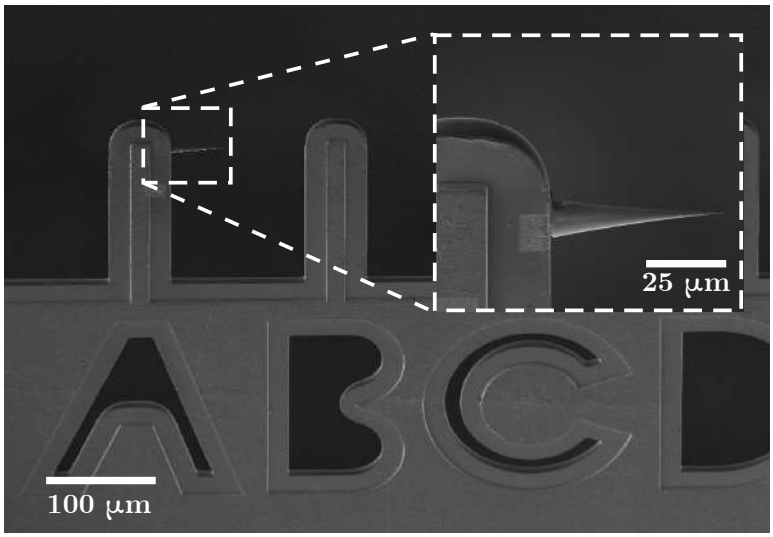

Figure XVI: nanopointe de tungstène orientée ¡310¿ soudée sur une grille FIB.

séquentielle de 52 spectres EEG avec un pas de 50 fs a été entrecoupée du même nombre d'acquisitions de pic de Zero Loss (ZLP) afin de corriger, à posteriori, une dérive du spectromètre. Chaque spectre a été acquis pendant t = 10 s. L'ouverture d'entrée du prisme était de 1 mm et la dispersion d'énergie de 0,05 eV/ canal. Les spectres EEG ont été acquis pour N_{epp} = 0.59, 2.34, 3.28 et 4. La figure XVII présente les spectres électroniques absolus (colonne de gauche) et des différences (colonne centrale) en fonction du temps de propagation pour le cas $N_{epp} = 4$. Les spectres de différence ont été obtenus en soustrayant du signal EEGS un spectre acquis avec un retard important (c'est-à-dire un ZLP). Le profil ondulé est dû aux instabilités du spectromètre qui n'ont été que partiellement corrigées. Dans les spectres absolus, la variation de la population électronique en fonction du retard est clairement visible : lorsque les impulsions électroniques et laser sont synchronisés, le ZLP s'épuise et les électrons peuplent les bandes latérales. Ceci explique la forte intensité négative dans les spectres de différence. Le coefficient de chirp des électrons $\partial \bar{t_E}/\partial E$ est visible dans les deux cas

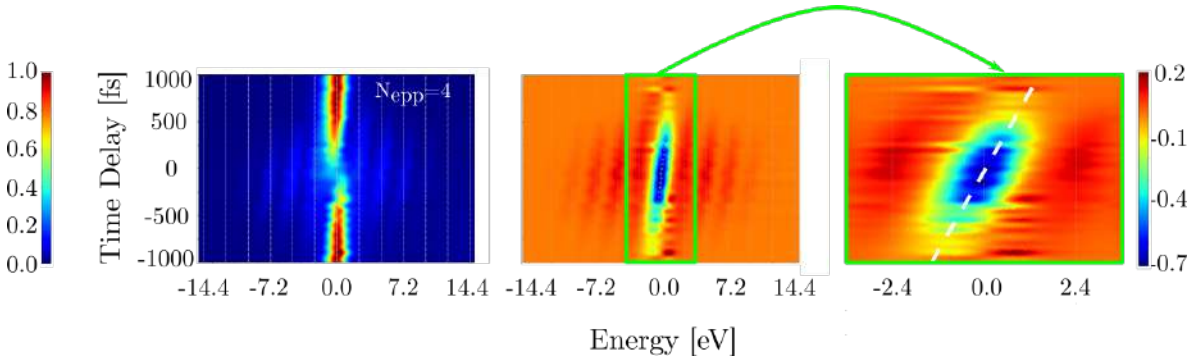

Figure XVII: Cartes de spectres de gain absolu (gauche) et de différence (centre) acquis avec 4 électrons dans la sonde. L'image de droite montre plus en détail le *chirp* du pulse électronique.

et est mis en évidence dans la Figure XVII (colonne de droite) par des lignes pointillées blanches. Une fois que le *chirp* des électrons a été évaluée, il est possible d'utiliser le formalisme théorique de Park *et al.* pour simuler les cartes expérimentales de la figure XVII et caractériser l'impulsion électronique. Le paragraphe suivant présente les résultats de ces simulations. Les spectres EEG ont été simulés pour $N_{epp} = 0.59$, 2.34, 3.28 et 4 en prenant également en compte les valeurs du chirp électronique. La nanopointe de tungstène utilisée dans l'expérience a été approché par un nanocylindre de rayon a = 200 nm. Nous avons supposé que le faisceau d'électrons pulsés de 280 fs en FWHM passe à 15 nm de la surface du cylindre. Le champ électrique laser incident est $E_0 = 0.075\,\mathrm{V/nm}$, correspondant à une intensité d'environ $7.5 \cdot 10^8\,\mathrm{W/cm^2}$. Le champ électrique au tour du cylindre est calculé à partir de la théorie de Mie. La figure XVIII présente la comparaison entre les cartes EEGS expérimentales et simulées dans le cas $N_{epp} = 0.59$. Pour évaluer la précision de la simulation, différents sections de la carte ainsi que le signal intégré ont été extraits et les résultats sont présentés dans la figure XIX. Les courbes bleues représentent les résultats expérimentaux et les courbes

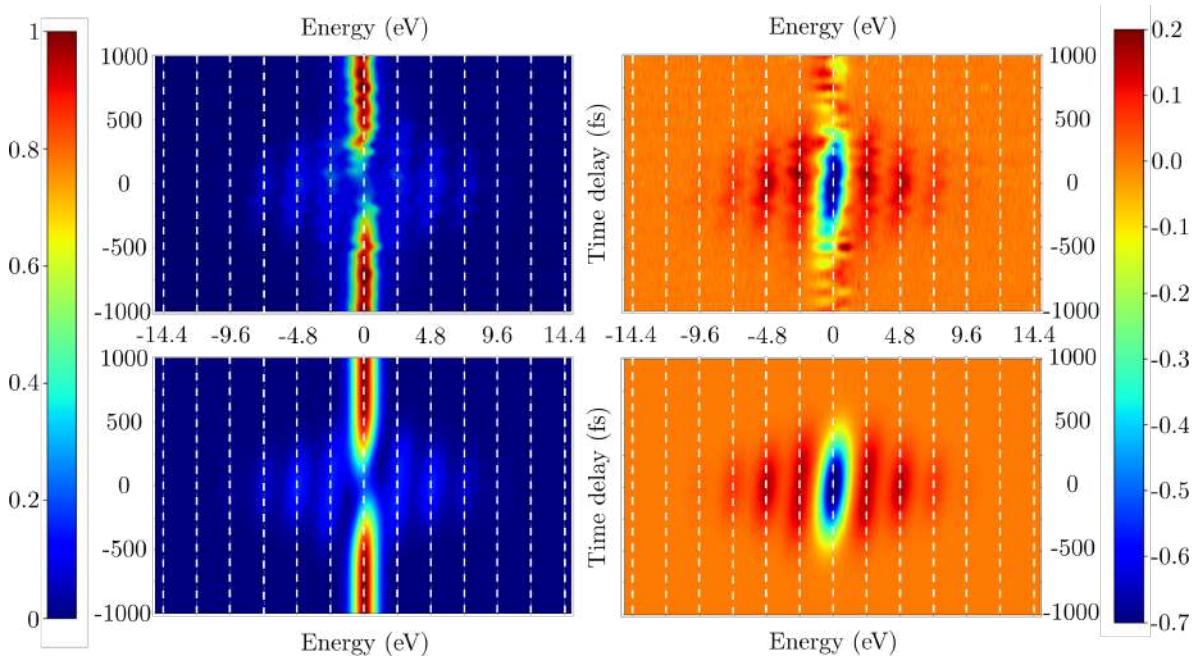

Figure XVIII: Comparaison entre les cartes EEGS expérimentales (rangée supérieure) et simulées (rangée inférieure). L'échelle d'intensité sur le côté gauche (droit) fait référence aux cartes absolues (de différence) EEGS. Le cas avec $N_{epp} = 0.59$ a été rapporté.

orange les simulés. On peut noter que malgré la différence de forme entre l'échantillon et le nanocylindre simulé, les deux courbes sont en bon accord. Nous pouvons voir que pour le cas $N_{epp} = 0.59$ la durée en FWHM est 400 fs avec une précision de 6%. En augmentant légèrement le nombre d'électrons par pulse, nous avons déterminé une augmentation d'environ 31% de la durée dans le cas de 4 électrons par impulsion.

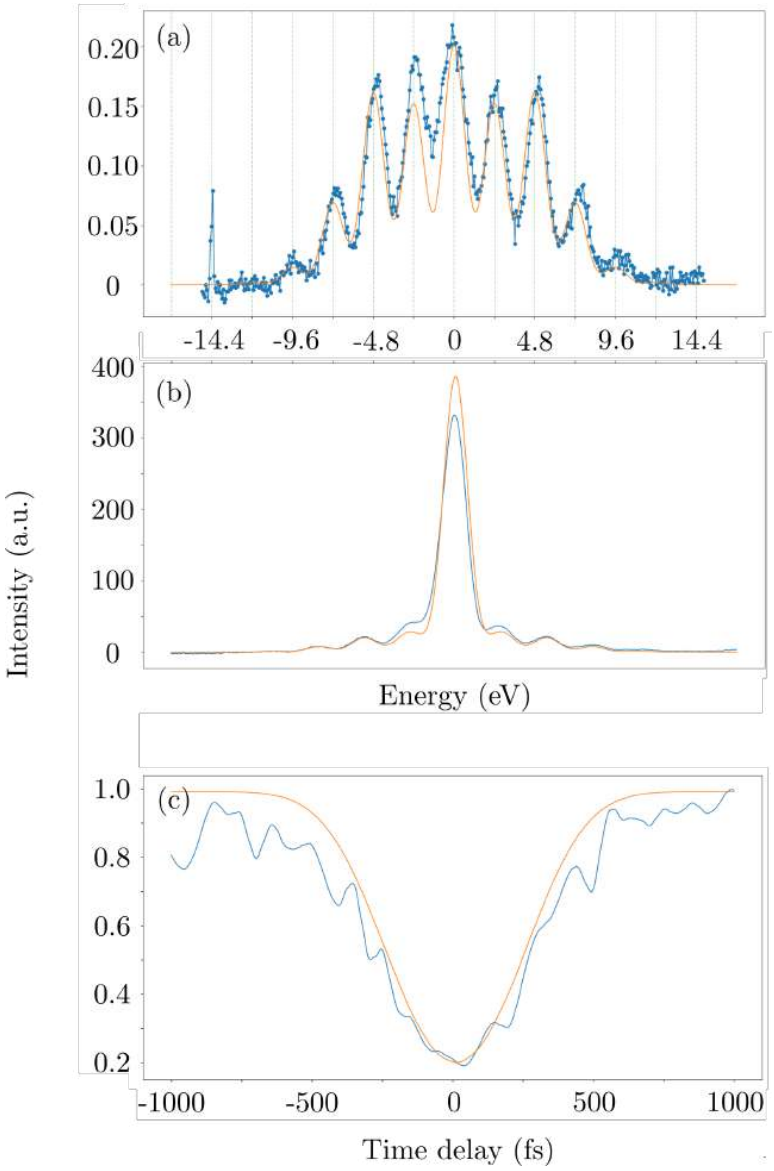

Figure XIX: Comparaison entre les données expérimentales (bleu) et simulées (orange). (a) Spectre EEG à $\tau = 0\,\text{fs}$. (b) Carte EEGS intégrée sur l'axe des temps. L'échelle verticale indique la valeur de l'intégrale en unités arbitraires pour les différentes énergies. (c) Profil de carte à E = 0 eV. Dans les deux cas (a) et (c) les échelles verticales représentent le signal EEGS normalisé en unités arbitraires.

Chapitre 4 - Vers l'holographie électronique hors-axe dans FemtoTEM

Dans le dernier chapitre, les perspectives sur l'holographie électronique ultra-rapide (UEH) utilisant la configuration hors-axe sont discutées. Au début, les aspects pratiques de la holographie électronique hors-axe (c'est-à-dire la cohérence des sources d'électrons, le bruit, les instabilités, l'éclairage) réalisée avec un faisceau d'électrons continu sera donnée. Par la suite, les obstacles à la réalisation d'une holographie électronique utilisant des impulsions électroniques ultra-courtes seront présentés et des solutions possibles seront discutées. Enfin, nous montrerons les résultats des premières expériences réalisées avec le microscope FemtoTEM.

4.1 Conditions pratiques et limites de détection en holographie électronique conventionnelle hors axe

Afin de produire des hologrammes électroniques avec un contraste optimal, une source d'électrons très cohérente est nécessaire. Les FEG, avec leur haute brillance, sont les sources optimales. En effet, grâce à leur petite taille de source, ils peuvent émettre un faisceau d'électrons à haute cohérence spatiale, comme décrit par le théorème de van Cittert-Zernike. Ce faisceau de haute qualité peut ensuite être utilisé pour éclairer à la fois l'échantillon et une zone de vide, appelés respectivement faisceau image et faisceau de référence. L'hologramme, généré par la superposition cohérente des deux faisceaux, est alors obtenu grâce à un biprisme électronique (EB). La figure XX montre un hologramme acquis sans échantillon sur lequel des paramètres utiles sont rapportés. La largeur de l'hologramme w correspond à la taille de la zone d'interférence et s à l'espacement des franges d'interférence. Les deux peuvent être réglés en ajustant la

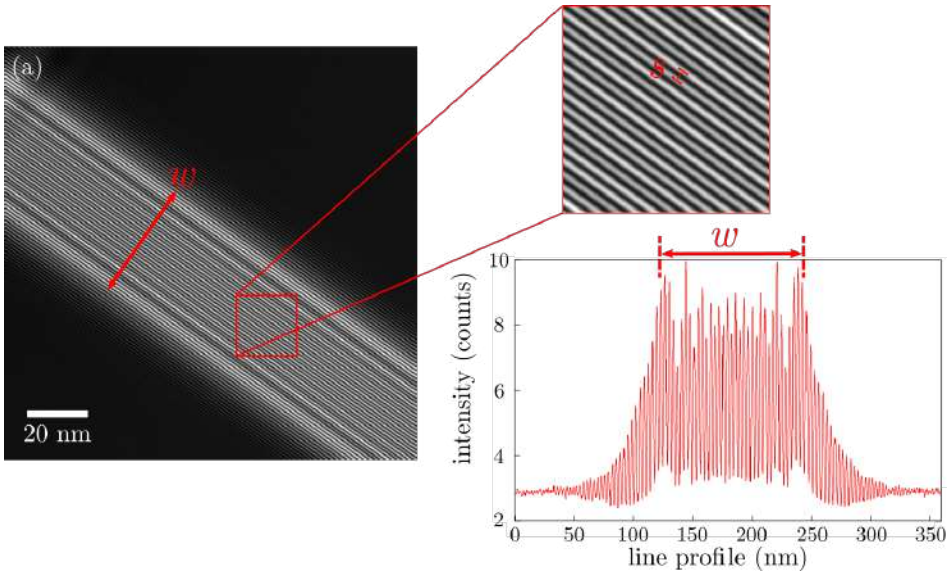

Figure XX: (a) Hologramme électronique ultra-rapide hors-axe acquis dans le vide. Encart: FFT de l'hologramme. Les cercles verts représentent le masque de résolution de 1 nm dans l'espace de Fourier. b) Carte de la phase reconstruite. Conditions expérimentales: temps d'exposition 150 s, $W_{LAS} = 9.5\,\mathrm{mW}$, $f = 2\,\mathrm{MHz}$, $N_{epp} \sim 11$, binning 4

tension du biprisme et la distance entre l'image et les plans du biprisme. Pour une distance fixe d, en augmentant la tension du biprisme, la largeur de l'hologramme augmente tandis que la distance entre les franges diminue. Cependant, ils peuvent également être modifiés indépendamment en utilisant une configuration à double biprisme. La figure de mérite d'un hologramme est le contraste des franges:

$$C = \frac{I_{max} - I_{min}}{I_{max} + I_{min}}$$

où I_{max} et I_{min} correspondent respectivement aux intensités maximale et minimale des franges. Des valeurs utiles de contraste, c'est-à-dire permettant d'extraire une phase avec un rapport signal sur bruit suffisant et une bonne résolution spatiale, sont communément acceptés pour être plus élevé de 15%. Les hologrammes électroniques sont

enregistrés à l'aide de caméras pixelisées et leur Fonction de Transfert de Modulation (MTF), ainsi que leur efficacité détective quantique (DQE) devront également être prises en compte dans la mesure du contraste. De plus, le nombre d'électrons par pixel N_{epx} et le temps d'exposition sont fondamentaux pour optimiser le contraste de l'hologramme.

4.1.1 Figures de mérite d'un hologramme électronique

L'holographie électronique est utilisée pour cartographier de manière quantitative la phase du faisceau image modifiée par l'interaction avec l'échantillon. Le bruit du faisceau d'électrons peut être décrit par une distribution de Poisson, connue sous le nom de *shot noise*. L'écart type (défini pour une certaine fréquence $\mathbf{g}$) d'une phase reconstruite peut s'écrire comme suit :

$$\sigma_\phi = \sqrt{\frac{2}{DQE \cdot C^2 \cdot N_{epx}}}.$$

Une autre figure de mérite de la qualité de l'hologramme rencontré dans la littérature est la limite de détection de phase, c'est-à-dire la plus petite différence de phase détectable :

$$\delta\phi = SNR\sqrt{\frac{2}{DQE \cdot C^2 \cdot N_{epx}}}$$

où le rapport signal sur bruit souhaité est un paramètre donné. Pour déterminer correctement le résultat d'une expérience sans ambiguïté, il est généralement admis qu'un SNR compris entre 3 et 10 est nécessaire. Comme le contraste des franges contribue à $\delta\phi$ avec un exposant 2 dans la racine carrée, il joue un rôle clé dans la limite de détection de phase par rapport aux autres paramètres. Une expression utile du contraste utilisé pour prendre en compte toutes ces contributions est :

$$C = C_{coh}C_{inel}C_{inst}MTF$$

où C_{inst}, C_{inel}, C_{coh} et MTF correspondent respectivement l'influence des instabilités, de la diffusion inélastique et de la cohérence partielle. Les MTF représentent la fonction de transfert de modulation du détecteur.
Dans le contexte des expériences MET ultra-rapides, le nombre d'électrons par pixel dans l'expression de $\delta\phi$ peut être déterminé par la relation:

$$N_{epx} = N_{ppx} \cdot N \cdot t_{exp}$$

où f est le taux de répétition du laser, t_{exp} le temps d'exposition et $N_{ppx} = \frac{N_{epp}}{N_{px}}$ le nombre d'électrons par pulse par pixel. En substituant l'expression de N_{epx} dans le définition de $\delta\phi$, on obtient:

$$\delta\phi = \frac{SNR}{C_{coh}\, C_{inst}\, MTF} \sqrt{\frac{2 \cdot N_{px}}{DQE\, N_{epp}\, f\, t_{exp}}}$$

où le contraste a été exprimé comme dans la précédente expression phénoménologique. La dernière expression de $\delta\phi$ met en évidence les différents paramètres affectant le contraste des hologrammes acquis avec des impulsions laser femtosecondes dans un UTEM.

4.1.2 Optimisation

Parmi les facteurs dont dépend le contraste (et donc la limite de détection de phase), la cohérence partielle doit être traitée avec une attention particulière lors d'une expérience d'holographie électronique. La longueur de cohérence d'un faisceau d'électrons sur un plan optique donné dépend du degré initial de cohérence spatiale de la source, c'est-à-dire de la brillance ainsi que des conditions d'éclairage. Compte tenu de la symétrie du biprisme électronique, la longueur de cohérence ne doit être optimisée que dans la direction de chevauchement du faisceau, c'est-à-dire perpendiculairement à l'axe du

biprisme. En conséquence, il est bien connu qu'un faisceau elliptique (un rapport optimal entre le petit axe et le grand axe est d'environ 0.1) peut être utilisé pour optimiser la longueur de cohérence dans la direction souhaitée. De plus, la diffusion inélastique aux électrons peut être optimisée avec une préparation d'échantillon dédiée et l'influence de la FTM dépend du type et des réglages du détecteur. Les instabilités instrumentales sont prépondérantes dans la UTEM. Ils doivent être traités avec un soin particulier et éventuellement optimisés en recourant à l'acquisition de *images stacks* (pile d'images), dans lesquelles chaque hologramme est acquis avec un temps d'exposition court. Ensuite, un post-traitement numérique réaligne les franges permet de reconstruire une figure d'interférence avec un rapport signal sur bruit élevé. En raison du courant de sonde réduit dans les UTEM, le choix du temps d'exposition optimal est crucial en holographie électronique. Les durées d'acquisition en émission continue sont généralement de l'ordre de la seconde ou de la dizaine de secondes pour les expériences nécessitant un rapport signal / bruit élevé. Cependant, dans des conditions semblables à celles d'une faible dose et dans nos conditions, les temps d'exposition compris entre 100 et 150 s sont optimaux. Le choix de la tension optimale du biprisme est limité par des temps d'exposition longs et donc par les instabilités. Les tensions utiles du biprisme se situent dans l'intervalle allant de 20 V à 35 V. La figure XXI montre un hologramme électronique acquis sous conditions optimales, c'est-à-dire 35 V, 150 s de temps d'exposition et 200 kX de grandissement total. Le microscope a été réglé en mode ZOOM (équivalent à la microsonde ou au mode TEM dans les microscopes FEI et Jeol, respectivement). Une ouverture de condenseur de 100 μm et un éclairage elliptique avec un rapport optimal a été utilisé. En utilisant les valeurs optimales de temps d'acquisition et de tension de biprisme déterminées précédemment, nous avons acquis des hologrammes hors-axe avec impulsions électroniques ultra-courtes sur un

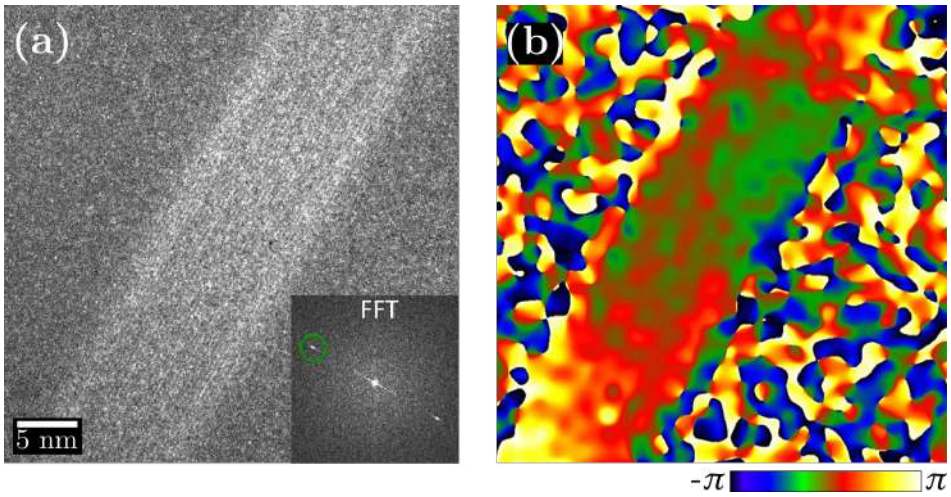

Figure XXI: (a) Hologramme électronique ultra-rapide hors-axe acquis dans le vide. Encart: FFT de l'hologramme. Les cercles verts représentent le masque de résolution de 1 nm dans l'espace de Fourier. b) Carte de la phase reconstruite. Conditions expérimentales: temps d'exposition 150 s, $W_{LAS} = 9.5\,\mathrm{mW}$, $f = 2\,\mathrm{MHz}$, $N_{epp} \sim 11$, binning 4

cube d'oxyde de manganèse (MgO) à titre de test. Les données brutes et le processus de reconstruction de phase sont reportés à la figure XXII. En raison du faible courant de sonde de notre UTEM cohérent et malgré la brillance élevée, l'holographie électronique hors axe reste très difficile.

4.3 Vers l'holographie électronique ultra-rapide

L'utilisation des *image stacks* peut contribuer à réduire l'effet des instabilités. Il consiste en une acquisition séquentielle de plusieurs hologrammes avec des temps d'exposition courts permettant de corriger l'effet des instabilités. Cependant, en raison de cette dernière, le simple fait d'additionner toutes les franges de l'hologramme n'améliorerait pas le contraste. L'hologramme résultant correspond à un standard acquis avec un temps total d'exposition égal à $t_{exp} \cdot N_{holo}$, où t_{exp} est le temps d'acquisition de chaque

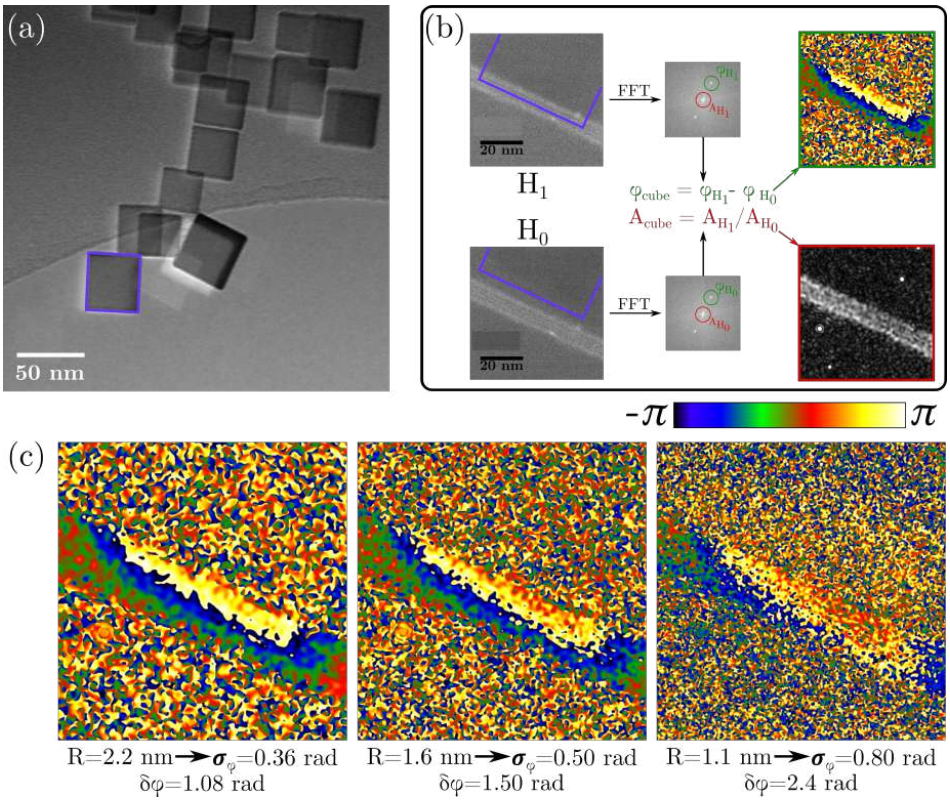

Figure XXII: Reconstruction de la phase d'un cube de MgO par holographie électronique. (a) Image MET de cubes de MgO. (b) Reconstruction de phase et amplitude en utilisant l'hologramme de référence (H_0) e celui du échantillon (H_1). (c) Effet de la taille de masque sur l'écart type de la phase électronique dans l'espace de Fourier. Les limites de détection ont été calculées sous conditions idéales ($SNR = 1$, $C_{inst} = 1$).

hologramme et N_{holo} le nombre d'hologrammes dans le *stack*. Pour exploiter correctement les piles d'hologrammes, un processus de réalignement est nécessaire. Le traitement des données a été effectué à l'aide de scripts développés au CEMES par Christophe Gatel. Tout d'abord, les pixels morts sont filtrés puis remplacés par l'intensité moyenne des pixels adjacents afin d'éviter des artefacts lors de la reconstruction de la phase électronique. Afin de prendre en charge les instabilités mécaniques du biprisme entre

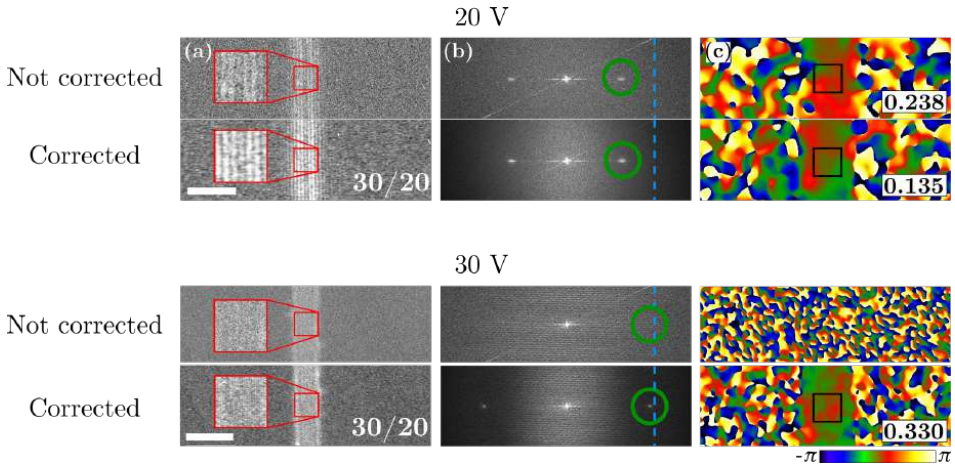

Figure XXIII: Effet de la correction des instabilités des hologrammes pour deux tensions différentes du biprisme. (a) Les nombres indiquent le nombre d'images dans le *stack* et le temps d'acquisition de chacune d'elles (en seconde). Dans les cas 20 V et 30 V, les échelles sont respectivement de 10 et 20 nm. (b) *Power spectrum* des hologrammes. Les cercles verts représentent un masque de résolution de 2.5 nm dans l'espace de Fourier. La ligne pointillée bleue indique la position de la fréquence spatial $(4 \cdot \text{pixel})^{-1}$. (c) Phases reconstruites. Les écart-type calculés à l'intérieur du carré noir sont affichés. Conditions expérimentales : $W_{LAS} = 8\,\text{mW}$, $f = 2\,\text{MHz}$, $N_{epp} \sim 6$, binning 2. Grandissement : 200 kX.

chaque hologramme, un premier alignement d'image est effectué en utilisant la position de la frange de Fresnel du biprisme électrostatique. Ensuite, pour corriger les instabilités du faisceau, les franges de l'hologramme sont alignées en comparant leurs positions. Dans chaque hologramme individuel de la pile, la phase est déterminée et comparée à celle sélectionnée comme référence. La différence de phase est ensuite convertie en un nombre de pixels utilisé pour réaligner chaque hologramme individuel par rapport à celui de référence. Une fois terminé ces processus d'alignement, tous les hologrammes individuels sont enfin additionnés (figure XXIII). La figure XXIV montre l'effet du temps d'exposition de l'hologramme et du seuil des instabilités dans le

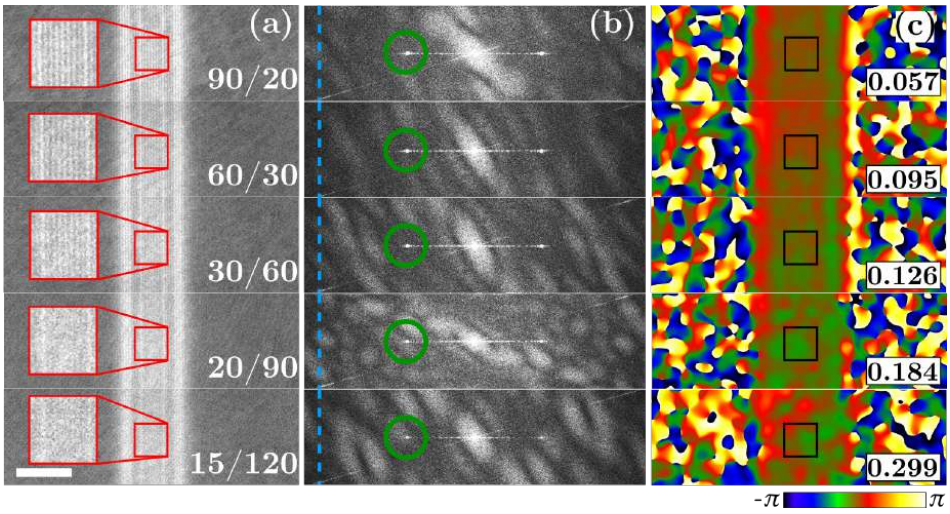

Figure XXIV: L'effet du temps d'exposition de chaque hologramme individuel dans le stack d'hologrammes corrigés. (a) Les nombres indiquent le nombre d'images dans le *stack* et le temps d'acquisitions individuelles de chaque hologramme. La durée totale d'exposition reste constante. Échelle : 10 nm. (b) *Power spectrum* des hologrammes. Les cercles verts représentent le masque de résolution 2.5 nm dans l'espace de Fourier. La ligne pointillée bleue montre la position de la fréquence spatial $(4 \cdot \text{pixel})^{-1}$. (c) Phases reconstruites. Les écarts-types calculés à l'intérieur du carré noir sont affichés. Conditions expérimentales : $W_{LAS} = 8\,\text{mW}$, $f = 2\,\text{MHz}$, $N_{epp} \sim 6$, binning 2. Grandissement : 400 kX. Tension du biprisme : 30 V.

contraste de l'hologramme. Le temps total d'exposition reste constant à 1800 s. Nous pouvons clairement voir qu'en augmentant le temps d'acquisition individuel, l'effet des instabilités devient plus important. Les temps d'acquisition individuels entre 20 et 30 secondes semblent être optimaux. La figure XXV affiche trois hologrammes corrigés pour différentes tensions de biprisme. En comparant les hologrammes acquis dans les mêmes conditions d'optique électronique mais avec un temps total d'exposition différent (150 s pour l'hologramme unique non corrigé et 20 s pour chacun des 90 hologrammes composant la pile), on constate une amélioration du 40% et 64% de l'écart types de la phase pour les cas 30 et 35 V, respectivement. De plus, on peut remarquer qu'en

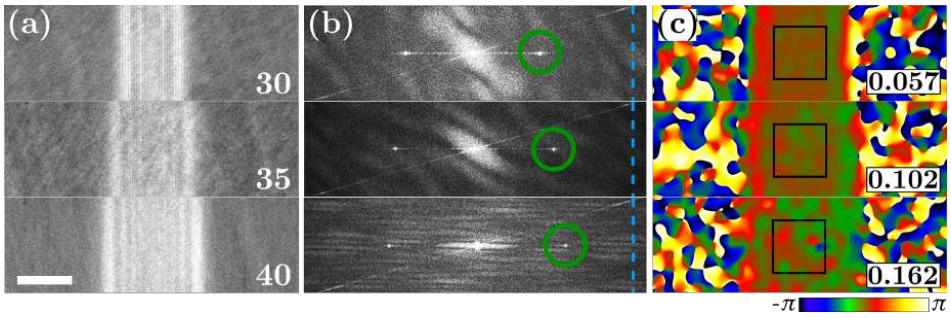

Figure XXV:L'effet de la tension de biprisme dans l'hologramme corrigé et sommé. (a) Les nombres indiquent la tension du biprisme (en volt). Échelle : 10 nm. (b) *Power spectrum* des hologrammes. Les cercles représentent le masque de résolution 2.5 nm dans l'espace de Fourier. La ligne pointillée bleue indique la position de la fréquence spatial $(4 \cdot \text{pixel})^{-1}$. (c) Phases reconstruites. Les écarts-types calculés à l'intérieur du carré noir sont affichés. Des *stacks* de 90 hologrammes et 20 s de temps d'exposition ont été acquises. Conditions expérimentales : $W_{LAS} = 8\,\text{mW}$, $f = 2\,\text{MHz}$, $N_{epp} \sim 6$, binning 2. Grandissement : 400 kX.

utilisant une tension de biprisme de 40 V, l'écart type est encore plus petit que la valeur obtenue pour le cas de 35 V avec $t_{exp} = 150\,\text{s}$ pour la même résolution spatiale dans la phase reconstruite.

Conclusions et perspectives

Depuis sa naissance, la microscopie électronique en transmission à résolution temporelle a permis d'explorer le monde à l'échelle nanométrique dans divers domaines scientifiques tels que la nanomécanique, le nanomagnétisme, chimie, biologie et nano-optique. Le développement de FemtoTEM a conduit à la création d'un laboratoire commun entre le CEMES-CNRS et Hitachi High Technologies Corporation qui a démarré très récemment en juillet 2018. Grâce à ce partenariat, un transfert de la technologie ultra-rapide de l'ancien HF2000 à un nouveau microscope, le FE-TEM HHT HF3300 à 300 kV est

prévu pour 2019. Ça renforcera les applications de l'UTEM cohérent vers de nouvelles techniques telles que l'holographie électronique hors-axe résolue en temps, qui sera fortement améliorée grâce à la mise en œuvre d'un contrôle automatisé, comme cela a déjà été fait dans le CEMES, en utilisant même génération de microscopes HF (I2TEM).

Acknowledgement

I always tried to picture the moment I'd have written this final part and I didn't know if I wanted to write it in Italian, in English or in French. So, finally I decided to mix them up in a text worthy of *Salvatore*, a peculiar character from *Il nome della rosa*, who speaks his unique language.

I would say that I have three mentors and I'd love to spend a few lines to thanks them individually.

La prima persona che voglio ringraziare è Simona Boninelli. Simona è una delle persone migliori che io conosca. Lei si è spesa tantissimo per me fin dalla nostra conoscenza e continua a farlo a distanza di anni. Simona, tu mi hai insegnato tanto e non intendo solo a livello scientifico. Hai creduto in me e nelle mie capacità fin dai primi momenti che abbiamo trascorso insieme. "Se continui a voler fare microscopia dopo aver ascoltato questo seminario, allora siamo sulla strada giusta!". Ti riferivi ad un seminario tenuto a Catania da Giulio Pozzi che ha mostrato le meraviglie dell'olografia elettronica. Il fatto di poter vedere un campo (elettrico o magnetico che fosse) attraverso il TEM mi ha assolutamente sorpreso. Tu mi hai insegnato a non mollare mai e l'hai fatto in modo così delicato, quasi intangibile...portandomi a *le pic des trois seigneurs*. Una riposante scalata di 8 ore, dove indossavo un paio di converse, il cappello della *Bubba Gump Shrimp Company* ed avevamo con noi una scorta di acqua insufficiente anche per

un giro del quartiere. La neve (a Luglio!) ci salvò ed io non dimenticai mai la lezione impartitami da te e dalla montagna. Il tuo essere orgogliosa di me e le tue belle parole sono sempre state di ispirazione. "COLLEGA!!!" è così che mi hai chiamato poche ore dopo la difesa della tesi. Grazie Simo. Grazie per avermi fatto conoscere Toulouse, il CEMES e tutto quello che è venuto di conseguenza.

Je dois remercier mes deux autres mentors ensemble. Parce-que on a bossè ensemble, on a fini le parcours du projet FemtoTEM ensemble et parce-que eux, ils ont été à mes cotes ensemble. Du début à la fin de la thèse. Arnaud et Florent, vous m'avez appris la plus grand part des choses que maintenant j'utilise chaque jour au boulot. Je n'en vais pas faire une liste, mais il faut que vous sachiez que le scientific que je suis aujourd'hui c'est là grâce à vous. Et si maintenant je sens d'être plus sur de moi-même et de mes capacité, c'est grâce à vous. C'était énorme quand on a eu notre premier "spot" pulsé sur la camera et notre premier spectre de gain. Arnaud, toi t'était arrivé d'une conf avec un collègue pour lui montrer le bunker exactement au bon moment! On a crié et réjoui, Flo ne voulait pas aller à l'escrime et on a bossé jusqu'à tard pour profiter de ce qu'on avait trouvé. Ça c'est un bon souvenir. T'avais même appris un peu l'italien (avec des bons résultats) et je me souviens du petit livre de Baptiste! "Giuseppe, ça va?" chaque fois que tu venait quand t'avais plus de nouvelles quand j'étais enfermé au bunker pour aligner plus de 6 m de chemin optique! J'ai même une chanson que depuis la thèse est lié à toi. C'est *Blowing in the wind*.

Je ne oubli pas, Flo, toutes les fois qu'on a pu démonté notre canon. Monter et descendre de l'échelle avec une *housing*, en équilibre comme au cirque. Mais surtout, je ne peut pas oublier la mission à Nantes, quand on est aller chercher un autre HF2000. L'avion qui ne pouvait pas atterrir, l'arbre tombé sur le toit du labo ("GIUSEPPE??!! QU'EST-CE-QUE T'AS FAIT??!!"), l'*hangar à bananes* et "Est-ce vous avez vu qu'est

elle est grande la Loire! C'est pas comme la Garonne chez nous!". On ne peut pas pas citer l'accident sur l'autoroute vers l'aéroport pour le retour et le fait que apparemment t'avait oublié comme on mange et boit.

J'ai un super souvenir de mon mariage à Catane, c'était superbe de vous avoir eu comme hôtes, plus en général de vous avoir eu comme directeurs de thèse et de vous avoir comme pots dans ma vie. Merci.

My french experience was not only work. Toulouse gave me the possibility to meet new friends, whom I'm still in touch with. Starting from my beloved office I would like to spend some words onto the guys I shared to office with. Dear Peter, I found a very good friend in you and I want to share some good memories I have. I remember a very personal discussion we had some months after my thesis started and the reassuring words you used. The Italy-Spain match we watched together with Simon and the time we spent in trying to buy tickets for Italy-Germany match in Bordeaux!! Your wedding in Toulouse and mine in Catania (and also the odyssey to have a new passport for Oscar!). Dinners together with Adriana, Cristina and the kids. Ridiculous beers at the Delirium bar. And finally this funny moment I have in mind during the last world cup. This image of you, completely focused on your code screens but with a disastrous Germany match in a window! All the best for you, Cristina, Simon, Oscar, Daniel and Paula. Love you all.

Ale. Ale, per te potrei spendere forse una quantità innumerevole di belle parole e sicuramente non basterebbero. Tu sei in assoluto la persona che mi è stata più vicino in assoluto a Toulouse. Dall'inizio, quando facevi le telefonate per me e ci accompagnavi (a me e mamma) in giro a cercare case, fino alla fine quando io ero incredibilmente stressato per la difesa e tu mi hai cucinato, accudito e viziato come solo qualcuno di famiglia può fare. Se ripenso a tutti i momenti che abbiamo passato insieme, mi ven-

gono le lacrime. Ti ricordi quando ci facevi le improvvisate a casa, il campanello non funzionava e lanciavi i sassolini alla finestra? "Aspetta, ma u misi u sali?" e le innumerevoli prese in giro ad Adri. Il Rio Loco con la parrucca e le magliette serigrafate, il kebab più buono del mondo e la lampada più brutta dell'universo. Gli incrontri allucinanti avuti per strada, le canzoni, le sigle dei cartoni animati come se non ci fosse un domani, "ho una nuova parola in francese!!", i soprannomi e gli ordini di agrumi dalla Sicilia. Il primo trasloco e quello improvviso per tornare a Catania. Il viaggio interminabile in macchina (panino subito dopo Genova e una coda infinita a Roma). A casa tua c'è sempre stato spazio per me e le mie cose. Nel mio cuore c'è uno spazio che ha il tuo nome. E mi manchi tanto ora che siamo distanti (solo fisicamente).

Une mentionne spéciale va à mon pot Clément, qui est arrivé au labo en tant que stagiaire de M1, après de M2 et finalement en thèse. Avec lui j'ai partagé un grand morceau de ma thèse. T'es un super copain, mec! On a passé des beaux moment ensemble, surtout le soir qu'on a fêté ma thèse et la récente mission à Nice! Mais on n'oublie pas le *pimp my burger* et heures de discussion sur les mangas, les séries et Nintendo. Je te respect profondément mec. T'es super.

Maintenant c'est à vous deux. La couple française la plus sicilienne. Aurélie et Lionel, pardon, *Lia* et *Nello*. Quoi dire? Grâce à vous j'ai découvert la vraie culture du sud-ouest. Et pas que ça! J'ai un énorme souvenir des nos soirée, cela en Dordogne avant le grand départ et toutes les petites soirées chez nous, chez vous où ailleurs. Les rivières de bière, l'escalade, dormir dans la voiture au pied d'une falaise, la bonne bouffe, les échanges culturelles. RRRrrr!!! et "c'est pour ça!". Et maintenant avec l'arrivée de *Nuccio* on a un nouveau lien! Je suis très fier d'être son *padrino*. On a toujours une chambre chez nous pour vous.

I spent a lot of good moments at CEMES and with the people working there. Merci

Cécile pour tes mots rassurants et pour avoir partagé avec moi ton expérience avec ton copain de bureau! Merci à Béa, pour ta douceur et ta disponibilité! Merci Elodie, pour avoir pris en charge une partie de mes cadeaux de thèse et pour les choix superbes! Merci Robin pour les soirées ensembles et le vélo!!

Grazie mamma e papà. Ed è inutile elencare perchè. Infine voglio lasciare i ringraziamenti finali ad Adriana, la persona che mi è stata vicina prima, durante e dopo. La ragazza che ho avuto l'onore di sposare durante questo percorso di tre anni. Toulouse CI ha regalato tanto. Ci ha permesso di vivere insieme e di iniziare a costruire nel nostro piccolo la nostra famiglia. E per questo le saremo sempre grati.

Au revoir, Toulouse!

Bibliography

[1] L. W. Swanson and G. A. Schwind. Chapter 2 A Review of the Cold-Field Electron Cathode. In *Advances in Imaging and Electron Physics*, volume 159 of *Advances in Imaging and Electron Physics*, pages 63–100. Elsevier, January 2009.

[2] A. V. Crewe, D. N. Eggenberger, J. Wall, and L. M. Welter. Electron Gun Using a Field Emission Source. *Review of Scientific Instruments*, 39(4):576–583, April 1968.

[3] Hiromi Inada, Hiroshi Kakibayashi, Shigeto Isakozawa, Takahito Hashimoto, Toshie Yaguchi, and Kuniyasu Nakamura. Chapter 4 - Hitachi's Development of Cold-Field Emission Scanning Transmission Electron Microscopes. In *Advances in Imaging and Electron Physics*, volume 159 of *Advances in Imaging and Electron Physics*, pages 123–186. Elsevier, January 2009.

[4] D. Gabor. A New Microscopic Principle. *Nature*, May 1948.

[5] Rafal E. Dunin-Borkowski, Takeshi Kasama, and Richard J. Harrison. Electron Holography of Nanostructured Materials. In *Nanocharacterisation*, pages 158–210. August 2015.

[6] O. L. Krivanek, N. Dellby, and A. R. Lupini. Towards sub-Å electron beams. *Ultramicroscopy*, 78(1):1–11, June 1999.

[7] Tetsuya Akashi, Yoshio Takahashi, Toshiaki Tanigaki, Tomokazu Shimakura, Takeshi Kawasaki, Tadao Furutsu, Hiroyuki Shinada, Heiko Müller, Maximilian Haider, Nobuyuki Osakabe, and Akira Tonomura. Aberration corrected 1.2-MV cold field-emission transmission electron microscope with a sub-50-pm resolution. *Applied Physics Letters*, 106(7):074101, February 2015.

[8] Ondrej L. Krivanek, Jonathan P. Ursin, Neil J. Bacon, George J. Corbin, Niklas Dellby, Petr Hrncirik, Matthew F. Murfitt, Christopher S. Own, and Zoltan S. Szilagyi. High-energy-resolution monochromator for aberration-corrected scanning transmission electron microscopy/electron energy-loss spectroscopy. *Philosophical Transactions. Series A, Mathematical, Physical, and Engineering Sciences*, 367(1903):3683–3697, September 2009.

[9] K. Tsuno. Monochromators in electron microscopy. *Nuclear Instruments and Methods in Physics Research Section A: Accelerators, Spectrometers, Detectors and Associated Equipment*, 645(1):12–19, July 2011.

[10] Fan Wu and Nan Yao. In Situ Transmission Electron Microscopy Studies in Gas/Liquid Environment. *Microscopy and Analysis*, 2016.

[11] DAISUKE SHINDO and Hiraga Kenji. *High-Resolution Electron Microscopy for Materials Science*. Springer Japan, 1998.

[12] Hirsch P. B. TEM in materials science—past, present and future. *Journal of Microscopy*, 155(3):361–371, August 2011.

[13] M. A. Hayat. Principles and techniques of electron microscopy. Biological applications. *Principles and techniques of electron microscopy. Biological applications.*, 1981.

[14] P. D. Gupta and H. Yamamoto. Electron microscopy in medicine and biology. *Electron microscopy in medicine and biology.*, 2000.

[15] Łukasz Mielańczyk, Natalia Matysiak, and Olesya Klymenko and Romuald Wojnicz. Transmission Electron Microscopy of Biological Samples. *The Transmission Electron Microscope - Theory and Applications*, 2015.

[16] Jacques Dubochet, Marc Adrian, Jiin-Ju Chang, Jean-Claude Homo, Jean Lepault, Alasdair W. McDowall, and Patrick Schultz. Cryo-electron microscopy of vitrified specimens. *Quarterly Reviews of Biophysics*, 21(2):129–228, May 1988.

[17] Marc Adrian, Jacques Dubochet, Jean Lepault, and Alasdair W. McDowall. Cryo-electron microscopy of viruses. *Nature*, 308(5954):32–36, March 1984.

[18] J. M. Baldwin, R. Henderson, E. Beckman, and F. Zemlin. Images of purple membrane at 2.8 Å resolution obtained by cryo-electron microscopy. *Journal of Molecular Biology*, 202(3):585–591, August 1988.

[19] M. Radermacher, V. Rao, R. Grassucci, J. Frank, A. P. Timerman, S. Fleischer, and T. Wagenknecht. Cryo-electron microscopy and three-dimensional reconstruction of the calcium release channel/ryanodine receptor from skeletal muscle. *The Journal of Cell Biology*, 127(2):411–423, October 1994.

[20] Krinsley David and Takahashi Taro. Applications of electron microscopy to geology*. *Transactions of the New York Academy of Sciences*, 25(1 Series II):3–22, April 2012.

[21] L. P. Kubin and F. Louchet. Analysis of softening in the Fe - C system from in situ and conventional experiments-I. In situ experiments. *Acta Metallurgica*, 27(3):337–342, March 1979.

[22] Aurélien Masseboeuf. In Situ Characterization Methods in Transmission Electron Microscopy. In *Transmission Electron Microscopy in Micro-Nanoelectronics*, pages 199–218. Wiley-Blackwell, January 2013.

[23] Marc Legros. In situ mechanical TEM: Seeing and measuring under stress with electrons. *Comptes Rendus Physique*, 15(2):224–240, February 2014.

[24] Clement N., Souquet S., Gerard C., and Traverse J. P. High-temperature in-situ TEM study of carbides precipitation in sintered or melted molybdenum. *physica status solidi (a)*, 141(1):109–118, February 2006.

[25] L. de Knoop, C. Gatel, F. Houdellier, M. Monthioux, A. Masseboeuf, E. Snoeck, and M. J. Hÿtch. Low-noise cold-field emission current obtained between two opposed carbon cone nanotips during in situ transmission electron microscope biasing. *Applied Physics Letters*, 106(26):263101, June 2015.

[26] K2 Direct Detection 16-Megapixel Camera — Gatan, Inc. http://www.gatan.com/products/tem-imaging-spectroscopy/k2-direct-detection-cameras.

[27] Søren B. Simonsen, Ib Chorkendorff, Søren Dahl, Magnus Skoglundh, Jens Sehested, and Stig Helveg. Direct Observations of Oxygen-induced Platinum Nanoparticle Ripening Studied by In Situ TEM. *Journal of the American Chemical Society*, 132(23):7968–7975, June 2010.

[28] Marc Legros, Daniel S. Gianola, and Kevin J. Hemker. In situ TEM observations of fast grain-boundary motion in stressed nanocrystalline aluminum films. *Acta Materialia*, 56(14):3380–3393, August 2008.

[29] O. Bostanjoglo and Th Rosin. Ultrasonically Induced Magnetic Reversals Observed by Stroboscopic Electron Microscopy. *Optica Acta: International Journal of Optics*, 24(6):657–664, June 1977.

[30] O. Bostanjoglo, R. P. Tornow, and W. Tornow. Nanosecond transmission electron microscopy and diffraction. *Journal of Physics E: Scientific Instruments*, 20(5):556, 1987.

[31] O. Bostanjoglo. High-speed electron microscopy. In Peter W. Hawkes, editor, *Advances in Imaging and Electron Physics*, volume 121 of *Electron Microscopy and Holography*, pages 1–51. Elsevier, January 2002.

[32] H. Dömer and O. Bostanjoglo. High-speed transmission electron microscope. *Review of Scientific Instruments*, 74(10):4369–4372, September 2003.

[33] T. LaGrange, M. R. Armstrong, K. Boyden, C. G. Brown, G. H. Campbell, J. D. Colvin, W. J. DeHope, A. M. Frank, D. J. Gibson, F. V. Hartemann, J. S. Kim, W. E. King, B. J. Pyke, B. W. Reed, M. D. Shirk, R. M. Shuttlesworth, B. C. Stuart, B. R. Torralva, and N. D. Browning. Single-shot dynamic transmission electron microscopy. *Applied Physics Letters*, 89(4):044105, July 2006.

[34] Vladimir A. Lobastov, Ramesh Srinivasan, and Ahmed H. Zewail. Four-dimensional ultrafast electron microscopy. *Proceedings of the National Academy of Sciences of the United States of America*, 102(20):7069–7073, May 2005.

[35] Ahmed H. Zewail. Diffraction, crystallography and microscopy beyond three dimensions: Structural dynamics in space and time. *Philosophical Transactions. Series A, Mathematical, Physical, and Engineering Sciences*, 364(1827):315–329, February 2005.

[36] Gustaaf Van Tendeloo. 4D Electron Microscopy. Imaging in Space and Time. By Ahmed H. Zewail and John M. Thomas. *Angewandte Chemie International Edition*, 50(13):2888–2888, March 2011.

[37] Ahmed H. Zewail and John Meurig Thomas. *4D Electron Microscopy: Imaging in Space and Time*. World Scientific, 2010.

[38] Andreas Gahlmann, Sang Tae Park, and Ahmed H. Zewail. Ultrashort electron pulses for diffraction, crystallography and microscopy: Theoretical and experimental resolutions. *Physical chemistry chemical physics: PCCP*, 10(20):2894–2909, May 2008.

[39] Hyun Soon Park, J. Spencer Baskin, Oh-Hoon Kwon, and Ahmed H. Zewail. Atomic-Scale Imaging in Real and Energy Space Developed in Ultrafast Electron Microscopy. *Nano Letters*, 7(9):2545–2551, September 2007.

[40] Ahmed H. Zewail. Four-Dimensional Electron Microscopy. *Science*, 328(5975):187–193, April 2010.

[41] Louis De Broglie. Waves and Quanta. *Nature*, 112(2815):540, October 1923.

[42] Max Born and Emil Wolf. *Principles of Optics: Electromagnetic Theory of Propagation, Interference and Diffraction of Light*. Elsevier, June 2013.

[43] Naoya Eguchi, Michio Oka, Yutaka Imai, Masaki Saito, and Shigeo R. Kubota. New deep-UV microscope. In *Optical Engineering for Sensing and Nanotechnology (ICOSN '99)*, volume 3740, pages 394–398. International Society for Optics and Photonics, May 1999.

[44] G. Vaschenko, C. Brewer, F. Brizuela, Y. Wang, M. A. Larotonda, B. M. Luther, M. C. Marconi, J. J. Rocca, C. S. Menoni, E. H. Anderson, W. Chao, B. D. Harteneck, J. A. Liddle, Y. Liu, and D. T. Attwood. Sub-38 nm resolution tabletop microscopy with 13 nm wavelength laser light. *Optics Letters*, 31(9):1214–1216, May 2006.

[45] Wilbur C. Bigelow. *Vacuum Methods in Electron Microscopy*. Portland Press, London, April 1994.

[46] Jon Orloff. *Handbook of Charged Particle Optics, Second Edition*. CRC Press, December 2017.

[47] R. F. Egerton. Choice of operating voltage for a transmission electron microscope. *Ultramicroscopy*, 145:85–93, October 2014.

[48] K. Tsuno. Chapter 4 - Magnetic Lenses for Electron Microscopy. In J. Orloff, editor, *Handbook Of Charged Particle Optics*. CRC Press, second edition, 2017.

[49] R. F. Egerton. Electron Optics. In *Physical Principles of Electron Microscopy*, pages 27–54. Springer, Cham, 2016.

[50] Bohumila Lencová. Chapter 5 - Electrostatic Lenses. In Jon Orloff, editor, *Handbook Of Charged Particle Optics*. CRC Press, second edition, 2017.

[51] David B. Williams and C. Barry Carter. The Instrument. In *Transmission Electron Microscopy*, pages 141–171. Springer, Boston, MA, 2009.

[52] Marc De Graef. The transmission electron microscope. In *Introduction to Conventional Transmission Electron Microscopy*, pages 136–234. Cambridge University Press, 2003.

[53] MAX Born and EMIL Wolf. CHAPTER V - GEOMETRICAL THEORY OF ABERRATIONS. In *Principles of Optics (SIXTH (CORRECTED) EDITION)*, pages 203–232. Pergamon, 1980.

[54] D. L. Misell and R. A. Crick. An estimate of the effect of chromatic aberration in electron microscopy. *Journal of Physics D: Applied Physics*, 4(11):1668, 1971.

[55] David B. Williams and C. Barry Carter. High-Resolution TEM. In *Transmission Electron Microscopy*, pages 483–509. Springer, Boston, MA, 2009.

[56] P. W. Hawkes and John C. H. Spence. *Science of Microscopy*. Springer Science & Business Media, August 2008.

[57] Maximilian Haider, Stephan Uhlemann, Eugen Schwan, Harald Rose, Bernd Kabius, and Knut Urban. Electron microscopy image enhanced. *Nature*, 392(6678):768–769, April 1998.

[58] M. Lentzen, B. Jahnen, C. L. Jia, A. Thust, K. Tillmann, and K. Urban. High-resolution imaging with an aberration-corrected transmission electron microscope. *Ultramicroscopy*, 92(3):233–242, August 2002.

[59] Knut Urban, Bernd Kabius, Max Haider, and Harald Rose. A way to higher resolution: Spherical-aberration correction in a 200 kV transmission electron microscope. *Journal of Electron Microscopy*, 48(6):821–826, January 1999.

[60] Fumio Hosokawa, Takeshi Tomita, Mikio Naruse, Toshikazu Honda, Peter Hartel, and Max Haider. A spherical aberration-corrected 200 kV TEM. *Journal of Electron Microscopy*, 52(1):3–10, 2003.

[61] Max Haider, Harald Rose, Stephan Uhlemann, Eugen Schwan, Bernd Kabius, and Knut Urban. A spherical-aberration-corrected 200kV transmission electron microscope. *Ultramicroscopy*, 75(1):53–60, October 1998.

[62] Alignment of the Transmission Electron Microscope.

[63] D. L. Smith. Focusing properties of electric and magnetic quadrupole lenses. *Nuclear Instruments and Methods*, 79(1):144–164, March 1970.

[64] R. F. Egerton. *Electron Energy-Loss Spectroscopy in the Electron Microscope*. Springer Science & Business Media, July 2011.

[65] R. F. Egerton. Energy-Loss Instrumentation. In *Electron Energy-Loss Spectroscopy in the Electron Microscope*, pages 29–109. Springer, Boston, MA, 2011.

[66] O. L. Krivanek, C. C. Ahn, and R. B. Keeney. Parallel detection electron spectrometer using quadrupole lenses. *Ultramicroscopy*, 22(1):103–115, January 1987.

[67] Ondrej L. Krivanek. United States Patent: 4743756 - Parallel-detection electron energy-loss spectrometer, May 1988.

[68] Ondrej L. Krivanek. United States Patent: 4851670 - Energy-selected electron imaging filter, July 1989.

[69] K. L. Brown and G. W. Tautfest. Faraday-Cup Monitors for High-Energy Electron Beams. *Review of Scientific Instruments*, 27(9):696–702, September 1956.

[70] David B. Williams and C. Barry Carter. How to 'See' Electrons. In *Transmission Electron Microscopy*, pages 115–126. Springer, Boston, MA, 2009.

[71] Direct electron detector, March 2009.

[72] R. N. Clough, G. Moldovan, and A. I. Kirkland. Direct Detectors for Electron Microscopy. *Journal of Physics: Conference Series*, 522(1):012046, 2014.

[73] A.R. Faruqi, R. Henderson, M. Pryddetch, P. Allport, and A. Evans. Direct single electron detection with a CMOS detector for electron microscopy. *Nuclear Instruments and Methods in Physics Research Section A: Accelerators, Spectrometers, Detectors and Associated Equipment*, 546(1-2):170–175, July 2005.

[74] G. McMullan, A. R. Faruqi, and R. Henderson. Chapter One - Direct Electron Detectors. In R. A. Crowther, editor, *Methods in Enzymology*, volume 579 of *The Resolution Revolution: Recent Advances In cryoEM*, pages 1–17. Academic Press, January 2016.

[75] Neil W. Ashcroft and N. David Mermin. *Solid State Physics*. Holt, Rinehart and Winston, 1976.

[76] Kittel. *INTRODUCTION TO SOLID STATE PHYSICS, 7TH ED.* Wiley India Pvt. Limited, 2007.

[77] Ludwig Reimer. Kinematical and Dynamical Theory of Electron Diffraction. In *Transmission Electron Microscopy*, Springer Series in Optical Sciences, pages 259–313. Springer, Berlin, Heidelberg, 1984.

[78] Shih-Lin Chang. Kinematical Theory of Diffraction. In *Multiple Diffraction of X-Rays in Crystals*, Springer Series in Solid-State Sciences, pages 35–71. Springer, Berlin, Heidelberg, 1984.

[79] P. H. Dederichs. Dynamical Diffraction Theory by Optical Potential Methods. In Henry Ehrenreich, Frederick Seitz, and David Turnbull, editors, *Solid State Physics*, volume 27, pages 135–236. Academic Press, January 1972.

[80] H. Köhler. On Abbe's Theory of Image Formation in the Microscope. *Optica Acta: International Journal of Optics*, 28(12):1691–1701, December 1981.

[81] O. Scherzer. The Theoretical Resolution Limit of the Electron Microscope. *Journal of Applied Physics*, 20(1):20–29, January 1949.

[82] David B. Williams and C. Barry Carter. Amplitude Contrast. In *Transmission Electron Microscopy*, pages 371–388. Springer, Boston, MA, 2009.

[83] J. E. Bonevich, G. Pozzi, and A. Tonomura. Electron Holography of Electromagnetic Fields. In *Introduction to Electron Holography*, pages 153–181. Springer, Boston, MA, 1999.

[84] Martin Hÿtch, Florent Houdellier, Florian Hüe, and Etienne Snoeck. Nanoscale holographic interferometry for strain measurements in electronic devices. *Nature*, 453(7198):1086–1089, June 2008.

[85] Martin Hÿtch, Florent Houdellier, Nikolay Cherkashin, Shay ReboH, Elsa Javon, Patrick Benzo, Christophe Gatel, Etienne Snoeck, and Alain Claverie. Dark-Field Electron Holography for Strain Mapping. In *Transmission Electron Microscopy in Micro-Nanoelectronics*, pages 81–106. Wiley-Blackwell, 2013.

[86] Murray Peshkin and Akira Tonomura. *The Aharonov-Bohm Effect*. Lecture Notes in Physics. Springer-Verlag, Berlin Heidelberg, 1989.

[87] Y. Aharonov and D. Bohm. Significance of electromagnetic potentials in the quantum theory. *Phys.Rev.*, 115:485–491, 1959.

[88] Y. Aharonov and D. Bohm. Further Considerations on Electromagnetic Potentials in the Quantum Theory. *Physical Review*, 123(4):1511–1524, August 1961.

[89] Akira Tonomura. The Aharonov-Bohm effect and its applications to electron phase microscopy. *Proceedings of the Japan Academy. Series B, Physical and Biological Sciences*, 82(2):45–58, April 2006.

[90] Akira Tonomura, Nobuyuki Osakabe, Tsuyoshi Matsuda, Takeshi Kawasaki, Junji Endo, Shinichiro Yano, and Hiroji Yamada. Evidence for Aharonov-Bohm effect with magnetic field completely shielded from electron wave. *Physical Review Letters*, 56(8):792–795, February 1986.

[91] J. M. Cowley. Twenty forms of electron holography. *Ultramicroscopy*, 41(4):335–348, June 1992.

[92] G. Möllenstedt. The History of the Electron Biprism. In *Introduction to Electron Holography*, pages 1–15. Springer, Boston, MA, 1999.

[93] Hannes Lichte. Gottfried Möllenstedt and his electron biprism: Four decades of challenging and exciting electron physics. *Journal of Electron Microscopy*, 47(5):387–394, January 1998.

[94] Michael Lehmann and Hannes Lichte. Tutorial on off-axis electron holography. *Microscopy and Microanalysis: The Official Journal of Microscopy Society of*

America, Microbeam Analysis Society, Microscopical Society of Canada, 8(6):447–466, December 2002.

[95] Hannes Lichte and Michael Lehmann. Electron holography—basics and applications. *Reports on Progress in Physics*, 71(1):016102, 2008.

[96] Edgar Völkl, Lawrence F. Allard, and David C. Joy, editors. *Introduction to Electron Holography*. Springer US, 1999.

[97] J. W. Gadzuk and E. W. Plummer. Field Emission Energy Distribution (FEED). *Reviews of Modern Physics*, 45(3):487–548, July 1973.

[98] George N. Fursey. *Field Emission in Vacuum Microelectronics*. Microdevices. Kluwer Academic/Plenum Publishers, 1 edition, 2005.

[99] Metal-Semiconductor Contacts. In *Physics of Semiconductor Devices*, pages 134–196. Wiley-Blackwell, 2006.

[100] Owen Willans Richardson. *On the Negative Radiation from Hot Platinum ...* University Press, 1901.

[101] ISI 2 Pin Base Tungsten Filaments. https://www.microtonano.com/Electron-Microscopy-Supplies/ISI-2-Pin-Base-Tungsten-Filaments.php.

[102] CeBix Cathodes. http://www.a-p-tech.com/cebix-cathodes.html.

[103] G. A. Schwind, G. Magera, and L. W. Swanson. Comparison of parameters for Schottky and cold field emission sources. *Journal of Vacuum Science & Technology B: Microelectronics and Nanometer Structures Processing, Measurement, and Phenomena*, 24(6):2897–2901, November 2006.

[104] W. P. Dyke, J. K. Trolan, W. W. Dolan, and George Barnes. The Field Emitter: Fabrication, Electron Microscopy, and Electric Field Calculations. *Journal of Applied Physics*, 24(5):570–576, May 1953.

[105] R. H. Fowler, F. R. S, and Dr L. Nordheim. Electron emission in intense electric fields. *Proc. R. Soc. Lond. A*, 119(781):173–181, May 1928.

[106] J. P. Ibe, P. P. Bey, S. L. Brandow, R. A. Brizzolara, N. A. Burnham, D. P. DiLella, K. P. Lee, C. R. K. Marrian, and R. J. Colton. On the electrochemical etching of tips for scanning tunneling microscopy. *Journal of Vacuum Science & Technology A: Vacuum, Surfaces, and Films*, 8(4):3570–3575, July 1990.

[107] Reiner Bormann, Stefanie Strauch, Sascha Schäfer, and Claus Ropers. An ultrafast electron microscope gun driven by two-photon photoemission from a nanotip cathode. *Journal of Applied Physics*, 118(17):173105, November 2015.

[108] Foundry - Lexicon. https://www.giessereilexikon.com/en/foundry-lexicon/Encyclopedia/show/scanning-electron-microscope-3234/.

[109] M. J. Fransen, J. S. Faber, Th. L. van Rooy, P. C. Tiemeijer, and P. Kruit. Experimental evaluation of the extended Schottky model for ZrO/W electron emission. *Journal of Vacuum Science & Technology B: Microelectronics and Nanometer Structures Processing, Measurement, and Phenomena*, 16(4):2063–2072, July 1998.

[110] M. J. Fransen, Th. L. Van Rooy, P. C. Tiemeijer, M. H. F. Overwijk, J. S. Faber, and P. Kruit. On the Electron-Optical Properties of the ZrO/W Schottky Electron Emitter. In Peter W. Hawkes, editor, *Advances in Imaging and Electron Physics*, volume 111, pages 91–166. Elsevier, January 1999.

[111] M. S. Bronsgeest, J. E. Barth, L. W. Swanson, and P. Kruit. Probe current, probe size, and the practical brightness for probe forming systems. *Journal of Vacuum Science & Technology B: Microelectronics and Nanometer Structures Processing, Measurement, and Phenomena*, 26(3):949–955, April 2008.

[112] Arnaud Arbouet, Giuseppe M. Caruso, and Florent Houdellier. Chapter One - Ultrafast Transmission Electron Microscopy: Historical Development, Instrumentation, and Applications. In *Advances in Imaging and Electron Physics*, volume 207, pages 1–72. Elsevier, January 2018.

[113] Hannes Lichte and Bert Freitag. Inelastic electron holography. *Ultramicroscopy*, 81(3):177–186, April 2000.

[114] Angus I. Kirkland, Shery L.-Y. Chang, and John L. Hutchison. Atomic Resolution Transmission Electron Microscopy. In *Science of Microscopy*, pages 3–64. Springer, New York, NY, 2007.

[115] T. LaGrange, B. Reed, W. DeHope, R. Shuttlesworth, and G. Huete. Movie Mode Dynamic Transmission Electron Microscopy (DTEM): Multiple Frame Movies of Transient States in Materials with Nanosecond Time Resolution. *Microscopy and Microanalysis*, 17(S2):458–459, July 2011.

[116] Thomas LaGrange, Bryan W. Reed, and Daniel J. Masiel. Movie-mode dynamic electron microscopy. *MRS Bulletin*, 40(1):22–28, January 2015.

[117] Bernd Hüttner. Femtosecond Laser Pulse Interactions with Metals. In *The Theory of Laser Materials Processing*, Springer Series in Materials Science, pages 315–337. Springer, Dordrecht, 2009.

[118] Sergei I. Anisimov and Baerbel Rethfeld. Theory of ultrashort laser pulse interaction with a metal. In *Nonresonant Laser-Matter Interaction (NLMI-9)*, volume 3093, pages 192–204. International Society for Optics and Photonics, April 1997.

[119] Albert Einstein. Concerning an heuristic point of view toward the emission and transformation of light. *Annalen Phys.*, 17:132–148, 1905.

[120] R Yen, J Liu, and N Bloembergen. *Thermally Assisted Multiphoton Photoelectric Emission from Tungsten*, volume 35. November 1980.

[121] Martin Weinelt. Time-resolved two-photon photoemission from metal surfaces. *Journal of Physics: Condensed Matter*, 14(43):R1099, 2002.

[122] J. H. Bechtel, W. Lee Smith, and N. Bloembergen. Two-photon photoemission from metals induced by picosecond laser pulses. *Physical Review B*, 15(10):4557–4563, May 1977.

[123] M. V. Fedorov. L. V. Keldysh's "Ionization in the Field of a Strong Electromagnetic Wave" and modern physics of atomic interaction with a strong laser field. *Journal of Experimental and Theoretical Physics*, 122(3):449–455, March 2016.

[124] L. V. Keldysh. IONIZATION IN THE FIELD OF A STRONG ELECTROMAGNETIC WAVE. *Zh. Eksperim. i Teor. Fiz.*, Vol: 47, November 1964.

[125] Hirofumi Yanagisawa, Matthias Hengsberger, Dominik Leuenberger, Martin Klöckner, Christian Hafner, Thomas Greber, and Jürg Osterwalder. Energy Distribution Curves of Ultrafast Laser-Induced Field Emission and Their Implications for Electron Dynamics. *Physical Review Letters*, 107(8):087601, August 2011.

[126] Hirofumi Yanagisawa, Christian Hafner, Patrick Doná, Martin Klöckner, Dominik Leuenberger, Thomas Greber, Jürg Osterwalder, and Matthias Hengsberger. Laser-induced field emission from a tungsten tip: Optical control of emission sites and the emission process. *Physical Review B*, 81(11):115429, March 2010.

[127] Hirofumi Yanagisawa, Sascha Schnepp, Christian Hafner, Matthias Hengsberger, Dong Eon Kim, Matthias F. Kling, Alexandra Landsman, Lukas Gallmann, and Jürg Osterwalder. Delayed electron emission in strong-field driven tunnelling from a metallic nanotip in the multi-electron regime. *Scientific Reports*, 6:35877, October 2016.

[128] L. Wu and L. K. Ang. Nonequilibrium model of ultrafast laser-induced electron photofield emission from a dc-biased metallic surface. *Physical Review B*, 78(22):224112, December 2008.

[129] Bao-Liang Qian and Hani E. Elsayed-Ali. Comment on "Ultrafast electron optics: Propagation dynamics of femtosecond electron packets" [J. Appl. Phys. 92, 1643 (2002)]. *Journal of Applied Physics*, 94(1):803–806, June 2003.

[130] S. Passlack, S. Mathias, O. Andreyev, D. Mittnacht, M. Aeschlimann, and M. Bauer. Space charge effects in photoemission with a low repetition, high intensity femtosecond laser source. *Journal of Applied Physics*, 100(2):024912, July 2006.

[131] Y. Kubo, C. Gatel, E. Snoeck, and F. Houdellier. Optimising electron microscopy experiment through electron optics simulation. *Ultramicroscopy*, 175:67–80, April 2017.

[132] Peter Hommelhoff, Yvan Sortais, Anoush Aghajani-Talesh, and Mark A. Kasevich. Field Emission Tip as a Nanometer Source of Free Electron Femtosecond Pulses. *Physical Review Letters*, 96(7):077401, February 2006.

[133] Peter Hommelhoff, Catherine Kealhofer, and Mark A. Kasevich. Ultrafast Electron Pulses from a Tungsten Tip Triggered by Low-Power Femtosecond Laser Pulses. *Physical Review Letters*, 97(24):247402, December 2006.

[134] C. Ropers, D. R. Solli, C. P. Schulz, C. Lienau, and T. Elsaesser. Localized Multiphoton Emission of Femtosecond Electron Pulses from Metal Nanotips. *Physical Review Letters*, 98(4):043907, January 2007.

[135] Ding-Shyue Yang, Omar F. Mohammed, and Ahmed H. Zewail. Scanning ultrafast electron microscopy. *Proceedings of the National Academy of Sciences*, 107(34):14993–14998, August 2010.

[136] Omar F. Mohammed, Ding-Shyue Yang, Samir Kumar Pal, and Ahmed H. Zewail. 4D Scanning Ultrafast Electron Microscopy: Visualization of Materials Surface Dynamics. *Journal of the American Chemical Society*, 133(20):7708–7711, May 2011.

[137] Armin Feist, Nora Bach, Nara Rubiano da Silva, Thomas Danz, Marcel Möller, Katharina E. Priebe, Till Domröse, J. Gregor Gatzmann, Stefan Rost, Jakob Schauss, Stefanie Strauch, Reiner Bormann, Murat Sivis, Sascha Schäfer, and Claus Ropers. Ultrafast transmission electron microscopy using a laser-driven field emitter: Femtosecond resolution with a high coherence electron beam. *Ultramicroscopy*, 176(Supplement C):63–73, May 2017.

[138] Dominik Ehberger, Jakob Hammer, Max Eisele, Michael Krüger, Jonathan Noe, Alexander Högele, and Peter Hommelhoff. Highly Coherent Electron Beam from a Laser-Triggered Tungsten Needle Tip. *Physical Review Letters*, 114(22):227601, June 2015.

[139] Nahid Talebi. Spectral Interferometry with Electron Microscopes. *Scientific Reports*, 6:33874, September 2016.

[140] Giuseppe Mario Caruso, Florent Houdellier, Pierre Abeilhou, and Arnaud Arbouet. Development of an ultrafast electron source based on a cold-field emission gun for ultrafast coherent TEM. *Applied Physics Letters*, 111(2):023101, July 2017.

[141] R. F. Egerton, Y. Y. Yang, and S. C. Cheng. Characterization and use of the Gatan 666 parallel-recording electron energy-loss spectrometer. *Ultramicroscopy*, 48(3):239–250, March 1993.

[142] Arnaud Arbouet and Florent Houdellier. Device and method for electron emission and device including such an electron emission system, February 2016.

[143] David A Dahl. Simion for the personal computer in reflection. *International Journal of Mass Spectrometry*, 200(1):3–25, December 2000.

[144] SIMION® Ion and Electron Optics Simulator. http://simion.com/.

[145] Bohumila Lencová and Jakub Zlámal. A new program for the design of electron microscopes. *Physics Procedia*, 1(1):315–324, August 2008.

[146] EOD - Electron Optical Design software, electron and ion optics. http://www.lencova.com/.

[147] COMSOL Multiphysics® Modeling Software. https://www.comsol.it/.

[148] Hideo Todokoro, Norio Saitou, and Shigehiko Yamamoto. Role of Ion Bombardment in Field Emission Current Instability. *Japanese Journal of Applied Physics*, 21(Part 1, No. 10):1513–1516, October 1982.

[149] A. Van Der Ziel. Flicker Noise in Electronic Devices. In L. Marton and C. Marton, editors, *Advances in Electronics and Electron Physics*, volume 49, pages 225–297. Academic Press, January 1979.

[150] Sergei I. Anisimov, V. A. Benderskiĭ, and G. Farkas. Nonlinear photoelectric emission from metals induced by a laser radiation. *Soviet Physics Uspekhi*, 20(6):467, 1977.

[151] David B. Williams and C. Barry Carter. Electron Sources. In *Transmission Electron Microscopy*, pages 73–89. Springer, Boston, MA, 2009.

[152] S. A. Hilbert, A. Neukirch, C. J. G. J. Uiterwaal, and H. Batelaan. Exploring temporal and rate limits of laser-induced electron emission. *Journal of Physics B: Atomic, Molecular and Optical Physics*, 42(14):141001, 2009.

[153] Sang Tae Park, Milo Lin, and Ahmed H. Zewail. Photon-induced near-field electron microscopy (PINEM): Theoretical and experimental. *New Journal of Physics*, 12(12):123028, 2010.

[154] A. Howie. Electrons and photons: Exploiting the connection. *Inst. Phys. Conf. Ser.*, 161(7):311, 1999.

[155] O. Stéphan, D. Taverna, M. Kociak, K. Suenaga, L. Henrard, and C. Colliex. Dielectric response of isolated carbon nanotubes investigated by spatially resolved

electron energy-loss spectroscopy: From multiwalled to single-walled nanotubes. *Physical Review B*, 66(15):155422, October 2002.

[156] F. J. García de Abajo and M. Kociak. Electron energy-gain spectroscopy. *New Journal of Physics*, 10(7):073035, 2008.

[157] Brett Barwick, David J. Flannigan, and Ahmed H. Zewail. Photon-induced near-field electron microscopy. *Nature*, 462(7275):902, December 2009.

[158] W. D. Kimura, G. H. Kim, R. D. Romea, L. C. Steinhauer, I. V. Pogorelsky, K. P. Kusche, R. C. Fernow, X. Wang, and Y. Liu. Laser Acceleration of Relativistic Electrons Using the Inverse Cherenkov Effect. *Physical Review Letters*, 74(4):546–549, January 1995.

[159] P. L. Kapitza and P. a. M. Dirac. The reflection of electrons from standing light waves. *Mathematical Proceedings of the Cambridge Philosophical Society*, 29(2):297–300, May 1933.

[160] Daniel L. Freimund, Kayvan Aflatooni, and Herman Batelaan. Observation of the Kapitza–Dirac effect. *Nature*, 413(6852):142–143, September 2001.

[161] P. H. Bucksbaum, D. W. Schumacher, and M. Bashkansky. High-Intensity Kapitza-Dirac Effect. *Physical Review Letters*, 61(10):1182–1185, September 1988.

[162] K. Mizuno, J. Pae, T. Nozokido, and K. Furuya. Experimental evidence of the inverse Smith–Purcell effect. *Nature*, 328(6125):45, July 1987.

[163] L. D. Landau and E. M. Lifshitz. CHAPTER 3 - CHARGES IN ELECTROMAGNETIC FIELDS. In L. D. Landau and E. M. Lifshitz, editors, *The Classical*

Theory of Fields (Fourth Edition), volume 2 of *Course of Theoretical Physics*, pages 43–65. Pergamon, Amsterdam, January 1975.

[164] Sang Tae Park, Oh-Hoon Kwon, and Ahmed H. Zewail. Chirped imaging pulses in four-dimensional electron microscopy: Femtosecond pulsed hole burning. *New Journal of Physics*, 14(5):053046, 2012.

[165] L. Veisz, G. Kurkin, K. Chernov, V. Tarnetsky, A. Apolonski, F. Krausz, and E. Fill. Hybrid dc–ac electron gun for fs-electron pulse generation. *New Journal of Physics*, 9(12):451, 2007.

[166] G. H. Kassier, K. Haupt, N. Erasmus, E. G. Rohwer, and H. Schwoerer. Achromatic reflectron compressor design for bright pulses in femtosecond electron diffraction. *Journal of Applied Physics*, 105(11):113111, June 2009.

[167] Sang Tae Park and Ahmed H. Zewail. Enhancing image contrast and slicing electron pulses in 4D near field electron microscopy. *Chemical Physics Letters*, 521:1–6, January 2012.

[168] Mohammed T. Hassan, Haihua Liu, John Spencer Baskin, and Ahmed H. Zewail. Photon gating in four-dimensional ultrafast electron microscopy. *Proceedings of the National Academy of Sciences*, 112(42):12944–12949, October 2015.

[169] David C. Joy, Y. S. Zhang, X. Zhang, T. Hashimoto, R. D. Bunn, L. Allard, and T. A. Nolan. Practical aspects of electron holography. *Ultramicroscopy*, 51(1):1–14, June 1993.

[170] Ken Harada, Akira Tonomura, Yoshihiko Togawa, Tetsuya Akashi, and Tsuyoshi Matsuda. Double-biprism electron interferometry. *Applied Physics Letters*, 84(17):3229–3231, April 2004.

[171] Florent Houdellier. *Contribution Au Développement Du CBED et de l'holographie HREM Pour l'analyse Des Déformations de Couches Épitaxiées*. Toulouse, INSA, January 2006.

[172] Alex Harscher and Hannes Lichte. Experimental study of amplitude and phase detection limits in electron holography. *Ultramicroscopy*, 64(1):57–66, August 1996.

[173] W. J. de Ruijter and J. K. Weiss. Detection limits in quantitative off-axis electron holography. *Ultramicroscopy*, 50(3):269–283, August 1993.

[174] Michael Lehmann. Influence of the elliptical illumination on acquisition and correction of coherent aberrations in high-resolution electron holography. *Ultramicroscopy*, 100(1):9–23, July 2004.

[175] Shery L. Y. Chang, Christian Dwyer, Chris B. Boothroyd, and Rafal E. Dunin-Borkowski. Optimising electron holography in the presence of partial coherence and instrument instabilities. *Ultramicroscopy*, 151:37–45, April 2015.

[176] Victor Boureau, Robert McLeod, Benjamin Mayall, and David Cooper. Off-axis electron holography combining summation of hologram series with double-exposure phase-shifting: Theory and application. *Ultramicroscopy*, 193:52–63, October 2018.

[177] C. Gatel, J. Dupuy, F. Houdellier, and M. J. Hÿtch. Unlimited acquisition time in electron holography by automated feedback control of transmission electron microscope. *Applied Physics Letters*, 113(13):133102, September 2018.